

UC Merced

UC Merced Electronic Theses and Dissertations

Title

Systems Biology Interrogation of Mammalian Cellular Metabolism

Permalink

<https://escholarship.org/uc/item/06x1s12m>

Author

Singh, Simar Jeet

Publication Date

2018

Peer reviewed|Thesis/dissertation

UNIVERSITY OF CALIFORNIA, MERCED

Systems Biology Interrogation of Mammalian Cellular Metabolism

by

Simar J. Singh

A dissertation submitted in partial fulfillment for the
degree of Doctor of Philosophy

in the

Program for Quantitative & Systems Biology
School of Natural Sciences

August 2018

Committee in charge:

Professor Fabian V. Filipp, Advisor

Professor Andy LiWang, Chair

Professor Michael Cleary

Professor Axel Visel

Copyright
Simar Jeet Singh, 2018
All rights reserved

The Dissertation of Simar Jeet Singh is approved, and it is acceptable in quality and form for publication on microfilm and electronically:

Professor Fabian V. Filipp, Advisor

Professor Andy LiWang, Chair

Professor Michael Cleary

Professor Axel Visel

University of California, Merced
2018

*“The woods are lovely, dark and deep,
But I have promises to keep,
And miles to go before I sleep,
And miles to go before I sleep.”*

Robert Frost

UNIVERSITY OF CALIFORNIA, MERCED

Abstract

Program for Quantitative & Systems Biology
School of Natural Sciences

Doctor of Philosophy

by Simar J. Singh

Cellular metabolism is a defining feature in every physiologic and pathologic process. Through advances in metabolomics, systems biologists can now track the dynamic interactions of the metabolome with the epigenome, genome, transcriptome and proteome. Metabolomics as an analytical platform is still in its infancy, and the quality of data is highly dependent on sample preparation, including derivatization for gas chromatography coupled mass spectrometry (GCMS). Using a GCMS based approach, metabolism was found to play an important role in cellular proliferation, differentiation, apoptotic and autocrine signaling, and resistance to targeted cancer therapies. These results highlight how understanding cellular metabolism can provide important insights into cellular processes both in development and disease. Increased attention to how metabolism supports and regulates such diverse cellular responses will allow for more precise engineering of biological function and the identification of targeted therapies to cure disease. . . .

Acknowledgements

This work would not have been possible without the many people who have been supportive throughout my education. I am especially grateful to my advisor Dr. Fabian Filipp whose guidance, unwavering support and tireless dedication have been instrumental in my development as a scholar and a person. You have taught me to strive for excellence in all that I do. I am forever thankful for being the first of many fine graduates under your mentorship.

I would like to thank each member of my committee for their continuing support. Dr. Andy LiWang, Dr. Micheal Cleary and Dr. Axel Visel: each of you has served as a positive role model. I extend particular thanks to Dr. Visel for our timely scientific discussions and for providing the opportunity to conduct experiments with your research group at the Lawrence Berkeley National Laboratory.

To the many collaborators with whom I have had the pleasure of working with on the projects described in this work, I extend my sincerest thanks for your hard work, dedication and perseverance. I would like to explicitly thank the following for their contributions: Dr. Kara McCloskey and her stem cell engineering group at UC Merced; Dr. Nathan Lanning at California State University, Los Angeles and Dr. Carrie Graveel at the Van Andel Research Institute; Dr. Feng Liu and Dr. Frank Meyskens and their melanoma research groups at the University of California, Irvine; Dr. Laurent Dejean at California State University, Fresno; and Raj Shah and Dr. Suzie Chen at Rutgers.

To my fellow graduate students in the Filipp Lab, your advice, encouragement and assistance have helped me more than I can faithfully express. I look forward to watching your amazing careers take off. And a special thanks to my colleagues Rohit Gupta and Daniel Tveit for sharing with me their expertise in LaTeX.

I have been fortunate to work with an amazing group of undergraduate researchers: Ajay Singh Baniwal, Brandon Brynes, Muhammad Karabala, Kirandeep Kaur, Taranpreet Kaur, Bryan Maldonado, Franziska Mudlaff, Yanirong Phok, Aman-deep Singh Sanghera, Sandeep Kaur Sanghera, Shuan Teo and Brian Young. Your

effort, energy, and enthusiasm have been of immeasurable value. I could not have done this without you.

Finally to my family, your support, guidance and patience have made this work and all else possible. Mom, Dad, Bonnie, Vikram, Harry, Mani, Boni Chacha, Irvin Chachi, Gama and Chloe, I am forever grateful to have you in my life. You are my inspiration. ...

Contents

Abstract	iv
Acknowledgements	v
1 Introduction	1
2 Methods	22
3 Metabolic shift in density-dependent stem cell differentiation	45
4 Metabolic profiling of triple-negative breast cancer cells reveals metabolic vulnerabilities	58
5 Systems biology analysis of mitogen activated protein kinase inhibitor resistance in malignant melanoma	73
6 Increased glutaminolytic flux and activation of mitochondrial metabolism by BCL2 hyperactivity in lymphoma	86
7 Inhibition of metabotropic glutamate receptor 1 and glutaminase in GRM1-expressing melanoma restricts glutamate bioavailability	134
8 Future Studies	144
9 Conclusion	148

To my family...

Chapter 1

Introduction

1.1 Overview

Cellular metabolism is a key feature of every biological process, whether physiologic or pathologic. The advent of metabolomics as an analytical paradigm has enabled systems level interrogation of these cellular processes, with gas chromatography coupled mass spectrometry (GCMS) providing a powerful yet accessible platform for metabolomics analysis. What follow in subsequent chapters of this dissertation are a reflection of my published and submitted work applying systems biology strategies to investigate the contribution of metabolic processes to diverse cellular functions including differentiation[1], cellular proliferation[1-3], cell-cell communication[1], tumor heterogeneity[2], anti-apoptotic signaling[3], cancer resistance[4], and autocrine[5] signaling.

Author contributions to the work presented in this dissertation:

Chapter 1: Performed literature review, prepared all figures and text.

Chapter 2: Performed literature review, prepared all figures and text.

Chapter 3: Collected and analyzed the data presented in Figures 3, 4, 5, 6. Performed literature review, prepared figures, wrote manuscript.

Chapter 4: Collected and analyzed the data in Figure 1. Wrote mass spectrometry methods section of manuscript. Edited manuscript.

Chapter 5: Analyzed publicly available data presented in Figures 1, 2 and Table 1. Collected and analyzed all other data presented. Performed literature review, prepared figures, wrote text.

Chapter 6: Performed literature review, prepared all figures, wrote text.

Chapter 7: Prepared text.

References

1. **Singh SJ**, Turner W, Glaser DE, McCloskey KE, Filipp F V. Metabolic shift in density-dependent stem cell differentiation. *Cell Commun Signal*. 2017;15(1):44. doi: 10.1186/s12964-017-0173-2.
2. Lanning NJ, Castle JP, **Singh SJ**, Leon AN, Tovar EA, Sanghera A, MacKeigan JP, Filipp FV, Graveel CR. Metabolic profiling of triple-negative breast cancer cells reveals metabolic vulnerabilities. *Cancer Metab*. 2017;5(1):6. doi:10.1186/s40170-017-0168-x.
3. **Singh SJ**, Kaur K, Dejean L, Filipp FV. Increased glutaminolytic flux and activation of mitochondrial metabolism by BCL2 hyperactivity in lymphoma. *Cell Rep*. 2017. - *In Revision*
4. Zecena H, Tveit D, Wang Z, Farhat A, Panchal P, Liu J, **Singh SJ**, Sanghera A, Bainiwal A, Teo SY, Meyskens FL Jr, Liu-Smith F, Filipp FV. Systems biology analysis of mitogen activated protein kinase inhibitor resistance in malignant melanoma. *BMC Syst Biol*. 2018;12(1):33. doi:10.1186/s12918-018-0554-1.
5. Shah R*, **Singh SJ***, Filipp FV, Chen S. Inhibition of metabotropic glutamate receptor 1 (GRM1) and glutaminase (GLS) in GRM1-expressing melanoma restricts glutamate bioavailability. *Cancer Res*. 2018. - *Submitted*

* Denotes equal contribution

1.2 Background

1.2.1 Overview of Metabolism

Central carbon metabolism refers to the flow of organic molecules through glycolysis, the pentose phosphate pathway (PPP), and the tricarboxylic acid (TCA) cycle. Generally, under normoxic conditions, a molecule of glucose is oxidized in the cytosol via glycolysis to yield pyruvate, adenosine triphosphate (ATP) and reduced nicotinamide adenine dinucleotide (NADH). Pyruvate is then decarboxylated by mitochondrial pyruvate dehydrogenase (PDH) into acetyl-coenzyme A (acetyl-CoA) before further oxidation in the TCA cycle. The result of this oxidative flow is the generation of NADH and reduced flavin adenine dinucleotide (FADH₂) and the transfer of electrons to the electron transport chain (ETC). The ETC couples the flow of electrons to an electrochemical gradient by pumping protons across the inner mitochondrial membrane thereby driving ATP synthesis via oxidative phosphorylation (OXPHOS). As the final electron acceptor for the ETC, oxygen is necessary for the coupling of glycolysis to OXPHOS. In hypoxia, lactate dehydrogenase (LDH) transfers electrons from NADH to pyruvate, creating lactate and replenishing the pool of oxidized NAD⁺ for continued glycolysis, a process known as fermentation. Under idealized conditions, glycolysis, TCA cycle, and OXPHOS generate a combined 36-38 molecules of ATP per glucose molecule, while fermentation produces only 2 molecules of ATP.

Central carbon metabolism is however not a unidirectional system existing for the sole purpose of ATP generation. Rather it is a dynamic hub of metabolic pathways with numerous entry and exit points serving multiple functions. Cataplerosis refers to the exit of a metabolic intermediate, while anaplerosis refers to the entry of an intermediate metabolite into a metabolic pathway[3,6]. For example, transamination of the TCA cycle intermediate alpha-ketoglutarate (AKG) generates the multifunctional amino acid glutamate in a biosynthetic and cataplerotic reaction. Conversely, the amino acid glutamine can be imported from the extracellular space, metabolized into glutamate and then AKG, providing an alternative, replenishing fuel for the TCA cycle via anaplerosis [7-9]. These metabolic side streets provide a

flexible framework for cells to couple bioenergetics and diverse processes such as macromolecular biosynthesis, redox balance, signaling, and gene regulation[10,11]

The following sections highlight how cells engage cellular metabolism to support distinct cellular processes and the methods employed by systems biologists to understand the confluence of metabolism and cell biology.

1.2.2 Cancer metabolism

The importance of cellular metabolism in permitting cellular growth and proliferation has only recently garnered increasing attention[12]. If a cell is to divide, it must double its biomass; it will need more nucleic acids to replicate its DNA, more lipids for additional cell membrane, and more amino acids for protein synthesis. The constant need to survive and divide under diverse nutrient conditions places a premium on metabolic adaptability that is borne out during the metastatic progression and evolution of a tumor.

Metabolic reprogramming is an emerging hallmark of cancer, particularly melanoma, and is driven by the mutational activation of oncogenes and the inactivation of tumor suppressors[8,13-15]. Despite widespread heterogeneity, what is consistent across the metabolic landscape of cancer is that proliferating cells must fuel increased demands for 1) macromolecular building blocks (nucleotide, amino acid, and fatty acid synthesis), 2) high energy molecules (NADH and ATP generation), and 3) maintenance of redox balance (glutathione and peroxiredoxin synthesis)[16-20].

1.2.2.1 Glycolysis

The increased metabolic demands of highly proliferative cells are partially supported by aerobic glycolysis (the Warburg effect) which provides energy and building blocks for macromolecule biosynthesis[17,21,22]. In normoxia, melanoma cells of various oncogenic backgrounds convert 60-80% of glucose into lactate, a value that increases to 90% in hypoxia[23]. Under both normoxic and hypoxic con-

ditions, hypoxia inducible factors (HIFs) induce a transcriptional program that profoundly impacts central carbon metabolism[24,25]. Increased pyruvate dehydrogenase kinase 1 (PDK1) and decreased pyruvate dehydrogenase (PDH) activity lower mitochondrial respiration[25]. Interestingly, under hypoxia, the acetyl-CoA necessary to support fatty acid biosynthesis is partially produced via the reductive carboxylation of glutamine derived AKG, which proceeds in reverse through the TCA cycle and is dependent upon isocitrate dehydrogenase (IDH) 1 and 2[8,27]. Other glycolysis related changes included increased glucose uptake and increased LDH and pyruvate kinase expression[28 – 30].

Pyruvate kinase (PK), termed the pacemaker of glycolysis, is the terminal enzyme of glycolysis and catalyzes the irreversible dephosphorylation of phosphoenolpyruvate (PEP) to pyruvate. The oncofetal isoform of pyruvate kinase (PKM2), is unique among PK isoforms is that it may exist in a dimeric form that is capable of being regulated by both post-translational modification and allosteric interaction[29,31]. By integrating complex inputs from growth factor and metabolite signaling, PKM2 is able control the rate of glycolysis, and therefore the level of glycolytic intermediates available for biosynthetic processes, termed anaplerosis. In this fashion, increased PKM2 expression in proliferating cells provides for the generation of cellular building blocks necessary for replication.

Besides its metabolic role, several non-metabolic functions of PKM2 have been described within the nucleus. Multiple lines of evidence suggest an important role for nuclear PKM2 in regulating gene transcription. Firstly, diverse signals elicit the nuclear translocation of PKM2 from the cytosol, including phosphorylation by ERK1, acetylation on Lys 433, pro-apoptotic signaling, interleukin-3 response, lipopolyscharraide (LPS) stimulation, and interaction with the dioxygenase/demethylase JMJD5[32-37].

Within the nucleus, PKM2 acts as both a transcriptional coactivator and a protein kinase. When complexed with JMJD5, PKM2 mediates the HIF1a-mediated transcriptional reprogramming of metabolic genes in hypoxic cancer cells[34]. Nuclear PKM2 interacts with Oct-4 to enhance the transcription potential of this master transcription factor, and PKM2 interacts with phosphorylated β -catenin to

induce c-Myc expression and the subsequent Myc directed upregulation of glycolytic genes during tumorigenesis[33,38,39]. Additionally, PKM2 promotes the spatial proximity of tumor necrosis factor alpha (TNF α) alleles and their transcription by binding GA repeat nucleotides within the tnfa promoter upon LPS stimulation of murine macrophages[37].

As a protein kinase, PKM2 activates STAT3, resulting in the enhanced transcription of several proliferation related genes[40,41]. This interaction with STAT3 also promotes cell migration via STAT3-mediated expression of Snail-2 (a repressor of E-cadherin) and the upregulation of matrix metalloproteinases MMP-2 and MMP-9[42,43]. Lastly, PKM2 phosphorylates histone 3 (H3) on Thr11, a prerequisite for the dissociation of histone deacetylase 3 (HDAC3) and the subsequent acetylation on lysine 9 (H3K9Ac) near promoter regions, including the promoters of the oncogenes Myc and cyclin D1[44]. This data suggests that nuclear PKM2 plays a pivotal role in the regulation of cellular proliferation, metabolism, migration and metastasis via epigenetic and transcriptional control of gene expression. However, a comprehensive global map of nuclear PKM2 activity and regulated gene expression changes does not yet exist.

1.2.2.2 Amino acid metabolism

Serine and glycine are biosynthetically linked nutrients found at the intersection of multiple biochemical pathways important for cancer proliferation[15, 45 – 47]. Together they provide the essential precursors for the synthesis of proteins, nucleic acids, and lipids crucial to cancer growth[46,48-52]. Moreover, serine/glycine biosynthesis affects antioxidant capacity, and by fueling the folate cycle, provides one-carbon units for a diverse set of biochemical reactions including purine biosynthesis and epigenetic modifications[45,49,50,53-56]. The importance of serine/glycine metabolism is further highlighted by genetic and functional evidence indicating that over-activation of the serine/glycine biosynthetic pathway is a driver of oncogenesis[57,58]. Similar to serine, alanine is synthesized at greater rates in melanoma cells compared to melanocytes, despite both alanine and serine being abundant in plasma and cell culture media[8,23] Given that melanoma cells

generate alanine from both glycolysis and glutaminolysis, alanine bridges two highly active pathways promoting cancer cell proliferation[8,23]. Identifying the enzymes and pathways involved in alanine and amino acid metabolism.

1.2.2.3 Metabolism in stem cell fate and pluripotency

Stem cells are defined as clonogenic cells capable of both self-renewal and multi-lineage differentiation[59,60]. Traditionally, metabolism was thought to serve the basic energy demands of stem cells, in what was considered a secondary consequence of signaling pathways related to a given cell state and function[61,62]. However it is now apparent that metabolism can dictate the functional state of stem cells and control cell fate decisions[61,63,64]. Pluripotent stem cells (PSCs) are highly glycolytic, displaying elevated expression of glycolytic enzymes, decreased PDH, and high lactate production[1,65]. During differentiation however, stem cells undergo a shift away from lactate fermentation towards mitochondrial OXPHOS[1,66-68]. Moreover, induction of pluripotency in human and mouse somatic cells requires the acquisition of a highly glycolytic metabolic state, and is more efficient under hypoxia[69,70]. However, it is also clear that a functioning mitochondrial TCA cycle and ETC are also vital for the maintenance of pluripotency[66,70], indicating that a bivalent balance between glycolysis and mitochondrial metabolism regulates pluripotency.

What benefit a glycolytic predominance provides to the maintenance of pluripotency and self-renewal is unknown. In many ways, glycolysis skewed stem cells resemble cancer cells that have de-differentiated and participate in high rates of aerobic glycolysis, known as the Warburg phenomenon[21,71-73]. In cancer cells, increased glucose uptake and aerobic glycolysis supports not only ATP production, but provides precursors for macromolecule biosynthesis, including serine/glycine for folate and nucleotide production, acetyl-CoA for fatty acid synthesis and histone acetylation[23,57,74]. This glycolytic phenotype is similarly reinforced in stem cells by transcription factors including the hypoxia inducible factors (HIF). HIF1 α promotes glycolysis in cancer and stem cells by upregulating glycolytic

genes such as LDHA and PDK, the latter of which limits mitochondrial respiration by inhibiting PDH and preventing the entry of pyruvate into the TCA cycle[75-82].

1.2.2.4 Metabolism in Stem Cell Quiescence

Metabolism also regulates quiescence, a state of growth and proliferation arrest reversible by extracellular signals[83]. Quiescent hematopoietic stem cells (HSCs) maintain low mitochondrial respiration and rely on glycolysis in a HIF1 α dependent manner, but require a shift to OXPHOS for activation and differentiation[75,77-82]. In HSCs HIF1a promotes quiescence by activating PDK2/4, which also reduces cellular reactive oxygen species (ROS)[75]. Loss of HIF1a, PDK2/4, increased mitochondrial mass, and exposure to oxygen all lead to loss of quiescence, likely due to the presence of increased ROS species[75,81,84,85].

1.2.2.5 Redox metabolism in Stem Cell Function

Metabolic control of redox states during stem cell function is important because increasing ROS levels trigger differentiation and decreased ROS levels limit differentiation of several quiescent stem cell populations[86-89]. Moreover, low ROS levels are required for self-renewal capacity[90-92]. Aberrantly high levels of ROS lead to DNA damage, promote stem cell exhaustion and tissue damage, and accelerate stem cell aging[93,94]. A common theme that is emerging is the necessity of low levels of mitochondrial ROS for stem cell quiescence and self-renewal, and a dependence on a physiological increase in ROS to drive normal stem cell proliferation and differentiation[62].

1.2.2.6 Metabolism and the Epigenome

The link between metabolism and the regulation of the stem cell epigenome is growing[95]. Typically, DNA and histone methylation promote self-renewal and pluripotency, while demethylation leads to activation and differentiation[96]. The hypoxic bone marrow niche lowers AKG and raises succinate, thereby stabilizing

HIF1 α , and inhibiting histone demethylases (HDMs) thereby promoting HSC maintenance[97,98]. The enzymatic requirement for AKG in Jumonji C domain containing histone lysine demethylases (KDMs) is a general phenomenon linking cellular metabolic states to epigenetic modification[99-101]. Threonine catabolism is critically vital for pluripotency because it provides one-carbon units via glycine cleavage that are necessary for histone 3 methylation at lysine residue 4 (H3K4) hypomethylation of which leads to loss of self-renewal, slowed growth and differentiation[102,103].

The link between metabolism and histone acetylation is more complex. Histone acetylation by histone acetyltransferases (HATs) generally promote gene transcription while deacetylation by histone deacetylases (HDACs) generally remove open chromatin marks. HAT-mediated acetylation is intimately tied to the pool of available acetyl-CoA, which is generated in mitochondria via the catabolism of glycolytic pyruvate, amino acids, or fatty acids[104]. HDACs, such as those belonging to the NAD⁺ dependent Class III SIRT family, are regulated by the ratio of NAD⁺/NADH[105]. Metabolic shifts resulting in altered acetyl-CoA and NAD⁺ levels however have been reported to affect both HAT and HDAC function and promote both pluripotency and differentiation[99,106,107]. Aging of stem cells is linked to changes in metabolite levels, HAT/HDAC expression, and epigenetic modification, raising the possibility that modulating affecting metabolic parameters, such as NAD⁺ and acetyl-CoA production could form the basis of rejuvenation strategies aiming to improve aged stem cell function[84,99,108,109].

1.3 References

1. Singh SJ, Turner W, Glaser DE, McCloskey KE, Filipp F V. Metabolic shift in density-dependent stem cell differentiation. *Cell Commun Signal*. 2017;15(1):44. doi: 10.1186/s12964-017-0173-2.
2. Lanning NJ, Castle JP, Singh SJ, Leon AN, Tovar EA, Sanghera A, MacKeigan JP, Filipp FV, Graveel CR. Metabolic profiling of triple-negative breast cancer cells

reveals metabolic vulnerabilities. *Cancer Metab.* 2017;5(1):6. doi:10.1186/s40170-017-0168-x.

3. Singh SJ, Kaur K, Dejean L, Filipp FV. Increased glutaminolytic flux and activation of mitochondrial metabolism by BCL2 hyperactivity in lymphoma. *Cell Rep.* 2017. - *In Revision*

4. Zecena H, Tveit D, Wang Z, Farhat A, Panchal P, Liu J, Singh SJ, Sanghera A, Bainiwal A, Teo SY, Meyskens FL Jr, Liu-Smith F, Filipp FV. Systems biology analysis of mitogen activated protein kinase inhibitor resistance in malignant melanoma. *BMC Syst Biol.* 2018;12(1):33. doi:10.1186/s12918-018-0554-1.

5. Shah R*, Singh SJ*, Filipp FV, Chen S. Inhibition of metabotropic glutamate receptor 1 (GRM1) and glutaminase (GLS) in GRM1-expressing melanoma restricts glutamate bioavailability. *Cancer Res.* 2018. - *Submitted*

* Denotes equal contribution

6. Owen OE, Kalhan SC, Hanson RW. The Key Role of Anaplerosis and Catepplerosis for Citric Acid Cycle Function. *J Biol Chem.* 2002;277(34):30409-30412. doi:10.1074/jbc.R200006200.

7. Jungas RL, Halperin ML, Brosnan JT. Quantitative analysis of amino acid oxidation and related gluconeogenesis in humans. *Physiol Rev.* 1992;72(2):419-448. doi:10.1152/physrev.1992.72.2.419.

8. Filipp FV, Ratnikov B, De Ingeniis J, Smith JW, Osterman AL, Scott DA. Glutamine-fueled mitochondrial metabolism is decoupled from glycolysis in melanoma. *Pigment Cell Melanoma Res.* 2012;25(6):732-739. doi:10.1111/pcmr.12000.

9. Zhang J, Pavlova NN, Thompson CB. Cancer cell metabolism: the essential role of the nonessential amino acid, glutamine. *EMBO J.* 2017;36(10):1302-1315. doi:10.15252/embj.201696151.

10. Palm W, Thompson CB. Nutrient acquisition strategies of mammalian cells. *Nature.* 2017;546(7657):234-242. doi:10.1038/nature22379.

11. Pavlova NN, Thompson CB. The Emerging Hallmarks of Cancer Metabolism. *Cell Metab.* 2016;23(1):27-47. doi:10.1016/j.cmet.2015.12.006.
12. Filipp F. Cancer metabolism meets systems biology: Pyruvate kinase isoform PKM2 is a metabolic master regulator. *J Carcinog.* 2013;12(1):14. doi:10.4103/1477-3163.115423.
13. Hanahan D, Weinberg RA. Hallmarks of cancer: the next generation. *Cell.* 2011;144(5):646-674. doi:10.1016/j.cell.2011.02.013.
14. Filipp F V, Scott DA, Ronai ZA, Osterman AL, Smith JW. NIH Public Access. 2013;25(3):375-383. doi:10.1111/j.1755-148X.2012.00989.x.Reverse.
15. DeBerardinis RJ. Serine metabolism: some tumors take the road less traveled. *Cell Metab.* 2011;14(3):285-286. doi:10.1016/j.cmet.2011.08.004.
16. Boroughs LK, DeBerardinis RJ. Metabolic pathways promoting cancer cell survival and growth. *Nat Cell Biol.* 2015;17(4):351-359. doi:10.1038/ncb3124.
17. Vander Heiden MG, Lunt SY, Dayton TL, et al. Metabolic pathway alterations that support cell proliferation. *Cold Spring Harb Symp Quant Biol.* 2011;76(0):325-334. doi:10.1101/sqb.2012.76.010900.
18. Cantor JR, Sabatini DM. Cancer cell metabolism: one hallmark, many faces. *Cancer Discov.* 2012;2(10):881-898. doi:10.1158/2159-8290.CD-12-0345.
19. Ward PS, Thompson CB. Metabolic reprogramming: a cancer hallmark even warburg did not anticipate. *Cancer Cell.* 2012;21(3):297-308. doi:10.1016/j.ccr.2012.02.014.
20. Ward PS, Thompson CB. Signaling in control of cell growth and metabolism. *Cold Spring Harb Perspect Biol.* 2012;4(7):a006783. doi:10.1101/cshperspect.a006783.
21. WARBURG O. On the origin of cancer cells. *Science.* 1956;123(3191):309-314. doi:10.1126/SCIENCE.123.3191.309.

22. Deberardinis RJ, Sayed N, Ditsworth D, Thompson CB. Brick by brick: metabolism and tumor cell growth. *Curr Opin Genet Dev.* 2008;18(1):54-61. doi:10.1016/j.gde.2008.02.003.
23. Scott DA, Richardson AD, Filipp F V, et al. Comparative metabolic flux profiling of melanoma cell lines: beyond the Warburg effect. *J Biol Chem.* 2011;286(49):42626-42634. doi:10.1074/jbc.M111.282046.
24. Kuphal S, Winklmeier A, Warnecke C, Bosserhoff A-K. Constitutive HIF-1 activity in malignant melanoma. *Eur J Cancer.* 2010;46(6):1159-1169. doi:10.1016/j.ejca.2010.01.031.
25. Majmundar AJ, Wong WJ, Simon MC. Hypoxia-Inducible Factors and the Response to Hypoxic Stress. *Mol Cell.* 2010;40(2):294-309. doi:10.1016/j.molcel.2010.09.022.
26. Kim J, Tchernyshyov I, Semenza GL, Dang C V. HIF-1-mediated expression of pyruvate dehydrogenase kinase: A metabolic switch required for cellular adaptation to hypoxia. *Cell Metab.* 2006;3(3):177-185. doi:10.1016/j.cmet.2006.02.002.
27. Scott DA, Richardson AD, Filipp F V., et al. Comparative Metabolic Flux Profiling of Melanoma Cell Lines. *J Biol Chem.* 2011;286(49):42626-42634. doi:10.1074/jbc.M111.282046.
28. Ho J, de Moura M, Lin Y, et al. Importance of glycolysis and oxidative phosphorylation in advanced melanoma. *Mol Cancer.* 2012;11(1):76. doi:10.1186/1476-4598-11-76.
29. Filipp FV. Cancer metabolism meets systems biology: Pyruvate kinase isoform PKM2 is a metabolic master regulator. *J Carcinog.* 2013;12:14. doi:10.4103/1477-3163.115423.
30. Koch A, Lang SA, Wild PJ, et al. Glucose transporter isoform 1 expression enhances metastasis of malignant melanoma cells. *Oncotarget.* 2015;6(32):32748-32760. doi:10.18632/oncotarget.4977.

31. Chaneton B, Hillmann P, Zheng L, et al. Serine is a natural ligand and allosteric activator of pyruvate kinase M2. *Nature*. 2012;491(7424):458-462. doi:10.1038/nature11540.
32. Lv L, Xu Y-P, Zhao D, et al. Mitogenic and oncogenic stimulation of K433 acetylation promotes PKM2 protein kinase activity and nuclear localization. *Mol Cell*. 2013;52(3):340-352. doi:10.1016/j.molcel.2013.09.004.
33. Yang W, Zheng Y, Xia Y, et al. ERK1/2-dependent phosphorylation and nuclear translocation of PKM2 promotes the Warburg effect. *Nat Cell Biol*. 2012;14(12):1295-1304. doi:10.1038/ncb2629.
34. Wang H-J, Hsieh Y-J, Cheng W-C, et al. JMJD5 regulates PKM2 nuclear translocation and reprograms HIF-1-mediated glucose metabolism. *Proc Natl Acad Sci U S A*. 2014;111(1):279-284. doi:10.1073/pnas.1311249111.
35. Hoshino A, Hirst JA, Fujii H. Regulation of cell proliferation by interleukin-3-induced nuclear translocation of pyruvate kinase. *J Biol Chem*. 2007;282(24):17706-17711. doi:10.1074/jbc.M700094200.
36. Stetk A, Veress R, Ovdi J, Csermely P, Kri G, Ullrich A. Nuclear translocation of the tumor marker pyruvate kinase M2 induces programmed cell death. *Cancer Res*. 2007;67(4):1602-1608. doi:10.1158/0008-5472.CAN-06-2870.
37. Stratigi K, Kapsetaki M, Aivaliotis M, Town T, Flavell RA, Spilianakis CG. Spatial proximity of homologous alleles and long noncoding RNAs regulate a switch in allelic gene expression. *Proc Natl Acad Sci U S A*. 2015;112(13):E1577-86. doi:10.1073/pnas.1502182112.
38. Lee J, Kim HK, Han Y-M, Kim J. Pyruvate kinase isozyme type M2 (PKM2) interacts and cooperates with Oct-4 in regulating transcription. *Int J Biochem Cell Biol*. 2008;40(5):1043-1054. doi:10.1016/j.biocel.2007.11.009.
39. Yang W, Xia Y, Ji H, et al. Nuclear PKM2 regulates -catenin transactivation upon EGFR activation. *Nature*. 2011;480(7375):118-122. doi:10.1038/nature10598.

40. Demaria M, Giorgi C, Lebedzinska M, et al. A STAT3-mediated metabolic switch is involved in tumour transformation and STAT3 addiction. *Aging (Albany NY)*. 2010;2(11):823-842.
41. Demaria M, Poli V. PKM2, STAT3 and HIF-1: The Warburgs vicious circle. *JAK-STAT*. 2012;1(3):194-196. doi:10.4161/jkst.20662.
42. Yang P, Li Z, Fu R, Wu H, Li Z. Pyruvate kinase M2 facilitates colon cancer cell migration via the modulation of STAT3 signalling. *Cell Signal*. 2014;26(9):1853-1862. doi:10.1016/j.cellsig.2014.03.020.
43. Bauvois B. New facets of matrix metalloproteinases MMP-2 and MMP-9 as cell surface transducers: outside-in signaling and relationship to tumor progression. *Biochim Biophys Acta*. 2012;1825(1):29-36. doi:10.1016/j.bbcan.2011.10.001.
44. Yang W, Xia Y, Hawke D, et al. PKM2 phosphorylates histone H3 and promotes gene transcription and tumorigenesis. *Cell*. 2012;150(4):685-696. doi:10.1016/j.cell.2012.07.018.
45. Locasale JW. Serine, glycine and one-carbon units: cancer metabolism in full circle. *Nat Rev Cancer*. 2013;13(8):572-583. doi:10.1038/nrc3557.
46. Dann SG, Abraham RT. Serine biosynthesis: fuel for the melanoma cell growth engine. 2011:1-2. doi:10.1038/ng.890.doi.
47. Kalhan SC, Hanson RW. Resurgence of Serine: An Often Neglected but Indispensable Amino Acid. *J Biol Chem*. 2012;287(24):19786-19791. doi:10.1074/jbc.R112.357194.
48. Jain M, Nilsson R, Sharma S, et al. Metabolite profiling identifies a key role for glycine in rapid cancer cell proliferation. *Science*. 2012;336(6084):1040-1044. doi:10.1126/science.1218595.
49. Tedeschi PM, Markert EK, Gounder M, et al. Contribution of serine, folate and glycine metabolism to the ATP, NADPH and purine requirements of cancer cells. *Cell Death Dis*. 2013;4(10):e877. doi:10.1038/cddis.2013.393.

-
50. Vazquez A, Tedeschi PM, Bertino JR. Overexpression of the mitochondrial folate and glycine-serine pathway: a new determinant of methotrexate selectivity in tumors. *Cancer Res.* 2013;73(2):478-482. doi:10.1158/0008-5472.CAN-12-3709.
51. Amelio I, Cutruzzol F, Antonov A, Agostini M, Melino G. Serine and glycine metabolism in cancer. *Trends Biochem Sci.* 2014;39(4):191-198. doi:10.1016/j.tibs.2014.02.004.
52. Kim D, Fiske BP, Birsoy K, et al. SHMT2 drives glioma cell survival in ischaemia but imposes a dependence on glycine clearance. *Nature.* 2015. doi:10.1038/nature14363.
53. Maddocks ODK, Berkers CR, Mason SM, et al. Serine starvation induces stress and p53-dependent metabolic remodelling in cancer cells. *Nature.* 2013;493(7433):542-546. doi:10.1038/nature11743.
54. Labuschagne CF, van den Broek NJF, Mackay GM, Vousden KH, Maddocks ODK. Serine, but not glycine, supports one-carbon metabolism and proliferation of cancer cells. *Cell Rep.* 2014;7(4):1248-1258. doi:10.1016/j.celrep.2014.04.045.
55. Katada S, Imhof A, Sassone-Corsi P. Connecting threads: epigenetics and metabolism. *Cell.* 2012;148(1-2):24-28. doi:10.1016/j.cell.2012.01.001.
56. Ye J, Fan J, Venneti S, et al. Serine Catabolism Regulates Mitochondrial Redox Control during Hypoxia. *Cancer Discov.* 2014;4(12):1406-1417. doi:10.1158/2159-8290.CD-14-0250.
57. Locasale JW, Grassian AR, Melman T, et al. Phosphoglycerate dehydrogenase diverts glycolytic flux and contributes to oncogenesis. *Nat Genet.* 2011;43(9):869-874. doi:10.1038/ng.890.
58. Possemato R, Marks KM, Shaul YD, et al. Functional genomics reveal that the serine synthesis pathway is essential in breast cancer. *Nature.* 2011;476(7360):346-350. doi:10.1038/nature10350.
59. Weissman IL. Stem cells: units of development, units of regeneration, and units in evolution. *Cell.* 2000;100(1):157-168.

60. TILL JE, McCULLOCH EA. A direct measurement of the radiation sensitivity of normal mouse bone marrow cells. *Radiat Res.* 1961;14:213-222.
61. Shyh-Chang N, Daley GQ, Cantley LC. Stem cell metabolism in tissue development and aging. *Development.* 2013;140(12):2535-2547. doi:10.1242/dev.091777.
62. Chandel NS, Jasper H, Ho TT, Passegu E. Metabolic regulation of stem cell function in tissue homeostasis and organismal ageing. *Nat Cell Biol.* 2016;18(8):823-832. doi:10.1038/ncb3385.
63. Kohli L, Passegu E. Surviving change: the metabolic journey of hematopoietic stem cells. *Trends Cell Biol.* 2014;24(8):479-487. doi:10.1016/j.tcb.2014.04.001.
64. Folmes CDL, Dzeja PP, Nelson TJ, Terzic A. Metabolic Plasticity in Stem Cell Homeostasis and Differentiation. *Cell Stem Cell.* 2012;11(5):596-606. doi:10.1016/j.stem.2012.10.002.
65. Teslaa T, Teitell MA. Pluripotent stem cell energy metabolism: an update. *EMBO J.* 2015;34(2):138-153. doi:10.15252/embj.201490446.
66. Cho YM, Kwon S, Pak YK, et al. Dynamic changes in mitochondrial biogenesis and antioxidant enzymes during the spontaneous differentiation of human embryonic stem cells. *Biochem Biophys Res Commun.* 2006;348(4):1472-1478. doi:10.1016/j.bbrc.2006.08.020.
67. Hom JR, Quintanilla RA, Hoffman DL, et al. The Permeability Transition Pore Controls Cardiac Mitochondrial Maturation and Myocyte Differentiation. *Dev Cell.* 2011;21(3):469-478. doi:10.1016/j.devcel.2011.08.008.
68. Tormos KV, Anso E, Hamanaka RB, et al. Mitochondrial Complex III ROS Regulate Adipocyte Differentiation. *Cell Metab.* 2011;14(4):537-544. doi:10.1016/j.cmet.2011.08.007.
69. Yoshida Y, Takahashi K, Okita K, Ichisaka T, Yamanaka S. Hypoxia Enhances the Generation of Induced Pluripotent Stem Cells. *Cell Stem Cell.* 2009;5(3):237-241. doi:10.1016/j.stem.2009.08.001.

-
70. Zhou W, Choi M, Margineantu D, et al. HIF1 induced switch from bivalent to exclusively glycolytic metabolism during ESC-to-EpiSC/hESC transition. *EMBO J.* 2012;31(9):2103-2116. doi:10.1038/emboj.2012.71.
71. Christofk HR, Vander Heiden MG, Harris MH, et al. The M2 splice isoform of pyruvate kinase is important for cancer metabolism and tumour growth. *Nature.* 2008;452(7184):230-233. doi:10.1038/nature06734.
72. Figueroa ME, Abdel-Wahab O, Lu C, et al. Leukemic IDH1 and IDH2 Mutations Result in a Hypermethylation Phenotype, Disrupt TET2 Function, and Impair Hematopoietic Differentiation. *Cancer Cell.* 2010;18(6):553-567. doi:10.1016/j.ccr.2010.11.015.
73. Lu C, Ward PS, Kapoor GS, et al. IDH mutation impairs histone demethylation and results in a block to cell differentiation. *Nature.* 2012;483(7390):474-478. doi:10.1038/nature10860.
74. Ratnikov BI, Scott DA, Osterman AL, Smith JW, Ronai ZA. Metabolic rewiring in melanoma. *Oncogene.* 2017;36(2):147-157. doi:10.1038/onc.2016.198.
75. Takubo K, Nagamatsu G, Kobayashi CI, et al. Regulation of Glycolysis by Pdk Functions as a Metabolic Checkpoint for Cell Cycle Quiescence in Hematopoietic Stem Cells. *Cell Stem Cell.* 2013;12(1):49-61. doi:10.1016/j.stem.2012.10.011.
76. Stacpoole PW. Therapeutic Targeting of the Pyruvate Dehydrogenase Complex/Pyruvate Dehydrogenase Kinase (PDC/PDK) Axis in Cancer. *J Natl Cancer Inst.* 2017;109(11). doi:10.1093/jnci/djx071.
77. Simsek T, Kocabas F, Zheng J, et al. The Distinct Metabolic Profile of Hematopoietic Stem Cells Reflects Their Location in a Hypoxic Niche. *Cell Stem Cell.* 2010;7(3):380-390. doi:10.1016/j.stem.2010.07.011.
78. Adelman DM, Gertsenstein M, Nagy A, Simon MC, Maltepe E. Placental cell fates are regulated in vivo by HIF-mediated hypoxia responses. *Genes Dev.* 2000;14(24):3191-3203.

79. Yu W-M, Liu X, Shen J, et al. Metabolic Regulation by the Mitochondrial Phosphatase PTPMT1 Is Required for Hematopoietic Stem Cell Differentiation. *Cell Stem Cell*. 2013;12(1):62-74. doi:10.1016/j.stem.2012.11.022.
80. Maryanovich M, Zaltsman Y, Ruggiero A, et al. An MTCH2 pathway repressing mitochondria metabolism regulates haematopoietic stem cell fate. *Nat Commun*. 2015;6(1):7901. doi:10.1038/ncomms8901.
81. Takubo K, Goda N, Yamada W, et al. Regulation of the HIF-1 Level Is Essential for Hematopoietic Stem Cells. *Cell Stem Cell*. 2010;7(3):391-402. doi:10.1016/j.stem.2010.06.020.
82. Maltepe E, Schmidt J V., Baunoch D, Bradfield CA, Simon MC. Abnormal angiogenesis and responses to glucose and oxygen deprivation in mice lacking the protein ARNT. *Nature*. 1997;386(6623):403-407. doi:10.1038/386403a0.
83. Cheung TH, Rando TA. Molecular regulation of stem cell quiescence. *Nat Rev Mol Cell Biol*. 2013;14(6):329-340. doi:10.1038/nrm3591.
84. Mohrin M, Shin J, Liu Y, et al. A mitochondrial UPR-mediated metabolic checkpoint regulates hematopoietic stem cell aging. *Science* (80). 2015;347(6228):1374-1377. doi:10.1126/science.aaa2361.
85. Mantel CR, OLeary HA, Chitteti BR, et al. Enhancing Hematopoietic Stem Cell Transplantation Efficacy by Mitigating Oxygen Shock. *Cell*. 2015;161(7):1553-1565. doi:10.1016/j.cell.2015.04.054.
86. Juntilla MM, Patil VD, Calamito M, Joshi RP, Birnbaum MJ, Koretzky GA. AKT1 and AKT2 maintain hematopoietic stem cell function by regulating reactive oxygen species. *Blood*. 2010;115(20):4030-4038. doi:10.1182/blood-2009-09-241000.
87. Malinska D, Kudin AP, Bejtka M, Kunz WS. Changes in mitochondrial reactive oxygen species synthesis during differentiation of skeletal muscle cells. *Mitochondrion*. 2012;12(1):144-148. doi:10.1016/j.mito.2011.06.015.
88. Biteau B, Jasper H. EGF signaling regulates the proliferation of intestinal stem cells in *Drosophila*. *Development*. 2011;138(6):1045-1055. doi:10.1242/dev.056671.

-
89. Hamanaka RB, Glasauer A, Hoover P, et al. Mitochondrial reactive oxygen species promote epidermal differentiation and hair follicle development. *Sci Signal*. 2013;6(261):ra8. doi:10.1126/scisignal.2003638.
90. Morimoto H, Iwata K, Ogonuki N, et al. ROS Are Required for Mouse Spermatogonial Stem Cell Self-Renewal. *Cell Stem Cell*. 2013;12(6):774-786. doi:10.1016/j.stem.2013.04.001.
91. Le Belle JE, Orozco NM, Paucar AA, et al. Proliferative Neural Stem Cells Have High Endogenous ROS Levels that Regulate Self-Renewal and Neurogenesis in a PI3K/Akt-Dependant Manner. *Cell Stem Cell*. 2011;8(1):59-71. doi:10.1016/j.stem.2010.11.028.
92. Paul MK, Bisht B, Darmawan DO, et al. Dynamic Changes in Intracellular ROS Levels Regulate Airway Basal Stem Cell Homeostasis through Nrf2-Dependent Notch Signaling. *Cell Stem Cell*. 2014;15(2):199-214. doi:10.1016/j.stem.2014.05.009.
93. Bakker ST, Passegu E. Resilient and resourceful: Genome maintenance strategies in hematopoietic stem cells. *Exp Hematol*. 2013;41(11):915-923. doi:10.1016/j.exphem.2013.09.007.
94. Adams PD, Jasper H, Rudolph KL. Aging-Induced Stem Cell Mutations as Drivers for Disease and Cancer. *Cell Stem Cell*. 2015;16(6):601-612. doi:10.1016/j.stem.2015.05.002.
95. Keating ST, El-Osta A. Epigenetics and Metabolism. *Circ Res*. 2015;116(4):715-736. doi:10.1161/CIRCRESAHA.116.303936.
96. Beerman I, Rossi DJ. Epigenetic Control of Stem Cell Potential during Homeostasis, Aging, and Disease. *Cell Stem Cell*. 2015;16(6):613-625. doi:10.1016/j.stem.2015.05.009.
97. Chinopoulos C. Which way does the citric acid cycle turn during hypoxia? The critical role of α -ketoglutarate dehydrogenase complex. *J Neurosci Res*. 2013;91(8):1030-1043. doi:10.1002/jnr.23196.

98. Koivunen P, Hirsil M, Remes AM, Hassinen IE, Kivirikko KI, Myllyharju J. Inhibition of Hypoxia-inducible Factor (HIF) Hydroxylases by Citric Acid Cycle Intermediates. *J Biol Chem.* 2007;282(7):4524-4532. doi:10.1074/jbc.M610415200.
99. Kaelin WGJ, McKnight SL. Influence of metabolism on epigenetics and disease. *Cell.* 2013;153(1):56-69. doi:10.1016/j.cell.2013.03.004.
100. Park SY, Park J-W, Chun Y-S. Jumonji histone demethylases as emerging therapeutic targets. *Pharmacol Res.* 2016;105:146-151. doi:10.1016/j.phrs.-2016.01.026.
101. Wilson S, Fan L, Sahgal N, Qi J, Filipp F V. The histone demethylase KDM3 regulates the transcriptional program of the androgen receptor in prostate cancer cells. *Oncotarget.* 2017;8(18):30328-30343. doi:10.18632/oncotarget.15681.
102. Shyh-Chang N, Locasale JW, Lyssiotis C a, et al. Influence of threonine metabolism on S-adenosylmethionine and histone methylation. *Science.* 2013;339(6116):222-226. doi:10.1126/science.1226603.
103. Wang J, Alexander P, Wu L, Hammer R, Cleaver O, McKnight SL. Dependence of Mouse Embryonic Stem Cells on Threonine Catabolism. *Science (80-).* 2009;325(5939):435-439. doi:10.1126/science.1173288.
104. Su X, Wellen KE, Rabinowitz JD. Metabolic control of methylation and acetylation. *Curr Opin Chem Biol.* 2016;30:52-60. doi:10.1016/j.cbpa.2015.10.030.
105. Imai S, Guarente L. NAD⁺ and sirtuins in aging and disease. *Trends Cell Biol.* 2014;24(8):464-471. doi:10.1016/j.tcb.2014.04.002.
106. Ryall JG, DellOrso S, Derfoul A, et al. The NAD⁺-Dependent SIRT1 Deacetylase Translates a Metabolic Switch into Regulatory Epigenetics in Skeletal Muscle Stem Cells. *Cell Stem Cell.* 2015;16(2):171-183. doi:10.1016/j.stem.2014.12.004.
107. Rimmel P, Bigarella CL, Liang R, et al. Aging-like Phenotype and Defective Lineage Specification in SIRT1-Deleted Hematopoietic Stem and Progenitor Cells. *Stem Cell Reports.* 2014;3(1):44-59. doi:10.1016/j.stemcr.2014.04.015.

-
108. Braidy N, Guillemin GJ, Mansour H, Chan-Ling T, Poljak A, Grant R. Age Related Changes in NAD⁺ Metabolism Oxidative Stress and Sirt1 Activity in Wistar Rats. Xu A, ed. PLoS One. 2011;6(4):e19194. doi:10.1371/journal.pone.001919
109. Chambers SM, Shaw CA, Gatz C, Fisk CJ, Donehower LA, Goodell MA. Aging hematopoietic stem cells decline in function and exhibit epigenetic dysregulation. PLoS Biol. 2007;5(8):e201. doi:10.1371/journal.pbio.0050201.

Chapter 2

Methods

Gas chromatography mass spectrometry (GCMS) based metabolomics is a young, rapidly evolving analytical platform consisting of sample generation and collection, metabolite extraction, derivatization, data acquisition and processing, metabolite identification and quantification, and statistical analysis. Of these, sample preparation has the biggest impact on the quality of data generated by GCMS, of which derivatization is the most variable. The optimal derivatization strategy often depends on the experimental question. The following is a review of GCMS based metabolomics with an emphasis on oximation and silylation for the derivatization of intracellular metabolites.

2.1 Introduction to Metabolomics

The term metabolome first entered the literature in 1998 when it was used to represent the entire set of molecules expressed by an organism[1]. In 2001, Fiehn defined the term metabolomics as the comprehensive and quantitative assessment of all metabolites in a biological system[2]. Several other terms have been proposed to represent specific types of metabolic analysis, such as metabonomics, metabolic footprinting and metabolic profiling, but each seeks to derive functional meaning from the quantitative analysis of metabolite levels[35].

A major limitation of many metabolomics studies is that they provide only a snapshot of the metabolome, and lack dynamic information regarding the movement of metabolites within metabolic pathways, or metabolic fluxes[6,7]. To address this, stable isotope tracing, in which one monitors the distribution of an isotope label originating on a metabolite of interest, is used to provide information of metabolic pathway activity[810].

Several analytical platforms have been applied to the field of metabolomics, namely mass spectrometry (MS) and nuclear magnetic resonance (NMR). NMR detects the magnetic spin of molecular nuclei under a defined magnetic frequency and is effective at identifying metabolites from complex mixtures, quantifying metabolite abundance, and assessing the position of specific nuclei (i.e. ^{13}C) within a metabolite of interest, all with excellent reproducibility[10,11]. Moreover, NMR has the advantage of not requiring significant sample preparation or derivatization, and is nondestructive, meaning it can be applied to *in vivo* studies[11,12]. NMR is also useful for compounds that are difficult to ionize and for compounds with identical masses, such as in isotope labeling when studying the same metabolite and its different isotopomer distributions[13]. The major weaknesses of NMR in its application to metabolomics are its relatively low sensitivity and selectivity, with highly complex spectra often difficult to deconvolute for metabolite identification and quantification[14]. Still, one dimensional ^1H NMR can be gainfully applied to specific questions in metabolomics research[15].

Mass spectrometry- (MS) based techniques detect the mass/charge (m/z) ratio of a metabolite and its fragments. While MS based techniques have higher sensitivity and specificity in comparison to NMR, analysis requires that complex mixtures of compounds first undergo a separation technique[16]. Separation reduces sample complexity, minimizes ionization suppression effects, thereby enhancing detection sensitivity and increasing metabolite coverage[16]. The separation techniques commonly employed for metabolomics research include gas chromatography (GC), liquid chromatography (LC), high-performance liquid chromatography (HPLC), ultra-performance liquid chromatography (UPLC), and capillary electrophoresis (CE). Of these, GCMS and LCMS are the most used MS platforms in metabolomics research.

GCMS is a well-accepted and widely used platform in metabolomics[1719]. GCMS instrumentation is of comparatively low cost and is easy to operate and maintain compared to NMR and other MS based platforms. While time consuming derivatization and sample preparation is necessary prior to GC separation, the structural specificity of derivatized adducts has made it easy to build dedicated spectral libraries that aid in metabolite identification[20]. Despite its time consuming sample preparation and relatively low throughput, GCMS provides a method to reliably measure several classes of metabolically important biomolecules, such as organic acids, amino acids and fatty acids in a robust and economical manner[21].

Compounds are usually identified based on their retention time in a GC column and their fragmentation pattern upon ionization in the MS. Several GC columns have been employed for metabolomics analysis. Column length, polarity, and composition of the stationary phase all affect chromatographic separation and retention time of metabolites. Most stationary phases are composed of high molecular weight, thermostable polymers, of which the polysiloxanes are amongst the most common due to their stability, robustness and versatility. Selection of a GC column depends upon the class of compounds to be analyzed.

After gas chromatographic separation, compounds are ionized and separated by m/z . Several ionization modes exist, with Electron Impact (EI) ionization the most common. Following ionization the now charged species, termed the molecular ion further decomposes to smaller fragments via predictable chemical rearrangement pathways[22]. The resulting ions are then accelerated through an ion focusing lens to a mass detector by positive voltage from the repeller electrode. Quadrupole mass analyzers, consisting of four oppositely charged rod electrodes, are commonly used because they are inexpensive and easy to use, but still have high sensitivity and a fast scan rate[21]. Mass analyzers convert the ions that reach the detector into electrons which are then amplified by an electron multiplier detector (EMD) into to a signal intensity for each m/z ratio, generating a fragmentation pattern for a given retention time.

Fragmentation patterns are then matched to curated spectral libraries. For targeted quantification of metabolites, a single specific m/z ratio is monitored, while

additional m/z ratios serve as confirming ions. The combined presence of these pre-identified, metabolite specific ions at a single retention time leads to the identification and quantification of a metabolite. Dilution series of metabolite standard mixtures of known concentrations are run and analyzed in parallel with experimental samples to yield experimental concentrations of metabolites.

The typical GCMS workflow is depicted in Figure 2.1. General steps include sample generation and collection, metabolite extraction, derivatization, data acquisition, data processing and metabolite identification, data transformation and statistical operations. Excellent instrument specific and third party software exists for the processing and analysis of GCMS data. Sample preparation has the biggest impact on the quality of data generated by GCMS, of which derivatization is perhaps the variable.

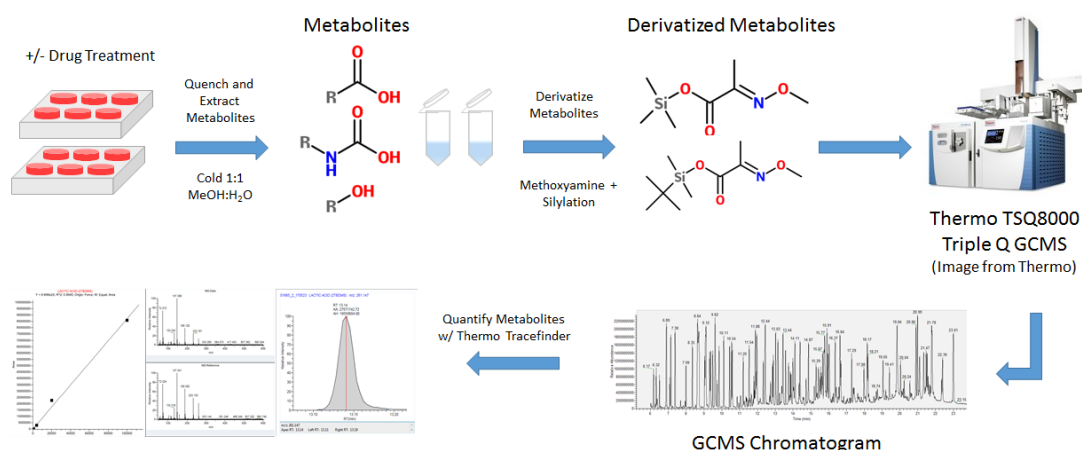


FIGURE 2.1: Typical workflow for GCMS analysis of mammalian cells.

2.1.1 Derivatization

In GCMS analysis, derivatization is defined as the modification of an analytes functionality to permit gas chromatographic separation and detection²³. Because volatility is a requirement for GCMS, derivatization is needed to render compounds sufficiently volatile for elution at reasonable temperatures without thermal decomposition or molecular rearrangement [24]. Derivatization not only optimizes the

volatility of an analyte, but also reduces polarity and adsorption in the GC system, improves detector response, peak separations, and peak symmetry[23].

Compounds capable of intermolecular hydrogen bonding (those containing -SH, -OH, -NH, =NH and COOH) necessitate derivatization as these active hydrogens affect volatility, column interaction, and thermal stability[25,26]. Several classes of derivatization reactions have been used to exchange these active hydrogens prior to GCMS analysis.

Alkylation was among the first derivatization procedures employed for GCMS[24]. It results in the replacement of an active hydrogen with an aliphatic or aliphatic-aromatic chain by esterification[23,24]. If the hydrogen replaced is not sufficiently polar, catalysis with a strong base and reaction with an alkyl halide may be required[24]. Common reagents used in alkylation reactions include dialkylacetals, diazoalkanes, benzylbromide, boron trifluoride (BF₃) in methanol or butanol and tetrabutylammonium hydroxide (TBH) among others[23]. The use of alkylation is limited by the harsh reaction conditions and toxic reagents.

Acylation with acid anhydrides, acid chlorides, and reactive amides is another common derivatization procedure in GCMS analysis[24]. Acylation is used to convert OH, -SH, and NH₂ into esters, thioesters, and amides, in the process generating a less polar, more thermostable derivative with a more predictable fragmentation pattern[27]. Acylation is particularly useful for the derivatization and chromatographic separation of sugars[23,28]. Common acylating agents include fluoracylimidazoles, fluorinated Anhydrides, N-methyl-bis(trifluoroacetamide) (MBTFA), pentafluorobenzoyl chloride (PFBCl) and pentafluoropropanol (PFPOH). Acylating reagents are moisture sensitive, toxic and odorous. Moreover, acylation derivatives are difficult to prepare owing to the significant acid byproducts formed during reaction[23]. Excess reagent and acid byproducts are hazardous to GC columns, and must be removed by pyridine or another acid scavenging solvent before analysis.

Esterification is similar in principle to alkylation in that the acid hydrogen of a carboxylic acid is exchanged for an aliphatic group. This process is especially useful in the derivatization of organic fatty acids into fatty acid methyl esters via methanolic hydrochloride[29,30]. Other common reagents include Pentafluoro-

robenzyl bromide (PFBBBr) and trimethylanilinium hydroxide. Disadvantages of esterification reagents are similar to those of alkylation and acylation, including toxic reagents, harsh reaction conditions, and acidic byproducts.

2.1.1.1 Silylation

Silylation has been used since nearly the beginning of GCMS analyses, and remains the most common derivatization method for GCMS analysis[24,31,33]. It allows for the simultaneous derivatization of several classes of metabolites under mild reaction conditions, with a wide range of injection and column settings[23,34]. Active hydrogens are typically replaced with a trialkylsilyl group such as dimethylsilyl [SiH(CH₃)₂], t-butyltrimethylsilyl [Si(CH₃)₂C(CH₃)₃] or chloromethyltrimethylsilyl [SiCH₂Cl(CH₃)₂]. Silylation forms thermostable derivatives of polar compounds with hydrogen atoms bound to electronegative atoms such as oxygen, nitrogen, sulfur or phosphorus, but also with numerous oxyanions, including phosphate, borate, carbamate, and oxalate[24,32,33]. Especially useful for compounds with hydroxyl or amino groups, silylation renders derivatives less polar, significantly more volatile, and more thermostable than non-derivatized analytes[35,36]. Generally, silylated derivatives have increased volatility and more stability than other derivatives, resulting in more narrow and symmetric peaks during GCMS analysis[37,38]. Silylation agents are highly moisture sensitive, requiring carefully dried samples and the minimal use of highly pure solvents, of which pyridine is the most common[23,25].

Because silylation occurs through nucleophilic (S_N2) attack, larger, more hindered substrates are more difficult to derivatize. The ease of reactivity of functional groups to silylation has been reported as: alcohols > phenols > carboxylic Acids > primary amines > secondary amines > amides[23]. Generally, the addition of a catalyst, increased reaction time, and added heat with or without microwave and ultrasonic assistance can improve the silylation of sterically hindered functional groups [24,33,39,40]. Oximation is applied prior to silylation to protect against enolization, prevent ring formation in sugars, and to reduce the complexity of chromatographic spectrum[41].

TABLE 2.1: Silylation reagents used in GCMS metabolomics

Reagent	Abbreviation
Trimethylchlorosilane	TMCS
Trimethyliodosilane	TMSI
t-Butyldimethylchlorosilane	TBDMCS
Hexamethyldisilazane	HMDS
N-Trimethylsilyldiethylamine	TMSDEA
N-Trimethylsilylimidazole	TMSIm
N-Methyl-N-trimethylsilylacetamide	MSTA
N-Methyl-N-trimethylsilyltrifluoroacetamide	MSTFA
N,O-Bis(trimethylsilyl)acetamide	BSA
N,O-Bis(trimethylsilyl)trifluoroacetamide	BSTFA
N,O-Bis(t-butyldimethylsilyl)trifluoroacetamide	MTBSTFA
Trimethylsilyl N,N-dimethylcarbamate	TMSDMC
Trimethylsilyl cyanide	TMSCN

Reagents used for silylation are listed in Table /refTMS table. The most commonly used are Bistrimethylsilyltrifluoroacetamide (BSTFA), N-methyltrimethylsilyltrifluoroacetamide (MSTFA), and N-methyl-N-t-butyldimethylsilyltrifluoroacetamide (MTBSTFA). Selected silylation agents are described further below.

BSTFA

BSTFA is one of the most reactive TMS donors for both hydroxyl groups and basic functional groups[33]. It reacts with most alcohols, phenols, carboxylic acids, amino acids, saccharides, thiols, amines, indoles, and nucleotides[4244]. For the derivatization of amides, secondary amines or hindered hydroxyl groups, a mixture of 1% or 10% (v/v) trimethylchlorosilane is often used. The by-products of BSTFA reactions are themselves volatile and minimize interference with chromatographic separation of target compounds.

MSTFA

MSTFA is the most volatile of the trimethylsilyl acetamides[23]. Its reaction profile is similar to BSTFA, but it performs better on dicarboxylic acids, carbohydrates, amines, and amino acids[4549]. MSTFA is more polar than BSTFA, and therefore can be used with no additional solvent[23]. Given its high polarity and volatility, MSTFA continues to be used as a simple, broad derivatization agent for the

GCMS analysis of complex metabolite mixtures, such as in eukaryotic central metabolism[50]. Like BSTFA, MSTFA is and its derivatives are water sensitive, and it requires the presence of 1% or 10% (v/v) trimethylchlorosilane as a catalyst for hindered or poorly reactive functional groups

MTBSTFA

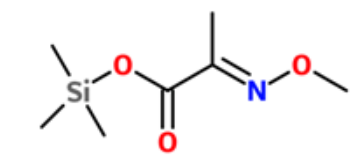
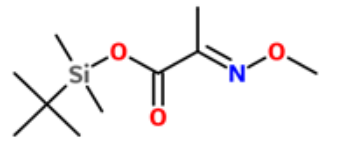
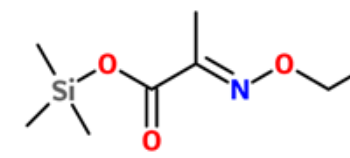
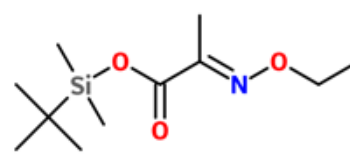
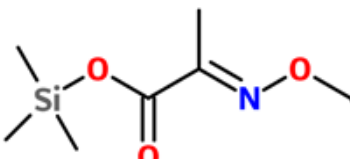
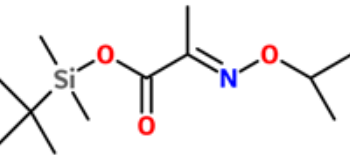
Reacts with analytes to form tertbutyldimethylsilyl (TBDMS) derivatives[51,52]. TBDMS derivatives not only have improved stability against hydrolysis, but they also have the added advantage of distinctive fragmentation patterns, which makes them useful in a variety of GC/MS applications, including stable isotope tracing of ^{13}C labelled metabolites[37,53,54]. This derivatization method is particularly advantageous for targeted quantification of small molecules with multiple functional groups, such as keto acids and amino acids[37,54], yielding very good precision with RSDs better than 5%[55]. However, TBDMS derivatives are very bulky, increasing steric hindrance so that polyhydroxy metabolites, for example, sugars, are not derivatized completely. MTBSTFA is frequently used together with t-butylchlorosilane as a catalyst to derivatize hindered functional groups.

2.1.1.2 Oximation

Oximation is often used with silylation to protect ketones and aldehydes from forming enolization products[41,56]. It protects alpha-ketoacids, such as those TCA metabolites, from decarboxylation[32]. Oximation also inhibits ring-formation, particularly in sugars, forming E (anti) - and Z (syn)-oxime isomers instead[20,57,58]. In many cases, the E/Z ratio can be assumed constant, allowing for accurate sugar quantification normally confounded by anomeric ring forms[22,59]. By reducing the number of isomers and chromatographic peaks, oximation increases signal intensity and therefore the sensitivity of detection[60].

Oximation is achieved by reaction of an analyte with hydroxylamine, or one of its O-substituted derivatives, such as O-methoxyamine, O-ethoxyamine, O-tert-butylxyamine, and O-benzyloxyamine[45,56,61,62]. Few head to head studies comparing the use of each oximation agent in conjunction with silylation exist

TABLE 2.2: Oximation and silylation of pyruvate with methoxyamine (MOX), ethoxyamine (EtOX) or tert-Butylhydroxyamine (tButOX) and trimethylsilane (TMS) or tert-butyldimethylsilane (TBDMS)

Oxime	TMS	TBDMS
MOX		
EtOX		
tButOX		

for mammalian metabolomics. Studies using plant and algal matter have suggested O-ethoxyamine followed by trimethylsilylation with BSTFA is superior to O-benzyloxyamine and trimethylsilylation[63]. However, it is also believed that oximation of sugars proceeds more favorably using smaller, less hindered protecting groups, such as O-methoxyamine[20]. Smaller analytes, such as pyruvate, may benefit from oximation with a bulkier adduct[64]. Systematic analysis of combinations oximation and silylation agents of different classes and sizes of analytes will be helpful for expanding the depth and breadth of metabolites monitored by GCMS.

2.1.2 Stable Isotope Labeling with Carbon-13 Tracers

Traditional metabolomics approaches provide only a snapshot of metabolic activity within a cell. While changes in intracellular metabolite concentrations indicate

altered activity of producing or consuming reactions, they do not provide information regarding metabolic fluxes (rates) or the direction of fluxes[9,6568]. This is because a change in concentration can be due to either changes in consumption or production of a metabolite. Stable isotope labeling, usually with ^{13}C , provides a dynamic readout of intracellular metabolism, and the flux through specific biochemical pathways[69]. In formal ^{13}C metabolic flux analysis, labeling patterns of intracellular metabolites from a ^{13}C labeled tracer are combined with data on cellular uptake and secretion rates, and prior knowledge of the biochemical reaction network to computationally estimate metabolic fluxes[7072]. Even without formal ^{13}C flux analysis, the direct interpretation of ^{13}C labeling patterns is often sufficient to provide information on relative pathway activities, the use of alternative metabolic routes, and nutrient contribution to the production of different metabolites[9]. This type of direct interpretation of ^{13}C labeling data has been termed ^{13}C tracer analysis[9].

The pattern of labeling refers specifically to a mass distribution vector (MDV), sometimes called a mass isotopomer distribution (MID) (Figure 2.2). The incorporation of heavy isotope, such as ^{13}C , in place of lighter isotope causes a shift in mass of a metabolite, which is reflected in the MDV. Isotopologues, or mass isotopomers, are metabolites that differ only in their isotopic composition. A metabolite with n carbons can have isotopologues that differ in mass (M) from M to $M + n$. For example, following oximation and trimethylsilylation, the three carbon metabolite pyruvate can fragment into an ion with mass 174 m/z (Figure 2.2). Its mass distribution vector therefore will range from 174 m/z to 177 m/z , with the fractional abundance of $M + 3$ representing the fully labeled isotopomer.

Before a MDV can be interpreted, it must be corrected for the presence of naturally occurring isotopes (Table ??) [73,74]. This includes correcting for the natural abundance of heavy isotopes found in derivatization adducts, such as in trimethylsilyl groups[75]. Typically, correction involves matrix multiplication between a MDV and correction matrix containing the natural abundance of heavy isotopes for each atom in the fragment to be analyzed. Construction of the correction matrix requires that the elemental composition of each fragment being analyzed be known prior to correction. Therefore this type of analysis is inherently

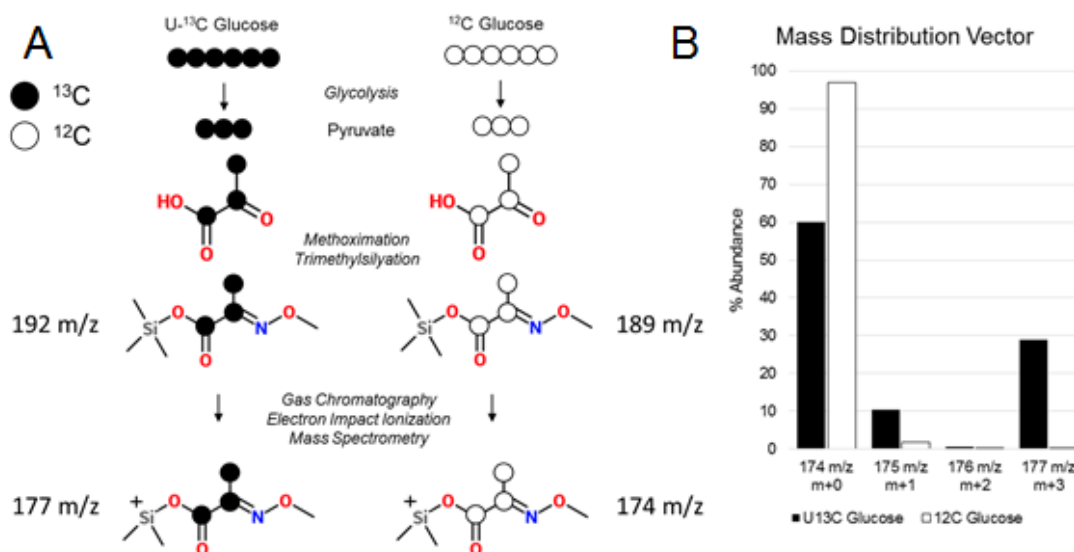


FIGURE 2.2: A) Expected labeling pattern and atom transitions for U- ^{13}C and ^{12}C Glucose to pyruvate. B) Typical mass distribution vector for labeled and unlabeled pyruvate

TABLE 2.3: Natural isotope abundance for atoms typically involved in metabolomics research

Isotope	Natural Abundance
^{13}C	1.07%
^{15}N	0.368%
^2H	0.0115%
^{17}O	0.038%
^{18}O	0.205%
^{29}Si	4.6832%
^{30}Si	3.0872%

a targeted approach. Several tools exist to assist with this type of correction[7678]. For untargeted analyses, MDV data from unlabeled samples can be compared to MDV data obtained from labeled samples, and several tools exist for the global detection of isotopic enrichment in tracer studies[9,7981].

2.1.2.1 Stable Isotope Labeled Tracers

Common tracers used in the study of cancer metabolism include ^{13}C labeled glucose and ^{13}C labeled glutamine. Several isotopomers of labeled glucose and glutamine are available as tracers (Table 2.4). These range from fully, or uniformly labeled molecules, to those with ^{13}C in one or two positions in the carbon backbone. The position of labeled atoms within a tracer allows the disambiguation of closely related pathways[82]. For example, $^{13}\text{C}_1$ -1 Glutamine enters the TCA cycle as AKG and may become oxidized to succinate, or proceed in reverse towards isocitrate and citrate via reductive carboxylation. The two pathways can be distinguished because the labeled carbon from $^{13}\text{C}_1$ -1 will be lost as carbon dioxide during the production of succinate. Positional tracers are often used to resolve specific pathways but are expensive. Uniformly labeled [$^{13}\text{C}_6$]-Glucose ([U^{13}C -GLUC]) and [$^{13}\text{C}_5$]-Glutamine ([U^{13}C]-GLN) are economical stable isotope tracers with broad applicability[83]. [U^{13}C]-GLUC is commonly used for measuring glycolysis as it labels all glycolytic carbons and enables tracing of glycolysis-derived precursors in other pathways, such as serine, glycine, and lactate[83]. [U^{13}C]-GLN is often used to interrogate the total contribution of glutamine in the TCA cycle and lipogenesis[84]. An atom transition map showing the flow of labeled carbon into the TCA cycle is shown in Figure 2.3. Understanding atomic transitions during the flow of metabolites through metabolic pathways allows not only for the selection of the most useful tracer, but also allows for accurate interpretation of labeling data.

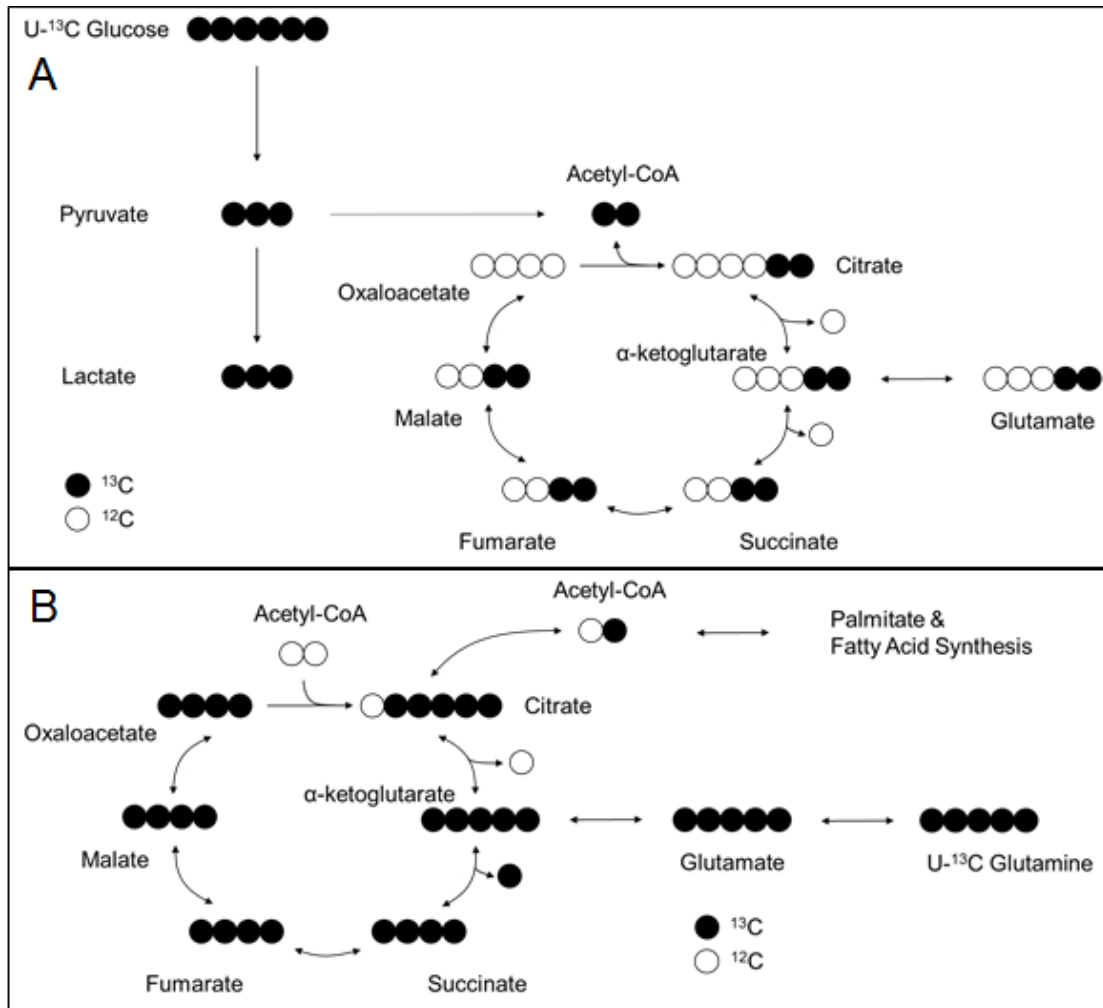


FIGURE 2.3: Atom transition map for ¹³C labeling with A) U-¹³C Glucose and B) U-¹³C Glutamine

TABLE 2.4: Common stable isotope tracers in metabolomics research and their uses. PPP - pentose phosphate pathway; TCA - Tricarboxylic acid

Tracer	Use
U- ¹³ C-Glucose	Glycolysis, PPP, Krebs cycle, hexosamine, nucleotide, lipid synthesis
1,2- ¹³ C-Glucose	Non-oxidative versus oxidative PPP
3,4- ¹³ C-Glucose	Pyruvate Carboxylase anaplerosis
U- ¹³ C/ ¹⁵ N-Glutamine	Glutaminolysis, nucleotide biosynthesis, Krebs cycle, and fatty acid synthesis
1- ¹³ C- and 5- ¹³ C- Glutamine	Oxidative TCA cycle versus reductive carboxylation, fatty acid synthesis
¹³ C ₃ -Glycerol-	Lipid synthesis, gluconeogenesis-pentose cycle interactions
¹³ C ₈ -Octanoate	β -Oxidation, lipid synthesis, phospholipid synthesis

2.2 References

1. Oliver SG, Winson MK, Kell DB, Baganz F. Systematic functional analysis of the yeast genome. *Trends Biotechnol.* 1998;16(9):373-378.
2. Fiehn O. Combining Genomics, Metabolome Analysis, and Biochemical Modelling to Understand Metabolic Networks. *Comp Funct Genomics.* 2001;2(3):155-168. doi:10.1002/cfg.82.
3. Nicholson JK, Lindon JC, Holmes E. Metabonomics: understanding the metabolic responses of living systems to pathophysiological stimuli via multivariate statistical analysis of biological NMR spectroscopic data. *Xenobiotica.* 1999;29(11):1181-1189. doi:10.1080/004982599238047.

4. Kell DB, Brown M, Davey HM, Dunn WB, Spasic I, Oliver SG. Metabolic footprinting and systems biology: the medium is the message. *Nat Rev Microbiol.* 2005;3(7):557-565. doi:10.1038/nrmicro1177.
5. Horning EC, Horning MG. Metabolic profiles: gas-phase methods for analysis of metabolites. *Clin Chem.* 1971;17(8):802-809.
6. Fan TW-M, Lorkiewicz PK, Sellers K, Moseley HNB, Higashi RM, Lane AN. Stable isotope-resolved metabolomics and applications for drug development. *Pharmacol Ther.* 2012;133(3):366-391. doi:10.1016/j.pharmthera.2011.12.007.
7. Klein S, Heinzle E. Isotope labeling experiments in metabolomics and fluxomics. *Wiley Interdiscip Rev Syst Biol Med.* 2012;4(3):261-272. doi:10.1002/wsbm.1167.
8. Metallo CM, Walther JL, Stephanopoulos G. Evaluation of ¹³C isotopic tracers for metabolic flux analysis in mammalian cells. *J Biotechnol.* 2009;144(3):167-174. doi:10.1016/j.jbiotec.2009.07.010.
9. Buescher JM, Antoniewicz MR, Boros LG, et al. A roadmap for interpreting ¹³C metabolite labeling patterns from cells. *Curr Opin Biotechnol.* 2015;34:189-201. doi:10.1016/j.copbio.2015.02.003.
10. Kaushik AK, DeBerardinis RJ. Applications of metabolomics to study cancer metabolism. *Biochim Biophys Acta - Rev Cancer.* 2018. doi:10.1016/j.bbcan.2018.04.009.
11. Markley JL, Brschweiler R, Edison AS, et al. The future of NMR-based metabolomics. *Curr Opin Biotechnol.* 2017;43:34-40. doi:10.1016/j.copbio.2016.08.001.
12. Choi C, Ganji SK, DeBerardinis RJ, et al. 2-hydroxyglutarate detection by magnetic resonance spectroscopy in IDH-mutated patients with gliomas. *Nat Med.* 2012;18(4):624-629. doi:10.1038/nm.2682.
13. Fan TW-M, Lane AN. Applications of NMR spectroscopy to systems biochemistry. *Prog Nucl Magn Reson Spectrosc.* 2016;92-93:18-53. doi:10.1016/j.pnmrs.2016.01.005.

14. Emwas A-HM. The Strengths and Weaknesses of NMR Spectroscopy and Mass Spectrometry with Particular Focus on Metabolomics Research. In: *Methods in Molecular Biology* (Clifton, N.J.). Vol 1277.; 2015:161-193. doi:10.1007/978-1-4939-2377-9-13.
15. Singh SJ, Turner W, Glaser DE, McCloskey KE, Filipp F V. Metabolic shift in density-dependent stem cell differentiation. *Cell Commun Signal*. 2017;15(1):44. doi:10.1186/s12964-017-0173-2.
16. Kuehnbaum NL, Britz-McKibbin P. New Advances in Separation Science for Metabolomics: Resolving Chemical Diversity in a Post-Genomic Era. *Chem Rev*. 2013;113(4):2437-2468. doi:10.1021/cr300484s.
17. Jonsson P, Gullberg J, Nordström A, et al. A Strategy for Identifying Differences in Large Series of Metabolomic Samples Analyzed by GC/MS. *Anal Chem*. 2004;76(6):1738-1745. doi:10.1021/ac0352427.
18. Fiehn O. Extending the breadth of metabolite profiling by gas chromatography coupled to mass spectrometry. *TrAC Trends Anal Chem*. 2008;27(3):261-269. doi:10.1016/J.TRAC.2008.01.007.
19. Koek MM, Jellema RH, van der Greef J, Tas AC, Hankemeier T. Quantitative metabolomics based on gas chromatography mass spectrometry: status and perspectives. *Metabolomics*. 2011;7(3):307-328. doi:10.1007/s11306-010-0254-3.
20. Kind T, Wohlgemuth G, Lee DY, et al. FiehnLib: mass spectral and retention index libraries for metabolomics based on quadrupole and time-of-flight gas chromatography/mass spectrometry. *Anal Chem*. 2009;81(24):10038-10048. doi:10.1021/ac9019522.
21. Grimm F, Fets L, Anastasiou D. Gas Chromatography Coupled to Mass Spectrometry (GCMS) to Study Metabolism in Cultured Cells. In: *Advances in Experimental Medicine and Biology*. Vol 899.; 2016:59-88. doi:10.1007/978-3-319-26666-45.
22. Lai Z, Fiehn O. Mass spectral fragmentation of trimethylsilylated small molecules. *Mass Spectrom Rev*. 2018;37(3):245-257. doi:10.1002/mas.21518.

23. Orata F. Derivatization Reactions and Reagents for Gas Chromatography Analysis. In: *Advanced Gas Chromatography - Progress in Agricultural, Biomedical and Industrial Applications*. InTech; 2012. doi:10.5772/33098.
24. Knapp DR. *Handbook of Analytical Derivatization Reactions*. Wiley; 1979.
25. Sobolevsky TG, Revelsky AI, Miller B, Oriedo V, Chernetsova ES, Revelsky IA. Comparison of silylation and esterification/acylation procedures in GC-MS analysis of amino acids. *J Sep Sci*. 2003;26(17):1474-1478. doi:10.1002/jssc.2003-01492.
26. Halket JM, Zaikin VG. Derivatization in Mass Spectrometry1. Silylation. *Eur J Mass Spectrom*. 2003;9(1):1-21. doi:10.1255/ejms.527.
27. Zaikin VG, Halket JM. Derivatization in Mass Spectrometry2. Acylation. *Eur J Mass Spectrom*. 2003;9(5):421-434. doi:10.1255/ejms.576.
28. Steinberg P, Fox A. Automated Derivatization Instrument: Preparation of Alditol Acetates for Analysis of Bacterial Carbohydrates Using Gas Chromatography/Mass Spectrometry. *Anal Chem*. 1999;71(9):1914-1917. doi:10.1021/ac981155g.
29. Stoffel W, Chu F, Ahrens EH. Analysis of Long-Chain Fatty Acids by Gas-Liquid Chromatography. *Anal Chem*. 1959;31(2):307-308. doi:10.1021/ac60146a047.
30. Fiehn O. Metabolomics by Gas Chromatography-Mass Spectrometry: Combined Targeted and Untargeted Profiling. In: *Current Protocols in Molecular Biology*. Vol 114. Hoboken, NJ, USA: John Wiley Sons, Inc.; 2016:30.4.1-30.4.32. doi:10.1002/0471142727.mb3004s114.
31. Kanani H, Chrysanthopoulos PK, Klapa MI. Standardizing GCMS metabolomics. *J Chromatogr B*. 2008;871(2):191-201. doi:10.1016/j.jchromb.2008.04.049.
32. Blau K, King GS. *Handbook of Derivatives for Chromatography*. London;;Philadelphia: Heyden; 1978.
33. Poole CF. Alkylsilyl derivatives for gas chromatography. *J Chromatogr A*. 2013;1296:2-14. doi:10.1016/j.chroma.2013.01.097.

34. Kvitvang HFN, Andreassen T, Adam T, Villas-Boas SG, Bruheim P. Highly Sensitive GC/MS/MS Method for Quantitation of Amino and Nonamino Organic Acids. *Anal Chem.* 2011;83(7):2705-2711. doi:10.1021/ac103245b.
35. Singh M, Lin J, Hocker TL, Tsao H. Genetics of melanoma tumorigenesis. *Br J Dermatol.* 2008;158(1):15-21. doi:10.1111/j.1365-2133.2007.08316.x.
36. Namkoong J, Shin S-S, Lee HJ, et al. Metabotropic glutamate receptor 1 and glutamate signaling in human melanoma. *Cancer Res.* 2007;67(5):2298-2305. doi:10.1158/0008-5472.CAN-06-3665.
37. Roessner U, Wagner C, Kopka J, Trethewey RN, Willmitzer L. Technical advance: simultaneous analysis of metabolites in potato tuber by gas chromatography-mass spectrometry. *Plant J.* 2000;23(1):131-142.
38. Kataoka H. Gas Chromatography of Amines as Various Derivatives. *J Chromatogr Libr.* 2005;70:364-404. doi:10.1016/S0301-4770(05)80016-8.
39. Sderholm SL, Damm M, Kappe CO. Microwave-assisted derivatization procedures for gas chromatography/mass spectrometry analysis. *Mol Divers.* 2010;14(4):869-888. doi:10.1007/s11030-010-9242-9.
40. Pietrogrande MC, Manarini F, Quintana JB, Rodil R, Villaverde-de-Sa E, Visentin M. Optimization of an ultrasound-assisted derivatization for GC/MS analysis of oxygenated organic species in atmospheric aerosol. *Anal Bioanal Chem.* 2017;409(17):4279-4291. doi:10.1007/s00216-017-0379-6.
41. Halket JM, Waterman D, Przyborowska AM, Patel RKP, Fraser PD, Bramley PM. Chemical derivatization and mass spectral libraries in metabolic profiling by GC/MS and LC/MS/MS. *J Exp Bot.* 2005;56(410):219-243. doi:10.1093/jxb/eri069.
42. Gehrke CW, Leimer K. Trimethylsilylation of amino acids derivatization and chromatography. *J Chromatogr A.* 1971;57:219-238. doi:10.1016/0021-9673(71)80-035-3.
43. Jurado-Snchez B, Ballesteros E, Gallego M. Determination of carboxylic acids in water by gas chromatography-mass spectrometry after continuous extraction and derivatisation. *Talanta.* 2012;93:224-232. doi:10.1016/j.talanta.2012.02.022.

44. Rojas-Escudero E, Alarcn-Jimnez AL, Elizalde-Galvn P, Rojo-Callejas F. Optimization of carbohydrate silylation for gas chromatography. *J Chromatogr A*. 2004;1027(1-2):117-120. doi:10.1016/J.CHROMA.2003.10.131.
45. Oliver Fiehn, Joachim Kopka, Richard N. Trethewey and Willmitzer L. Identification of Uncommon Plant Metabolites Based on Calculation of Elemental Compositions Using Gas Chromatography and Quadrupole Mass Spectrometry. 2000. doi:10.1021/AC991142I.
46. Gullberg J, Jonsson P, Nordstrm A, Sjstrm M, Moritz T. Design of experiments: an efficient strategy to identify factors influencing extraction and derivatization of *Arabidopsis thaliana* samples in metabolomic studies with gas chromatography/mass spectrometry. *Anal Biochem*. 2004;331(2):283-295. doi:10.1016/J.AB.2004.04.037.
47. Shareef A, Angove MJ, Wells JD. Optimization of silylation using N-methyl-N-(trimethylsilyl)-trifluoroacetamide, N,O-bis-(trimethylsilyl)-trifluoroacetamide and N-(tert-butyldimethylsilyl)-N-methyltrifluoroacetamide for the determination of the estrogens estrone and 17-ethinylestradiol. *J Chromatogr A*. 2006;1108(1):121-128. doi:10.1016/J.CHROMA.2005.12.098.
48. Ruiz-Matute AI, Hernndez-Hernndez O, Rodrguez-Snchez S, Sanz ML, Martnez-Castro I. Derivatization of carbohydrates for GC and GCMS analyses. *J Chromatogr B*. 2011;879(17-18):1226-1240. doi:10.1016/J.JCHROMB.2010.11.013.
49. Guida M, Salvatore M, FS. A Strategy for GC/MS Quantification of Polar Compounds via their Silylated Surrogates: Silylation and Quantification of Biological Amino Acids. *J Anal Bioanal Tech*. 2015;6(5). doi:10.4172/2155-9872.1000263.
50. Phlipp M, Coat R, Le Bras C, et al. Characterization of an easy-to-use method for the routine analysis of the central metabolism using an affordable low-resolution GCMS system: application to *Arthrospira platensis*. *Anal Bioanal Chem*. 2018;410(4):1341-1361. doi:10.1007/s00216-017-0776-x.

51. Corey EJ, Venkateswarlu A. Protection of hydroxyl groups as tert-butyl-dimethylsilyl derivatives. *J Am Chem Soc.* 1972;94(17):6190-6191. doi:10.1021/ja00772a043.
52. SCHUMMER C, DELHOMME O, APPENZELLER B, WENNIG R, MILLET M. Comparison of MTBSTFA and BSTFA in derivatization reactions of polar compounds prior to GC/MS analysis. *Talanta.* 2009;77(4):1473-1482. doi:10.1016/j.talanta.2008.09.043.
53. Scott DA, Richardson AD, Filipp F V., et al. Comparative Metabolic Flux Profiling of Melanoma Cell Lines. *J Biol Chem.* 2011;286(49):42626-42634. doi:10.1074/jbc.M111.282046.
54. Fiehn O, Kopka J, Trethewey RN, Willmitzer L. Identification of uncommon plant metabolites based on calculation of elemental compositions using gas chromatography and quadrupole mass spectrometry. *Anal Chem.* 2000;72(15):3573-3580.
55. Niehaus TD, Nguyen TND, Gidda SK, et al. Arabidopsis and Maize RidA Proteins Preempt Reactive Enamine/Imine Damage to Branched-Chain Amino Acid Biosynthesis in Plastids. *Plant Cell.* 2014;26(7):3010-3022. doi:10.1105/tpc.114.126854.
56. Koek MM, Mulwijk B, van der Werf MJ, Hankemeier T. Microbial metabolomics with gas chromatography/mass spectrometry. *Anal Chem.* 2006;78(4):1272-1281. doi:10.1021/ac051683+.
57. Ruiz-Matute AI, Hernandez-Hernandez O, Rodriguez-Sanchez S, Sanz ML, Martinez-Castro I. Derivatization of carbohydrates for GC and GC-MS analyses. *J Chromatogr B Analyt Technol Biomed Life Sci.* 2011;879(17-18):1226-1240. doi:10.1016/j.jchromb.2010.11.013.
58. Becker M, Liebner F, Rosenau T, Potthast A. Ethoximation-silylation approach for mono- and disaccharide analysis and characterization of their identification parameters by GC/MS. *Talanta.* 2013;115:642-651. doi:10.1016/j.talanta.2013.05.052.

59. Zweckmair T, Schiehser S, Rosenau T, Potthast A. Improved quantification of monosaccharides in complex lignocellulosic biomass matrices: A gas chromatography-mass spectrometry based approach. *Carbohydr Res.* 2017;446-447:7-12. doi:10.1016/j.carres.2017.04.011.
60. Fzfai Z, Boldizsr I, Molnr-Perl I. Characteristic fragmentation patterns of the trimethylsilyl and trimethylsilyl-oxime derivatives of various saccharides as obtained by gas chromatography coupled to ion-trap mass spectrometry. *J Chromatogr A.* 2008;1177(1):183-189. doi:10.1016/j.chroma.2007.11.023.
61. Andrews MA. Capillary gas-chromatographic analysis of monosaccharides: improvements and comparisons using trifluoroacetylation and trimethylsilylation of sugar O-benzyl- and O-methyl-oximes. *Carbohydr Res.* 1989;194:1-19.
62. Mason BS, Slover HT. Gas-chromatographic method for the determination of sugars in foods. *J Agric Food Chem.* 1971;19(3):551-554. doi:10.1021/jf60175a006.
63. Becker M, Liebner F, Rosenau T, Potthast A. Ethoximation-silylation approach for mono- and disaccharide analysis and characterization of their identification parameters by GC/MS. *Talanta.* 2013;115:642-651. doi:10.1016/J.TALANTA.2013.05.052.
64. Filipp FV, Ratnikov B, De Ingeniis J, Smith JW, Osterman AL, Scott D a. Glutamine-fueled mitochondrial metabolism is decoupled from glycolysis in melanoma. *Pigment Cell Melanoma Res.* 2012;25(6):732-739. doi:10.1111/pcmr.12000.
65. Fendt S-M, Buescher JM, Rudroff F, Picotti P, Zamboni N, Sauer U. Tradeoff between enzyme and metabolite efficiency maintains metabolic homeostasis upon perturbations in enzyme capacity. *Mol Syst Biol.* 2010;6:356. doi:10.1038/msb.2010.11.
66. Bennett BD, Kimball EH, Gao M, Osterhout R, Van Dien SJ, Rabinowitz JD. Absolute metabolite concentrations and implied enzyme active site occupancy in *Escherichia coli*. *Nat Chem Biol.* 2009;5(8):593-599. doi:10.1038/nchembio.186.

-
67. Link H, Kochanowski K, Sauer U. Systematic identification of allosteric protein-metabolite interactions that control enzyme activity in vivo. *Nat Biotechnol.* 2013;31(4):357-361. doi:10.1038/nbt.2489.
68. Buescher JM, Liebermeister W, Jules M, et al. Global Network Reorganization During Dynamic Adaptations of *Bacillus subtilis* Metabolism. *Science* (80-). 2012;335(6072):1099-1103. doi:10.1126/science.1206871.
69. Keibler MA, Fendt S-M, Stephanopoulos G. Expanding the concepts and tools of metabolic engineering to elucidate cancer metabolism. *Biotechnol Prog.* 2012;28(6):1409-1418. doi:10.1002/btpr.1629.
70. Wiechert W. ¹³C Metabolic Flux Analysis. *Metab Eng.* 2001;3(3):195-206. doi:10.1006/mben.2001.0187.
71. Wiechert W, Nh K. Isotopically non-stationary metabolic flux analysis: complex yet highly informative. *Curr Opin Biotechnol.* 2013;24(6):979-986. doi:10.1016/j.copbio.2013.03.024.
72. Antoniewicz MR. ¹³C metabolic flux analysis: optimal design of isotopic labeling experiments. *Curr Opin Biotechnol.* 2013;24(6):1116-1121. doi:10.1016/j.copbio.2013.02.003.
73. Fernandez CA, Rosiers C Des, Previs SF, David F, Brunengraber H. Correction of ¹³C Mass Isotopomer Distributions for Natural Stable Isotope Abundance. *J Mass Spectrom.* 1996;31(3):255-262.
74. Nanchen A, Fuhrer T, Sauer U. Determination of Metabolic Flux Ratios From ¹³C-Experiments and Gas Chromatography-Mass Spectrometry Data. In: *Methods in Molecular Biology* (Clifton, N.J.). Vol 358.; 2007:177-197. doi:10.1007/978-1-59745-244-111.
75. Antoniewicz MR, Kelleher JK, Stephanopoulos G. Accurate Assessment of Amino Acid Mass Isotopomer Distributions for Metabolic Flux Analysis. *Anal Chem.* 2007;79(19):7554-7559. doi:10.1021/ac0708893.

76. Moseley HN. Correcting for the effects of natural abundance in stable isotope resolved metabolomics experiments involving ultra-high resolution mass spectrometry. *BMC Bioinformatics*. 2010;11(1):139. doi:10.1186/1471-2105-11-139.
77. Wahl SA, Dauner M, Wiechert W. New tools for mass isotopomer data evaluation in ^{13}C flux analysis: Mass isotope correction, data consistency checking, and precursor relationships. *Biotechnol Bioeng*. 2004;85(3):259-268. doi:10.1002/bit.10909.
78. Jungreuthmayer C, Neubauer S, Mairinger T, Zanghellini J, Hann S. ICT: isotope correction toolbox. *Bioinformatics*. 2015;32(1):btv514. doi:10.1093/bioinformatics/btv514.
79. Weindl D, Wegner A, Hiller K. Non-targeted Tracer Fate Detection. In: *Methods in Enzymology*. Vol 561.; 2015:277-302. doi:10.1016/bs.mie.2015.04.003.
80. Cho K, Mahieu N, Ivanisevic J, et al. isoMETLIN: A Database for Isotope-Based Metabolomics. *Anal Chem*. 2014;86(19):9358-9361. doi:10.1021/ac5029177.
81. Bueschl C, Kluger B, Berthiller F, et al. MetExtract: a new software tool for the automated comprehensive extraction of metabolite-derived LC/MS signals in metabolomics research. *Bioinformatics*. 2012;28(5):736-738. doi:10.1093/bioinformatics/bts012.
82. Walther JL, Metallo CM, Zhang J, Stephanopoulos G. Optimization of ^{13}C isotopic tracers for metabolic flux analysis in mammalian cells. *Metab Eng*. 2012;14(2):162-171. doi:10.1016/j.ymben.2011.12.004.
83. Bruntz RC, Lane AN, Higashi RM, Fan TW-M. Exploring cancer metabolism using stable isotope-resolved metabolomics (SIRM). *J Biol Chem*. 2017;292(28):11601-11609. doi:10.1074/jbc.R117.776054.
84. Yoo H, Stephanopoulos G, Kelleher JK. Quantifying carbon sources for de novo lipogenesis in wild-type and IRS-1 knockout brown adipocytes. *J Lipid Res*. 2004;45(7):1324-1332. doi:10.1194/jlr.M400031-JLR200.

Chapter 3

Metabolic shift in density-dependent stem cell differentiation

RESEARCH

Open Access

Metabolic shift in density-dependent stem cell differentiation



Simar J. Singh¹, William Turner², Drew E. Glaser², Kara E. McCloskey² and Fabian V. Filipp^{1*}

Abstract

Background: Vascular progenitor cells (VPCs) derived from embryonic stem cells (ESCs) are a valuable source for cell- and tissue-based therapeutic strategies. During the optimization of endothelial cell (EC) inductions from mouse ESCs using our staged and chemically-defined induction methods, we found that cell seeding density but not VEGF treatment between 10 ng/mL and 40 ng/mL was a significant variable directing ESCs into FLK1⁺ VPCs during stage 1 induction. Here, we examine potential contributions from cell-to-cell signaling or cellular metabolism in the production of VPCs from ESCs seeded at different cell densities.

Methods: Using 1D ¹H-NMR spectroscopy, transcriptomic arrays, and flow cytometry, we observed that the density-dependent differentiation of ESCs into FLK1⁺ VPCs positively correlated with a shift in metabolism and cellular growth.

Results: Specifically, cell differentiation correlated with an earlier plateauing of exhaustive glycolysis, decreased lactate production, lower metabolite consumption, decreased cellular proliferation and an increase in cell size. In contrast, cells seeded at a lower density of 1,000 cells/cm² exhibited increased rates of glycolysis, lactate secretion, metabolite utilization, and proliferation over the same induction period. Gene expression analysis indicated that high cell seeding density correlated with up-regulation of several genes including cell adhesion molecules of the notch family (NOTCH1 and NOTCH4) and cadherin family (CDH5) related to vascular development.

Conclusions: These results confirm that a distinct metabolic phenotype correlates with cell differentiation of VPCs.

Keywords: Stem cells, Differentiation, Vascular fate, Cell seeding density, Systems biology, Metabolism, NMR, Metabolomics, Fluorescence-activated cell sorting, Flow cytometry, Cell adhesion, Cell contact, Cell communication, Microenvironment, Cancer stem cells, Embryonic stem cells, Vascular progenitor cells, Endothelial cells

Background

Vascular progenitor cells (VPCs) and endothelial cells (ECs) are desirable cell sources for cellular therapeutic and tissue engineering strategies including: peripheral vascular disease [1, 2], severe ischemic heart disease [3, 4] and lining the lumens of small diameter vascular grafts in order to minimize thrombosis or arteriosclerosis [5, 6]. In cancer, the vascular niche promotes cancer stem cells (CSCs) and is enriched with CSC-derived ECs, which promote tumor invasion and metastasis [7]. VPCs are important for maintenance of the stemness of normal

adult stem cells, including self-renewal, undifferentiated status, and dormancy. However, it is sometimes difficult to obtain sufficient numbers of proliferating VPCs and ECs, especially from aged adults and diseased patients [6]. Alternatively, embryonic stem cells (ESCs) and induced pluripotent stem cells (iPSCs) with their unlimited capacity for self-renewal, are considered excellent cell sources in a variety of cell-based therapies. In addition to their growing therapeutic applications, these cell sources in combination with derived VPCs and ECs can also serve as representative *in vitro* models of vascular development.

During early stages of vascular development, signaling from vascular endothelial growth factor (VEGF = VEGFA, vascular endothelial growth factor

* Correspondence: filipp@ucmerced.edu

¹Systems Biology and Cancer Metabolism, Program for Quantitative Systems Biology, University of California Merced, 2500 North Lake Road, Merced, CA 95343, USA

Full list of author information is available at the end of the article



© The Author(s). 2017 **Open Access** This article is distributed under the terms of the Creative Commons Attribution 4.0 International License (<http://creativecommons.org/licenses/by/4.0/>), which permits unrestricted use, distribution, and reproduction in any medium, provided you give appropriate credit to the original author(s) and the source, provide a link to the Creative Commons license, and indicate if changes were made. The Creative Commons Public Domain Dedication waiver (<http://creativecommons.org/publicdomain/zero/1.0/>) applies to the data made available in this article, unless otherwise stated.

A, GeneBank: 7422) and the VEGF receptor, FLK1 (FLK1 = VEGFR = KDR, kinase insert domain receptor, GeneBank: 3791) promotes ventral mesoderm and hematopoietic fate [8–10] leading to activation of the mitogen activated protein kinase pathway [11]. Endothelial, hematopoietic, and smooth muscle cells have been derived from outgrowths of FLK1⁺ VPCs, making this VEGF receptor a hallmark for identification of VPCs [12]. However, despite our growing understanding of the critical biochemical factors in development, the precise timing and quantitative levels of EC induction/activation for directing vascular fate from ESCs *in vitro* have remained confounding. This is complicated by the inherent variability in kinetic and autocrine signaling from ESC line-to-ESC line [13]. For example, the optimal time to induce the mouse D3-ESC line into FLK1⁺ VPCs has been reported to occur at day 4 (FLK1⁺ = FLK1 positive = VEGFR expressing cells) [14–16], while the optimal time for the corresponding mouse R1-ESC line has been reported at day 2 [17]. Additionally, while VEGF is the most published growth factor associated with directing EC differentiation, published treatment levels vary between 20 ng/mL and 50 ng/mL [12, 15, 18]. Matrix signaling is also an important signal in stem cell fate, but studies on this topic have also been conflicting. For example, it has been reported that collagen type-IV directs a higher percentage of ECs [12, 15, 18]. However, more recent studies show fibronectin promotes increased cell adhesion and/or proliferation, generating greater numbers of VPCs and ECs compared with collagen-type IV [1, 17]. Moreover, increasing evidence

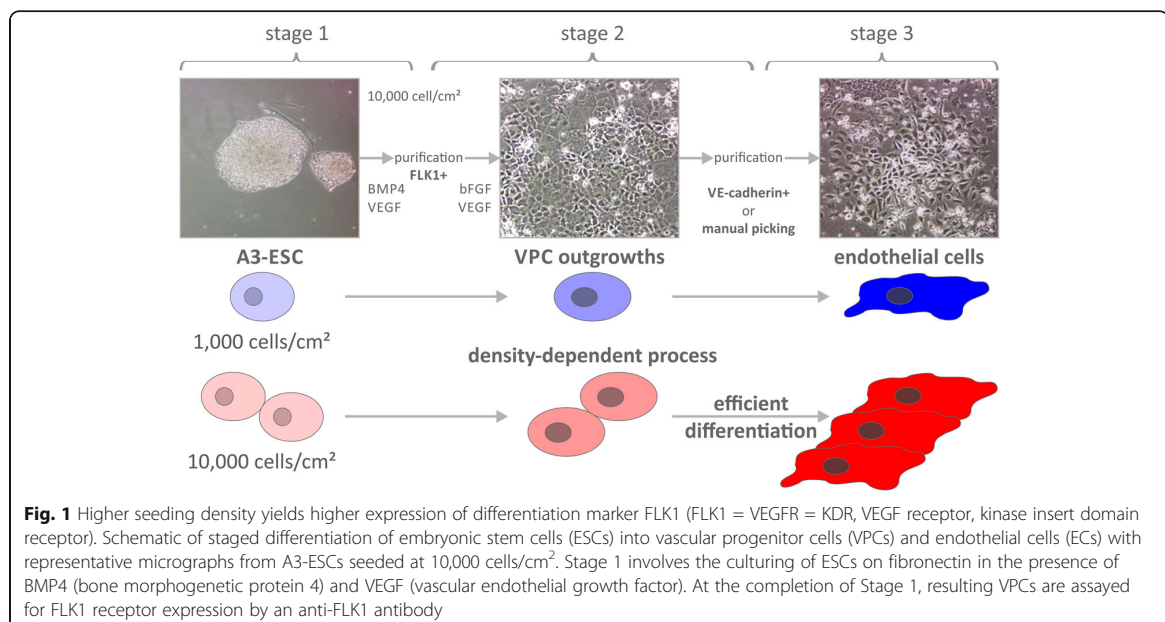
supports a role for modified cellular metabolism in the regulation of stem cell self-renewal, specification, and plasticity in cancer and development [19–21]. Despite this growing understanding of cellular metabolism as a regulator of cell function, the role of cell seeding density in metabolic alterations supporting vascular fate is not defined.

Therefore, using our established staged differentiation methodology and chemically-defined media formulations (Fig. 1a), we examined a number of combinatorial variables (induction time, VEGF treatment, matrix signaling, and cell seeding density) for directing the generation of VPCs (stage 1). The results indicated that cell seeding density was a significant factor in the first stages of induction of ESCs into VPCs, especially in the A3-ESC cell line [22] generated by our own laboratory. Therefore, we set out to further examine the underlying mechanisms related to density-dependent differentiation in this ESC line.

Methods

Embryonic stem cell culture

Mouse A3-ESCs were extracted, generated, and cultured at 3,000/cm² on inactivated mouse embryonic fibroblasts (MEFs; 20,000/cm²) [22]. Prior to induction, the A3-ESCs are purified from MEFs by gravity separation followed by MEF adhesion to tissue culture dishes for 1–2 hours and passaged onto 0.5% gelatin-coated plates in ESC culture media containing: Knockout Dulbecco's Modified Eagle Medium (KO-DMEM; Invitrogen), 15% Knockout Serum Replacer (KSR; Invitrogen), 1X penicillin-streptomycin



(Invitrogen), 1X non-essential amino acids (Invitrogen), 2 mM L-glutamine (Invitrogen), 0.1 mM 2-mercaptoethanol (Calbiochem), 2000 units/mL of leukemia inhibitory factor (LIF-ESGRO; Chemicon), and 10 ng/mL of bone morphogenetic protein 4 (BMP4, GeneBank: 652) (R&D Systems). Full media changes occurred every other day and cells were passaged every 4–5 days.

Induction of FLK1⁺ VPCs

A3-ESCs were harvested and plated at either 1,000, 5,000 or 10,000 cells/cm² in 12-well cell culture dishes, coated with 50 ng/mL fibronectin (BD Biosciences), and fed our induction media: alpha-minimal essential medium (MEM; Corning), 20% KSR (Invitrogen), 1X penicillin-streptomycin (Invitrogen), 1X nonessential amino acids (Invitrogen), 2 mM L-glutamine (Invitrogen), 0.05 mM 2-mercaptoethanol (Calbiochem), and 5 ng/mL BMP4 (R&D Systems), and 0 to 30 ng/mL of VEGF (R&D Systems) without media change for 4 days. Experiments were conducted in triplicate ($N = 3$) allowing for analysis of variance. The assessment of stage 1 VPCs, which are not contact-inhibited, was quantified by the percentage of FLK1⁺ cells over time, previously shown to correlate with down-regulation of the pluripotent stem cell marker POU class 5 homeobox 1 (POU5F1 = OCT3/4, GeneBank: 5460) over the same time period [22].

Characterization of VPCs

Adherent cells were harvested using Cell Dissociation Buffer (Invitrogen), fixed in 4% paraformaldehyde (Tousimis), rinsed 2X with phosphate buffered saline (PBS), blocked using 0.5% donkey serum (Fitzgerald) and 1% bovine-serum albumin (Sigma) for 1 h at room temperature, and stained with Alexa Fluor 647[®]-conjugated anti-FLK1 antibody (Biolegend) at 1:100 and allowed to incubate overnight at 4 °C. Cells were rinsed 2X with PBS before being analyzed on an LSR II flow cytometer (BD Biosciences) and FloJo Software (TreeStar) at 1, 2, and 3 days post induction of differentiation. Samples were analyzed in triplicate ($N = 3$) for each data point.

Exometabolome analysis

Triplicate samples of conditioned induction media ($N = 3$) were harvested at 1, 2 and 3 days post-induction and stored at -80 °C. Prior to 1D ¹H-NMR spectroscopy metabolomics analysis, supernatants were extracted using 1:1 cold methanol (BDH 67-56-1) and chloroform (Amresco 0757) mixture [7]. The extracts were cleared by centrifugation at 14,000 g and the aqueous phase was collected. Freeze-dried metabolite samples were resuspended in 200 μL of H₂O with 5% D₂O spiked with 0.75% 3-(trimethylsilyl)propanoic-2,2,3,3-d₄ acid (TSP) (Sigma 293040) to a final concentration of 2.409 mM into 3 mm NMR tubes (Norrell C-S-3-HT-7). Spectra

were recorded using 1D ¹H excitation sculpting at 512 scans, $d_1 = 1$ s, 1H pulse 11.0 μs, power level of shaped pulse 25.55db and an experimental time of 10 min at 300 K at an Avance II 600-MHz spectrometer fitted with a cryogenic probe operating with TOPSPIN 2.0 (Bruker BioSpin GmbH). All spectra were automatically phased, baseline corrected and referenced to TSP (δ 0.00 ppm) using Chenomx NMR spectroscopy suite 8.1 (Chenomx Inc). Metabolite concentrations were quantified on the basis of matching chemical shifts and multiplicities to the Chenomx reference compound library. Exometabolome analysis by NMR spectroscopy provides direct comparison of absolute metabolite concentrations of analytes. Not surprisingly, the amount of metabolites excreted or taken up scales with the initial seeding density. Therefore, by normalizing each time point to the first time point post-induction, dynamic information of the system can be obtained. The total cell count prior seeding was obtained in triplicate ($N = 3$) by analyzing cells accurately using multifocal plane analysis in the TC20 automated cell counter (Biorad).

Cell size and proliferation

Cell diameter and proliferation rates were measured over the 3 days of VPC induction using an automated image-based cytometer. Cells were harvested using 0.25% trypsin-EDTA (Corning) from fibronectin coated cultures dishes at 1, 2 and 3 days post induction of differentiation, stained with trypan blue, and pipetted into disposable counting chambers for counting and image analysis. Cell diameter measurements of live differentiating ESCs were obtained in the TC20 automated cell counter (Biorad). Multi-planar bright-field digital images were automatically collected, quantified, and assessed for cell number and diameter. Cell proliferation rates were calculated and densities validated from the live cells per dish ($N = 6$) over the 3 days of VPC induction.

Differential gene expression

Total RNA was extracted from undifferentiated ESCs as well as from cells 3 days post induction of differentiation using TRIzol (Sigma T9424). At least three biological replicates of RNA samples were analyzed per condition. The concentration of RNA was determined using a Nanodrop spectrophotometer (Thermo Scientific). Two micrograms of RNA was processed with the RT² profiler array PAMM-146Z (Qiagen SABiosciences) and used to synthesize cDNA using the RT² SYBR green master mix (Qiagen SABiosciences) in a 7300 real-time (RT) quantitative polymerase chain reaction (QPCR) System (Applied Biosystems). Gene expression profiles were analyzed using the $\Delta\Delta$ CT method. RT QPCR threshold cycle (CT) values were normalized using five different

housekeeping genes (HKG), ACTB, actin beta, GeneBank: 60, B2M, beta-2-microglobulin, GeneBank: 567, GAPDH, glyceraldehyde-3-phosphate dehydrogenase, GeneBank: 2597, GUSB, glucuronidase beta GeneBank: 2990, and HSP90AB1, heat shock protein 90 kDa alpha family class B member 1, GeneBank: 3326. The difference threshold cycle value (ΔCT) of any gene of interest (GOI) to the average housekeeping value was calculated using the formula $\Delta CT(GOI) = CT(GOI) - \text{AVERAGE}(CT(HKG))$ for ESCs, differentiating cells at seeding density of 1,000 cells/cm² and 10,000 cells/cm². In addition, change in gene expressions of any gene of interest was monitored by calculating $\Delta\Delta CT(GOI) = \Delta CT(GOI-10 K) - \Delta CT(GOI-1 K)$. RT² gene array profiles were normalized, separated according to differential expression between the two seeding densities in univariate T-tests with a random variance model using a *p*-value cut-off below 0.05, and ranked with LOG₂ fold-change of specimen seeded at 10,000 cells/cm² in comparison to 1,000 cells/cm² considered significant.

Differential protein expression analysis

Induced VPCs originally seeded as ESCs at 1,000 cells/cm² or 10,000 cells/cm² were harvested 3 days post induction. Cells were fixed, washed, and blocked in PBS supplemented with 2% fetal bovine serum (FBS; Corning 35-010-CV). Cells were incubated light-protected at 4 °C for 1 h with the following antibodies and staining reagents: FLK1 PerCP (Biolegend 121915), CDH2 rabbit polyclonal (Abcam ab12221), CDH5 (CD144) brilliant violet 421 (Biolegend 138013), and Fixable Viability Dye eFluor780 (eBioscience 65-0865-14). After washing, cells were incubated light protected at 4 °C for 1 h with FITC conjugated Donkey Anti-Rabbit IgG pre-adsorbed (Abcam ab7079). Samples were rinsed twice with PBS supplemented with 2% FBS before being analyzed on an LSR II flow cytometer (BD Biosciences) at a flow rate at least 500 events per second. 100,000 events per sample were recorded and samples were analyzed in triplicate (*N* = 3) for each data point. FloJo Software (TreeStar) was used for data analysis. Dead cells were gated out from analysis based on Viability Dye eFluor780 reactivity. FLK1⁺ cells were then analyzed for FITC (CDH2) and Brilliant Violet 421 (CDH5) fluorescence and the percentage of Flk1⁺/CDH2⁺CDH5⁺ cells were compared between low density and high density groups.

Results

Characterization of differentiated FLK1⁺ VPCs

Induction of mouse A3-ESCs [22] into VPCs was examined over a range of seeding densities, VEGF treatment levels, and time (Fig. 2a). The greatest number of FLK1⁺ cells was generated on day 3, with a reduction at day 4. Although the VEGF treatment levels led to variable

results, the greatest number of FLK1⁺ VPCs was consistently and statistically significant in cultures seeded at the highest seeding density (Fig. 2a-b) while cells initially seeded at 1,000 cells/cm² generated significantly fewer FLK1⁺ cells. Bright field microscopy revealed that after three days, the 10,000 cells/cm² seeding density remained subconfluent (Fig. 2c).

Metabolic shift during density-dependent differentiation

To identify density-dependent changes in cellular metabolism during differentiation, we measured metabolite abundance within conditioned media using 1D ¹H-NMR spectroscopy. This exometabolome analysis provides insights into metabolite utilization and secretion. A reduction in metabolite abundance is consistent with cellular uptake from our chemically defined induction media, whereas an increase in abundance correlates with active production and extracellular secretion. Of the metabolites in the differentiation media profiled, only lactate exhibited an increase in abundance. Cells seeded at a density of 10,000 cells/cm² displayed a rapid increase in lactate production between days 1 and 2, which then slowed between days 2 and 3 (Fig. 3a-b). Conversely, cells grown at a density of 1,000 cells/cm² produce, on a per cell basis, comparatively more lactate, and exhibit a significant increase in lactate abundance between days 1 and 3 (9.0 vs 3.8; *p*-value < 0.001) (Fig. 3a-b). The same trend is seen in metabolite utilization. Cells grown at a density of 10,000 cells/cm² exhibit higher rates of metabolite utilization between day 1 and day 2, and much lower utilization between days 2 and 3 (Fig. 3c-d). In contrast, cells seeded at lower density increase their metabolite uptake over time, exhibiting their highest levels of utilization between days 2 and 3 (Fig. 3c-d).

Differentiation correlates with increased cell size and reduced proliferation

To determine whether the observed shift in metabolite utilization coincides with a change in cellular proliferation, we measured the number of live cells present for both seeding densities following induction of differentiation. Cells induced at a density of 10,000 cells/cm² have a higher proliferation rate between day 1 and day 2 (3.32 vs. 2.07; *p*-value < 0.001) and a lower proliferation rate between day 2 and day 3 (2.01 vs. 3.73; *p*-value < 0.001) (Fig. 4a). In contrast, cells grown at low density continue to increase their proliferation rate over the 3 days of induction. Notably, while VPCs are not contact-inhibited, cell cultures at all seeding densities remain subconfluent after 3 days of culture (Fig. 1D) and continue to proliferate. A3-ESCs seeded at the highest density contained fewer cells of a small diameter representative of ESC size three days post induction compared with cells seeded at lower density (5–6 μm, 26% vs 36%; *p*-value < 0.001). Additionally, proportionately more cells of larger

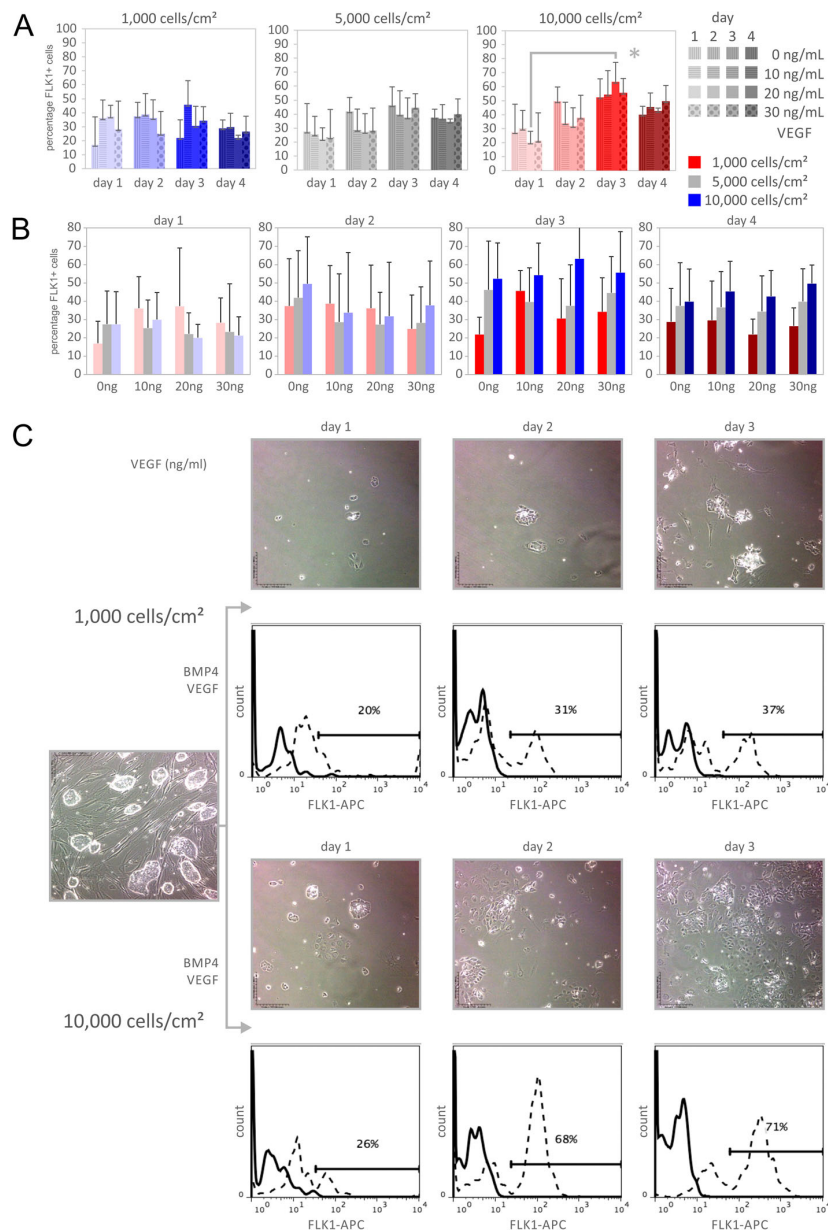


Fig. 2 Higher seeding density yields higher expression of differentiation marker FLK1 (FLK1 = VEGFR = KDR, kinase insert domain receptor). The effect of (a) seeding density, (b) vascular endothelial growth factor (VEGF) concentration, and induction time on the percentage of FLK1⁺ vascular progenitor cells (VPCs) generated from embryonic stem cells (ESCs). An induction time of three days combined with a seeding density of 10,000 cells/cm² resulted in high percentages of FLK1⁺ cells regardless of VEGF concentration. c Phase contrast images and flow cytometric cell scanning histograms of FLK1 expression of ESCs induced on 50 ng/mL fibronectin with 20 ng/mL VEGF treatment. Upper panel shows time course following seeding densities of 1,000 cells/cm². Lower panel shows time course following seeding densities of 10,000 cells/cm². By day 3 post induction, the majority of cells seeded at 10,000 cells/cm² exhibit FLK1 receptor expression. In contrast, cells initially seeded at 1,000 cells/cm² exhibit less FLK1 receptor expression and exhibit fewer cell clusters at day 3

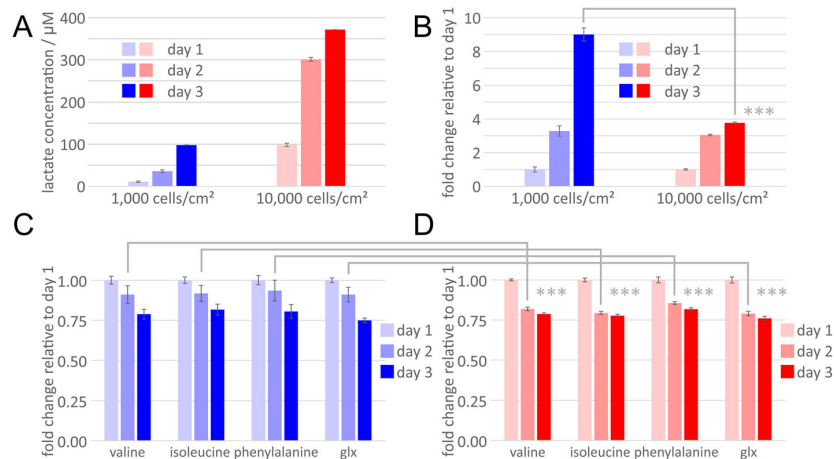


Fig. 3 Density-dependent shift of metabolic rate. 1D ¹H-NMR spectroscopic exometabolome analysis of conditioned media from induced embryonic stem cells (ESCs) initially seeded at 1,000 cells/cm² (blue) and 10,000 cells/cm² (red). **a** By day 3, cells seeded at higher density reduce production of lactate whereas cells initially seeded at low density continue to increase lactate production and exhibit a significantly higher fold increase in lactate abundance between days 1 and 3 (9.0 vs 3.8; *** *p*-value < 0.001). **b** Fold change of lactate production relative to day 1. **c** Amino acid uptake of valine, isoleucine, phenylalanine, and glutamine/glutamate (glx) significantly increases in the low density group after two days of induction (***) *p*-value < 0.001). **d** Amino acid uptake plateaus between 2 and 3 days post induction in the higher density group. Fold change of amino acid uptake relative to day 1

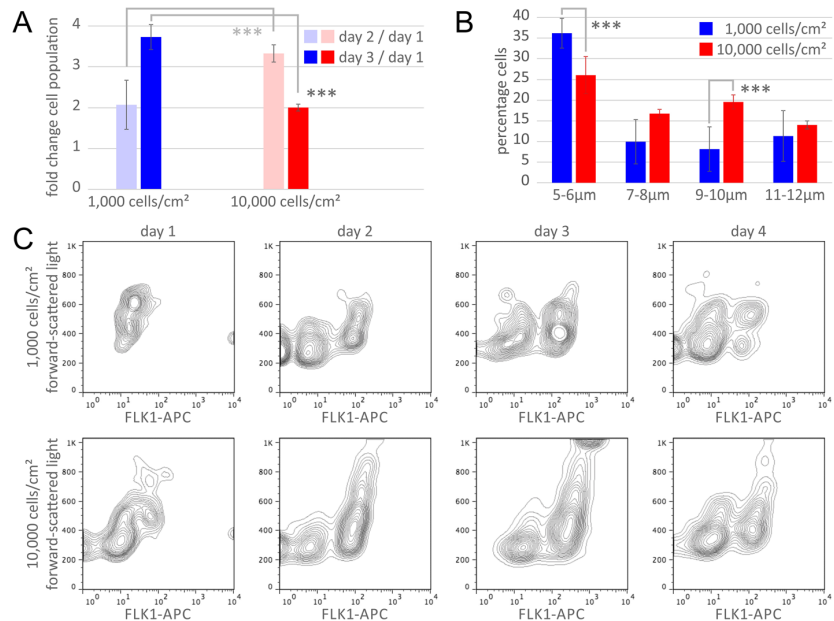


Fig. 4 Density-dependent shift of proliferation and cell diameter. **a** Proliferation rate significantly slows at day 3 in cells seeded at 10,000 cells/cm² (red) but increases in cells seeded at 1,000 cells/cm² (blue; fold increase of 2.1 vs 3.7; *** *p*-value < 0.001). **b** Higher density cells have a greater percentage of cells with large diameter (9–10 µm, 19.6% vs 8.2%; *** *p*-value < 0.001) and fewer small diameter cells (5–6 µm, 26.1% vs 36.2%; *** *p*-value < 0.001). **c** Flow cytometric cell scanning contour plot indicating 10,000 cells/cm² seeding density results in a greater proportion of cells exhibiting high forward scatter and FLK1 allophycocyanin conjugate (APC) positivity

diameter were found in cultures seeded at a density of 10,000 cells/cm² compared with lower density (9–10 μm, 20% vs 8%; *p*-value < 0.001) (Fig. 4b). The forward scatter measurements from fluorescence-activated cell sorting in flow cytometry, another indication of cell size, show that the early A3-ESCs are smaller compared with the larger differentiated FLK1⁺ VPCs (Fig. 4c).

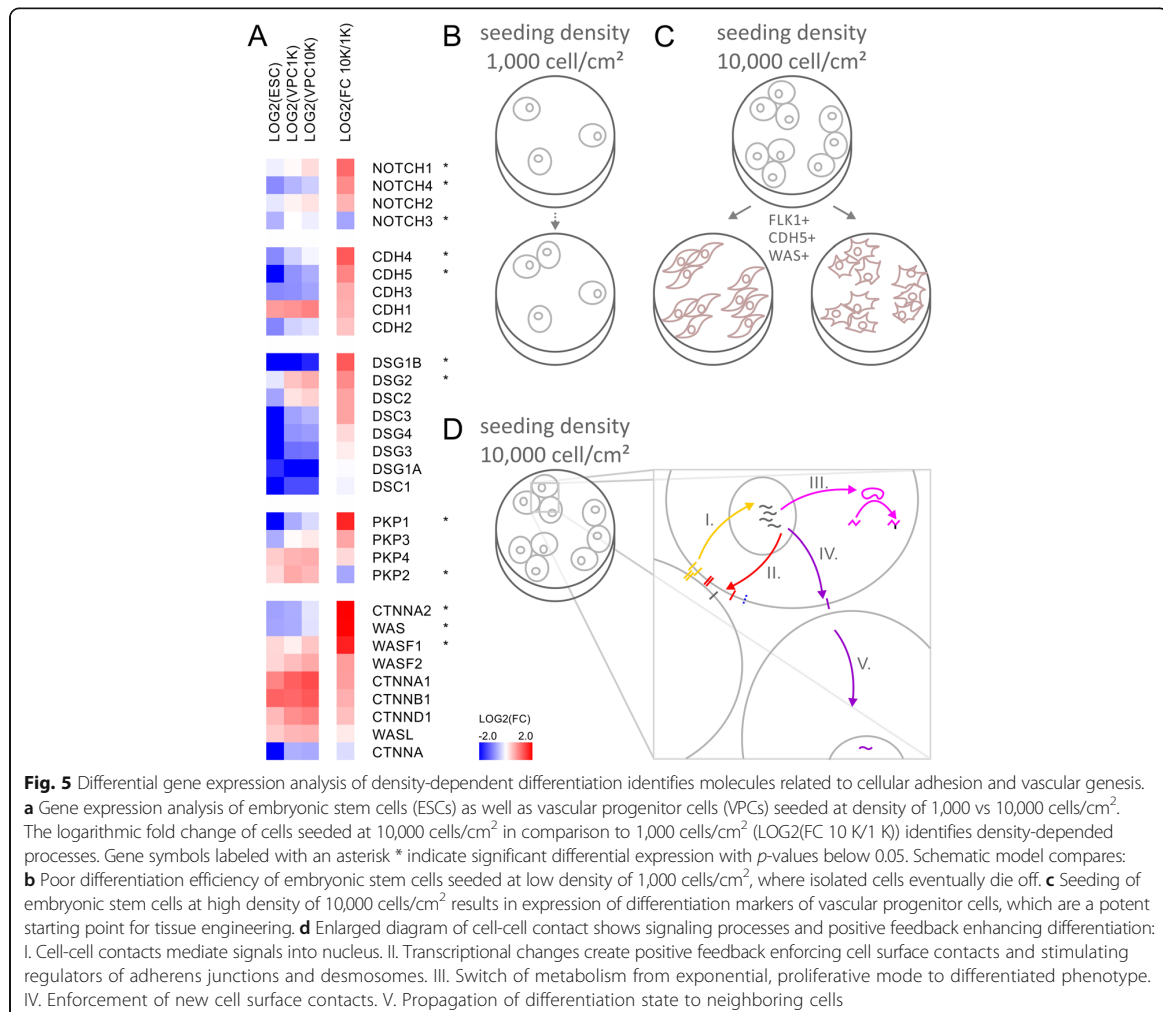
Differential gene expression of cell-to-cell signaling molecules during density-dependent differentiation

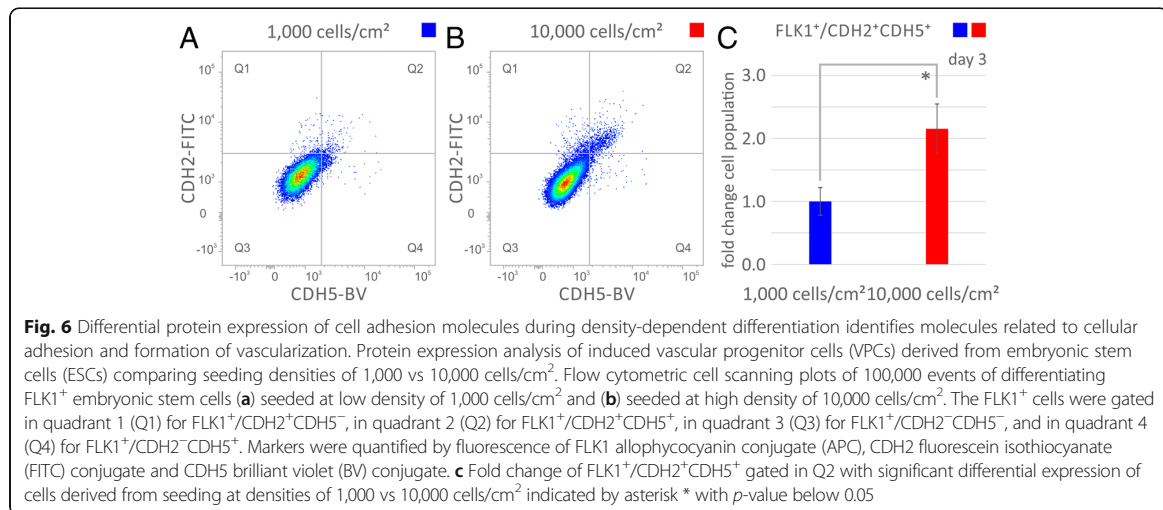
In order to further investigate the density-dependent signaling directing FLK1⁺ VPCs, a number of cell-to-cell signaling molecules were examined using a targeted PCR array. The expression pattern of cells seeded at densities of 10,000 cells/cm² or 1,000 cell/cm² revealed significant differential expression with *p*-values below 0.05 and a fold change of 2.0 or higher (Fig. 5a). Gene expression

pattern included significant up-regulation of NOTCH1 (GeneBank: 4851), NOTCH4 (GeneBank: 4855), CDH4, cadherin 4, retinal, R-cadherin (GeneBank: 1002), CDH5, cadherin 5, vascular endothelium, VE-cadherin (GeneBank: 1003), DSG1B, desmoglein 1 (GeneBank: 1828), DSG2, desmoglein 2 (GeneBank: 1829), PKP1, plakophilin 1 (GeneBank: 5317), CTNNA2, catenin cadherin-associated protein alpha 2 (GeneBank: 1496), WAS, Wiskott-Aldrich syndrome (GeneBank: 7454), and WASF1, WAS protein family, member 1 (GeneBank: 8936) as well as significant down-regulation of NOTCH3 (GeneBank: 4854), and PKP2, plakophilin 2 (GeneBank: 5318).

Differential protein expression of cell-to-cell signaling molecules during density-dependent differentiation

Protein level differences in cell-to-cell signaling molecule expression were quantified by flow cytometry (Fig. 6).





Induced VPCs originally seeded at 1,000 cell/cm² or 10,000 cells/cm² were stained and analyzed for FLK1, CDH2 (cadherin 2, neuronal, N-cadherin, GeneBank: 1000) and CDH5 expression. Importantly, the cell adhesion molecule CDH5, VE-cadherin, is indicative of vascular endothelial differentiation. The percentage of cells staining positive for FLK1, CDH2, and CDH5, FLK⁺/CDH2⁺CDH5⁺, quadrant 2, (Fig. 6a-b) was higher for cells originally seeded at 10,000 cells/cm² than those seeded at 1,000 cells/cm² (1.51% vs 0.70%, *p* < 0.01) (Fig. 6c).

Discussion

The generation of FLK1⁺ VPCs from ESCs peaks on day 3, followed by a reduction in FLK1⁺ numbers (Fig. 2ab) within the range of reported days (2–5) during mesoderm induction from ESCs [15, 17, 22–25]. The other significant variable in the efficient induction of VPCs was a high cell seeding density (Fig. 2a-b), while VEGF treatment level was not significant. The higher density and robustly differentiating VPC cultures also correlated with reduced proliferation rates and greater cell diameters, both indicative of differentiation (Fig. 4). Although these cells are not contact inhibited nor were they confluent cultures, hypoxia is known to drive mesoderm commitment [26, 27] and endothelial fate [19] from ESCs. To determine whether hypoxia could drive ESC differentiation, we calculated the molar fraction of oxygen at the cell surface of our high density cell dishes cultures. Using our experimental cell proliferation rates, estimated oxygen solubility in saline solution, and oxygen consumption rates reported for both ESCs = 27.5×10^{-18} [28] and ECs = 50×10^{-18} mol/cell/s [20], it was determined that, although oxygen would be reduced at higher cell seeding densities, none of the conditions would generate a hypoxic environment (defined as 1–3% oxygen).

Interestingly, VEGF treatment was not a determining or statistically significant variable in directing VPC fate. A large body of data implicates VEGF signaling in mesoderm and endothelial cell fate and that the FLK1/VEGF receptor is one of the key markers defining the angioblast cell [12, 14, 29, 30]. However, since BMP4 signaling can also activate the VEGF/VEGFR signaling [31, 32], it is sufficient in the inductions shown. Moreover, the two distinct VEGF binding domains in the fibronectin matrix [33] may stabilize and protect autocrine VEGF production from degradation [33], as well as, aid in cell presentation. The presumptive requirement of VEGF treatment in chemically-defined media for EC fate has been most rigorously examined using single cells cultured in collagen-type IV coated 96-well plates [12, 30, 34]. Without fibronectin matrix to sequester and protect the VEGF generated by the cells, one might expect that VEGF treatment would be required in these cultures. However, our results suggest that the utilization of fibronectin matrix mitigates the need for VEGF supplementation in VPC induction cultures.

Differential gene expression array analysis identified a number of cell-to-cell signaling molecules that were up-regulated in the higher density cultures containing more VPCs. Differential expression of cell surface receptors, desmosome, catenins, and cytoskeleton regulators could be required for, or facilitate, the density-dependent differentiation of ESCs (Fig. 5b-d). Vascular cells take advantage of many different cell adhesion contacts demonstrated by the global up-regulation of cadherins, desmosomal and desmoglein components. Since cell surface molecules have the ability to communicate extracellular changes into the cytosol, such as contact formation with neighboring cells, the gene expression data suggests a positive feedback reinforcing cellular contacts (Fig. 5d). Initial cell-cell contacts mediate signals into the nucleus,

where transcriptional changes create positive feedback promoting and strengthening cell surface contacts and stimulating regulators of adherens junctions and desmosomes. Positive feedback circuits have the ability to create threshold densities for successful differentiation. Once established and supported by the cell type specific cell surface contacts molecules, signals of differentiation can lead to lineage committed cell fates and organized tissue formation.

Amongst genes exhibiting the strongest change in the context of seeding density-dependent differentiation of VPCs were the cytoskeleton regulators WAS and CTNNA2. The expression pattern for both genes is unaffected in the lower density cohort but was consistently up-regulated in the higher density cohort. Wiskott-Aldrich syndrome protein (WASP) is a key regulator of endothelial cell-cell junctions and cytoskeleton dynamics and helps form and maintain the integrity and function of EC monolayers [35]. Moreover, WASP organizes actin and vascular epithelium-cadherins at EC junctions, and hence is vital for the assembly of vascular structures [35–37]. Importantly, along with FLK1 expression, WAS and CDH5 are also indicators of vascular differentiation [8]. Other studies have identified members of the E-twenty six (ETS) transcription factor family associating with FLK1 and CDH5 promoters in vascular epithelia to regulate vascular specification from primitive mesoderm [8–10, 38]. In murine and amphibian model organisms, plakophilins have been found localized to the nucleus of ESCs and form complexes with members of the ETS family of transcription factors to direct development related gene transcription events [39].

Similar to PKP1, CTNNA1, catenin cadherin-associated protein, alpha 1 (GeneBank: 1495) and AJAP1, adherens junctions associated protein 1 (GeneBank: 55966) expression levels are correlated with advancing tumor stage and inversely related to cell proliferation [32, 40, 41]. While CTNNA2 has been found as hub for extracellular matrix organization, loss of CTNNA1 is exhibited by multiple cancer types, and restoration of CTNNA1 expression in acute myeloid leukemia cells led to lower proliferation [27, 40]. Additionally CTNNA1 regulates differentiation events in the developing nervous system by maintaining beta-catenin signaling [42]. It is possible that the higher levels of PKP1 and CTNNA1 seen in the 10,000 cells/cm² density group causes these cells to slow their proliferation in favor of differentiation and growth. The regulation of desmosomal assembly by DSG1B, DSG2, and PKP1 not only enforces cell surface adhesion contacts between ECs but also regulates the cell signaling events in the cytoplasm and nucleus. DSG2 regulates actin assembly in ECs and affects proliferation via modulation of EGFR signaling [43, 44]. PKP1

associates with eukaryotic translation initiation factor 4A1 to stimulate protein translation [45] and loss of PKP1 is linked to prostate cancer proliferation [46]. Nuclear PKP1 complexes with catenin and is found bound to single stranded DNA [47]. PKP2, which is more abundant in the lower density group, binds to catenin and complexes with the RNA polymerase III holoenzyme [48].

The cadherin family uniformly responds to density-dependent differentiation [36, 37]. All cadherins assayed show up-regulation in the higher density cohort. CDH4 shows the highest density-dependent fold-change of the cadherin family. In addition to significant density-dependent up-regulation, vascular endothelial CDH5 is also significantly different between undifferentiated and induced ESCs. Of the desmosomal, desmocollin, and desmoglein components, DSG1B, DSG2, and PKP1 stand out as positive responders to density-dependent differentiation supporting formation of cell surface adhesion contacts in endothelial formation. For the majority of cell surface, cell junction and desmosomal components, a global increase in gene expression in response to density-dependent seeding is observed.

Among the differentiation and density-dependent effects on gene expression, perhaps the most profound is differential expression of the NOTCH receptor family. NOTCH signaling is a highly conserved intercellular signaling mechanism essential for proper cell fate choices during development [49]. Both NOTCH1 and NOTCH4 have both been implicated in vascular morphogenesis [50]. Moreover, NOTCH1 is found expressed in both endothelial and hematopoietic progenitor cells [51], while NOTCH4 is expressed in ECs, but not in hematopoietic progenitor cells [50]. NOTCH3 signaling is highest in late stage smooth muscle cell differentiation [52] and neural differentiation [53]. In the high cell density cultures, NOTCH1 and NOTCH4 were significantly up-regulated, while NOTCH3 is significantly down-regulated at induction conditions of 10,000 cells/cm² compared with the lower density cultures.

It is expected that differential expression of NOTCH components within ESCs seeded at higher density is, at least indirectly, responsible for the shift in metabolite utilization observed during the differentiation process. Specifically, NOTCH signaling has recently been linked to the regulation of cellular metabolism [54, 55], inducing glutamate uptake during the terminal differentiation of astrocytes [54]. Furthermore, NOTCH inhibition in glioma stem cells led to reductions in intracellular glutamate and glutamine, and increased lactate and threonine [55]. In the same study, it was noted that NOTCH blockade modulated the expression of multiple genes

regulating glutamate metabolism, including glutaminase and several glutamate transporters [55]. Tight regulation of glutaminase activity and glutamate metabolism are vital features of both stem cell function and tumor survival [11, 30, 44]. Interestingly, glutamine metabolism also regulates chromatin structure and pluripotency related transcription factors, such as OCT4, and therefore may play a pivotal role in vascular development [20]. Additional studies examining the role of cell-cell signaling components, particularly NOTCH, in the regulation of glutaminergic and other metabolic pathways could help optimize strategies for ESC differentiation and understand NOTCH-mediated cancer progression.

An increase in cell size correlating with stem cell differentiation is intimately coupled to loss of “stemness”. Moreover, larger cells proliferate more slowly compared to smaller cells [56]. While in cancer cells, a positive feedback is used to rapidly ramp up a distinct metabolic program [57], cellular differentiation is accompanied by a switch in metabolism from an exponential proliferative mode into a differentiated phenotype. During the time course of differentiation, ESCs start out as small, rapidly dividing cells, but rapidly shift away from exhaustive glycolysis and high metabolite consumption to a reduced metabolic demand per cell. This observed switch in metabolism also supports the changing demands of larger, more differentiated VPCs. Our data shows that the gene expression program of these differentiating ESCs also dynamically responds to the culture conditions at higher cellular density, and actively reinforces cell surface signaling components leading to up-regulation of genes associated with VPC fate. This strengthening of cellular communication may help regulate the concurrent switch of metabolism from an exponential, proliferative mode to a differentiated, growth permissive phenotype.

Conclusions

In summary, we have identified a density-dependent metabolic shift correlating with increased differentiation of VPCs from ESCs. This density-dependent differentiation model is associated with reduced cellular metabolism, highlighted by a decrease in exhaustive glycolysis, by a decrease in proliferation, and by an increase in cell size. Concomitant is enhanced expression of cell-cell signaling components, including those known to regulate the differentiation and metabolism of stem cells via density-sensing positive feedback circuits. In the future, efficient tissue engineering approaches may take advantage of such density-dependent switches and control crosstalk between cell-cell signaling and cellular metabolism.

Abbreviations

CSCs: Cancer stem cells; CT: Threshold cycle; ECs: Endothelial cells; ESCs: Embryonic stem cells; ETS: E-twenty six; FBS: Fetal bovine serum; GOI: Gene of interest; HKG: Housekeeping genes; iPSCs: Induced pluripotent stem cells; KO-DMEM: Knockout Dulbecco’s Modified Eagle Medium; KSR: Knockout serum replacer; LIF: Leukemia inhibitory factor; MEFs: Mouse embryonic fibroblasts; MEM: Minimal essential medium; PBS: Phosphate buffered saline; QPCR: Quantitative polymerase chain reaction; RT: Real-time; TSP: (trimethylsilyl)propanoic-2,2,3,3-d4 acid; VPCs: Vascular progenitor cells; WASP: Wiskott-Aldrich syndrome protein; Δ CT: Difference threshold cycle value

Used gene symbols

ACTB: actin beta, GeneBank: 60; AJAP1: adherens junctions associated protein 1, GeneBank: 55966; B2M: beta-2-microglobulin, GeneBank: 567; BMP4: bone morphogenetic protein 4, GeneBank: 652; CDH2: cadherin 2, type 1, neuronal, N-cadherin, GeneBank: 1000; CDH4: cadherin 4, type 1, retinal, R-cadherin, GeneBank: 1002; CDH5: cadherin 5, type 2, vascular endothelium, VE-cadherin, GeneBank: 1003; CTNNA1: catenin (cadherin-associated protein), alpha 1, GeneBank: 1495; CTNNA2: catenin (cadherin-associated protein), alpha 2, GeneBank: 1496; DSG1B = DSG1: desmoglein 1, GeneBank: 1828; DSG2: desmoglein 2, GeneBank: 1829; FLK1 = VEGFR = KDR: kinase insert domain receptor, GeneBank: 3791; GAPDH: glyceraldehyde-3-phosphate dehydrogenase, GeneBank: 2597; GUSB: glucuronidase beta, GeneBank: 2990; HSP90AB1: heat shock protein 90kDa alpha class B member 1, GeneBank: 3326; NOTCH1: notch1, GeneBank: 4851; NOTCH3: notch3, GeneBank: 4854; NOTCH4: notch4, GeneBank: 4855; PKP1: plakophilin 1, GeneBank: 5317; PKP2: plakophilin 2, GeneBank: 5318; POU5F1: OCT3/4, POU class 5 homeobox 1, GeneBank: 5460; VEGFA = VEGF: vascular endothelial growth factor A, GeneBank: 7422; WAS: Wiskott-Aldrich syndrome, GeneBank: 7454; WASF1: WAS protein family, member 1, GeneBank: 8936.

Funding

F.V.F. is grateful for the support of grant CA154887 from the National Institutes of Health, National Cancer Institute. The cell differentiation studies were funded through an NSF Integrative Graduate Education and Research Traineeship Award, an National Science Foundation Science and Technology Center for the Emergent Behavior of Integrated Biological Systems Award, and California Institute for Regenerative Medicine Award. This collaborative endeavor was supported by grants from the University of California Cancer Research Coordinating Committee CRCC CRN-17-427258, University of California Academic Senate Graduate and Research Council and the Health Sciences Research Institute.

Availability data and materials

Not applicable to this article as all data generated is included in this study.

Authors’ contributions

SJS, WT, FVF carried out cell density experiments, FVF conducted metabolomics experiments, SJS quantified metabolite levels and cell proliferation rates, DEG, SJS, FVF carried out flow cytometry analysis and image processing. FVF, KEM conceived and designed the study. FVF, SJS wrote the manuscript. All authors read and approved the final manuscript.

Competing interests

The authors declare that they have no competing interests.

Ethics approval and consent to participate

Not applicable.

All experimental protocols were approved by the Institutional Review Board at the University of California Merced. The study was carried out as part of IRB UCM13-0025 of the University of California Merced as part of dbGap ID 5094.

Publisher’s Note

Springer Nature remains neutral with regard to jurisdictional claims in published maps and institutional affiliations.

Author details

¹Systems Biology and Cancer Metabolism, Program for Quantitative Systems Biology, University of California Merced, 2500 North Lake Road, Merced, CA

95343, USA. ²Program for Biological Engineering and Small-scale Technologies, School of Engineering, University of California Merced, 5200 North Lake Road, Merced, CA 95343, USA.

Received: 26 October 2016 Accepted: 2 May 2017
Published online: 20 October 2017

References

- Kalka C, Masuda H, Takahashi T, Kalka-Moll WM, Silver M, Kearney M, Li T, Isner JM, Asahara T. Transplantation of ex vivo expanded endothelial progenitor cells for therapeutic neovascularization. *Proc Natl Acad Sci U S A*. 2000;97:3422–7.
- Soker S, Machado M, Atala A. Systems for therapeutic angiogenesis in tissue engineering. *World J Urol*. 2000;18:10–8.
- Kawamoto A, Gwon HC, Iwaguro H, Yamaguchi JI, Uchida S, Masuda H, Silver M, Ma H, Kearney M, Isner JM, Asahara T. Therapeutic potential of ex vivo expanded endothelial progenitor cells for myocardial ischemia. *Circulation*. 2001;103:634–7.
- Kocher AA, Schuster MD, Szabolcs MJ, Takuma S, Burkhoff D, Wang J, Homma S, Edwards NM, Itescu S. Neovascularization of ischemic myocardium by human bone-marrow-derived angioblasts prevents cardiomyocyte apoptosis, reduces remodeling and improves cardiac function. *Nat Med*. 2001;7:430–6.
- Kaushal S, Amiel GE, Guleserian KJ, Shapira OM, Perry T, Sutherland FW, Rabkin E, Moran AM, Schoen FJ, Atala A, et al. Functional small-diameter neovessels created using endothelial progenitor cells expanded ex vivo. *Nat Med*. 2001;7:1035–40.
- Griese DP, Ehsan A, Melo LG, Kong D, Zhang L, Mann MJ, Pratt RE, Mulligan RC, Dzau VJ. Isolation and transplantation of autologous circulating endothelial cells into denuded vessels and prosthetic grafts: implications for cell-based vascular therapy. *Circulation*. 2003;108:2710–5.
- Ping YF, Zhang X, Bian XW. Cancer stem cells and their vascular niche: Do they benefit from each other? *Cancer Lett*. 2016;380:561–7.
- Kohler EE, Wary KK, Li F, Chatterjee I, Urao N, Toth PT, Ushio-Fukai M, Rehman J, Park C, Malik AB. Flk1+ and VE-cadherin+ endothelial cells derived from iPSCs recapitulates vascular development during differentiation and display similar angiogenic potential as ESC-derived cells. *PLoS ONE*. 2013;8:e85549.
- Lee D, Park C, Lee H, Lugas JJ, Kim SH, Arentson E, Chung YS, Gomez G, Kyba M, Lin S, et al. ER71 acts downstream of BMP, Notch, and Wnt signaling in blood and vessel progenitor specification. *Cell Stem Cell*. 2008;2:497–507.
- Kataoka H, Hayashi M, Nakagawa R, Tanaka Y, Izumi N, Nishikawa S, Jakt ML, Tarui H. ETV2/ER71 induces vascular mesoderm from Flk1+ PDGFRalpha+ primitive mesoderm. *Blood*. 2011;118:6975–86.
- Teng L, Lei HM, Sun F, An SM, Tang YB, Meng S, Wang CH, Shen Y, Chen HZ, Zhu L. Autocrine glutamatergic transmission for the regulation of embryonal carcinoma stem cells. *Oncotarget*. 2016;7:49552–64.
- Yamashita J, Itoh H, Hirashima M, Ogawa M, Nishikawa S, Yurugi T, Naito M, Nakao K. Flk1-positive cells derived from embryonic stem cells serve as vascular progenitors. *Nature*. 2000;408:92–6.
- Kattman SJ, Witty AD, Gagliardi M, Dubois NC, Niapour M, Hotta A, Ellis J, Keller G. Stage-specific optimization of activin/nodal and BMP signaling promotes cardiac differentiation of mouse and human pluripotent stem cell lines. *Cell Stem Cell*. 2011;8:228–40.
- Glaser DE, Gower RM, Lauer NE, Tam K, Blancas AA, Shih AJ, Simon SI, McCloskey KE. Functional Characterization of Embryonic Stem Cell-Derived Endothelial Cells. *J Vasc Res*. 2011;48:415–28.
- McCloskey KE, Lyons I, Rao RR, Stice SL, Nerem RM. Purified and proliferating endothelial cells derived and expanded in vitro from embryonic stem cells. *Endothelium*. 2003;10:329–36.
- McCloskey KE, Smith DA, Jo H, Nerem RM. Embryonic Stem Cell-Derived Endothelial Cells May Lack Complete Functional Maturation in vitro. *J Vasc Res*. 2006;43:411–21.
- Blancas A, Shih, AJ, Lauer, NE, McCloskey KE. Endothelial Cells from Embryonic Stem Cells in a Chemically Defined Medium. *Stem Cells Dev*. 2011;20:2153–61.
- Nishikawa SI, Nishikawa S, Hirashima M, Matsuyoshi N, Kodama H. Progressive lineage analysis by cell sorting and culture identifies FLK1+ VE-cadherin+ cells at a diverging point of endothelial and hemopoietic lineages. *Development*. 1998;125:1747–57.
- Sasaki M, Knobbe CB, Munger JC, Lind EF, Brenner D, Brustle A, Harris IS, Holmes R, Wakeham A, Haight J, et al. IDH1(R132H) mutation increases murine haematopoietic progenitors and alters epigenetics. *Nature*. 2012;488:656–9.
- Marsboom G, Zhang GF, Pohl-Avila N, Zhang Y, Yuan Y, Kang H, Hao B, Brunengraber H, Malik AB, Rehman J. Glutamine Metabolism Regulates the Pluripotency Transcription Factor OCT4. *Cell Rep*. 2016;16:323–32.
- Harjes U, Verfaillie C, Carmeliet P. Endothelial Barrier and Metabolism: New Kids on the Block Regulating Bone Marrow Vascular Niches. *Dev Cell*. 2016;37:210–2.
- Glaser DE, Burns AB, Hatano R, Medrzycki M, Fan Y, McCloskey KE. Specialized mouse embryonic stem cells for studying vascular development. *Stem Cells Cloning*. 2014;7:79–88.
- Wu Z, Wei D, Gao W, Xu Y, Hu Z, Ma Z, Gao C, Zhu X, Li Q. TPO-Induced Metabolic Reprogramming Drives Liver Metastasis of Colorectal Cancer CD110+ Tumor-Initiating Cells. *Cell Stem Cell*. 2015;17:47–59.
- Blancas AA, Lauer NE, McCloskey KE. Endothelial differentiation of embryonic stem cells. *Curr Protoc Stem Cell Biol*. 2008;Chapter 1:Unit 1F 5.
- McCloskey KE, Stice SL, Nerem RM. In vitro derivation and expansion of endothelial cells from embryonic stem cells. *Methods Mol Biol*. 2006;330:287–301.
- Hamilton LK, Dufresne M, Joppe SE, Petryszyn S, Aumont A, Calon F, Barnabe-Heider F, Furtos A, Parent M, Chaurand P, Fernandes KJ. Aberrant Lipid Metabolism in the Forebrain Niche Suppresses Adult Neural Stem Cell Proliferation in an Animal Model of Alzheimer's Disease. *Cell Stem Cell*. 2015;17:397–411.
- Zhang J, Ratanasirintrao S, Chandrasekaran S, Wu Z, Ficarro SB, Yu C, Ross CA, Cacchiarelli D, Xia Q, Seligson M, et al. LIN28 Regulates Stem Cell Metabolism and Conversion to Primed Pluripotency. *Cell Stem Cell*. 2016;19:66–80.
- Drehmer DL, de Aguiar AM, Brandt AP, Petiz L, Cadena SM, Rebelatto CK, Brofman PR, Filipak Neto F, Dallagiovanna B, Abud AP. Metabolic switches during the first steps of adipogenic stem cells differentiation. *Stem Cell Res*. 2016;17:413–21.
- Marcelo KL, Goldie LC, Hirschi KK. Regulation of endothelial cell differentiation and specification. *Circ Res*. 2013;112:1272–87.
- Rosenberg SA, Niglio SA, Salehomoum N, Chan JL, Jeong BS, Wen Y, Li J, Fukui J, Chen S, Shin SS, Goydos JS. Targeting Glutamatergic Signaling and the PI3 Kinase Pathway to Halt Melanoma Progression. *Transl Oncol*. 2015;8:1–9.
- Suzuki Y, Montagne K, Nishihara A, Watabe T, Miyazono K. BMPs promote proliferation and migration of endothelial cells via stimulation of VEGF-A/VEGFR2 and angiopoietin-1/Tie2 signalling. *J Biochem*. 2008;143:199–206.
- Ezaka K, Kanda M, Sugimoto H, Shimizu D, Oya H, Nomoto S, Sueoka S, Tanaka Y, Takami H, Hashimoto R, et al. Reduced Expression of Adherens Junctions Associated Protein 1 Predicts Recurrence of Hepatocellular Carcinoma After Curative Hepatectomy. *Ann Surg Oncol*. 2015;22 Suppl 3:1499–507.
- Wijelath ES, Murray J, Rahman S, Patel Y, Ishida A, Strand K, Aziz S, Cardona C, Hammond WP, Savidge GF, et al. Novel vascular endothelial growth factor binding domains of fibronectin enhance vascular endothelial growth factor biological activity. *Circ Res*. 2002;91:25–31.
- Hojfeldt JW, Helin K. Regional tumour glutamine supply affects chromatin and cell identity. *Nat Cell Biol*. 2016;18:1027–9.
- Mooren OL, Kim J, Li J, Cooper JA. Role of N-WASP in Endothelial Monolayer Formation and Integrity. *J Biol Chem*. 2015;290:18796–805.
- Vittet D, Buchou T, Schweitzer A, Dejana E, Huber P. Targeted null-mutation in the vascular endothelial-cadherin gene impairs the organization of vascular-like structures in embryoid bodies. *Proc Natl Acad Sci U S A*. 1997;94:6273–8.
- Lenard A, Ellersdottir E, Herwig L, Krudewig A, Sauteur L, Belting HG, Affolter M. In vivo analysis reveals a highly stereotypic morphogenetic pathway of vascular anastomosis. *Dev Cell*. 2013;25:492–506.
- Rasmussen TL, Kwon J, Diekmann MA, Belema-Bedada F, Song Q, Bowlin K, Shi X, Ferdous A, Li T, Kyba M, et al. ER71 directs mesodermal fate decisions during embryogenesis. *Development*. 2011;138:4801–12.
- Munoz WA, Lee M, Miller RK, Ahmed Z, Ji H, Link TM, Lee GR, Kloc M, Ladbury JE, McCrea PD. Plakophilin-3 catenin associates with the ETV1/ER81 transcription factor to positively modulate gene activity. *PLoS ONE*. 2014;9:e86784.
- Liu TX, Becker MW, Jelinek J, Wu WS, Deng M, Mikhalkovich N, Hsu K, Bloomfield CD, Stone RM, DeAngelo DJ, et al. Chromosome 5q deletion and epigenetic suppression of the gene encoding alpha-catenin (CTNNA1) in myeloid cell transformation. *Nat Med*. 2007;13:78–83.

41. Han L, Zhang KL, Zhang JX, Zeng L, Di CH, Fee BE, Rivas M, Bao ZS, Jiang T, Bigner D, et al. AJAP1 is dysregulated at an early stage of gliomagenesis and suppresses invasion through cytoskeleton reorganization. *CNS Neurosci Ther*. 2014;20:429–37.
42. Stocker AM, Chenn A. Focal reduction of alphaE-catenin causes premature differentiation and reduction of beta-catenin signaling during cortical development. *Dev Biol*. 2009;328:66–77.
43. Giusti B, Margheri F, Rossi L, Lapini I, Magi A, Serrati S, Chilla A, Laurenzana A, Magnelli L, Calorini L, et al. Desmoglein-2-integrin Beta-8 interaction regulates actin assembly in endothelial cells: deregulation in systemic sclerosis. *PLoS ONE*. 2013;8:e68117.
44. Ryu JM, Lee SH, Seong JK, Han HJ. Glutamine contributes to maintenance of mouse embryonic stem cell self-renewal through PKC-dependent downregulation of HDAC1 and DNMT1/3a. *Cell Cycle*. 2015;14:3292–305.
45. Wolf A, Krause-Gruszczynska M, Birkenmeier O, Ostareck-Lederer A, Huttelmaier S, Hatzfeld M. Plakophilin 1 stimulates translation by promoting eIF4A1 activity. *J Cell Biol*. 2010;188:463–71.
46. Yang C, Fischer-Keso R, Schlechter T, Strobel P, Marx A, Hofmann I. Plakophilin 1-deficient cells upregulate SPOCK1: implications for prostate cancer progression. *Tumour Biol*. 2015;36:9567–77.
47. Sobolik-Delmaire T, Reddy R, Pashaj A, Roberts BJ, Wahl 3rd JK. Plakophilin-1 localizes to the nucleus and interacts with single-stranded DNA. *J Invest Dermatol*. 2010;130:2638–46.
48. Mertens C, Hofmann I, Wang Z, Teichmann M, Sepehri Chong S, Schnolzer M, Franke WW. Nuclear particles containing RNA polymerase III complexes associated with the junctional plaque protein plakophilin 2. *Proc Natl Acad Sci U S A*. 2001;98:7795–800.
49. Artavanis-Tsakonas S, Rand MD, Lake RJ. Notch signaling: cell fate control and signal integration in development. *Science*. 1999;284:770–6.
50. Krebs LT, Xue Y, Norton CR, Shutter JR, Maguire M, Sundberg JP, Gallahan D, Closson V, Kitajewski J, Callahan R, et al. Notch signaling is essential for vascular morphogenesis in mice. *Genes Dev*. 2000;14:1343–52.
51. Lardelli M, Lendahl U. Motch A and motch B—two mouse Notch homologues coexpressed in a wide variety of tissues. *Exp Cell Res*. 1993;204:364–72.
52. Granata A, Bernard WG, Zhao N, McCafferty J, Lilly B, Sinha S. Temporal and embryonic lineage-dependent regulation of human vascular SMC development by NOTCH3. *Stem Cells Dev*. 2015;24:846–56.
53. Rusanescu G, Mao J. Notch3 is necessary for neuronal differentiation and maturation in the adult spinal cord. *J Cell Mol Med*. 2014;18:2103–16.
54. Angulo-Rojo C, Manning-Cela R, Aguirre A, Ortega A, Lopez-Bayghen E. Involvement of the Notch pathway in terminal astrocytic differentiation: role of PKA. *ASN Neuro*. 2013;5:e00130.
55. Kahlert UD, Cheng M, Koch K, Marchionni L, Fan X, Raabe EH, Maciaczyk J, Glunde K, Eberhart CG. Alterations in cellular metabolome after pharmacological inhibition of Notch in glioblastoma cells. *Int J Cancer*. 2016;138:1246–55.
56. Dolfi SC, Chan LL, Qiu J, Tedeschi PM, Bertino JR, Hirshfield KM, Oltvai ZN, Vazquez A. The metabolic demands of cancer cells are coupled to their size and protein synthesis rates. *Cancer Metab*. 2013;1:20.
57. Wang Y, Huang Y, Zhao L, Li Y, Zheng J. Glutaminase 1 is essential for the differentiation, proliferation, and survival of human neural progenitor cells. *Stem Cells Dev*. 2014;23:2782–90.

Submit your next manuscript to BioMed Central and we will help you at every step:

- We accept pre-submission inquiries
- Our selector tool helps you to find the most relevant journal
- We provide round the clock customer support
- Convenient online submission
- Thorough peer review
- Inclusion in PubMed and all major indexing services
- Maximum visibility for your research

Submit your manuscript at
www.biomedcentral.com/submit



Chapter 4

Metabolic profiling of
triple-negative breast cancer cells
reveals metabolic vulnerabilities

RESEARCH

Open Access

Metabolic profiling of triple-negative breast cancer cells reveals metabolic vulnerabilities



Nathan J. Lanning^{1*}, Joshua P. Castle², Simar J. Singh³, Andre N. Leon¹, Elizabeth A. Tovar², Amandeep Sanghera³, Jeffrey P. MacKeigan^{2,4}, Fabian V. Filipp³ and Carrie R. Graveel^{2*}

Abstract

Background: Among breast cancers, the triple-negative breast cancer (TNBC) subtype has the worst prognosis with no approved targeted therapies and only standard chemotherapy as the backbone of systemic therapy. Unique metabolic changes in cancer progression provide innovative therapeutic opportunities. The receptor tyrosine kinases (RTKs) epidermal growth factor receptor (EGFR), and MET receptor are highly expressed in TNBC, making both promising therapeutic targets. RTK signaling profoundly alters cellular metabolism by increasing glucose consumption and subsequently diverting glucose carbon sources into metabolic pathways necessary to support the tumorigenesis. Therefore, detailed metabolic profiles of TNBC subtypes and their response to tyrosine kinase inhibitors may identify therapeutic sensitivities.

Methods: We quantified the metabolic profiles of TNBC cell lines representing multiple TNBC subtypes using gas chromatography mass spectrometry. In addition, we subjected MDA-MB-231, MDA-MB-468, Hs578T, and HCC70 cell lines to metabolic flux analysis of basal and maximal glycolytic and mitochondrial oxidative rates. Metabolic pool size and flux measurements were performed in the presence and absence of the MET inhibitor, INC280/capmatinib, and the EGFR inhibitor, erlotinib. Further, the sensitivities of these cells to modulators of core metabolic pathways were determined. In addition, we annotated a rate-limiting metabolic enzymes library and performed a siRNA screen in combination with MET or EGFR inhibitors to validate synergistic effects.

Results: TNBC cell line models displayed significant metabolic heterogeneity with respect to basal and maximal metabolic rates and responses to RTK and metabolic pathway inhibitors. Comprehensive systems biology analysis of metabolic perturbations, combined siRNA and tyrosine kinase inhibitor screens identified a core set of TCA cycle and fatty acid pathways whose perturbation sensitizes TNBC cells to small molecule targeting of receptor tyrosine kinases.

Conclusions: Similar to the genomic heterogeneity observed in TNBC, our results reveal metabolic heterogeneity among TNBC subtypes and demonstrate that understanding metabolic profiles and drug responses may prove valuable in targeting TNBC subtypes and identifying therapeutic susceptibilities in TNBC patients. Perturbation of metabolic pathways sensitizes TNBC to inhibition of receptor tyrosine kinases. Such metabolic vulnerabilities offer promise for effective therapeutic targeting for TNBC patients.

Keywords: Triple-negative breast cancer, Metabolism, Rate-limiting enzymes, Receptor tyrosine kinase, Tyrosine kinase inhibitor, Metabolic inhibitor

* Correspondence: nllanning@calstatela.edu; Carrie.Graveel@vai.org

¹California State University, Los Angeles, 5151 State University Drive, Los Angeles, CA 90032, USA

²Van Andel Research Institute, 333 Bostwick Ave, NE, Grand Rapids, MI 49503, USA

Full list of author information is available at the end of the article



© The Author(s). 2017 **Open Access** This article is distributed under the terms of the Creative Commons Attribution 4.0 International License (<http://creativecommons.org/licenses/by/4.0/>), which permits unrestricted use, distribution, and reproduction in any medium, provided you give appropriate credit to the original author(s) and the source, provide a link to the Creative Commons license, and indicate if changes were made. The Creative Commons Public Domain Dedication waiver (<http://creativecommons.org/publicdomain/zero/1.0/>) applies to the data made available in this article, unless otherwise stated.

Background

Triple-negative breast cancer

Triple-negative breast cancer (TNBC) accounts for 15–20% of invasive breast cancers. TNBC is characterized by the lack of estrogen receptor (ER) and progesterone receptor (PR) expression and human epidermal growth factor receptor 2 (HER2) amplification. TNBCs are associated with advanced stage at diagnosis and poorer outcome compared to other breast cancer subtypes [1]. Characteristic TNBC clinical features include a peak in recurrence risk within the first 3 years, a weak relationship between the tumor size and lymph node metastasis, and a peak of cancer-related death in the first 5 years [2]. At the molecular level, TNBC has significant overlap with the basal-like subtype as approximately 80% of TNBCs are classified as basal-like [1]. Currently, TNBCs are treated with cytotoxic combination chemotherapy. Even though TNBC patients have significantly higher rates of pathologic complete response compared to non-TNBC, TNBC patients have decreased 3-year progression-free survival and overall survival rates [1, 3]. Hence, there is a vital need for a comprehensive understanding of the molecular basis of TNBC progression and emerging treatment approaches.

TNBC is a highly heterogeneous disease at the molecular level, and this heterogeneity likely underlies the variable treatment responses in patients. Recent studies involving comprehensive gene expression analysis revealed extensive molecular heterogeneity within TNBC cases and identified four to six distinct molecular TNBC subtypes [4, 5]. These subtypes have unique expression signatures and ontologies and are defined as basal-like, mesenchymal and luminal androgen receptor subtypes. To identify novel treatment strategies for TNBC patients, it is essential that we understand the unique and common molecular features of these TNBC subtypes.

Current treatment options for TNBC patients are restricted to chemotherapy; however, receptor tyrosine kinases (RTK) are promising druggable targets due to their high expression in TNBC. The epidermal growth factor receptor (EGFR) and MET receptor are highly expressed in multiple TNBC subtypes with EGFR overexpression in 54% of basal breast cancers (predominantly TNBC). Additionally, EGFR is a biomarker for identification of basal breast cancers [6–10]. Similarly, MET is associated with poor clinical outcome in breast cancer [11–15], and high MET expression correlates with TNBC [16, 17]. Previously, we demonstrated that the MET inhibitor cabozantinib inhibited TNBC growth, invasion, and metastasis [18]. Recently, we determined that combined MET and EGFR inhibition was highly effective at abrogating tumor growth in patient-derived TNBC tumorgrafts and significantly decreased the variability in treatment response compared to monotherapy with MET or EGFR inhibitors [19]. These results highlight

that MET and/or EGFR inhibition may be a highly effective treatment strategy for TNBC patients. Metabolic alterations are now widely understood to support the cancer phenotype, and RTKs such as MET and EGFR have been implicated in driving some of these the metabolic alterations [20–25].

Metabolic characteristics of TNBC

Particular metabolic characteristics of TNBC have been investigated, and overall TNBC cell models and patient samples are characterized by elevated glycolysis. Along these lines, a genome wide screen identified a small subset of metabolic genes, including core glycolytic and oxidative phosphorylation (OXPHOS) genes, whose suppression was lethal in a TNBC cell model [26]. Compared to ER+ breast cancer cell lines, MDA-MB-231 and MDA-MB-468 TNBC cell models are reported to harbor high glycolytic flux and low OXPHOS activity [27] and are more primed to switch to a glycolytic program in the context of limited oxygen than non-transformed cells [28]. In patient samples, high glucose transporter, GLUT1, expression is observed in TNBC compared to non-TNBC tumors [29]. GLUT1 may also enhance invasion by localizing to the invasive edge of *in vivo* tumor models [30]. Mechanistically, high MYC expression in TNBC cell models suppresses expression of the glycolytic inhibitor, thioredoxin-interacting protein, TXNIP, resulting in increased glycolytic flux [31]. In addition, a siRNA screen revealed that TNBC cell line models are dependent on elevated glycolysis through the LDHB (lactate dehydrogenase B) as opposed to their non-TNBC counterparts [32].

Recent evidence indicates that the metabolic characteristics of TNBC correlate with therapeutic response. The glycolytic potential of TNBC cells may be associated with chemotherapeutic resistance as exposing TNBC cell models to increasing concentrations of glucose increases proliferation and decreases the efficacy of metformin-induced apoptosis [33, 34]. Additionally, PKM2, a glycolytic enzyme associated with high tumoral glycolytic flux [35], may confer some resistance to doxorubicin treatment *in vitro* and in MDA-MB-231 orthotopic breast cancer models [36]. Other studies demonstrate that stimulation of mitochondrial activity and concurrent inhibition of mitochondrial respiratory complex I [37] or a combination of glycolytic and mitochondrial inhibitors [38] effectively kills TNBC cells and TNBC xenografts.

Collectively, the above studies demonstrate a clear role for altered metabolism supporting the aggressive TNBC phenotype. Much like the genetic and signaling heterogeneity found in cancers in general and TNBC in particular [39], metabolic heterogeneity also likely exists in TNBC patients [40, 41] and cell models [33, 42] and likely drives differential responses to therapeutics. Therefore, comprehensive and systematic investigations into the

metabolism of TNBC and TNBC cell models are necessary in order to gain insight into the best therapeutic strategies. Some previous approaches referenced above undertook genome-wide siRNA screening approaches or utilized computational approaches [43]. In the present study, we provide detailed metabolic analyses of the commonly used MDA-MB-231, MDA-MB-468, Hs578T, and HCC70 TNBC cell line models, which represent the two major basal-like subtype and the mesenchymal subtypes [4]. We determined the basal and maximal metabolic rates, as well as the metabolic rates in response to EGFR and MET inhibitors in these TNBC lines. We also measure viability in response to chemical modulation of five metabolic pathways. Finally, we report the viability effects of suppressing each KEGG metabolic pathway in combination with EGFR (erlotinib) or MET (INC280) inhibition in these cell lines. Overall, these results provide a more thorough view of the metabolic landscape of TNBC and the effect of RTK inhibition on TNBC metabolism.

Methods

Cell culture

All cells were purchased from ATCC. MDA-MB-231, MDA-MB-468, Hs578T, and HCC70 cells were cultured in DMEM (ThermoFisher) supplemented with 10% fetal bovine serum. hTERT-HME1 cells were cultured in MEM (Lonza) supplemented with hEGF, insulin, hydrocortisone, and BPE (Lonza).

Metabolomics profiling

For metabolite quantification, cells were seeded in triplicate ($n = 3$) in 6-well plates with DMEM supplemented with 10% FBS. After 24 h, the media was removed and replaced with fresh media. Upon reaching 70% confluency, cells were washed twice with phosphate buffered saline (PBS, 46-013-CM, Corning) and lifted from culture wells using 0.25% Trypsin/2.21 mM EDTA (25-053-CI, Corning). Cells were then washed with PBS containing 10% FBS followed by 0.9% NaCl (Sigma, S9888). Cell pellets frozen in liquid nitrogen before storage at 193 K.

Frozen cell pellets were thawed on ice for 10 min before addition of 1 mL cold extraction solvent containing acetonitrile/isopropanol/water (3:3:2) at 253 K. Samples were then vortexed (15 s \times 5) and frozen on dry ice for 20 mins and the freeze/thaw/vortex cycle repeated twice. Samples were dried via vacuum centrifugal evaporation and stored at -80°C before analysis.

Dried samples were derivatized first by addition of 10 μL of MOX Reagent (20 mg/mL methoxyamine-hydrochloride in dry pyridine (TS-45950, Thermo Fisher Scientific) followed by 90-min incubation in a digital heating shaking drybath at 303 K and 1100 rpm. Next, 90 μL N-Methyl-N-(trimethylsilyl)trifluoroacetamide (MSTFA, Sigma 394,866)

was added and samples were incubated at 310 K and 1000 rpm for 30mins before centrifugation for 5 min at 14,000 rpm/277 K. The supernatant was transferred to an auto sampler vial for gas chromatography-mass spectrometry (GC-MS) analysis.

Derivatized samples were analyzed on a Triple Quadrupole GC-MS (TSQ8000, Thermo Fisher Scientific) equipped with a TG-5MS (30 m \times 0.25 mm i.d. \times 0.25 μm , 26098-1420, Thermo Fisher Scientific) capillary column and run under electron ionization at 70 eV. The GC was programmed with an injection temperature of 523 K and splitless injection volume of 1 μL . The GC oven temperature program started at 232 K for 1 min, rising to 523 K at 10 K/min with a final hold at this temperature for 6 min. The GC flow rate with helium carrier gas was 1.2 mL/min. The transfer line temperature was set at 563 K and ion source temperature at 568 K. A range of 50–600 m/z was scanned with a scan time of 0.25 s.

Metabolites were identified using TraceFinder software v 3.3 (Thermo Fisher Scientific) based on in-house libraries of metabolite retention time and fragmentation patterns. Identified metabolites were quantified using the total ion count peak area for specific mass ions, and standard curves generated from reference standards run in parallel. The mean, standard deviation, and 95% confidence interval were calculated for each cell line and treatment condition. ANOVA with student's *t* test was used to compare treatment conditions within each cell line.

Metabolic flux analysis

For all metabolic flux analyses, a Seahorse 96 XFe was used. Twenty-four hours prior to metabolic flux analyses, cells were cultured in identical media (10 mM glucose, 2 mM glutamine, 1 mM pyruvate). Cells were plated at a density of 40,000 cells per well in a Seahorse 96-well assay plate 16 h prior to analysis. For basal and maximal metabolic profiles, four independent experiments were performed, each with three biological replicates and five technical replicates. For basal metabolic profiles in the context of RTK inhibitor treatment, three biological replicates each with five technical replicates were performed, and cells were treated with 10 μM erlotinib or INC280/capmatinib (Selleck Chemicals) for 18 h prior to metabolic rate analysis. After metabolic rate analyses, extracellular acidification rate (ECAR) and oxygen consumption rate (OCR) measurements were normalized to CyQUANT (Invitrogen) measurements cell count measurements in each well. For basal rate measurements, ECAR and OCR measurements were spaced 6 min apart. For maximal rate measurements, basal rates were measured twice at an interval of 6–7 min, followed by carbonyl cyanide-p-trifluoromethoxyphenylhydrazone (FCCP)

(1 μM final concentration) injection, mixture, and measurement 6–7 min later, followed another measurement 6–7 min later, followed by 2-deoxyglucose (2-DG, 100 mM final concentration) or rotenone + antimycin (1 μM each final concentration) injection, mixture, and measurement 6–7 min later, followed by a final measurement 6–7 min later. Maximal rate data are representative experiments displayed as averages of three biological replicates with error bars representing standard deviation.

Cell viability in response to metabolic modulators

Cells were plated at a density of 2500 cells per well in 96-well plates in growth media. Cells were treated with vehicle or the following concentrations of chemicals: 25 mM 2-DG, 200 μM 6-aminonicotinamide (6-AN), 1 μM rotenone, 10 mM metformin, and 1 mM 5-Aminoimidazole-4-carboxamide ribonucleotide (AICAR). After 48 h of treatment, viability was measured by CellTiter-Glo (Promega). Two independent experiments, each containing six biological replicates, were performed. Data are from one representative experiment and provided as averages with error bars representing standard deviation.

siRNA screen

Screen design

All small interfering RNAs (siRNAs) were from Qiagen (Additional file 1: Table S1) and were transfected into cells with siLentFect (BioRad, 1 μl per ml, for transfection efficiency for each cell line, see Additional file 2: Figure S1A). Rate-limiting enzymes were collated through KEGG annotation (<http://www.genome.jp/kegg/>), the Rate-Limiting Enzyme Regulation Database (<http://rle.cbi.pku.edu.cn/home.cgi>, [44]), and literature searches and categorized according to KEGG. Genes and metabolic categories and pathways are provided in Additional file 3: Table S2 according to these KEGG-based annotations. For the siRNA screen, cells were transfected with control (non-targeting) siRNAs or siRNAs targeting the above-described rate-limiting enzymes, then treated with either DMSO, INC280, or erlotinib (Additional file 2: Figure S1A). Cells were plated in 96-well assay plates at 2500 cells per well. Sixteen hours later, cells were transfected with a pool of two siRNAs per gene. Twenty-four hours post-transfection, fresh media was added containing 10 μM INC280, 10 μM erlotinib, or 0.1% DMSO (the final DMSO concentration in wells containing INC280 or erlotinib). The screen was carried out in duplicate for each siRNA and each condition (DMSO, INC280, or erlotinib) in each cell line. Seventy-two hours post-transfection (48-h post-drug treatment), cell viability was assessed by CellTiter-Glo (Promega).

Screen analysis

The siRNA screen was performed in duplicate, and sensitivity index (below) values were derived from replicate

averages. Replicates resulting in a variance larger than 0.04 were not considered for further analysis. To determine which siRNAs resulted in the greatest loss of viability in combination with INC280 or erlotinib compared to DMSO, a variation on the sensitivity index (SI) equation developed by Hoffman and Gardner (1983) was used to estimate the effect of siRNA knockdown on drug sensitivity [45]. The SI value for each siRNA was calculated using the following equation:

$$SI = \left(\frac{R_c}{C_c} \times \frac{C_d}{C_c} \right) - \left(\frac{R_d}{C_c} \right).$$

In this equation, R_c is the average viability in drug-untreated (DMSO) wells transfected with siRNA targeting rate-limiting enzymes, R_d is the average viability in drug-treated wells (INC280 or erlotinib) with siRNA targeting rate-limiting enzymes, C_c is the average viability in drug-untreated (DMSO) wells with control (non-targeting) siRNA, and C_d is the average viability in drug-treated (INC280 or erlotinib) wells with control (non-targeting) siRNA [46]. The SI ranges from -1 to 1 , with negative values indicating an antagonistic effect on drug performance and positive values indicating a sensitizing effect. This is accomplished by comparing the predicted effect of drug and siRNA exposure ($R_c/C_c \times C_d/C_c$) to the observed effect of combined exposure (R_d/C_c). Although the SI allows for rapid analysis of siRNA screening data that surpasses the power observed in simple fold-change analysis, it does not allow for the calculation of a p value, as it does not consider probability distribution [46, 47]. As a result, the top 10% of sensitizing siRNAs was used in metabolic pathway analysis. These resulting genes were grouped into KEGG-annotated Metabolic Categories for each drug treatment in each cell line and into KEGG-annotated Metabolic Pathways for each drug treatment.

Results

Metabolomics profiles of TNBC cell lines

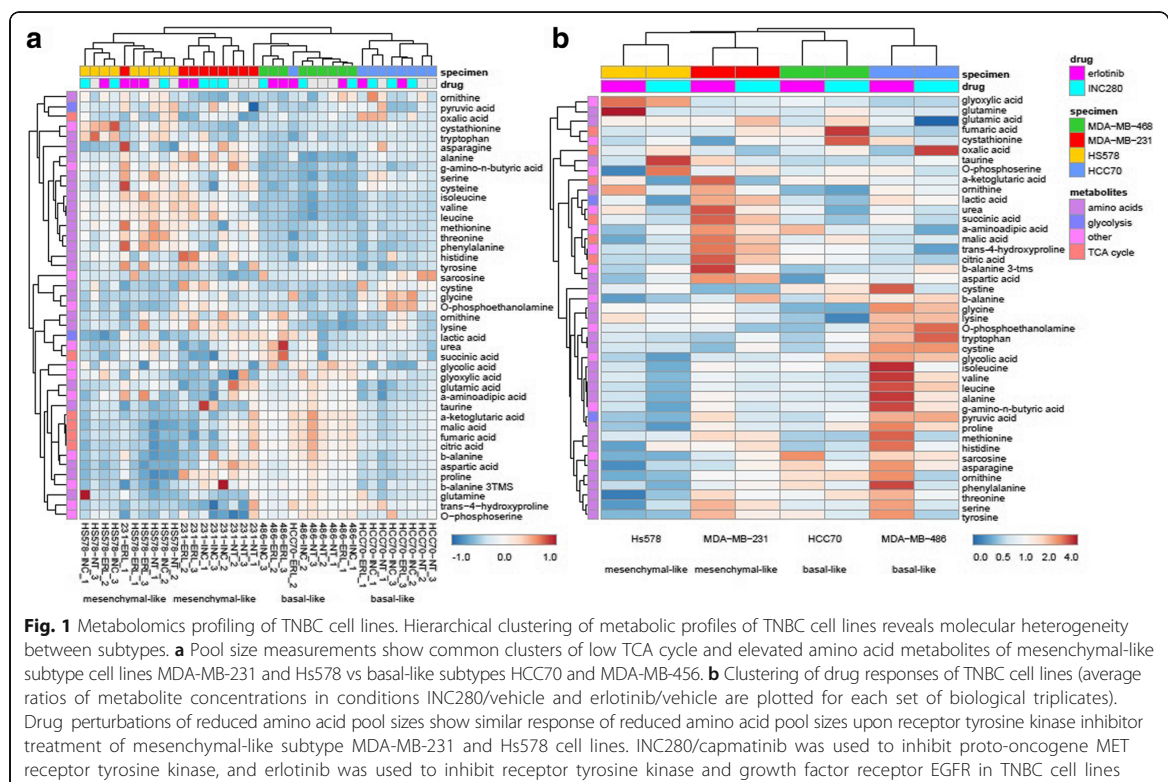
To understand the diversity of metabolic activity in TNBC, we examined multiple TNBC cell lines that are representative of several TNBC subtypes identified by Lehmann et al. [4]. These cell lines correspond to the two major basal-like subtypes and a mesenchymal-like subtype. This included Hs578t (mesenchymal stem-like; basal B), MDA-MB-231 (mesenchymal stem-like; basal B), MDA-MB-468 (basal-like 1; basal A), and HCC-70 (basal-like 2, basal A) cells (Additional file 2: Figure S1B). To produce initial metabolic profiles of TNBC, we measured the basal glycolytic and mitochondrial oxidative metabolism rates in four TNBC cell models (MDA-MB-231, MDA-MB-468, HS578t, HCC70) and one immortalized, non-transformed mammary gland epithelial cell model (hTERT-HME1) (Additional file 2: Figure S1C).

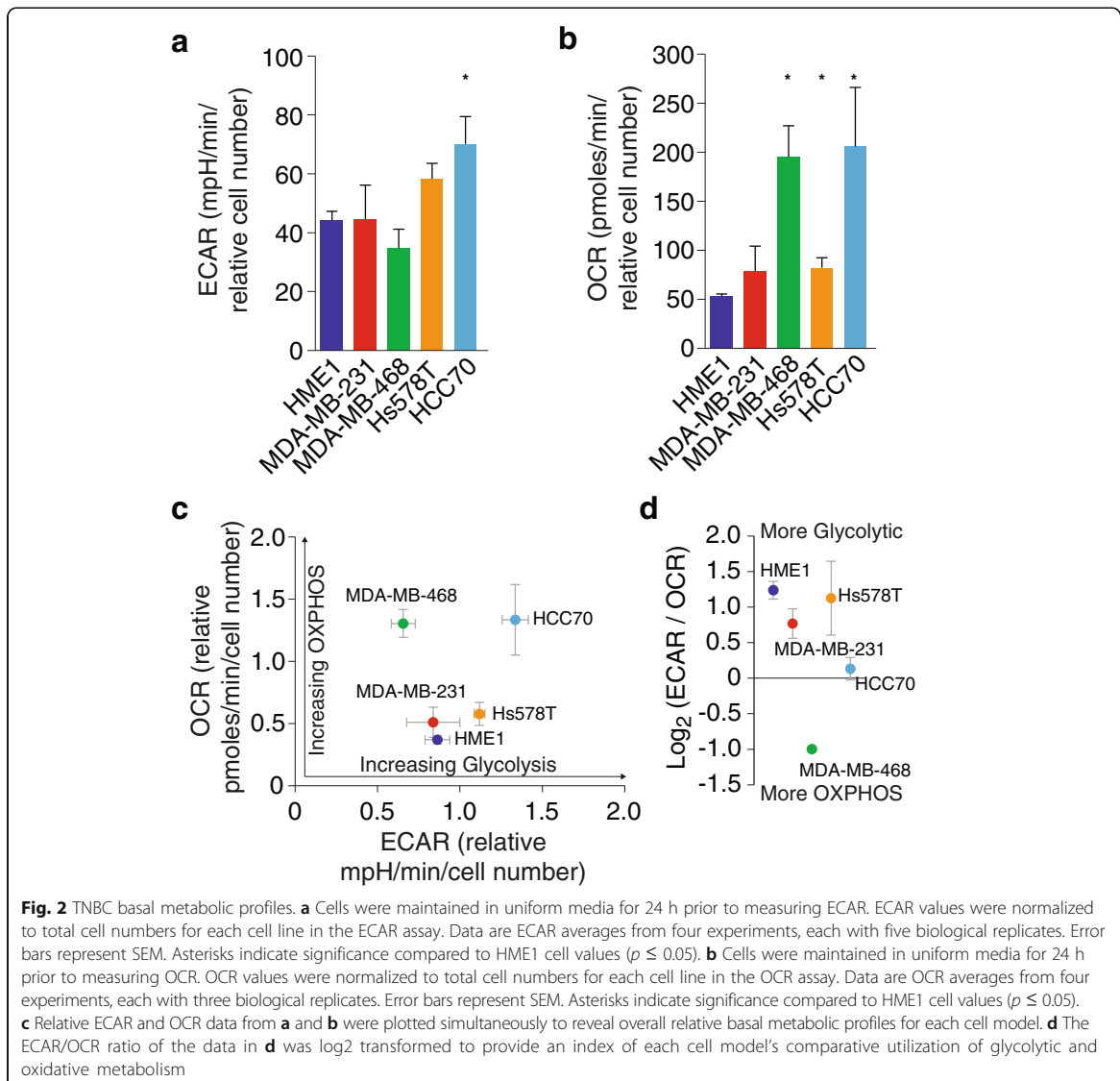
We profiled pool sizes of 43 central carbon metabolites of subconfluent TNBC cell lines in exponential growth phase. In addition, we quantified pool size changes following treatment with small molecule inhibitors of the RTKs MET and EGFR. Both MET and EGFR were prominently expressed in the assayed cell lines. Hierarchical clustering of metabolic profiles of TNBC cell lines reveals molecular heterogeneity between the TNBC mesenchymal-like and basal-like subtypes (Fig. 1). Pool size measurements showed common clusters of low TCA cycle and elevated amino acid metabolites of mesenchymal-like MDA-MB-231 and Hs578 which were distinct from the basal-like MDA-MB-468 and HCC70 cell lines (Fig. 1a, Additional file 4: Table S3). Drug perturbations of amino acid pool sizes demonstrated similar response of mesenchymal-like subtype MDA-MB-231 and Hs578 cell lines to both, INC280 or erlotinib, treatment (Fig. 1b). Clusters of each subtype and cell line were well separated by metabolic profiles and drug responses showing that each subtype had major similarities but each breast cancer cell line also had distinct components. The TCA cycle organic acid α -ketoglutaric acid is significantly reduced upon INC280 treatment with p values below 0.05 for all tested TNBC cell lines. Similarly, TCA cycle and central carbon metabolites aspartic acid, fumaric acid, and malic acid are significantly reduced upon erlotinib treatment with p values

below 0.05 for all cell lines. In addition, the MDA-MB-231 cell lines show significant perturbation of amino acid metabolism for both inhibitors. Interestingly, the MDA-MB-231 cell line stands out for its strong metabolic perturbation affecting TCA cycle metabolites, many amino and keto acids (Fig. 1b).

TNBC basal metabolic profiles

MDA-MB-231 and MDA-MB-468 cells exhibited similar glycolytic rates (extracellular acidification rate, ECAR) compared to HME1 cells, while HS578t and HCC70 cells displayed approximately 1.5 and two times the glycolytic rate of HME1 cells, respectively (Fig. 2a, c). MDA-MB-231 and HS578t cells exhibited slightly elevated oxygen consumption rates (OCR) compared to HME1 cells, whereas MDA-MB-468 and HCC70 displayed approximately four times the oxygen consumption rate of HME1 cells (Fig. 2b, c). Determining each cell lines' relative ECAR/OCR ratio provides a relative index of which metabolic program each cell line utilizes more in the basal state (Fig. 2d). HME1 cells utilize relatively more basal glycolytic than oxidative metabolism, as do HS578T and MDA-MB-231 cells. HCC70 cells utilize relatively similar basal glycolytic and oxygen metabolism, while MDA-MB-468 cells utilize relatively more oxygen metabolism than

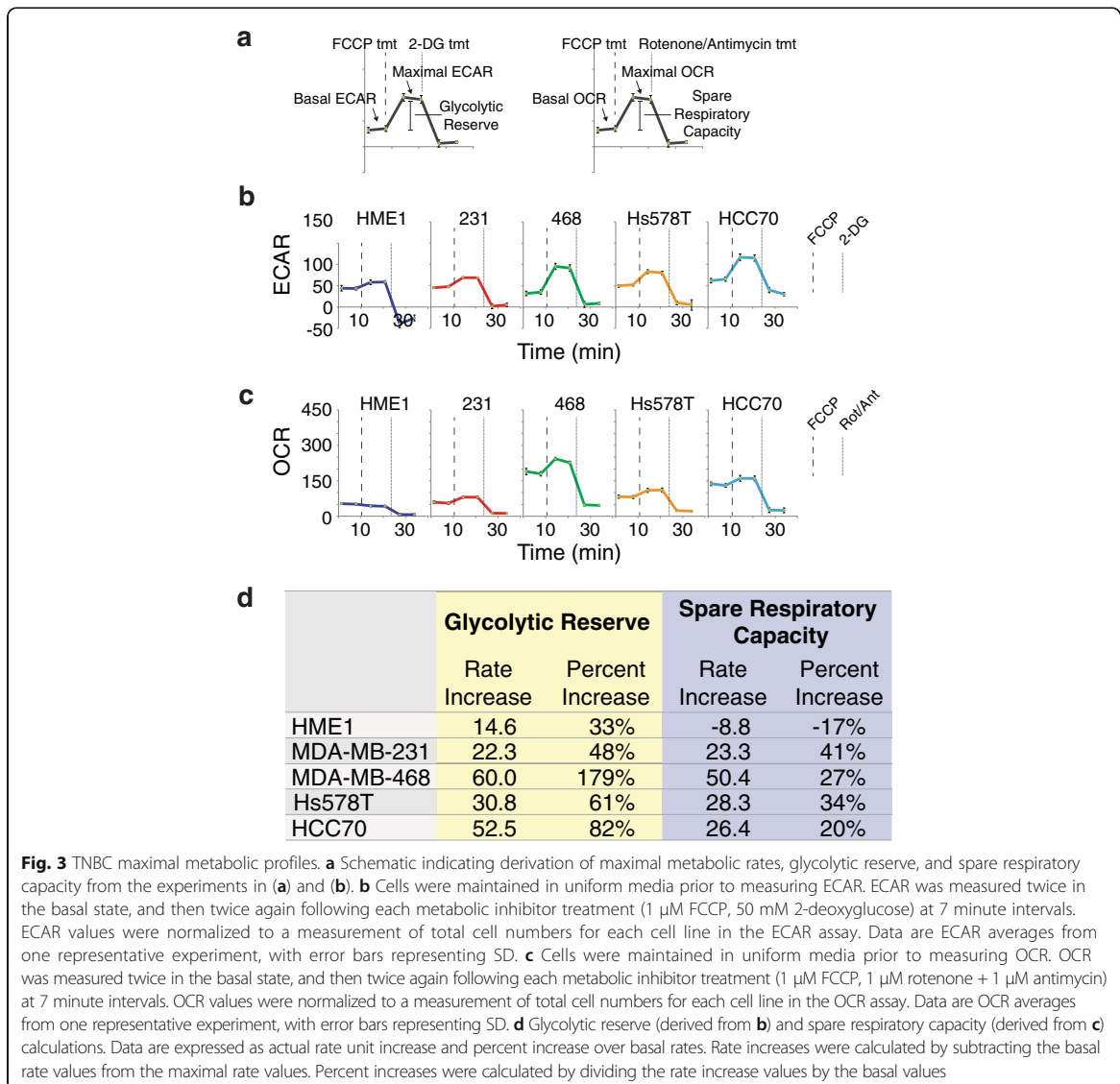




glycolytic metabolism (Fig. 2d). Together, the analyses of basal metabolic rates indicate that HME1, MDA-MB231, and Hs578T are all more poised to rely on glycolytic metabolism, while MDA-MB-468 cells are more poised to rely on oxidative metabolism in the basal state. Interestingly, in the basal state, HCC70 cells exhibited the greatest glycolytic and oxidative metabolism rates (Fig. 2a–c), but also exhibited the most balance between these rates (Fig. 2d). Understanding basal metabolic rates and the relative metabolic index may provide insight into which metabolic program specific cancers or cancer cell models may be especially sensitive (Fig. 4).

TNBC maximal metabolic profiles

While basal metabolic rates (Fig. 2) are informative, most cells harbor the ability to alter one metabolic program in order to compensate when another metabolic program is perturbed. Therefore, inhibition of one metabolic program (e.g., glycolysis) allows measurement of the maximal capability of the other metabolic program (e.g., oxidative metabolism) (Fig. 3a). To determine the maximal glycolytic and oxygen consumption metabolic capabilities (Additional file 5: Figure S2A, B) in these TNBC cell models, we measured respiration arrest-induced maximal glycolytic rates and depolarization-induced maximal



OXPHOS rates (Fig. 3b, c). The MDA-MB-231 cell line and the non-transformed mammary gland epithelial cell model, HME1, exhibited the least metabolic flexibility, as demonstrated by only moderate adjustments in ECAR and OCR (changes in values post-FCCP addition, Fig. 3b) and subsequent calculated glycolytic reserve and spare respiratory capacity rates (Fig. 3c). Interestingly, these two cell lines also displayed very modest basal metabolic rates (Fig. 2). Hs578T maximal ECAR and OCR were moderately elevated above basal rates, above those of HME1 and MDA-MB-231 but below MDA-MB-468 and HCC70. Both MDA-MB-468 and HCC70 maximal ECAR were

nearly double basal rates, with HCC70 displaying the greatest glycolytic capacity. MDA-MB-468 and HCC70 maximal OCR were moderately elevated above basal rates, and MDA-MB-468 displayed the greatest capacity for oxidative metabolism. From these measurements, glycolytic reserve and spare respiratory capacity can be calculated (Fig. 3a). While all cell models displayed some glycolytic reserve, HCC70 and MDA-MB-468 cells exhibited the greatest glycolytic reserves (Fig. 3d). MDA-MB-468 also exhibited the greatest spare respiratory capacity (Fig. 3d). These data indicate that each of the TNBC cells possesses a measure of metabolic

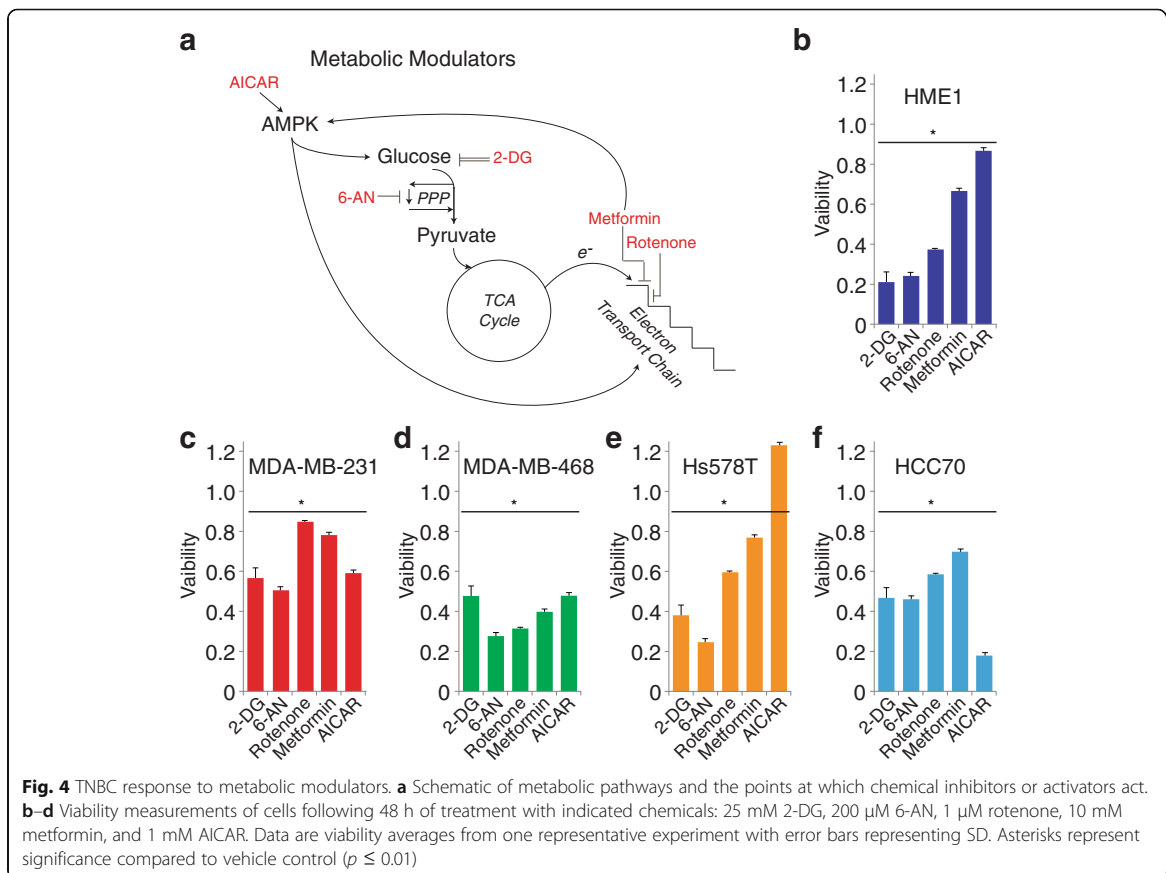
flexibility as defined by their abilities to increase ECAR or OCR when the one program is perturbed, with MDA-MB-468 cells exhibiting the greatest metabolic flexibility.

TNBC response to metabolic modulators

To further characterize the metabolic profiles of these cell models, we assessed the effects on viability following treatment with metabolic modulators at concentrations commonly utilized in published literature (Fig. 4). These experiments evaluated the effects of the 5' adenosine monophosphate-activated protein kinase (AMPK) activator [5-aminoimidazole-4-carboxamide-1 β riboside (AICAR)] [48], the glycolytic inhibitor 2-deoxy-glucose (2DG) [49], the pentose phosphate inhibitor 6-amino-nicotinamide (6-AN) [50], the mitochondrial complex I inhibitor rotenone [51], and the AMPK activator/Complex I inhibitor metformin [52, 53] (Fig. 4a). Similar to the metabolic rate investigations above, the TNBC models exhibited heterogeneous responses to these treatments; however, from these results, some interesting patterns were observed (Fig. 4b–f). Each TNBC model exhibited an

approximately 40–60% loss of viability in response to the glycolytic inhibitor 2-DG. Interestingly, HME1 cells, which exhibited the greatest bias towards basal utilization of glycolytic metabolism (Fig. 2e), were most affected by 2-DG treatment, as well as the pentose phosphate inhibitor 6-AN (Fig. 4b). Conversely, MDA-MB-468 cells, which exhibited the greatest bias towards basal utilization of oxidative metabolism (Fig. 2e), were most affected by the electron transport chain inhibitor, rotenone (Fig. 4d).

Also of note, Hs578T cells exhibited enhanced proliferation in response to AICAR while other cell lines exhibited variable decreases in viability compared to control. While AICAR and metformin are both commonly used as AMPK activators, they activate AMPK via disparate mechanisms. However, metformin and rotenone both perturb oxidative phosphorylation through respiratory chain complex I (RCI) inhibition. Our results reveal more similar viability effects between metformin and rotenone (common RCI inhibitors) than between metformin and AICAR (common AMPK activators) (Fig. 4b–f).

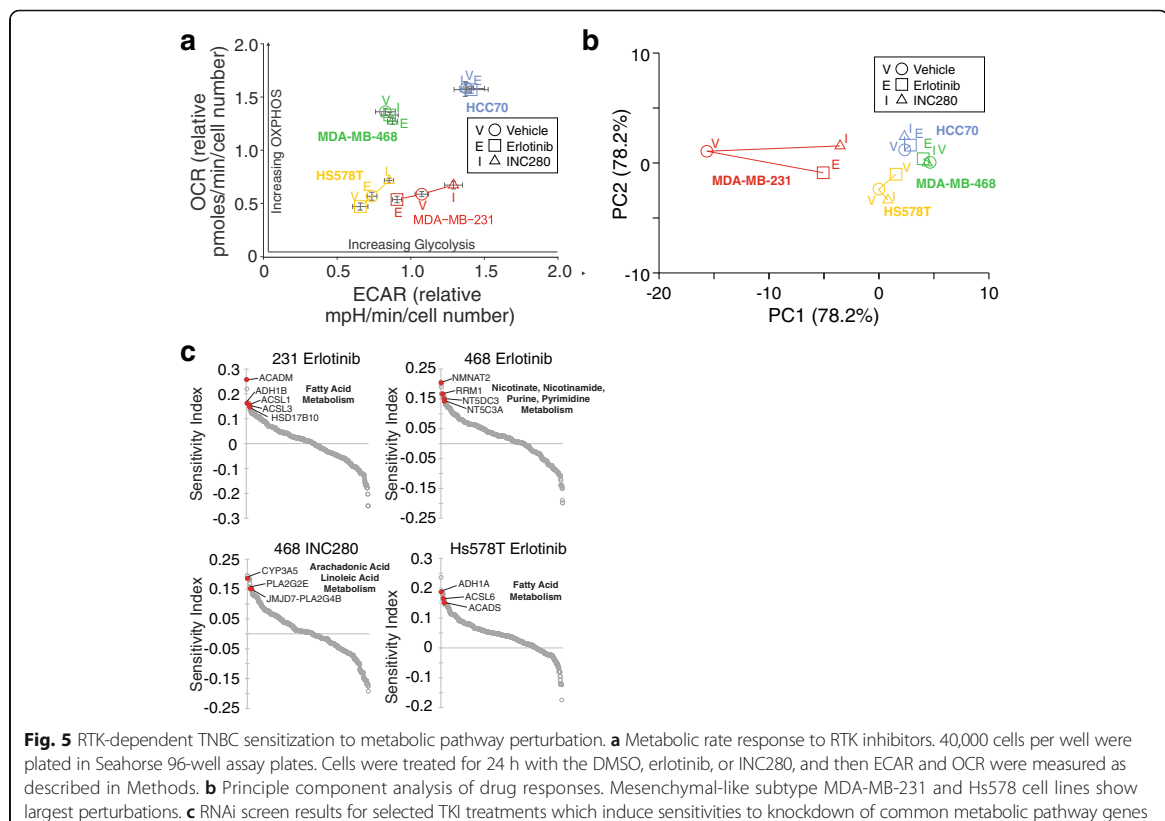


Comprehensive analysis of rate-limiting enzymes and RTK inhibition

EGFR and MET receptors are known to drive tumorigenic progression, and RTKs are known to regulate metabolic signaling pathways [54]. To investigate the effects of EGFR and MET inhibition on TNBC metabolism, we measured ECAR and OCR in TNBC cells treated with the EGFR inhibitor erlotinib and the MET inhibitor INC280 (capmatinib). As in the above analyses, the TNBC cell models displayed heterogeneous responses to the tyrosine kinase inhibitors (TKIs). We observed that MET and EGFR inhibition had little effect on the glycolytic and oxidative metabolism rates of basal A/B subtype MDA-MB-468 or HCC70 cell lines (Fig. 5a). In contrast, in both mesenchymal-like MDA-MB-231 and Hs578T cell lines, both MET and EGFR inhibition strongly perturbed both glycolysis and oxidative metabolism (Fig. 5a). Importantly, comparing these data to a principal component analysis of our metabolomics data revealed that metabolic changes of mesenchymal-like MDA-MB-231 and Hs578T cell lines upon drug treatment recapitulated the observed changes of metabolic fluxes (Fig. 5b). Both cell lines show perturbation of the top two principal components

(reflecting 84.9% of the data) in the same direction and magnitude. In contrast, major principle components of metabolic perturbations do not change for basal-like subtype MDA-MB-468 or HCC70. Despite the metabolic responses of MDA-MB-231 and Hs578T cell lines to INC280 vs erlotinib based on amino acid and TCA cycle metabolism of mesenchymal-like cell lines are in agreement, glycolytic rates show differential perturbation. Among the assessed TNBC cell lines, mesenchymal-like subtypes showed strong, consistent perturbations, despite underlying heterogeneity of breast cancer subtypes.

To more comprehensively investigate the metabolic consequences of EGFR and MET inhibition in TNBC models, we performed a siRNA screen in each cell line targeting all 323 rate-limiting enzymes in the human KEGG metabolic pathways and Rate Limiting Enzyme Regulation databases. This complement of enzymes was divided into 11 major metabolic categories representing 89 metabolic pathways (Additional file 3: Table S2). The siRNA screen was performed in duplicate in each cell line in cells treated with vehicle (DMSO), INC280, or erlotinib. A sensitivity index was applied to viability measurements to determine the effect of siRNA knockdown



on drug sensitivity, and therefore identifies genes whose knockdown preferentially reduces viability in TNBC cells treated with a TKI vs vehicle alone (see Methods, Additional file 6: Table S4). Eight of the 11 major metabolic categories were represented in the sensitivity index to varying levels for each TNBC model and each TKI (Additional file 7: Figure S3, see also Additional file 6: Table S4, Additional file 8: Table S5). Notably, lipid metabolism was prominent (represented > 15% of hits) in each TNBC model treated with INC280 or erlotinib, while amino acid metabolism was also prominent in each TNBC model treated with INC280. Evaluating individual significant rate-limiting enzymes in each group revealed potential sensitivities associated with specific TKI for some TNBC subtypes (Fig. 5c). MDA-MB-231 and Hs578T cells treated with erlotinib were sensitive to knockdown of fatty acid genes, while MDA-MB-468 cells treated with the same TKI were sensitive to knockdown of specific nucleotide metabolism pathways. INC280 sensitized MDA-MB-468 cells to knockdown of arachidonic and linoleic acid metabolism rate limiting enzymes. Interestingly, a broader analysis of metabolic pathways across cell TNBC subtypes in response to TKI treatments identified additional sensitivities. The top ten metabolic pathways identified by the sensitivity index displayed significant overlap between the TKI treatments (Additional file 7: Figure S3, see also Additional file 8: Table S5). Additionally, within this set of common pathways, three pathways which are engaged to counteract oxidative stress were enriched in the screen results (Glutathione metabolism, cytochrome P450 metabolism, and non-P450 drug metabolism pathways). These results suggest that even with the molecular heterogeneity that is present in TNBC, there are common metabolic programs that can be targeted in TNBC subtypes. Taken together, these data shows that targeting pathways such as fatty acid metabolism, pyrimidine metabolism, or oxidative stress relief pathways in combination with MET or EGFR inhibition may represent an effective therapeutic strategy.

Discussion

In this study, we characterized the metabolic heterogeneity of TNBC and identified a core set of metabolic pathways that are common among the TNBC subtypes, yet observed diverse metabolic profiles among TNBC cell lines. Genetic and signaling heterogeneity is observed in most solid cancers, and studies have indicated that there is a particularly high level of genomic heterogeneity among TNBC patients [39]. These observations of heterogeneity have been borne out in metabolic analyses of TNBC as well. Analyses of TNBC patient tissues have demonstrated heterogeneity of glycolytic and mitochondrial protein expression [40, 41, 55]. TNBC cell lines have

also exhibited heterogeneity with respect to glutamine metabolism [42] and response to the metabolic modulator, metformin [33, 34]. Therefore, the heterogeneity evident between TNBC cell lines in our detailed metabolic characterization extends these previous findings. Metabolic pool sizes and drug responses revealed common patterns between TNBC subtypes but also highlighted cell line-specific responses (Fig. 1). Importantly, drug responses of metabolic rates and principle metabolic components identified a theme of metabolic capacity and adaptability as major difference of mesenchymal-like vs basal-like subtypes (Fig. 5) [56]. Basal-like cell lines are metabolically most active with the highest OCR and ECAR (Fig. 2c), resulting in low, depleted metabolic pool sizes (Fig. 1a). Mesenchymal-like cell lines have significantly lower OXPHOS allowing them to modulate and adaptively respond to the drug challenges (Fig. 5a, b). The HCC70 cell is an example of extremely high OCR and ECAR that allows for minimal adjustment to drug challenges. The unique metabolic profiles (Figs. 1, 2, and 3) response to chemical modulators (Fig. 4) and sensitivities to combined RTK, and metabolic pathway inhibition (Fig. 5) provides platforms which can help place the responses of these TNBC cell line models in previous and future studies into a broader metabolic context. For example, previous work demonstrated that MDA-MB-468 cells are more sensitive to metformin than MDA-MB-231 cells. Here, we provide a potential basis for that observation as we found MDA-MB-468 cells to be more poised to rely on OXPHOS than MDA-MB-231 cells (Fig. 2d). Therefore, this comprehensive metabolic analysis provides a platform in which to identify therapeutic sensitivities within the TNBC metabolic landscape.

In the TNBC cell models that we evaluated, an index mapping, the relative affinities for basal metabolic rates (Fig. 2d), appeared more useful for predicting response to chemical modulators (Fig. 4) than did an analysis of maximal metabolic rates (Fig. 3). Cells which displayed relatively higher OXPHOS rates than glycolytic rates (MDA-MB-468) were the most sensitive to rotenone treatment. On the other hand, cells which displayed relatively higher glycolytic rates than OXPHOS rates (HME1, Hs578T) were the most sensitive to 2-DG and 6-AN treatment. Therefore, although a cell may harbor the ability to greatly increase glycolytic rate when OXPHOS is disrupted (MDA-MB-468, Fig. 3a, d), its higher basal OXPHOS rate may reflect an absolute requirement for high, sustained oxidative metabolism. Therefore, it is possible that cells which display the ability to upregulate alternative metabolic pathways in response to metabolic insults still remain dependent on the metabolic pathways which they preferentially utilize in the basal state.

In addition to glycolytic and mitochondrial oxidative metabolism alterations, TNBC patient samples display

evidence of altered glutamine metabolism compared to HER2 positive cancers [57]. TNBC cancer cell line models enhance glutamine uptake and metabolism, which are associated with epigenetic changes favoring expression of pro-tumorigenic genes [58, 59]. Other studies provide evidence of altered amino acid metabolism in TNBC. MDA-MB-231 and MDA-MB-468 cells exhibit elevated serine metabolism protein expression compared to HER2 positive cell lines, an observation that is shared in patient samples [60, 61]. Metabolomics analyses of patient samples identified lower amino acid levels in TNBC patients compared to healthy controls [62]. A folate metabolism enzyme may also serve as a biomarker for TNBC in distinct ethnic populations [63]. Finally, altered lipid metabolism appears to play a part in TNBC. Patient TNBC and non-TNBC tissues can be discriminated based on markers of lipid metabolism [64, 65], and MDA-MB-231 and MDA-MB-468 cells are effectively induced to undergo apoptosis upon suppressing expression of the lipogenic transcription factors, SREBP1/2 [66]. Recent metabolomics analyses identified metabolites associated with the Warburg effect, and the oxidative stress response, and specific metabolite signatures associated with different driver mutations [67]. Metabolomics have also identified potential global differences in breast cancer-associated metabolites between patients of different races [61], and miRNA-associated thiamine homeostasis specific to TNBC patient samples [68].

RTKs are promising drug targets due to their high expression in TNBC. The success of trastuzumab in HER2⁺ breast cancer underscores the potential of targeting tyrosine kinases yet, in spite of this promising start, monotherapy with tyrosine kinase inhibitors (TKIs) has had limited success in the clinic. In this study, we evaluated the effects of RTK inhibition on metabolic pathways in TNBC. This analysis highlighted the unique metabolic dependencies in our TNBC models, but also revealed reveal a core set of metabolic pathways that are universally affected by TKI treatment. Collectively, TNBC cells were commonly sensitized to inhibition of redox homeostasis, fatty acid metabolism, and nucleotide metabolism by erlotinib and INC280 treatment. The metabolomics results provide a mechanistic basis for the lipid metabolism sensitivity identified in the RLE siRNA screen. Flux analyses of multiple cancers demonstrate that altering TCA cycle flux significantly impinges upon lipid metabolism [69]. Therefore, the sensitivities to lipid metabolism RLE knockdown could be predicted by the concurrent changes in amino acid metabolites. Glutathione metabolism, cytochrome P450 metabolism, and non-P450 drug metabolism pathways, each of which ameliorate oxidative stress, were enriched in the siRNA screen, highlighting the importance of redox homeostasis in this context. Clinically, redox pathways have been shown to be upregulated

in TNBC vs ER⁺ tumors [70] and heightened glycolytic metabolism may be regulated in part by oxidative stress in TNBC cells [71]. Our data provide additional impetus for co-targeting these metabolic and kinase pathways in TNBC patients [72]. siRNAs targeting fatty acid metabolism and specifically arachidonic acid metabolism genes were also common hits in the screen. Expression of fatty acid metabolism enzymes have previously been associated with TNBC metastasis [64] and survival rates [65]. Arachidonic acid metabolism itself may also be linked to cytochrome P450 metabolism in breast cancers [72]. Interestingly, suppression of tryptophan metabolism enhances INC280 treatment (Additional file 7: Figure S3). A previous investigation of BT549 TNBC cells demonstrated a link between tryptophan metabolism-dependent kynurenine production and breast cancer cell anoikis resistance, particularly in ER negative cell [73]. Because the data in Fig. 3d show that MDA-MB-468 cells have very little relative glycolytic activity while maintaining high OXPHOS activity, it would be reasonable to expect less effects from suppression of carbon metabolism RLEs. The data in Additional file 2: Figure S3 bear this out as carbon metabolism RLE knockdown has the least effect on MDA-MB-468 cells. A potential mechanism for this observation may be the KRAS mutational status of MDA-MB-468 cells which is not shared by the other TNBC lines under study. A previous study has demonstrated that some KRAS-driven cancers cells significantly upregulate OXPHOS metabolism [74]. Finally, MET or EGFR inhibition collectively sensitized TNBC cells to knockdown of pyrimidine and purine metabolism enzymes. Interestingly, a significant proportion of the siRNA hits driving enrichment of these metabolic pathways in our study are 5'-nucleotidases and nucleotide kinases. These results suggest that regulation of nucleotide phosphorylation plays an important role in determining sensitivity to RTK inhibitors in TNBC. Therefore, small molecules disrupting nucleotide phosphorylation dynamics may prove effective at enhancing RTK inhibition in TNBC.

Conclusions

The findings in this study provide comprehensive information on the metabolic background of TNBC subtypes, their unique and common metabolic dependencies, and how they respond to metabolic insults. These results provide a valuable resource for investigators who utilize these TNBC cell lines. Additionally, our siRNA analysis establishes a comprehensive analysis of metabolic rate-limiting enzymes and identifies erlotinib- and INC280-sensitized pathways. Overall, this comprehensive metabolic analysis demonstrates the metabolic heterogeneity within TNBC and identifies therapeutic sensitivities that may be exploited in treating TNBC patients.

Additional files

Additional file 1: Table S1. Genes targeted and siRNA sequences used in siRNA screen. (XLSX 57 kb)

Additional file 2: Figure S1. RNAi screen, cell lines, and metabolic rates. (A) Schematic of RNAi screen (left) and transfection efficiency under screen conditions (right). (B) Characteristics of each cell line used in this study. (C) Schematic representing biological compartments and metabolic pathways assessed for metabolic rates. (PDF 957 kb)

Additional file 3: Table S2. Genes and metabolic categories and pathways used in siRNA screen. Rate-limiting enzymes were collated through KEGG annotation (<http://www.genome.jp/kegg/>), the Rate-Limiting Enzyme Regulation Database (<http://rle.cbi.pku.edu.cn/home.cgi>, [51]), and literature searches and categorized according to KEGG. (XLSX 25 kb)

Additional file 4: Table S3. Quantitation of metabolic pool sizes, ratios for cell lines, and drug responses with statistical values. Total ion count integrated over peak area for metabolite-specific mass ion validated by multiple precursor-product ion combinations. Mean, standard deviation, and ANOVA with student's t test compares triple-negative breast cancer (TNBC) cell lines and treatment with INC280 or erlotinib vs control vehicle (DMSO). (XLSX 52 kb)

Additional file 5: Figure S2. OCR and ECAR measurement explanation. (A) i. Normally functioning cellular respiration utilizes electrons in the form of NADH and FADH₂ to pass down the electron transport chain (ETC) gradient. These redox reactions in the ETC pump hydrogen ions from the mitochondrial matrix into the mitochondrial inner membrane space (IMS), providing an electrochemical gradient which in turn powers ATP synthase-dependent ATP production. ii. FCCP is a lipid-soluble ionophore that allows hydrogen ions to escape the IMS, functionally uncoupling the ETC from ATP synthase-mediated ATP production. iii. In order to restore FCCP-mediated depletion of ATP levels, glycolytic flux increases to maximum capacity. iv. In order to maintain a minimal hydrogen ion gradient in the IMS, mitochondrial complex IV activity increases to maximum capacity, thus inducing maximum oxygen consumption. (B) The order of metabolic rate measurements and metabolic toxin treatment for maximal rate measurements. i. Basal glycolytic rate. ii. Respiration arrest-induced maximal glycolytic rate. iii. Glycolytic arrest. iv. Basal OXPHOS rate. v. Depolarization-induced maximal OXPHOS rate. vi. OXPHOS arrest. (PDF 997 kb)

Additional file 6: Table S4. Drug response and sensitivity index for siRNA treatment of triple-negative breast cancer (TNBC) cell lines. (XLSX 128 kb)

Additional file 7: Figure S3. Sensitization to metabolic pathway perturbation. (A) Graphical representation of the proportion which each metabolic category (Table S2) was represented in the top 10% sensitivity index scores. (B) The combined top ten pathways as defined by high-scoring sensitivity index genes for each TKI (INC280 or erlotinib). (PDF 801 kb)

Additional file 8: Table S5. Top 10% scoring siRNAs in the siRNA screen for each condition. (XLSX 27 kb)

Abbreviations

2-DG: 2-deoxyglucose; 6-AN: 6-aminonicotinamide; AICAR: 5-Aminoimidazole-4-carboxamide ribonucleotide; AMPK: 5' adenosine monophosphate-activated protein kinase; DMSO: Dimethyl sulfoxide; ECAR: Extracellular acidification rate; EGFR: Epidermal growth factor receptor; ER: Estrogen receptor, ESR1; HER2: Human epidermal growth factor receptor 2, NEU, ERBB2; INC280: Capmatinib, MET small molecule inhibitor; KEGG: Kyoto Encyclopedia of Genes and Genomes; MET: Hepatocyte growth factor receptor; OCR: Oxygen consumption rate; OXPHOS: Oxidative phosphorylation; PR: Progesterone receptor, PGR; RCI: Respiratory chain complex I; RTK: Receptor tyrosine kinase; SI: Sensitivity index; siRNA: Small interfering RNA; TKI: Tyrosine kinase inhibitor; TNBC: Triple negative breast cancer

Funding

This work was supported by NIH National Cancer Institute grants CA159709 (NJL) and CA154887 (F.V.F.), The Frederik and Lena Meijer Student Internship Program (JC), The Van Andel Foundation (JM, CRG), The Breast Cancer Research Foundation (CRG), Health Science Research Institute Grant (F.V.F.),

and University of California Cancer Research Coordinating Committee research grant CRN-17-427258 (F.V.F.).

Availability of data and materials

The datasets used and/or analyzed during the current study are available from the corresponding author on reasonable request.

Authors' contributions

NJL participated in study conception and design, carried out all experiments except metabolomics experiments, analyzed all data, and wrote the manuscript. JPC and EAT participated in assay development and RTKi experiments. ANL analyzed RNAi screen data. JPM participated in study conception, design, and coordination, and data analysis. SJS and AS extracted, derivatized, and quantitated metabolites. FVF designed and analyzed metabolomics experiments and conducted data interpretation and writing of the manuscript. CRG conceived of the study, participated in study design, coordination, and data analysis, and wrote the manuscript. All authors read and approved the final manuscript.

Ethics approval and consent to participate

Not applicable.

Consent for publication

Not applicable.

Competing interests

The authors declare that they have no competing interests.

Publisher's Note

Springer Nature remains neutral with regard to jurisdictional claims in published maps and institutional affiliations.

Author details

¹California State University, Los Angeles, 5151 State University Drive, Los Angeles, CA 90032, USA. ²Van Andel Research Institute, 333 Bostwick Ave, NE, Grand Rapids, MI 49503, USA. ³Systems Biology and Cancer Metabolism, Program for Quantitative Systems Biology, University of California Merced, 2500 North Lake Road, Merced, CA 95343, USA. ⁴College of Human Medicine, Michigan State University, 15 Michigan St. NE, Grand Rapids, MI 49503, USA.

Received: 10 February 2017 Accepted: 7 August 2017

Published online: 22 August 2017

References

- Foulkes WD, Smith IE, Reis-Filho JS. Triple-negative breast cancer. *N Engl J Med*. 2010;363:1938–48.
- Dent R, Trudeau M, Pritchard KI, Hanna WM, Kahn HK, Sawka CA, Lickley LA, Rawlinson E, Sun P, Narod SA. Triple-negative breast cancer: clinical features and patterns of recurrence. *Clin Cancer Res*. 2007;13(15 Pt 1):4429–34.
- Liedtke C, Mazouni C, Hess KR, André F, Tordai A, Mejia JA, Symmans WF, Gonzalez-Angulo AM, Hennessy B, Green M, Cristofanilli M, Hortobagyi GN, Pusztai L. Response to neoadjuvant therapy and long-term survival in patients with triple-negative breast cancer. *J Clin Oncol*. 2008;26:1275–81.
- Lehmann BD, Bauer JA, Chen X, Sanders ME, Chakravarthy AB, Shyr Y, Pietenpol JA. Identification of human triple-negative breast cancer subtypes and preclinical models for selection of targeted therapies. *J Clin Invest*. 2011;121:2750–67.
- Burstein MD, Tsimelzon A, Poage GM, Covington KR, Contreras A, Fuqua SAW, Savage MI, Osborne CK, Hilsenbeck SG, Chang JC, Mills GB, Lau CC, Brown PH. Comprehensive genomic analysis identifies novel subtypes and targets of triple-negative breast cancer. *Clin Cancer Res*. 2015;21:1688–98.
- Koenders PG, Beex LV, Geurts-Moespot A, Heuvel JJ, Kienhuis CB, Benraad TJ. Epidermal growth factor receptor-negative tumors are predominantly confined to the subgroup of estradiol receptor-positive human primary breast cancers. *Cancer Res*. 1991;51:4544–8.
- Sainsbury JR, Farndon JR, Needham GK, Malcolm AJ, Harris AL. Epidermal-growth-factor receptor status as predictor of early recurrence of and death from breast cancer. *Lancet (London, England)*. 1987;1:1398–402.
- Singletary SE, Baker FL, Spitzer G, Tucker SL, Tomasovic B, Brock WA, Ajani JA, Kelly AM. Biological effect of epidermal growth factor on the in vitro growth of human tumors. *Cancer Res*. 1987;47:403–6.

9. Toi M, Osaki A, Yamada H, Toge T. Epidermal growth factor receptor expression as a prognostic indicator in breast cancer. *Eur J Cancer*. 1991;27:977–80.
10. Cheang MCU, Voduc D, Bajdik C, Leung S, McKinney S, Chia SK, Perou CM, Nielsen TO. Basal-like breast cancer defined by five biomarkers has superior prognostic value than triple-negative phenotype. *Clin Cancer Res*. 2008;14:1368–76.
11. Ghossein RA, Dillon DA, D'Aquila T, Rimm EB, Fearon ER, Rimm DL. Expression of c-met is a strong independent prognostic factor in breast carcinoma. *Cancer*. 1998;82:1513–20.
12. Camp RL, Rimm EB, Rimm DL. Met expression is associated with poor outcome in patients with axillary lymph node negative breast carcinoma. *Cancer*. 1999;86:2259–65.
13. Tolgay Ocal I, Dolled-Filhart M, D'Aquila TG, Camp RL, Rimm DL. Tissue microarray-based studies of patients with lymph node negative breast carcinoma show that met expression is associated with worse outcome but is not correlated with epidermal growth factor family receptors. *Cancer*. 2003;97:1841–8.
14. Edakuni G, Sasatomi E, Satoh T, Tokunaga O, Miyazaki K. Expression of the hepatocyte growth factor/c-Met pathway is increased at the cancer front in breast carcinoma. *Pathol Int*. 2001;51:172–8.
15. Lengyel E, Prechtel D, Resau JH, Gauger K, Welk A, Lindemann K, Salanti G, Richter T, Knudsen B, Vande Woude GF, Harbeck N. C-Met overexpression in node-positive breast cancer identifies patients with poor clinical outcome independent of Her2/neu. *Int J Cancer*. 2005;113:678–82.
16. Graveel CR, DeGroot JD, Su Y, Koeman J, Dykema K, Leung S, Snider J, Davies SR, Swiatek PJ, Cottingham S, Watson MA, Ellis MJ, Sigler RE, Furge KA, Vande Woude GF. Met induces diverse mammary carcinomas in mice and is associated with human basal breast cancer. *Proc Natl Acad Sci*. 2009;106:12909–14.
17. Ponzio MG, Lesurf R, Petkiewicz S, O'Malley FP, Pinnaduwage D, Andrulis IL, Bull SB, Chughtai N, Zuo D, Souleimanova M, Germain D, Omeroglu A, Cardiff RD, Hallett M, Park M. Met induces mammary tumors with diverse histologies and is associated with poor outcome and human basal breast cancer. *Proc Natl Acad Sci U S A*. 2009;106:12903–8.
18. Sameni M, Tovar EA, Essenburg CJ, Chalasani A, Linklater ES, Borgman A, Cherba DM, Anbalagan A, Winn ME, Graveel CR, Sloane BF. Cabozantinib (XL184) inhibits growth and invasion of preclinical TNBC models. *Clin Cancer Res*. 2016;22:923–34.
19. Linklater ES, Tovar EA, Essenburg CJ, Turner L, Madaj Z, Winn ME, Melnik MK, Korkaya H, Maroun CR, Christensen JG, Steensma MR, Boerner JL, Graveel CR. Targeting MET and EGFR crosstalk signaling in triple-negative breast cancers. *Oncotarget*. 2016;7(43):69903–15.
20. Wellen KE, Thompson CB. A two-way street: reciprocal regulation of metabolism and signalling. *Nat Rev Mol Cell Biol*. 2012;13:270–6.
21. De Rosa V, Iommelli F, Monti M, Fonti R, Votta G, Stoppelli MP, Del Vecchio S. Reversal of warburg effect and reactivation of oxidative phosphorylation by differential inhibition of EGFR signaling pathways in non-small cell lung cancer. *Clin Cancer Res*. 2015;21(22):5110–20.
22. Bian Y, Yu Y, Wang S, Li L. Up-regulation of fatty acid synthase induced by EGFR/ERK activation promotes tumor growth in pancreatic cancer. *Biochem Biophys Res Commun*. 2015;463:612–7.
23. Li X, Lu Y, Lu H, Luo J, Hong Y, Fan Z. AMPK-mediated energy homeostasis and associated metabolic effects on cancer cell response and resistance to cetuximab. *Oncotarget*. 2015;6:11507–18.
24. Borlak J, Singh P, Gazzana G. Proteome mapping of epidermal growth factor induced hepatocellular carcinomas identifies novel cell metabolism targets and mitogen activated protein kinase signaling events. *BMC Genomics*. 2015;16:124.
25. Natan S, Tsarfaty G, Horev Y, Haklai R, Kloog Y, Tsarfaty I. Interplay between HGF/SF-met-Ras signaling, tumor metabolism and blood flow as a potential target for breast cancer therapy. *Oncoscience*. 2014;1:30–8.
26. Petrocca F, Altschuler G, Tan SM, Mendillo ML, Yan H, Jerry DJ, Kung AL, Hide W, Ince TA, Lieberman J. A genome-wide siRNA screen identifies proteasome addiction as a vulnerability of basal-like triple-negative breast cancer cells. *Cancer Cell*. 2013;24:182–96.
27. Pelicano H, Zhang W, Liu J, Hammoudi N, Dai J, Xu R-H, Pusztai L, Huang P. Mitochondrial dysfunction in some triple-negative breast cancer cell lines: role of mTOR pathway and therapeutic potential. *Breast Cancer Res*. 2014;16:434.
28. Diers AR, Vayalil PK, Oliva CR, Griguer CE, Darley-Usmar V, Hurst DR, Welch DR, Landar A. Mitochondrial bioenergetics of metastatic breast cancer cells in response to dynamic changes in oxygen tension: effects of HIF-1 α . *PLoS One*. 2013;8:e68348.
29. Choi J, Jung W-H, Koo JS. Metabolism-related proteins are differentially expressed according to the molecular subtype of invasive breast cancer defined by surrogate immunohistochemistry. *Pathobiology*. 2013;80:41–52.
30. Estrella V, Chen T, Lloyd M, Wojtkowiak J, Cornell HH, Ibrahim-Hashim A, Bailey K, Balagurunathan Y, Rothberg JM, Sloane BF, Johnson J, Gatenby RA, Gillies RJ. Acidity generated by the tumor microenvironment drives local invasion. *Cancer Res*. 2013;73:1524–35.
31. Shen L, O'Shea JM, Kaadige MR, Cunha S, Wilde BR, Cohen AL, Welm AL, Ayer DE. Metabolic reprogramming in triple-negative breast cancer through Myc suppression of TXNIP. *Proc Natl Acad Sci U S A*. 2015;112:5425–30.
32. McClelland ML, Adler AS, Shang Y, Hunsaker T, Truong T, Peterson D, Torres E, Li L, Haley B, Stephan J-P, Belvin M, Hatzivassiliou G, Blackwood EM, Corson L, Evangelista M, Zha J, Firestein R. An integrated genomic screen identifies LDHB as an essential gene for triple-negative breast cancer. *Cancer Res*. 2012;72:5812–23.
33. Wahdan-Alaswad R, Fan Z, Edgerton SM, Liu B, Deng X-S, Arnadottir SS, Richer JK, Anderson SM, Thor AD. Glucose promotes breast cancer aggression and reduces metformin efficacy. *Cell Cycle*. 2013;12:3759–69.
34. Zielinski DC, Filipp FV, Bordbar A, Jensen K, Smith JW, Herrgard MJ, Mo ML, Palsson BO, Mjorndal T, Pirmohamed M, Arrowsmith J, Arrowsmith J, Loffler W, Kilian R, Toumi M, Angermeyer MC, Passarelli MC, Jacob-Filho W, Figueiras A, Begaud B, Martin K, Fourrier A, Haramburu F, Pirmohamed M, Park BK, Kuhn M, Ong SE, Manolio TA, Lee S, Lee KH, et al. Pharmacogenomic and clinical data link non-pharmacokinetic metabolic dysregulation to drug side effect pathogenesis. *Nat Commun*. 2015;6:7101.
35. Filipp F V. Cancer metabolism meets systems biology: Pyruvate kinase isoform PKM2 is a metabolic master regulator. *J Carcinog*. 2013;12.
36. Wang F, Yang Y. Inhibition of PKM2 sensitizes triple-negative breast cancer cells to doxorubicin. *Biochem Biophys Res Commun*. 2014;454:465–70.
37. Palorini R, Simonetto T, Cirulli C, Chiaradonna F. Mitochondrial complex I inhibitors and forced oxidative phosphorylation synergize in inducing cancer cell death. *Int J Cell Biol*. 2013;2013:243876.
38. Cheng G, Zielonka J, Dranka BP, McAllister D, Mackinnon AC, Joseph J, Kalyanaraman B. Mitochondria-targeted drugs synergize with 2-deoxyglucose to trigger breast cancer cell death. *Cancer Res*. 2012;72:2634–44.
39. Jiang T, Shi W, Natowicz R, Ononye SN, Wali VB, Kluger Y, Pusztai L, Hatzis C. Statistical measures of transcriptional diversity capture genomic heterogeneity of cancer. *BMC Genomics*. 2014;15:876.
40. Kim S, Kim DH, Jung W-H, Koo JS. Metabolic phenotypes in triple-negative breast cancer. *Tumour Biol*. 2013;34:1699–712.
41. Choi J, Kim DH, Jung WH, Koo JS. Metabolic interaction between cancer cells and stromal cells according to breast cancer molecular subtype. *Breast Cancer Res*. 2013;15:R78.
42. Timmerman LA, Holton T, Yuneva M, Louie RJ, Padró M, Daemen A, Hu M, Chan DA, Ethier SP, van't Veer LJ, Polyak K, McCormick F, Gray JW. Glutamine sensitivity analysis identifies the xCT antiporter as a common triple-negative breast tumor therapeutic target. *Cancer Cell*. 2013;24:450–65.
43. Yizhak K, Le Dévédec SE, Rogkoti VM, Baenke F, de Boer VC, Frezza C, Schulze A, van de Water B, Ruppin E. A computational study of the Warburg effect identifies metabolic targets inhibiting cancer migration. *Mol Syst Biol*. 2014;10:744.
44. Zhao M, Chen X, Gao G, Tao L, Wei L. RLedB: a database of rate-limiting enzymes and their regulation in human, rat, mouse, yeast and E. coli. *Cell Res*. 2009;19:793–5.
45. Hoffman FO, Miller CW. Uncertainties in environmental radiological assessment models and their implications. 1983.
46. Ye F, Bauer JA, Pietenpol JA, Shyr Y. Analysis of high-throughput RNAi screening data in identifying genes mediating sensitivity to chemotherapeutic drugs: statistical approaches and perspectives. *BMC Genomics*. 2012;13(Suppl 8):S3.
47. Hamby DM. A comparison of sensitivity analysis techniques. *Health Phys*. 1995;68:195–204.
48. Corton JM, Gillespie JG, Hawley SA, Hardie DG. 5-aminoimidazole-4-carboxamide ribonucleoside. A specific method for activating AMP-activated protein kinase in intact cells? *Eur J Biochem*. 1995;229:558–65.
49. BROWN J. Effects of 2-deoxyglucose on carbohydrate metabolism: review of the literature and studies in the rat. *Metabolism*. 1962;11:1098–112.
50. Koutcher JA, Alfieri AA, Matei C, Meyer KL, Street JC, Martin DS. Effect of 6-aminonicotinamide on the pentose phosphate pathway: 31P NMR and tumor growth delay studies. *Magn Reson Med*. 1996;36:887–92.
51. Singer TP, Ramsay RR. The reaction sites of rotenone and ubiquinone with mitochondrial NADH dehydrogenase. *Biochim Biophys Acta*. 1994;1187:198–202.

52. Owen MR, Doran E, Halestrap AP. Evidence that metformin exerts its anti-diabetic effects through inhibition of complex 1 of the mitochondrial respiratory chain. *Biochem J.* 2000;348(Pt 3):607–14.
53. Zhou G, Myers R, Li Y, Chen Y, Shen X, Fenyk-Melody J, Wu M, Ventre J, Doebber T, Fujii N, Musi N, Hirshman MF, Goodyear LJ, Moller DE. Role of AMP-activated protein kinase in mechanism of metformin action. *J Clin Invest.* 2001;108:1167–74.
54. Ward PS, Thompson CB. Metabolic reprogramming: a cancer hallmark even warburg did not anticipate. *Cancer Cell.* 2012;21:297–308.
55. Kim M-J, Kim D-H, Jung W-H, Koo J-S. Expression of metabolism-related proteins in triple-negative breast cancer. *Int J Clin Exp Pathol.* 2014;7:301–12.
56. Filipp FV, Ratnikov B, De Ingeniis J, Smith JW, Osterman AL, Scott DA. Glutamine-fueled mitochondrial metabolism is decoupled from glycolysis in melanoma. *Pigment Cell Melanoma Res.* 2012;25:732–9.
57. Cao MD, Lamichhane S, Lundgren S, Bofin A, Fjøsne H, Giskeødegård GF, Bathen TF. Metabolic characterization of triple negative breast cancer. *BMC Cancer.* 2014;14:941.
58. Simpson NE, Tryndyak VP, Beland FA, Pogribny IP. An in vitro investigation of metabolically sensitive biomarkers in breast cancer progression. *Breast Cancer Res Treat.* 2012;133:959–68.
59. Simpson NE, Tryndyak VP, Pogribna M, Beland FA, Pogribny IP. Modifying metabolically sensitive histone marks by inhibiting glutamine metabolism affects gene expression and alters cancer cell phenotype. *Epigenetics.* 2012;7:1413–20.
60. Kim SK, Jung WH, Koo JS. Differential expression of enzymes associated with serine/glycine metabolism in different breast cancer subtypes. *PLoS One.* 2014;9:e101004.
61. Noh S, Kim DH, Jung WH, Koo JS. Expression levels of serine/glycine metabolism-related proteins in triple negative breast cancer tissues. *Tumour Biol.* 2014;35:4457–68.
62. Shen J, Yan L, Liu S, Ambrosone CB, Zhao H. Plasma metabolomic profiles in breast cancer patients and healthy controls: by race and tumor receptor subtypes. *Transl Oncol.* 2013;6:757–65.
63. López-Cortés A, Echeverría C, Oña-Cisneros F, Sánchez ME, Herrera C, Cabrera-Andrade A, Rosales F, Ortiz M, Paz-Y-Miño C. Breast cancer risk associated with gene expression and genotype polymorphisms of the folate-metabolizing MTHFR gene: a case-control study in a high altitude Ecuadorian mestizo population. *Tumour Biol.* 2015;36:6451–61.
64. Jung YY, Kim HM, Koo JS. Expression of lipid metabolism-related proteins in metastatic breast cancer. *PLoS One.* 2015;10:e0137204.
65. Kim S, Lee Y, Koo JS. Differential expression of lipid metabolism-related proteins in different breast cancer subtypes. *PLoS One.* 2015;10:e0119473.
66. Griffiths B, Lewis CA, Bensaad K, Ros S, Zhang Q, Ferber EC, Konisti S, Peck B, Miess H, East P, Wakelam M, Harris AL, Schulze A. Sterol regulatory element binding protein-dependent regulation of lipid synthesis supports cell survival and tumor growth. *Cancer Metab.* 2013;1:3.
67. Tang X, Lin C-C, Spasojevic I, Iversen ES, Chi J-T, Marks JR. A joint analysis of metabolomics and genetics of breast cancer. *Breast Cancer Res.* 2014;16:415.
68. Kim S, Rhee J, Yoo HJ, Lee HJ, Lee EJ, Lee JW, Yu JH, Son BH, Gong G, Kim SB, Singh SR, Ahn SH, Chang S. Bioinformatic and metabolomic analysis reveals miR-155 regulates thiamine level in breast cancer. *Cancer Lett.* 2015;357:488–97.
69. Boroughs LK, DeBerardinis RJ. Metabolic pathways promoting cancer cell survival and growth. *Nat Cell Biol.* 2015;17:351–9.
70. Kanaan YM, Sampey BP, Beyene D, Esnakula AK, Naab TJ, Ricks-Santi LJ, Dasi S, Day A, Blackman KW, Frederick W, Copeland RL, Gabrielson E, Dewitty RL. Metabolic profile of triple-negative breast cancer in African-American women reveals potential biomarkers of aggressive disease. *Cancer Genomics Proteomics.* 2014;11:279–94.
71. Hart PC, Mao M, de Abreu ALP, Ansenberger-Fricano K, Ekoue DN, Ganini D, Kajdacsy-Balla A, Diamond AM, Minshall RD, Consolaro MEL, Santos JH, Bonini MG. MnSOD upregulation sustains the Warburg effect via mitochondrial ROS and AMPK-dependent signaling in cancer. *Nat Commun.* 2015;6:6053.
72. Go R-E, Hwang K-A, Choi K-C. Cytochrome P450 1 family and cancers. *J Steroid Biochem Mol Biol.* 2015;147:24–30.
73. D'Amato NC, Rogers TJ, Gordon MA, Greene LI, Cochrane DR, Spoelstra NS, Nemkov TG, D'Alessandro A, Hansen KC, Richer JK. A TDO2-AhR signaling axis facilitates anoikis resistance and metastasis in triple-negative breast cancer. *Cancer Res.* 2015;75:4651–64.
74. Viale A, Pettazzoni P, Lyssiotis CA, Ying H, Sánchez N, Marchesini M, Carugo A, Green T, Seth S, Giuliani V, Kost-Alimova M, Muller F, Colla S, Nezi L, Genovese G, Deem AK, Kapoor A, Yao W, Brunetto E, Kang Y, Yuan M, Asara JM, Wang YA, Heffernan TP, Kimmelman AC, Wang H, Fleming JB, Cantley LC, DePinho RA, Draetta GF. Oncogene ablation-resistant pancreatic cancer cells depend on mitochondrial function. *Nature.* 2014;514:628–32.

Submit your next manuscript to BioMed Central and we will help you at every step:

- We accept pre-submission inquiries
- Our selector tool helps you to find the most relevant journal
- We provide round the clock customer support
- Convenient online submission
- Thorough peer review
- Inclusion in PubMed and all major indexing services
- Maximum visibility for your research

Submit your manuscript at
www.biomedcentral.com/submit



Chapter 5


Systems biology analysis of mitogen activated protein kinase inhibitor resistance in malignant melanoma

RESEARCH ARTICLE

Open Access



Systems biology analysis of mitogen activated protein kinase inhibitor resistance in malignant melanoma

Helma Zecena¹, Daniel Tveit¹, Zi Wang^{2,3}, Ahmed Farhat², Parvita Panchal², Jing Liu^{2,3}, Simar J. Singh¹, Amandeep Sanghera¹, Ajay Baniwal¹, Shuan Y. Teo¹, Frank L. Meyskens Jr², Feng Liu-Smith^{2,4*} and Fabian V. Filipp^{1*} 

Abstract

Background: Kinase inhibition in the mitogen activated protein kinase (MAPK) pathway is a standard therapy for cancer patients with activating BRAF mutations. However, the anti-tumorigenic effect and clinical benefit are only transient, and tumors are prone to treatment resistance and relapse. To elucidate mechanistic insights into drug resistance, we have established an in vitro cellular model of MAPK inhibitor resistance in malignant melanoma.

Methods: The cellular model evolved in response to clinical dosage of the BRAF inhibitor, vemurafenib, PLX4032. We conducted transcriptomic expression profiling using RNA-Seq and RT-qPCR arrays. Pathways of melanogenesis, MAPK signaling, cell cycle, and metabolism were significantly enriched among the set of differentially expressed genes of vemurafenib-resistant cells vs control. The underlying mechanism of treatment resistance and pathway rewiring was uncovered to be based on non-genomic adaptation and validated in two distinct melanoma models, SK-MEL-28 and A375. Both cell lines have activating BRAF mutations and display metastatic potential.

Results: Downregulation of dual specific phosphatases, tumor suppressors, and negative MAPK regulators reengages mitogenic signaling. Upregulation of growth factors, cytokines, and cognate receptors triggers signaling pathways circumventing BRAF blockage. Further, changes in amino acid and one-carbon metabolism support cellular proliferation despite MAPK inhibitor treatment. In addition, treatment-resistant cells upregulate pigmentation and melanogenesis, pathways which partially overlap with MAPK signaling. Upstream regulator analysis discovered significant perturbation in oncogenic forkhead box and hypoxia inducible factor family transcription factors.

Conclusions: The established cellular models offer mechanistic insight into cellular changes and therapeutic targets under inhibitor resistance in malignant melanoma. At a systems biology level, the MAPK pathway undergoes major rewiring while acquiring inhibitor resistance. The outcome of this transcriptional plasticity is selection for a set of transcriptional master regulators, which circumvent upstream targeted kinases and provide alternative routes of mitogenic activation. A fine-woven network of redundant signals maintains similar effector genes allowing for tumor cell survival and malignant progression in therapy-resistant cancer.

Keywords: Cancer systems biology, Precision medicine, Omics, RNA-Seq, Transcriptomics, Upstream regulator analysis, Transcription factor, Master regulator, Regulome, Non-genomic, Rewiring, Adaptation, Genetic selection, Drug resistance, Therapy resistance, Melanoma, Melanogenesis

* Correspondence: liufe@uci.edu; filipp@ucmerced.edu

²Department of Medicine, School of Medicine, Chao Family Comprehensive Cancer Center, University of California Irvine, Irvine, CA 92697, USA

¹Systems Biology and Cancer Metabolism, Program for Quantitative Systems Biology, University of California Merced, 2500 North Lake Road, Merced, CA 95343, USA

Full list of author information is available at the end of the article



© The Author(s). 2018 **Open Access** This article is distributed under the terms of the Creative Commons Attribution 4.0 International License (<http://creativecommons.org/licenses/by/4.0/>), which permits unrestricted use, distribution, and reproduction in any medium, provided you give appropriate credit to the original author(s) and the source, provide a link to the Creative Commons license, and indicate if changes were made. The Creative Commons Public Domain Dedication waiver (<http://creativecommons.org/publicdomain/zero/1.0/>) applies to the data made available in this article, unless otherwise stated.

Background

Therapy resistance in cancer

Cancer drug resistance is a major obstacle in achieving durable clinical responses with targeted therapies. This highlights a need to elucidate the underlying mechanisms responsible for resistance and identify strategies to overcome this challenge. In malignant melanoma, activating point-mutations in the mitogen activated protein kinase (MAPK) pathway in BRAF kinase (B-Raf proto-oncogene, serine/threonine kinase, Gene ID: 673) [1–3] made it possible to develop potent kinase inhibitors matched to genotyped kinase mutations in precision medicine approaches [4–6]. In tumors expressing the oncoprotein BRAF(V600E), the inhibitor molecules vemurafenib, dabrafenib, and encorafenib are designed to lock the ATP binding site into an inactive conformation of the kinase [4], the preferred state of wild-type RAF proteins. Trametinib and cobimetinib target MAP2K7 (MEK, mitogen-activated protein kinase kinase 7, Gene ID: 5609), the BRAF target and downstream effector molecule. In MAPK signaling, combinations of specific inhibitors have proven to be superior to single-agent regimens: BRAF inhibitors (BRAFi) in combination with MEK inhibitors (MEKi) improved survival compared to single MAPK inhibitors (MAPKi) [7–10]. However, many patients responding to small molecule inhibition of the MAPK pathway will develop resistance. Ultimately, disease progression will take place and patients relapse with lethal drug-resistant disease.

Mechanism of resistance beyond mutations

Acquired resistance has been shown to involve a diverse spectrum of oncogenic mutations in the MAPK pathway [11–15]. In addition, non-genomic activation of parallel signaling pathways has been noted [16]. Cell-to-cell variability in BRAF(V600E) melanomas generates drug-tolerant subpopulations. Selection of genetically distinct, fully drug-resistant clones arise within a set of heterogeneous tumor cells surviving the initial phases of therapy due to drug adaptation [17]. Non-genomic drug adaptation can be accomplished reproducibly in cultured cells, and combination therapies that block adaptive mechanisms *in vitro* have shown promise in improving rates and durability of response [18]. Thus, better understanding of mechanisms involved in drug adaptation is likely to improve the effectiveness of melanoma therapy by delaying or controlling acquired resistance.

Methods

Cellular models of malignant melanoma

SK-MEL-28 and A375 are human skin malignant melanoma cell lines with BRAF(V600E) activation that are tumorigenic in xenografts [19–22] (HTB-72 and CRL-1619, American Type Culture Collection, Manassas,

VA). The cell lines are maintained in DMEM medium supplemented with 10% fetal bovine serum and antibiotics (10–017-CV, 35–010-CV, 30–002-CI Corning, Corning, NY). All experimental protocols were approved by the Institutional Review Boards at the University of California Merced and Irvine. The study was carried out as part of IRB UCM13–0025 of the University of California Merced and as part of dbGap ID 5094 on somatic mutations in cancer and conducted in accordance with the Helsinki Declaration of 1975.

BRAFi-resistant (BRAFi-R) models were obtained by challenging cancer cell lines with incrementally increasing vemurafenib (PLX4032, PubChem CID: 42611257, Selleckchem, Houston, TX) concentrations in the culture media. Starting at 0.25 μ M, which matched the naïve half maximal inhibitory concentration (IC₅₀) of the parental cell lines, the vemurafenib concentrations were increased every 7 days in an exponential series up to 100-fold the naïve IC₅₀ concentrations. Following this 6-week selection protocol, vemurafenib-adapted, cancer therapy resistance models were maintained in media supplemented with 5.0 μ M vemurafenib.

Transcriptomic profiling and differential gene expression analysis

Total RNA from malignant melanoma cells was extracted using a mammalian RNA mini preparation kit (RTN10-1KT, GenElute, Sigma EMD Millipore, Darmstadt, Germany) and then digested with deoxyribonuclease I (AMPD1-1KT, Sigma EMD Millipore, Darmstadt, Germany). Complementary DNA (cDNA) was synthesized using random hexamers (cDNA SuperMix, 95,048–500, Quanta Biosciences, Beverly, MA). The purified DNA library was sequenced using a High-Seq2500 (Illumina, San Diego, CA) at the University of California Irvine Genomics High-Throughput Facility. Purity and integrity of the nucleic acid samples were quantified using a Bioanalyzer (2100 Bioanalyzer, Agilent, Santa Clara, CA). Libraries for next generation mRNA transcriptome sequencing (RNA-Seq) analysis were generated using the TruSeq kit (TruSeq RNA Library Prep Kit v2, RS-122-2001, Illumina, San Diego, CA). In brief, the workflow involves purifying the poly-A containing mRNA molecules using oligo-dT attached magnetic beads. Following purification, the mRNA is chemically fragmented into small pieces using divalent cations under elevated temperature. The cleaved RNA fragments are copied into first strand cDNA using reverse transcriptase and random primers. Second strand cDNA synthesis follows, using DNA polymerase I and RNase H. The cDNA fragments are end repaired by adenylation of the 3' ends and ligated to barcoded adapters. The products are then purified and enriched by nine cycles of PCR to create the final cDNA library subjected to

sequencing. The resulting libraries were validated by qPCR and size-quantified by a DNA high sensitivity chip (Bioanalyzer, 5067–4626, Agilent, Santa Clara, CA). Sequencing was performed using 50 base pair read length, single-end reads, and more than 10^7 reads per sample. Raw sequence reads in the file format for sequences with quality scores (FASTQ) were mapped to human reference Genome Reference Consortium GRCh38 using Bowtie alignment with an extended Burrows-Wheeler indexing for an ultrafast memory efficient alignment within the Tuxedo suite followed by Tophat to account for splice-isoforms [23, 24]. Read counts were scaled via the median of the geometric means of fragment counts across all libraries. Transcript abundance was quantified using normalized single-end RNA-Seq reads in read counts as well as reads per kilobase million (RPKM). Since single-end reads were acquired in the sequencing protocol, quantification of reads or fragments yielded similar results. Statistical testing for differential expression was based on read counts and performed using EdgeR in the Bioconductor toolbox [25]. Differentially expressed genes were further analyzed using Ingenuity Pathways Analysis (IPA, Qiagen, Redwood City, CA), classification of transcription factors (TFClass), and gene set enrichment analysis (GSEA, Broad Institute, Cambridge, MA) [26, 27]. For real-time quantitative polymerase chain reaction (RT-qPCR) validation of RNA-Seq signals of differentially expressed target genes in BRAFi-R melanoma cells, gene expression profiles were analyzed using the $\Delta\Delta$ threshold cycle (CT) method. Oligonucleotides spanning exon-exon-junctions of transcripts were used for RT-qPCR validation (Additional file 1: Table 1). Triple replicate samples were subjected to SYBR green (SYBR green master mix, PerfeCTa® SYBR® Green FastMix®, 95072-05k, Quanta Biosciences, Beverly, MA) RT-qPCR analysis in an Eco system (Illumina, San Diego). CT values were normalized using multiple housekeeping genes like actin beta (ACTB, Gene ID: 60), cyclophilin A (PPIA, peptidylprolyl isomerase A, Gene ID: 5478) and RNA polymerase II subunit A (POLR2A, GeneID: 5430).

Inhibitor cytotoxicity studies

Chemical BRAFi against BRAF(V600E), vemurafenib, was dissolved in dimethyl sulfoxide (DMSO, Sigma) as a 10.0 mM stock solution and used in treatments in final concentrations between 0.01 μ M and 50.0 μ M. Melanoma control experiments were carried out in the presence of equivalent amounts of DMSO solvent without drug. Cell viability was determined using a 2,3-bis(2-methoxy-4-nitro-5-sulfophenyl)-2H-tetrazolium-5-carboxanilide (XTT, X4626, Sigma EMD Millipore, Darmstadt, Germany) absorbance assay by subtracting background readout at 650 nm from response readout at 570 nm wavelength. IC₅₀ concentrations were determined after 72 h of drug

treatment between 0.01–100 μ M in two-fold dilution series. Analysis was performed using CalcuSyn (v2.0, BioSoft, Cambridge, UK).

Melanin quantification

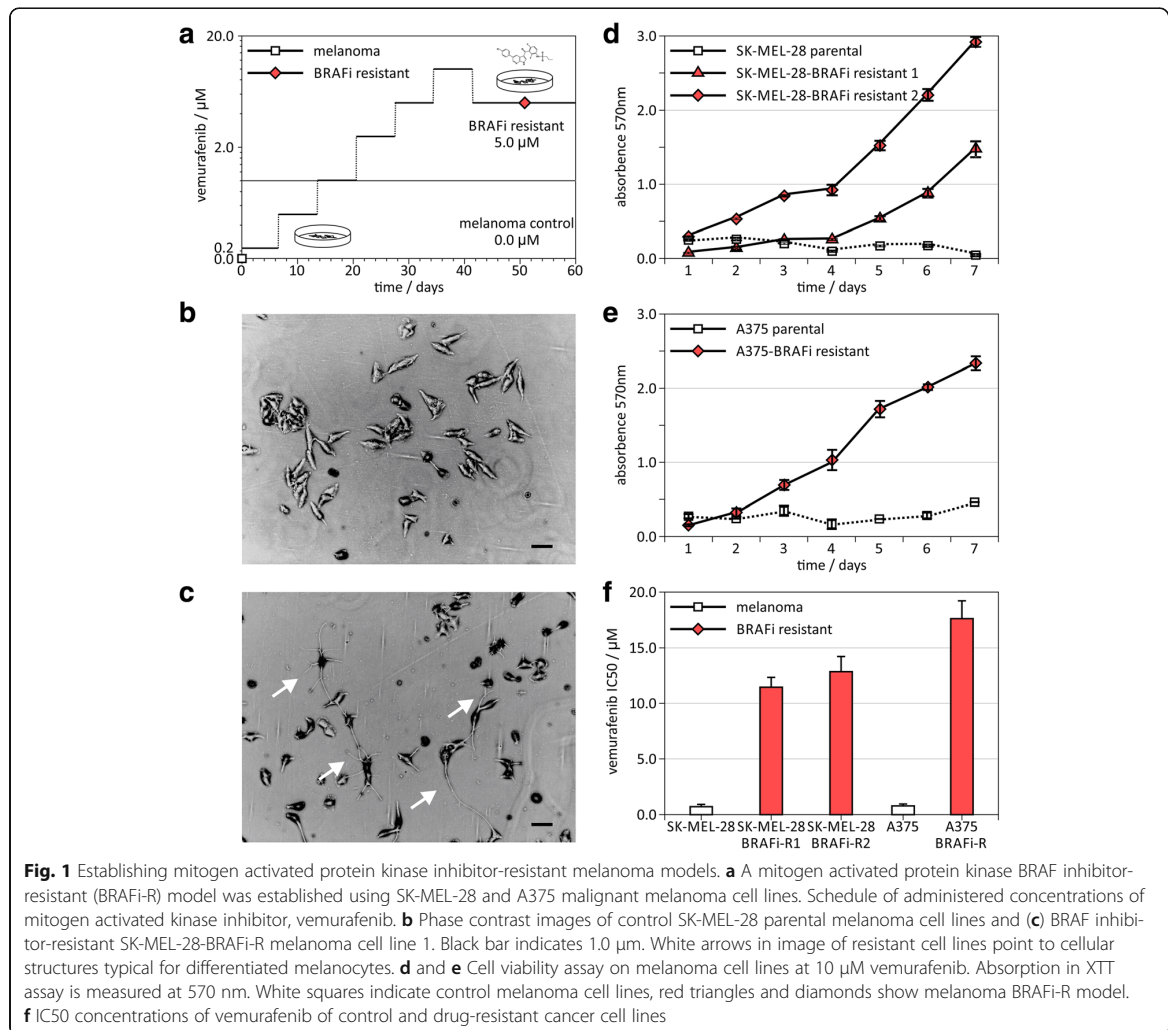
Melanin pigment production of cultured cells was determined by colorimetric measurements normalized for total protein levels in arbitrary units [28, 29]. Melanoma cells were harvested by centrifugation at 3000 rpm (3830 g, Z326K, Labnet International, Edison, NJ) and dissolved in either 1.0 N NaOH for melanin assay or lysis 250 for protein assay. The cell lysates were sonicated, incubated at room temperature for 24 h, and cleared by centrifugation at 13,000 rpm for 10 min (17,000 g, Z326K, Labnet International, Edison, NJ). The absorption of the supernatant was measured at 475 nm in a spectrophotometer (Smartspec3000, Bio-Rad, Carlsbad, CA). Cells were lysed in mild denaturing conditions in lysis 250 buffer (25 mM Tris, [pH 7.5], 5 mM EDTA, 0.1% NP-40, 250 mM NaCl) containing proteinase inhibitors (10 μ g/ml aprotinin, 10 μ g/ml leupeptin, 10 μ g/ml pepstatin, 5 μ g/ml antipain, 1 mM phenylmethylsulfonyl fluoride). The total protein amount in the lysates was quantified using a colorimetric Bradford assay (5000001, Bio-Rad, Richmond, CA) at 595 nm and an incubation time of 30 min [30].

Results

Generation of BRAFi-resistant melanoma cell lines

The parental melanoma cell lines SK-MEL-28 and A375 were exposed to incrementally increasing concentrations of the mutant-BRAF inhibitor vemurafenib (Fig. 1a). At the initial inhibitor concentration matching the IC₅₀ of vemurafenib in the naïve parental melanoma cells [11, 31] cell proliferation decreased. Surviving cells were propagated and subjected to an exponential series of increasing vemurafenib concentrations until BRAFi-R sublines were obtained tolerating at least 5 μ M vemurafenib in the culture media with similar cell proliferation rates as the parental cell lines of 0.67 doublings per day.

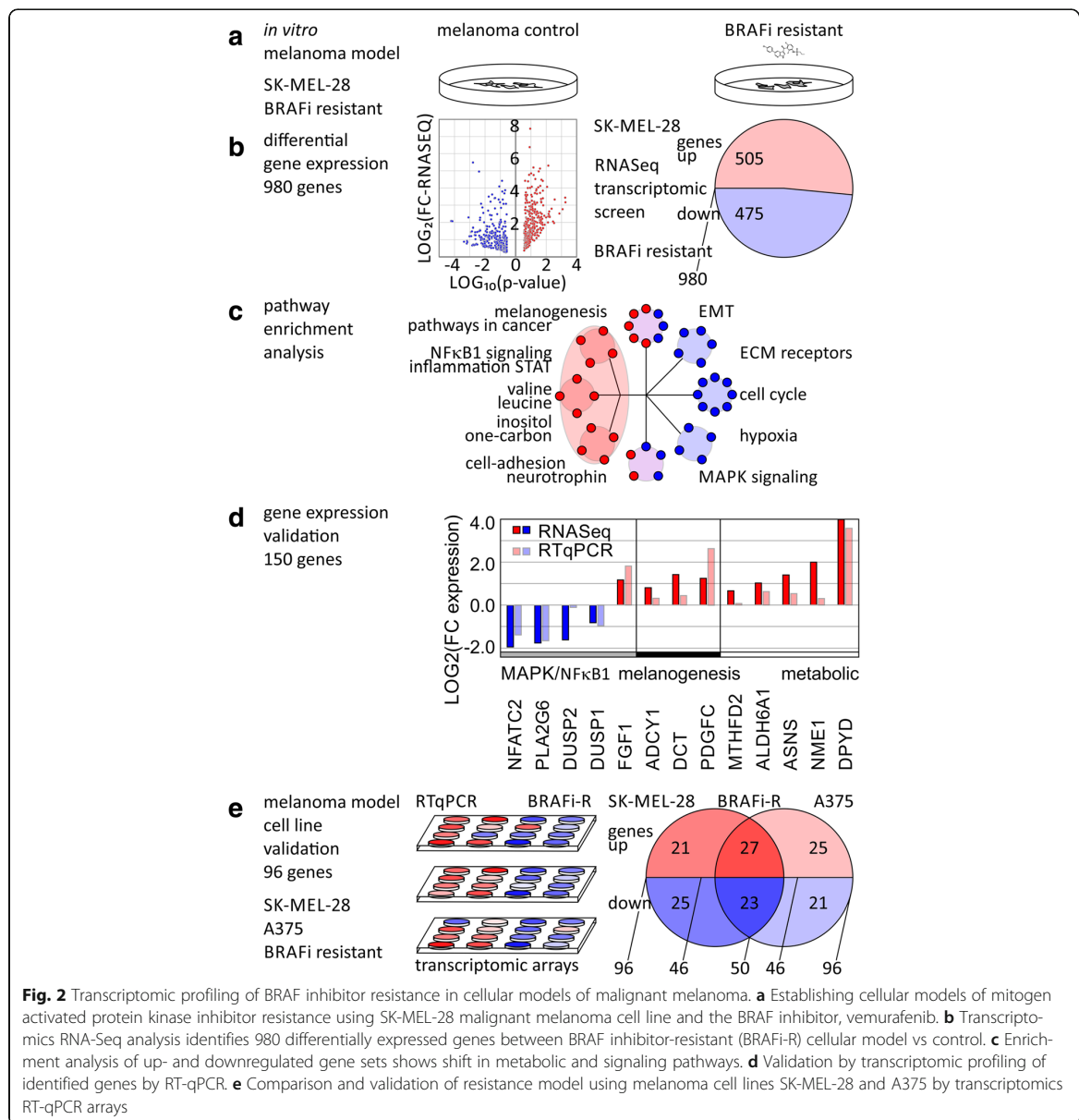
Some BRAFi-R cell lines showed structures typically observed in differentiated melanocytes (Fig. 1b-c). In the presence of 5 μ M vemurafenib, however, the parental cells were not able to grow but the resistant cells proliferated comparable to naïve cell lines (Fig. 1d-e). For the SK-MEL-28 cell line, two resistant sublines were established. The resistant sublines displayed IC₅₀ values of 11.5 ± 0.9 μ M and 13.3 ± 1.2 μ M for SK-MEL-28-BRAFi-R1 and SK-MEL-28-BRAFi-R2 respectively, which is approximately 10–20 fold of the IC₅₀ in a low micromolar range for the parental cells with 0.74 ± 0.05 μ M. For the A375 cell line, the IC₅₀ of the A375-BRAFi-R cell line was observed at 17.7 ± 1.5 μ M, 22.7 fold of IC₅₀ for the parental A375 cells with 0.78 ± 0.22 μ M (Fig. 1f).



Transcriptomic profiling identifies non-genomic rewiring of treatment-resistant cancer cells

We conducted transcriptomic gene expression profiling of BRAFi treatment-resistant SK-MEL-28-BRAFi-R1 and SK-MEL-28-BRAFi-R2 cell lines by RNA-Seq and looked for differential expression versus the parental SK-MEL-28 cell line. In total, 980 unique transcripts showed significant differential expression in RNA-Seq experiments with p values below 0.05, absolute log-fold change (LOG(FC)) greater or equal 1.0 (Fig. 2a-b). The differentially expressed genes included 505 upregulated transcripts and 475 downregulated transcripts (Additional file 1: Table S2–3). We subjected the identified directional sets to pathway enrichment analysis (Additional file 1: Table S4). Distinct clusters stood out and showed significant enrichment with p values below 0.05 and

q values below 0.10 (Fig. 2c). Melanogenesis and pathways in cancer, inflammation, nuclear factor kappa-light-chain-enhancer of activated B cells (NFkB) and signal transducer and activator of transcription (STAT) signaling, metabolic pathways including alanine, tyrosine, valine, leucine, inositol, one-carbon metabolism, cell-adhesion molecules, neurotrophin signaling were over-represented in the upregulated dataset. MAPK signaling and epithelial-mesenchymal transition (EMT) were differentially expressed and characterized by both strong up- and downregulation. Extra-cellular matrix (ECM) receptors, cell cycle, and hypoxia signaling were enriched in the downregulated dataset. Of the 980 differential expressed genes, we validated expression changes of 150 genes by RT-qPCR (Fig. 2d, Additional file 1: Table S3). Of these, a majority, 64.0% (96 of 150), responded



significantly (with p values below 0.05) in the same direction as RNA-Seq data for treatment-resistant melanoma. When both treatment resistance models of SK-MEL-28 and A375 were taken into consideration, about half of the tested genes, 50 of 96, showed consistent regulation (Fig. 2e, Additional file 1: Table S3). Genes in MAPK signaling included nuclear factor of activated T-cells 2 (NFATC2, Gene ID: 4773), phospholipase A2 group VI (PLA2G6, Gene ID: 8398), dual specificity phosphatase 1 (DUSP1, Gene ID: 1843), and dual

specificity phosphatase 2 (DUSP2, Gene ID: 1844), which were downregulated in the BRAFi-R cells compared to control. Genes contributing to melanogenesis adenylate cyclase 1 (ADCY1, Gene ID: 107), dopachrome tautomerase (DCT, TYRP2, Gene ID: 1638), and platelet derived growth factor C (PDGFC, Gene ID: 56034) were upregulated. Lastly, metabolic regulators such as methylenetetrahydrofolate dehydrogenase 2 (MTHFD2, Gene ID: 10797) for folate metabolism, asparagine synthetase (ASNS, Gene ID: 440)

for amino acid metabolism, and NME/NM23 nucleoside diphosphate kinase 1 (NME1, Gene ID: 4830) and dihydropyrimidine dehydrogenase (DPYD, Gene ID: 1806) for pyrimidine metabolism were significantly upregulated (Fig. 2d). Taken together, the adaptive transcriptomic changes were validated in two distinct melanoma models, SK-MEL-28 and A375, both cell lines with metastatic potential showed differential expression of MAPK signaling while activating alternative mitogenic signaling interactions and metabolic processes.

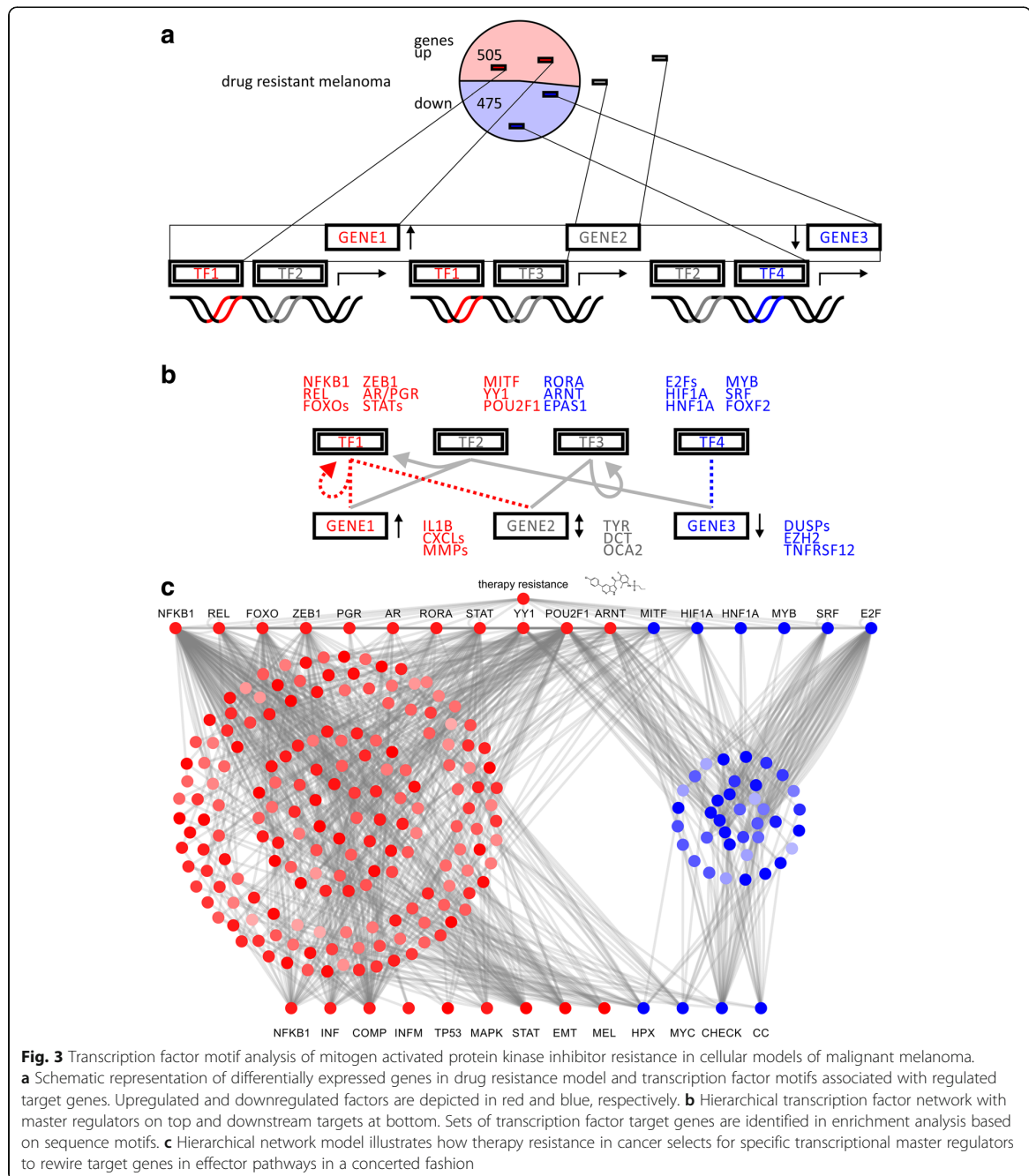
Upstream regulator analysis suggests control by transcription factor families

Next, the gene list was subjected to hierarchical transcription factor motif analysis to identify master regulators [32]. We asked whether any of the enriched transcription factor motif families were represented in the differential gene expression data. In detail, we looked for transcription factors as well as their target genes whose promoters show respective transcription factor binding sites among the same list of regulated genes (Fig. 3a). It is expected that differentially expressed transcription factors show motif enrichment in promoter sites of significantly deregulated target genes. Further, identified target genes with enriched transcription factor motifs will have major contributions to significantly deregulated pathways under treatment resistance (Fig. 3b). A network illustration of transcriptional master regulators, target genes, and dysregulated effector network upon treatment resistance demonstrates transcriptional synergy (Fig. 3c). Upregulated transcription factor families included Rel homology region (RHR) NF κ B-related factors, forkhead box (FOX), Zinc finger E-box-binding homeobox domain factors (ZEB), nuclear steroid hormone receptor subfamily 3 (NR3C, androgen receptor and progesterone receptor), hypoxia-inducible and endothelial PAS domain-containing factors (HIF, EPAS), and the cell cycle transcription factor family (E2F) (Fig. 3b). Downstream enriched target genes comprised members of interleukin (IL), chemokine receptor (CXCL), matrix metallo proteinase (MMP) families, transcription factors forkhead box O1 (FOXO1, Gene ID: 2308), endothelial PAS domain protein 1 (EPAS1, HIF2A, Gene ID: 2034) and melanogenesis associated metabolic genes, tyrosinase (TYR, OCA1, Gene ID: 7299), DCT, and melanosomal transmembrane protein (OCA2, oculocutaneous albinism II, Gene ID: 4948). Downregulated transcription factors included forkhead box F2 (FOXF2, Gene ID: 2295), which has DUSP2 or transforming growth factor beta 3 (TGFB3, Gene ID: 7043) as target genes. Upstream regulator analysis suggested gene expression changes of nuclear factor kappa B subunit 1 (NF κ B1, Gene ID: 4790, V\$NF κ B_Q6, motif M11921) in complex with REL proto-oncogene (REL Gene ID: 5966, V\$CREL_01, motif M10143), EMT

modulator zinc finger E-box binding homeobox 1 (ZEB1, Gene ID: 6935, V\$AREB6_01, M11244), forkhead box (V\$FOXO1_01, motif M11512), and hypoxia inducible factor family transcription factors (V\$HIF1_Q3, motif M14011) as master regulators of transcriptional effector networks upon BRAFi treatment resistance.

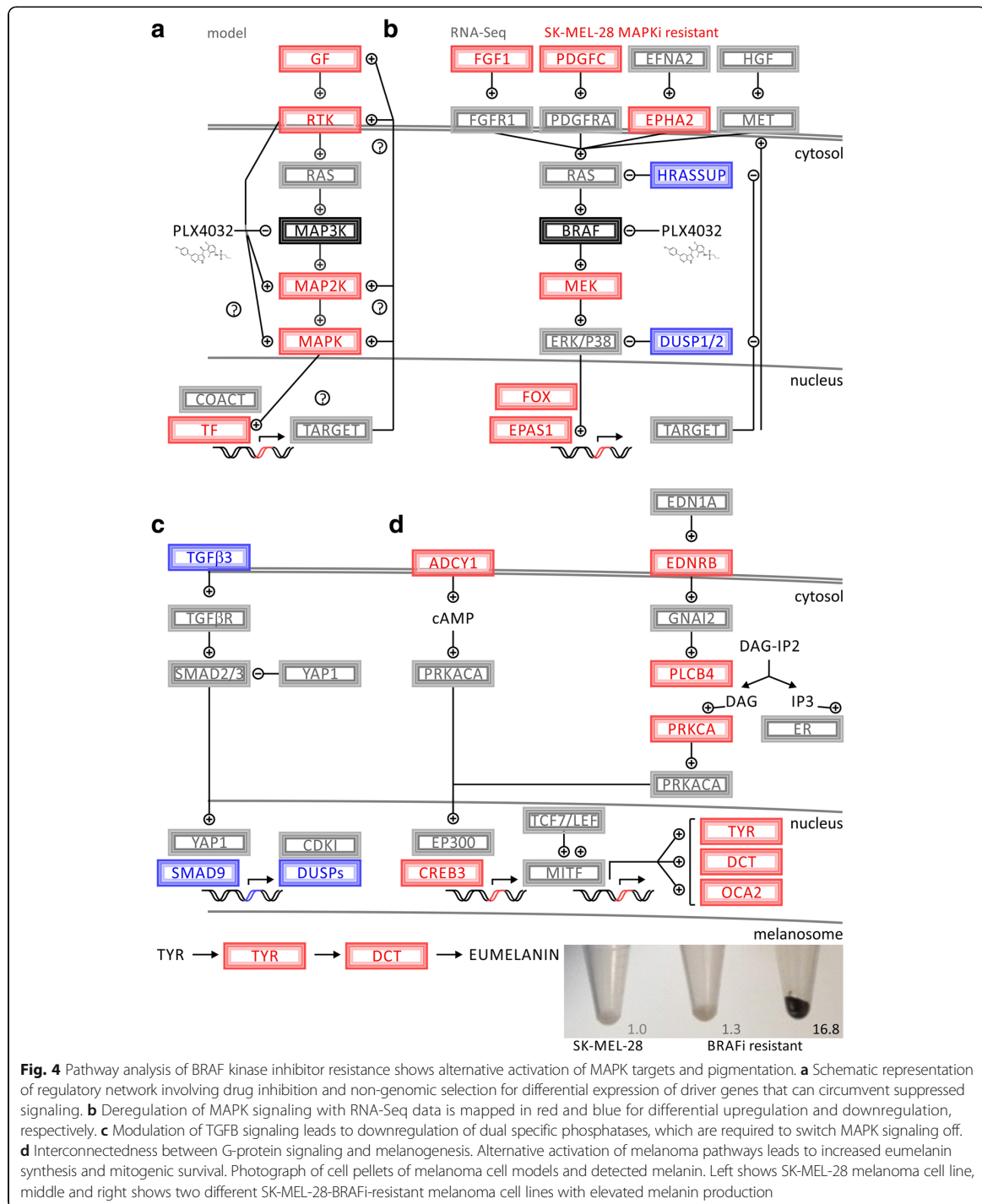
Validation of pathway rewiring in drug resistance in multiple cell lines by transcriptomics arrays

Transcriptome analysis of reversible drug resistance identified distinct pathways that allowed for circumvention of BRAF blockage (Fig. 4a). Cell-to-cell variability in combination with drug exposure selects for distinct subpopulations of MAPKi-resistant (MAPKi-R) cell lines. In a hierarchical fashion, transcriptional master regulators promote a distinct set of target genes resulting in circumvention of MAPK inhibition. Receptor activation by fibroblast growth factor 1 (FGF1, Gene ID: 2246) or PDGFC can lead to activated receptor tyrosine signaling parallel to canonical MAPK signaling [16] (Fig. 4b). In addition, downregulation of tumor suppressors reengages mitogenic signaling. The dual specific phosphatases, DUSP1 and DUSP2, have the ability to switch MAPK signaling off and rank among the top downregulated hits. Thus, downregulation of dual specific phosphatases facilitates and reinforces alternative MAPK effector activation under BRAF blockage (Fig. 4b). One of the mitogen-activated protein kinase 1 (MAPK1, ERK2, Gene ID: 5594) effector targets, transcription factor EPAS1, showed upregulation and the ability to maintain its transcriptional program. The pro-apoptotic program of TGFB3 was downregulated including SMAD family member 9 (SMAD9, Gene ID: 4093) and DUSP1/2 (Fig. 4c). Adenylate cyclase, G-protein, and phospholipase signaling are alternative cascades observed in cutaneous and uveal melanoma (Fig. 4d). Upregulation of ADCY1, endothelin receptor type B (EDNRB, Gene ID: 1910), phospholipase C beta 4 (PLCB4, Gene ID: 5332), and cAMP responsive element binding protein 3 (CREB3, Gene ID: 10488) promote MITF activity, the master transcription factor for pigmentation genes. Downstream metabolic enzymes, TYR and DCT, are both MITF target genes and contribute to enhanced eumelanin production observed in some therapy-resistant cell lines. The observed pigmentation showed a wide range of from 1.3-fold to up to 16.8-fold upregulation (Fig. 4d). While both cell lines showed dysregulation of melanogenesis, the regulators and effectors involved were different. SK-MEL-28-BRAFi-R2 has ASIP prominently expressed (TYR (2.1), DCT (2.8), tyrosinase related protein 1 (TYRP1, OCA3, Gene ID: 7306) (0.5), MITF (0.7), agouti signaling protein (ASIP, Gene ID: 434) (18.9)), while A375-BRAFi-R showed strongest regulation of TYRP1 and MITF (TYR (0.34), DCT (0.24), TYRP1 (41.8), MITF (2.94), ASIP (0.41)).



In summary, upregulation of growth factors or receptors triggers signaling pathways circumventing BRAF blockage. Changes in amino acid and one-carbon metabolism support cellular proliferation despite inhibitor treatment. In addition, alternative MAPK signaling coincides with differential response of melanogenesis and

pigmentation pathways, which partially overlap with MAPK effectors. In particular, NFKB1, REL, ZEB1, FOXO1, and EPAS1 may serve as master regulators to enact broad transcriptional changes implemented in altered cascades of MAPK, TGFB, ADCY, and MITF signaling.



Discussion

Activation of the MAPK pathway is the central and most common oncogenic event in the pathogenesis of

malignant melanoma [3, 33]. About 50% of all melanoma patients have activating somatic mutations in the activator loop involving L597, T599, V600, and K601

switching proto-oncogene BRAF into a constitutively active protein kinase and cancer driver. Such activation is supported by somatic copy number amplifications of chromosome 7 [34], often coinciding with somatic V600E/G/K/M/R mutations. Another 20–30% of the patients show non-genomic activation of BRAF by transcriptional upregulation or post-translational modification induced by somatic mutations of upstream signaling molecules like KIT proto-oncogene receptor tyrosine kinase (KIT, Gene ID: 3815), proto-oncogene neuroblastoma RAS viral oncogene homolog (NRAS, Gene ID: 4893), or loss-of-function neurofibromin 1 (NF1, Gene ID: 4763). Constitutively activated BRAF phosphorylates MAPK1 and downstream kinases resulting in mitogenic signaling, proliferation, and cell growth. Integrated into this cellular program is negative feedback resulting in reduction of NRAS expression [35, 36].

Genomic and non-genomic mechanisms of therapy resistance

Genomic sequencing has facilitated the understanding of acquired resistance mechanisms to MAPKis [14–16, 37–40]. Detected genetic aberrations included mutations in NRAS, MAPK1/2, phosphatidylinositol-4,5-bisphosphate 3-kinase catalytic subunit alpha (PIK3CA, Gene ID: 5290), and phosphatase and tensin homolog (PTEN, Gene ID: 5728). Somatic melanoma mutations provide examples of how single, well-defined genomic events can confer resistance against vemurafenib treatment. In contrast, transcriptomic as well as epigenomic regulation can provide insight into resistance states that may involve larger networks. Eventually, resistance-conferring genomic, epigenomic, and transcriptomic alterations result in sustained mitogenic effector signaling and persist to promote proliferation.

Network rewiring of therapy-resistant melanoma

The transcriptomic profiles revealed a network of genes involved in adenylate cyclase signaling conferring resistance and contributing to melanogenesis. ADCY1 and CREB3 are prominent members of the melanogenesis pathway exhibiting mitogenic control and MITF activation. Similarly, a gain-of-function screen confirmed a cyclic-AMP-dependent melanocytic signaling network including G-protein-coupled receptors, adenylate cyclase, protein kinase cAMP-activated catalytic subunit alpha (PRKACA, Gene ID: 5566), and cAMP responsive element binding protein 1 (CREB1, Gene ID: 1385) [41]. The MAPK pathway negatively regulates MITF protein level as well as activity [29], which in turn regulates a series of cell cycle regulating genes. In particular, P16INK4A and P21CIP1, gene products of cyclin dependent kinase inhibitor 2A (CDKN2A, Gene ID: 1029) and cyclin dependent kinase inhibitor 1A (CDKN1A, Gene ID: 1026), respectively, differentiation genes TYR, DCT, TYRP1 as well as survival genes B-cell lymphoma 2 apoptosis regulator

(BCL2, Gene ID: 596) and BCL2 family apoptosis regulator (MCL1, Gene ID: 4170) are effector genes under the control of MITF. Indeed, inhibition of MITF increases sensitivity to chemotherapy drugs [42]. In contrast, upregulation of MITF in therapy-resistance may present itself as a survival mechanism, which coincides with upregulation of melanin, hence it may serve as prognostic biomarker for drug adaptation.

Dual specific phosphatases (DUSPs) act downstream of BRAF on phosphorylated MAPK members to provide attenuation of signal. Loss of DUSP activity results in constitutive activation of the pathway. Prominent members of this family DUSP1 and DUSP2 are consistently downregulated at the transcriptional level. In prior clinical studies, somatic mutation of DUSP4 in MAPKi-R has been reported [39]. Although in that case a genomic mechanism of resistance was utilized, the outcome of reduced DUSP activity by genomic or transcriptomic changes is equivalent and leads to persistent triggering of MAPK effectors.

Metabolic support of therapy resistance

Metabolic genes support the rewiring of acquired resistance and have been shown to play an intricate role in the malignancy of skin cutaneous tissues. Glutamine and glucose metabolism showed sensitivity to combinations of MAPKi and metabolic inhibitors in preclinical studies [43]. The transcriptomic profiles identified key enzymes in related, branching glycolytic pathways of serine, folate and pyrimidine metabolism. A cancer systems biology analysis of skin cutaneous melanoma brought forward a new master regulator and diagnostic target in cancer metabolism. Somatic mutations of DPYD have the ability to reconfigure and activate pyrimidine metabolism promoting rapid cellular proliferation and metastatic progression [44].

Concertation of transcriptional regulators

The forkhead box family of transcription factors is an important downstream target of the MAPK pathway and is currently being considered as a new therapeutic target in cancer, including melanoma therapy [45]. In epithelial cells, these transcriptional factors are directly involved in the expression of cyclin dependent kinase inhibitors and CDKN2A gene under the control of TGFβ [46, 47]. Both downregulation of anti-apoptotic targets as well as activation of proliferative metabolism have been observed as mechanisms contributing to MAPKi-R. Downregulation of FOXF2 has been shown to promote cancer progression, EMT, and metastatic invasion [48]. In contrast, a different member of the FOX family, the stem cell transcription factor forkhead box D3 (FOXD3) has been identified as an adaptive mediator of the response to MAPK pathway inhibition selectively in mutant BRAF melanomas [49, 50].

We have discovered non-genomic rewiring of pathways in chemotherapy resistance by RNA-Seq data and

validated gene targets in two cell lines by transcriptomics arrays. Perturbation of these resistance pathways by drug molecules, RNA interference, or genomic editing will corroborate the translational impact of identified gene targets. The established cell culture models of treatment resistance provide a broadly applicable platform to utilize high-throughput screening tools in the search for effective combinations of targeted therapies in cancer.

Conclusion

The MAPK pathway undergoes major rewiring at the transcriptional level while acquiring inhibitor resistance. The outcome of such transcriptional plasticity is dysregulation at the level of different upstream master regulators, while maintaining similar effector genes. Combination therapies including targeted approaches and immune checkpoint inhibition are promising and rapidly improving. For these therapies to show durable, progression-free success in the clinical setting, adaptation mechanisms of treatment resistance need to be understood. Cellular model systems in combination with transcriptome-wide analyses provide insight into how non-genomic drug adaptation is accomplished. Ongoing efforts are focused on utilizing the established preclinical models to overcome drug adaptation as well as precision medicine profiling of cancer patients. Over time, a better understanding of mechanisms involved in drug adaptation is likely to improve the effectiveness of melanoma therapy by delaying or controlling acquired resistance.

Additional file

Additional file 1: Table S1–S4 are compiled as supplementary information. Table S1: Oligonucleotides for RT-qPCR arrays. Table S2: Differentially expressed gene set based on RNA-Seq data. Table S3: Validated transcripts. Table S4: enrichment based on directional transcriptomic data. (XLSX 94 kb)

Abbreviations

BRAF: B-Raf proto-oncogene, serine/threonine kinase; BRAFi: BRAF inhibitor; BRAFi-R: BRAFi-resistant; cDNA: complementary DNA; CT: threshold cycle; DMSO: dimethyl sulfoxide; DUSPs: dual specific phosphatase; ECM: extracellular matrix; EMT: epithelial-mesenchymal transition; FOX: forkhead box; HIF: hypoxia-inducible factor; IC50: half maximal inhibitory concentration; LOG(FC): log-fold change; MAPK: mitogen activated protein kinase; MAPKi: MAPK inhibitor; MAPKi-R: MAPKi-resistant; MEKi: MEK inhibitor; XTT: 2,3-bis(2-methoxy-4-nitro-5-sulphophenyl)-2H-tetrazolium-5-carboxanilide; RNA-Seq: next generation mRNA transcriptome sequencing; RPKM: RNA-Seq single-end reads in reads per kilobase million; RT-qPCR: real-time quantitative polymerase chain reaction; STAT: signal transducer and activator of transcription

Acknowledgements

We would like to thank Angela Garcia, Charles Fagundes, Garja Suner, Sandeep Sanghera, Taran Kaur, Kirandeep Kaur, Keedrian Olmstead, Stephen Wilson, and Rohit Gupta for help with maintaining the cellular models of drug-resistant cancer cells.

Availability of preprint publication

The manuscript was made publically available to the scientific community [51] on the preprint server bioRxiv under doi: <https://doi.org/10.1101/231142> following submission March 1, 2017.

Funding

FVF is grateful for the support of grant CA154887 from the National Institutes of Health, National Cancer Institute. The research of the University of California Merced Systems Biology and Cancer Metabolism Laboratory is generously supported by University of California, Cancer Research Coordinating Committee CRN-17-427258, National Science Foundation, University of California Senate Graduate Research Council, and Health Science Research Institute program grants. FLS is supported by grant CA160756 from the National Institutes of Health, National Cancer Institute. FLM and FLS are in part supported by the Walmart and Oxnard Foundations and Aldrich Chair Endowment.

Authors' contributions

Conception and design: FLS, FVF. Establishing of cellular models, data acquisition, and analysis of data: HZ, DT, ZW, AF, PP, JL, SS, AS, AB, SYT, FLM, FLS, FVF. Preparation of figures, data analysis, interpretation, writing, review, and revision of the manuscript: FVF. Study supervision: FLS, FVF. All authors read and approved the final manuscript.

Ethics approval and consent to participate

All experimental protocols were approved by the Institutional Review Boards at the University of California Merced and Irvine. The study was carried out as part of IRB UCM13-0025 of the University of California Merced and as part of dbGap ID 5094 for study accession phs000178.v9.p8 on somatic mutations in cancer and conducted in accordance with the Helsinki Declaration of 1975.

Competing interests

There is no competing financial interest. FLM is co-Founder and Medical director of Cancer Prevention Pharmaceuticals with no direct implications on the conducted study on melanoma resistance.

Publisher's Note

Springer Nature remains neutral with regard to jurisdictional claims in published maps and institutional affiliations.

Author details

¹Systems Biology and Cancer Metabolism, Program for Quantitative Systems Biology, University of California Merced, 2500 North Lake Road, Merced, CA 95343, USA. ²Department of Medicine, School of Medicine, Chao Family Comprehensive Cancer Center, University of California Irvine, Irvine, CA 92697, USA. ³The State Key Laboratory of Medical Genetics and School of Life Sciences, Department of Molecular Biology, Central South University, Changsha 410078, China. ⁴Department of Epidemiology, School of Medicine, University of California, Irvine, CA 92697, USA.

Received: 29 October 2017 Accepted: 21 February 2018

Published online: 04 April 2018

References

- Davies H, Bignell GR, Cox C, Stephens P, Edkins S, Clegg S, et al. Mutations of the BRAF gene in human cancer. *Nature*. 2002;417(6892):949–54. <https://doi.org/10.1038/nature00766>.
- Pollock PM, Harper UL, Hansen KS, Yudt LM, Stark M, Robbins CM, et al. High frequency of BRAF mutations in nevi. *Nat Genet*. 2003;33(1):19–20. <https://doi.org/10.1038/ng1054>.
- Guan J, Gupta R, Filipp FV. Cancer systems biology of TCGA SKCM: efficient detection of genomic drivers in melanoma. *Sci Rep*. 2015;5:7857. <https://doi.org/10.1038/srep07857>.
- Tsai J, Lee JT, Wang W, Zhang J, Cho H, Mamo S, et al. Discovery of a selective inhibitor of oncogenic B-Raf kinase with potent antimelanoma activity. *Proc Natl Acad Sci U S A*. 2008;105(8):3041–6. <https://doi.org/10.1073/pnas.0711741105>.
- Chapman PB, Hauschild A, Robert C, Haanen JB, Ascierto P, Larkin J, et al. Improved survival with vemurafenib in melanoma with BRAF V600E mutation. *N Engl J Med*. 2011;364(26):2507–16. <https://doi.org/10.1056/NEJMoa1103782>.

6. Flaherty KT, Robert C, Hersey P, Nathan P, Garbe C, Milhem M, et al. Improved survival with MEK inhibition in BRAF-mutated melanoma. *N Engl J Med*. 2012;367(2):107–14. <https://doi.org/10.1056/NEJMoa1203421>.
7. Flaherty KT, Infante JR, Daud A, Gonzalez R, Kefford RF, Sosman J, et al. Combined BRAF and MEK inhibition in melanoma with BRAF V600 mutations. *N Engl J Med*. 2012;367(18):1694–703. <https://doi.org/10.1056/NEJMoa1210093>.
8. Robert C, Karaszewska B, Schachter J, Rutkowski P, Mackiewicz A, Stroiakovski D, et al. Improved overall survival in melanoma with combined dabrafenib and trametinib. *N Engl J Med*. 2015;372(1):30–9. <https://doi.org/10.1056/NEJMoa1412690>.
9. Long GV, Stroyakovskiy D, Gogas H, Levchenko E, de Braud F, Larkin J, et al. Combined BRAF and MEK inhibition versus BRAF inhibition alone in melanoma. *N Engl J Med*. 2014;371(20):1877–88. <https://doi.org/10.1056/NEJMoa1406037>.
10. Cheng Y, Zhang G, Li G. Targeting MAPK pathway in melanoma therapy. *Cancer Metastasis Rev*. 2013;32(3–4):567–84. <https://doi.org/10.1007/s10555-013-9433-9>.
11. Nazarian R, Shi H, Wang Q, Kong X, Koya RC, Lee H, et al. Melanomas acquire resistance to B-RAF(V600E) inhibition by RTK or N-RAS upregulation. *Nature*. 2010;468(7326):973–7. <https://doi.org/10.1038/nature09626>.
12. Wagle N, Emery C, Berger MF, Davis MJ, Sawyer A, Pochanard P, et al. Dissecting therapeutic resistance to RAF inhibition in melanoma by tumor genomic profiling. *J Clin Oncol*. 2011;29(22):3085–96. <https://doi.org/10.1200/JCO.2010.33.2312>.
13. Poulikakos PI, Persaud Y, Janakiraman M, Kong X, Ng C, Moriceau G, et al. RAF inhibitor resistance is mediated by dimerization of aberrantly spliced BRAF(V600E). *Nature*. 2011;480(7377):387–90. <https://doi.org/10.1038/nature10662>.
14. Van Allen EM, Wagle N, Sucker A, Treacy DJ, Johannessen CM, Goetz EM, et al. The genetic landscape of clinical resistance to RAF inhibition in metastatic melanoma. *Cancer Discov*. 2014;4(1):94–109. <https://doi.org/10.1158/2159-8290.CD-13-0617>.
15. Moriceau G, Hugo W, Hong A, Shi H, Kong X, Yu CC, et al. Tunable-combinatorial mechanisms of acquired resistance limit the efficacy of BRAF/MEK cotargeting but result in melanoma drug addiction. *Cancer Cell*. 2015;27(2):240–56. <https://doi.org/10.1016/j.ccell.2014.11.018>.
16. Hugo W, Shi H, Sun L, Piva M, Song C, Kong X, et al. Non-genomic and immune evolution of melanoma acquiring MAPK1 resistance. *Cell*. 2015;162(6):1271–85. <https://doi.org/10.1016/j.cell.2015.07.061>.
17. Emmons MF, Faiao-Flores F, Smalley KS. The role of phenotypic plasticity in the escape of cancer cells from targeted therapy. *Biochem Pharmacol*. 2016;122:1–9. <https://doi.org/10.1016/j.bjcp.2016.06.014>.
18. Lito P, Rosen N, Solit DB. Tumor adaptation and resistance to RAF inhibitors. *Nat Med*. 2013;19(11):1401–9. <https://doi.org/10.1038/nm.3392>.
19. Carey TE, Takahashi T, Resnick LA, Oettgen HF, Old LJ. Cell surface antigens of human malignant melanoma: mixed hemadsorption assays for humoral immunity to cultured autologous melanoma cells. *Proc Natl Acad Sci U S A*. 1976;73(9):3278–82.
20. Fogh J, Fogh JM, Orfeo T. One hundred and twenty-seven cultured human tumor cell lines producing tumors in nude mice. *J Natl Cancer Inst*. 1977;59(1):221–6.
21. Giard DJ, Aaronson SA, Todaro GJ, Arnstein P, Kersey JH, Dosik H, et al. In vitro cultivation of human tumors: establishment of cell lines derived from a series of solid tumors. *J Natl Cancer Inst*. 1973;51(5):1417–23.
22. Xing F, Persaud Y, Pratilas CA, Taylor BS, Janakiraman M, She QB, et al. Concurrent loss of the PTEN and RB1 tumor suppressors attenuates RAF dependence in melanomas harboring (V600E)BRAF. *Oncogene*. 2012;31(4):446–57. <https://doi.org/10.1038/onc.2011.250>.
23. Langmead B, Salzberg SL. Fast gapped-read alignment with bowtie 2. *Nat Methods*. 2012;9(4):357–9. <https://doi.org/10.1038/nmeth.1923>.
24. Trapnell C, Roberts A, Goff L, Pertea G, Kim D, Kelley DR, et al. Differential gene and transcript expression analysis of RNA-seq experiments with TopHat and cufflinks. *Nat Protoc*. 2012;7(3):562–78. <https://doi.org/10.1038/nprot.2012.016>.
25. Robinson MD, McCarthy DJ, Smyth GK. edgeR: a Bioconductor package for differential expression analysis of digital gene expression data. *Bioinformatics*. 2010;26(1):139–40. <https://doi.org/10.1093/bioinformatics/btp616>.
26. Mootha VK, Lindgren CM, Eriksson KF, Subramanian A, Sihag S, Lehar J, et al. PGC-1 α -responsive genes involved in oxidative phosphorylation are coordinately downregulated in human diabetes. *Nat Genet*. 2003;34(3):267–73. <https://doi.org/10.1038/ng1180>.
27. Subramanian A, Tamayo P, Mootha VK, Mukherjee S, Ebert BL, Gillette MA, et al. Gene set enrichment analysis: a knowledge-based approach for interpreting genome-wide expression profiles. *Proc Natl Acad Sci U S A*. 2005;102(43):15545–50. <https://doi.org/10.1073/pnas.0506580102>.
28. Friedmann PS, Gilchrist BA. Ultraviolet radiation directly induces pigment production by cultured human melanocytes. *J Cell Physiol*. 1987;133(1):88–94. <https://doi.org/10.1002/jcp.1041330111>.
29. Liu F, Singh A, Yang Z, Garcia A, Kong Y, Meyskens FL, Jr. MITF links Erk1/2 kinase and p21 CIP1/WAF1 activation after UVC radiation in normal human melanocytes and melanoma cells. *Mol Cancer* 2010; 9:214. doi:<https://doi.org/10.1186/1476-4598-9-214>.
30. Bradford MM. A rapid and sensitive method for the quantitation of microgram quantities of protein utilizing the principle of protein-dye binding. *Anal Biochem*. 1976;72:248–54. doi: S0003269776699996 [pii].
31. Sondergaard JN, Nazarian R, Wang Q, Guo D, Hsueh T, Mok S, et al. Differential sensitivity of melanoma cell lines with BRAFV600E mutation to the specific Raf inhibitor PLX4032. *J Transl Med*. 2010;8:39. <https://doi.org/10.1186/1479-5876-8-39>.
32. Filipp FV. Epioncogenes in cancer—identification of epigenomic and transcriptomic cooperation-networks by multi-omics integration of ChIP-Seq and RNA-Seq data. *Syst Biol. Meth Mol Biol*. 2019;1800:101–21.
33. Shain AH, Bastian BC. From melanocytes to melanomas. *Nat Rev Cancer*. 2016;16(6):345–58. <https://doi.org/10.1038/nrc.2016.37>.
34. Tiffen J, Wilson S, Gallagher SJ, Hersey P, Filipp FV. Somatic copy number amplification and Hyperactivating somatic mutations of EZH2 correlate with DNA methylation and drive epigenetic silencing of genes involved in tumor suppression and immune responses in melanoma. *Neoplasia*. 2016;18(2):121–32. <https://doi.org/10.1016/j.neo.2016.01.003>.
35. Lito P, Pratilas CA, Joseph EW, Tadi M, Halilovic E, Zubrowski M, et al. Relief of profound feedback inhibition of mitogenic signaling by RAF inhibitors attenuates their activity in BRAFV600E melanomas. *Cancer Cell*. 2012;22(5):668–82. <https://doi.org/10.1016/j.ccr.2012.10.009>.
36. Yao Z, Torres NM, Tao A, Gao Y, Luo L, Li Q, et al. BRAF mutants evade ERK-dependent feedback by different mechanisms that determine their sensitivity to pharmacologic inhibition. *Cancer Cell*. 2015;28(3):370–83. <https://doi.org/10.1016/j.ccell.2015.08.001>.
37. Wagle N, Van Allen EM, Treacy DJ, Frederick DT, Cooper ZA, Taylor-Weiner A, et al. MAP kinase pathway alterations in BRAF-mutant melanoma patients with acquired resistance to combined RAF/MEK inhibition. *Cancer Discov*. 2014;4(1):61–8. <https://doi.org/10.1158/2159-8290.CD-13-0631>.
38. Shi H, Hugo W, Kong X, Hong A, Koya RC, Moriceau G, et al. Acquired resistance and clonal evolution in melanoma during BRAF inhibitor therapy. *Cancer Discov*. 2014;4(1):80–93. <https://doi.org/10.1158/2159-8290.CD-13-0642>.
39. Johnson DB, Menzies AM, Zimmer L, Eroglu Z, Ye F, Zhao S, et al. Acquired BRAF inhibitor resistance: a multicenter meta-analysis of the spectrum and frequencies, clinical behaviour, and phenotypic associations of resistance mechanisms. *Eur J Cancer*. 2015;51(18):2792–9. <https://doi.org/10.1016/j.ejca.2015.08.022>.
40. Filipp FV. Precision medicine driven by cancer systems biology. *Cancer Metastasis Rev*. 2017;36(1):91–108. <https://doi.org/10.1007/s10555-017-9662-4>.
41. Johannessen CM, Johnson LA, Piccioni F, Townes A, Frederick DT, Donahue MK, et al. A melanocyte lineage program confers resistance to MAP kinase pathway inhibition. *Nature*. 2013;504(7478):138–42. <https://doi.org/10.1038/nature12688>.
42. Garraway LA, Widlund HR, Rubin MA, Getz G, Berger AJ, Ramaswamy S, et al. Integrative genomic analyses identify MITF as a lineage survival oncogene amplified in malignant melanoma. *Nature*. 2005;436(7047):117–22. <https://doi.org/10.1038/nature03664>.
43. Hernandez-Davies JE, Tran TQ, Reid MA, Rosales KR, Lowman XH, Pan M, et al. Vemurafenib resistance reprograms melanoma cells towards glutamine dependence. *J Transl Med*. 2015;13:210. <https://doi.org/10.1186/s12967-015-0581-2>.
44. Edwards L, Gupta R, Filipp FV. Hypermutation of DPYD deregulates pyrimidine metabolism and promotes malignant progression. *Mol Cancer Res*. 2016;14(2):196–206. <https://doi.org/10.1158/1541-7786.MCR-15-0403>.
45. Yang JY, Hung MC. A new fork for clinical application: targeting forkhead transcription factors in cancer. *Clin Cancer Res*. 2009;15(3):752–7. <https://doi.org/10.1158/1078-0432.CCR-08-0124>.

46. Gomis RR, Alarcon C, He W, Wang Q, Seoane J, Lash A, et al. A FoxO-Smad synexpression group in human keratinocytes. *Proc Natl Acad Sci U S A*. 2006;103(34):12747–52. <https://doi.org/10.1073/pnas.0605333103>.
47. Lasfar A, Cohen-Solal KA. Resistance to transforming growth factor beta-mediated tumor suppression in melanoma: are multiple mechanisms in place? *Carcinogenesis*. 2010;31(10):1710–7. <https://doi.org/10.1093/carcin/bgg155>.
48. Kong PZ, Li GM, Tian Y, Song B, Shi R. Decreased expression of FOXF2 as new predictor of poor prognosis in stage I non-small cell lung cancer. *Oncotarget*. 2016;7(34):55601–10. <https://doi.org/10.18632/oncotarget.10876>.
49. Abel EV, Aplin AE. FOXD3 is a mutant B-RAF-regulated inhibitor of G(1)-S progression in melanoma cells. *Cancer Res*. 2010;70(7):2891–900. <https://doi.org/10.1158/0008-5472.CAN-09-3139>.
50. Abel EV, Basile KJ, Kugel CH 3rd, Witkiewicz AK, Le K, Amaravadi RK, et al. Melanoma adapts to RAF/MEK inhibitors through FOXD3-mediated upregulation of ERBB3. *J Clin Invest*. 2013;123(5):2155–68. <https://doi.org/10.1172/JCI65780>.
51. Zecena H, Tveit D, Wang Z, Farhat A, Panchal P, Liu J, et al. Systems biology analysis of mitogen activated protein kinase inhibitor resistance in malignant melanoma bioRxiv; 2017. <https://doi.org/10.1101/231142>.

Submit your next manuscript to BioMed Central and we will help you at every step:

- We accept pre-submission inquiries
- Our selector tool helps you to find the most relevant journal
- We provide round the clock customer support
- Convenient online submission
- Thorough peer review
- Inclusion in PubMed and all major indexing services
- Maximum visibility for your research

Submit your manuscript at
www.biomedcentral.com/submit



Chapter 6

Increased glutaminolytic flux and activation of mitochondrial metabolism by BCL2 hyperactivity in lymphoma

6.1 Abstract

B-cell lymphoma 2 (BCL2) is an important apoptosis regulator during developmental and pathological states, and its overexpression is a key feature of several malignancies. Genomic data from The Cancer Genome Atlas (TCGA) reveals significant somatic copy number amplification, overexpression, and/or elevated protein activity of BCL2 in 50% of diffuse large B-cell lymphoma (DLBC) patients. While its canonical role in mitochondria-directed apoptosis is well established, the effect of BCL2 on transcriptional and metabolic networks remains elusive. Using an established lymphocytic pro-B-cell line overexpressing BCL2, we identified dysregulated transcriptional and metabolic networks by transcriptomic profiling arrays. Elevated BCL2 levels affect transcription factor complexes and mitogenic programs of NF- κ B / REL, HIF-1 α /ARNT, AP1, E2F, and STAT factors. Using stable isotope-assisted metabolic flux measurements we quantify

that elevated BCL2 expression increases carbon utilization boosting cellular proliferation. Tumorigenic overexpression of BCL2 significantly increases glycolytic flux, glutaminolysis, and anaplerotic flux into the TCA cycle. At the same time, the mitochondrial acetyl-CoA pool is separated from the glycolytic one by inactivating the pyruvate dehydrogenase complex via transcriptional regulation of pyruvate dehydrogenase kinase (PDK3). As compensatory fuel, mitochondrial TCA cycle metabolism is supported by asparagine synthase (ASNS) and oxidative glutaminolysis creating targets for small molecule inhibition of glutaminase. Lymphoma cells overexpressing BCL2 contained more mitochondrial mass and were more sensitive to L-glutamine deprivation and glutaminase inhibition. Cells overexpressing a mutant BCL2 G145E, which is incapable of binding BH domain members, failed to increase proliferation, glycolysis, or glutaminolysis. Taken together, the oncogene BCL2 has the ability to ramp up a metabolic phenotype supporting proliferation independent of its anti-apoptotic role. The cellular model of BCL2 activation supports NF- κ B-positive subtypes of DLBC and identifies metabolic bottlenecks with dependency on anaplerotic flux as an actionable BCL2 effector network in cancer.

6.2 Introduction

The B-cell lymphoma 2 (BCL2, Gene ID: 596) family of proteins are essential regulators of the intrinsic, mitochondrial pathway of apoptosis[1]. They are characterized by the presence of BCL2 homology (BH) domains which interact with one another to regulate essential cellular processes such as survival pathways, apoptotic initiation, cell cycle propagation, mitochondrial activity, or autophagy transitions [2]. Phylogenetically, members of the BCL2 family classifies as either pro- or anti-apoptotic BCL2 homologs, members with canonical BH domains, or those with non-canonical BH domains. Of the pro-apoptotic BH member the BCL2 associated X apoptosis regulator (BAX, Gene ID: 581) and BCL2 antagonist/killer 1 (BAK, Gene ID: 578) are interaction partners and direct effectors of mitochondrial outer membrane permeabilization (MOMP). In contrast, in case there is no interaction with pro-apoptotic BH members, BCL2 and BCL2 like 1 (BCL2L1, better known

as BCL-XL, Gene ID: 598) exert their anti-apoptotic effect through inhibitory interactions with pro-apoptotic members such as BAX.

BCL2 was first described as part of the t(14:18) chromosomal translocation event in B-cell follicular lymphoma [3], where it functioned to block apoptosis [4, 5]. The translocation of BCL2 to the Ig heavy chain locus in chromosome 14 drives its constitutive expression [6-8]. Subsequent studies demonstrated that BCL2 is overexpressed in several hematological cancers[9] and may support cancer cell survival through chemotherapeutic resistance [10] and regulation of autophagy [11, 12]. Clinically, trials of BCL2 inhibitors such as ABT-199 (venetoclax, PubChem CID: 49846579) have shown promise in the treatment of hematological cancers and immune diseases[13-16].

Cellular proliferation, including both physiologic lymphoid cell expansion and pathologic malignancy, requires a metabolic phenotype that supports macromolecular biosynthesis. Mitochondrial activity, electron redox transfer in the inner mitochondrial membrane, and oxidative phosphorylation play key roles in satisfying the energy demands of growing and dividing cells. Despite a growing understanding of the role of BCL2 in mitochondria-directed apoptosis, little is known about whether BCL2 regulates metabolism under non-apoptotic conditions.

Interleukin 3 (IL3, Gene ID: 3562) dependent FL5.12 pro-B cells derived from murine fetal liver [17] have served as a useful model for studying B-lymphocyte development [18], oncogenesis [19, 20], apoptosis [21, 22], and BCL2 binding events [23, 24]. Overexpression of BCL2 in these cell lines [25] leads to increased survival following IL3 deprivation, and increased tumorigenesis in vivo [20]. Using the FL5.12 cell line, and stably expressing BCL2 [20, 26] or a mutant of BCL2 unable to bind BH members [23, 27-30], we sought to quantify the transcriptional and metabolic phenotype of BCL2 overexpression using metabolic flux and proliferation assays.

6.3 Methods

6.3.1 Cell Culture

Lymphocytic FL5.12 pro-B-cell lines including a parental lymphocytic cell line with BCL2 wild type [17], a tumorigenic lymphoma cell line with BCL2 overexpression [25], and a BCL2(G145E) mutant with loss of binding of BH domain interaction partners [23] were cultured in minimal essential media (MEM, 15-010-CV, Corning, Corning, NY) supplemented with 10.0 % fetal bovine serum (FBS, 35-010-CV, Corning, Corning, NY), 1.0 % penicillin-streptomycin solution (PS, 30-002-CI, Corning, Corning, NY), 1.0 % MEM vitamins (MEM VIT, 25-020-CI, Corning, Corning, NY), 0.8 ng/mL of interleukin 3 (IL3, I4144, Sigma Merck, Darmstadt, Germany), 2.0 L of 2-mercaptoethanol (M6250-100ML, Sigma Merck, Darmstadt, Germany), 1.0 g/L D-glucose (GLC, G7021-1KG, Sigma Merck, Darmstadt, Germany), and 2.0 mM L-glutamine (GLN, 25-005-CI, Corning, Corning, NY) at 37 C (310 K) with 5.0 % carbon dioxide (CO₂, CD50, Praxair, Danbury, CT).

6.3.2 Cell size and proliferation analysis

Cell diameter and proliferation rates of normal and cancer cells were quantified by automated imaged-based cytometry. Cells in suspension were harvested and mixed 1:1 with a 0.4 % solution (w/v) trypan blue (25-900-CI, Corning, Corning, NY), and pipetted into disposable counting chambers (1450003, Bio-Rad, Hercules, CA) for counting and image analysis. Cell diameter and proliferation rates measurements of live cells in exponential growth were obtained in an automated tissue cell counter (TC20, 145-0102, Bio-Rad, Hercules, CA). Multi-planar bright-field digital images were automatically collected, quantified, and assessed for cell number and diameter. Cell proliferation rates were calculated and densities validated from the live cells per flask (N=6) over a 3-day time course of a proliferation assay experiment. Proliferation data based on different initial seeding densities was

LOG2 transformed to fit a linear regression model with an explained variation R2 above 0.970.

6.3.3 Flow cytometry and mitochondrial stains

Cells were analyzed for mitochondrial content, membrane potential, and matrix oxidant burden as previously described [31]. Cells were collected by centrifugation, counted, and aliquots corresponding to 500,000 cells were incubated protected from light with 200 nM MitoTracker green fluorescent mitochondrial stain (MTG, M7514, Life Technologies, Thermo Fisher Scientific, Carlsbad, CA), 13.3 nM tetramethylrhodamine ethyl ester (TMRE, T669, Life Technologies, Thermo Fisher Scientific, Carlsbad, CA), or 6.6 μ M MitoSOX red mitochondrial superoxide indicator (MitoSOX, M36008, Life Technologies, Thermo Fisher Scientific, Carlsbad, CA). Cells were collected, centrifuged, and resuspended in phosphate buffered saline (PBS, 46-013-CM, Corning, Corning, NY) supplemented with 2.0 % FBS twice before being analyzed on an LSR II flow cytometer (BD Biosciences, San Jose, CA) at a flow rate at least 500 events per second. 100,000 events per sample were recorded and samples were analyzed in triplicate (N=3) for each data point. FlowJo (V10, FlowJo, Ashland, OR) was used for data analysis.

6.3.4 Custom-designed gene expression profiling arrays for high-throughput RT-QPCR

We generated custom-designed profiling arrays to validate differential expression of metabolic genes and transcription factors in the in vitro lymphoma progression model of BCL2 activation. Total RNA was extracted from FL5.12 murine prolymphocyte B-cells using NucleoSpin RNA Plus Columns (740984.25, Macherey-Nagel, Dren, Germany). At least three biological replicates of RNA samples were analyzed per condition. The concentration of RNA was determined using a microvolume plate (Take3, BioTek, Winooski, VT) and a multi-mode microplate reader (Synergy HT, BioTek, Winooski, VT) multi-mode microplate reader (Synergy HT, BioTek, Winooski, VT). One microgram of RNA was used to synthesize

complementary DNA (cDNA) using qScript cDNA SuperMix (95048-500, Quanta Biosciences, Beverly, MA). cDNA corresponding to 1/5 of the first strand synthesis was mixed with 500 nM custom-designed forward and reverse primers (Sigma Genosys, The Woodlands, TX) and PerfeCTa SYBR Green FastMix (95072-05k, Quanta Biosciences, Beverly, MA) and analyzed on a high-throughput real-time (RT) quantitative polymerase chain reaction (QPCR) System (ECO, EC-101-1001R, Illumina, San Diego, CA). Custom-designed gene expression profiling arrays were analyzed using the CT method. RT-QPCR threshold cycle (CT) values were normalized using three different housekeeping genes (HKG), ribosomal protein S13 (RPS13, Gene ID: 6207), TATA box binding protein (TBP, Gene ID: 6908), and polymerase (RNA) II (DNA directed) polypeptide A (POLR2A, Gene ID: 5430). The difference threshold cycle value (CT) of any gene of interest (GOI) to the average housekeeping value was calculated using the formula $CT(GOI) = CT(GOI) - \text{AVERAGE}(CT(HKG))$ for each cell line. In addition, change in expression of any gene of interest was monitored by calculating $CT(GOI) = CT(GOI^{\text{CONDITION}}) - CT(GOI^{\text{WT}})$ with CONDITION being cell lines overexpressing BCL2 or BCL2(G145E) and WT the reference lymphocytic pro-B-cell line. RT2 gene array profiles were normalized, separated according to differential expression between conditions in univariate T-tests with a random variance model using a p-value cut-off below 5.00E-02, and ranked with LOG2 fold-change between specimens considered significant.

6.3.5 Somatic copy number alteration analysis

The tool GISTIC, genomic identification of significant targets in cancer, 2.0.21 [32-34] was used to identify genomic regions that are significantly gained or lost across a set of 48 paired normal and tumors samples of TCGA DLBCL data set. We executed GISTIC 2.0.21 on Agilent SNP 6.0 gene expression microarrays G4502A_07.01, UNC Chapel Hill, NC. GISTIC 2.0.21 distinguishes arm-level events from focal events at a broad length cutoff of 0.7. Events whose length was greater or less than 50% of the chromosome arm on which they resided were called arm-level or focal events, respectively, and these groups of events were analyzed

separately. The data was concordant to segmented level 3 data publicly available at the TCGA data portal. Since GISTIC 2.0.21 uses ratios of segmented tumor copy number data relative to normal samples as input, segmented level 3 data aligned to HG19 served as input for analysis runs. For significant loci and genes a cutoff p-value of 0.05 and q-value of 0.1 was applied, and concordance determined by overlaying whole-genome sequencing and SNP data. All experiments on SCNAs were carried out at a confidence level of 0.99.

6.3.6 Cell culture for metabolomics flux measurements

For metabolite quantification and stable isotope tracing, 100,000 cells were seeded in tissue culture flasks with vented caps (430639, Corning, Corning, NY) in N=6 replicate. For stable isotope D-glucose and L-glutamine labeling experiments, MEM media was supplemented with 1 g/L [U-¹³C₆] D-glucose ([U-¹³C₆] GLC, 389374-2G, Sigma Isotec, Miamisburg, OH) or 2 mM [U-¹³C₅] L-glutamine ([U-¹³C₅] GLN, 605166-500MG, Sigma Isotec, Miamisburg, OH). After 24 h, cell suspensions were transfer to microcentrifuge tubes (MT-0200-BC, Biotix, San Diego, CA) and centrifuged for 5 min at 277 K and 300 g in a refrigerated centrifuge (X1R Legend, Sorvall, Thermo Fisher Scientific, Waltham, MA) using a fixed-angle rotor (F21-48x1.5, Sorvall, Thermo Fisher Scientific, Waltham, MA). For exometabolome analysis, 40 μ L of supernatant containing condition media was transferred to microcentrifuge tubes and dried by vacuum centrifugation in a speedvac concentrator (DNA120OP115, Savant, Thermo Fisher Scientific, Waltham, MA) overnight. The remaining supernatant was aspirated and the cell pellets frozen in liquid nitrogen before storage at 193 K.

6.3.7 Metabolite Extraction

Frozen cell pellets were thawed on ice for 10 min before addition of 1 mL 253 K cold extraction solvent containing acetonitrile/isopropanol/water (3:3:2) acetonitrile (ACN, 34998-4L, Sigma Merck, Darmstadt, Germany), isopropanol (IPA, 34965-1L, Sigma Merck, Darmstadt, Germany), water (H₂O, 46-000-CI, Corning,

Corning, NY). Samples were then vortexed 5 times for 15 s and frozen on dry ice for 20 min and the freeze/thaw/vortex cycle repeated twice. Extracted cell suspension or media supernatants were dried via vacuum centrifugal evaporation and stored at 193 K before analysis. Dried, extracted cell pellets or media supernatants were derivatized by addition of 20 μL of 2.0 % methoxyamine-hydrochloride in pyridine (MOX, TS-45950, Thermo Fisher Scientific, Waltham, MA) followed by 90min incubation in a digital heating shaking drybath (8888-0027, Thermo Fisher Scientific, Waltham, MA) at 303 K and 1100 rpm. 90 μL of N-methyl-N-(trimethylsilyl)trifluoroacetamide (MSTFA, 394866-10X1ML, Sigma Merck, Darmstadt, Germany) was added and samples incubated at 310 K and 1100 rpm for 30 min before centrifugation for 5 min at 14,000 rpm and 277K. The supernatant was transferred to an autosampler vial (C4000LV3W, Thermo Fisher Scientific, Waltham, MA) with caps (C5000-53B, Thermo Fisher Scientific, Waltham, MA) for separation by gas chromatography (GC, TRACE 1310, Thermo Fisher Scientific, San Jose, CA) coupled to a triple-quadrupole GC mass spectrometry system (QQQ GCMS, TSQ8000EI, TSQ8140403, Thermo Fisher Scientific, San Jose, CA) for analysis.

6.3.8 GCMS for metabolomics

Samples were analyzed on a QQQ GCMS system equipped with a 0.25 mm inner diameter, 0.25 μm film thickness, 30 m length, low polarity phase, 5% diphenyl/95% dimethyl polysiloxane capillary column (TraceGOLD TG-5MS, 2609-1420 Thermo Scientific, Waltham, MA) and run under electron ionization at 70 eV. The GC was programmed with an injection temperature of 523 K and splitless injection volume of 1.0 μl . The GC oven temperature program started at 323 K for 1 min, rising to 573 K at 10 K/min with a final hold at this temperature for 6 min. The GC flow rate with helium carrier gas (HE, HE 5.0UHP, Praxair, Danbury, CT) was 1.2 mL/min. The transfer line temperature was set at 290 C (563 K) and ion source temperature at 295 568 K. A range of 50-600 mass over charge (m/z) was scanned with a scan time of 0.25s.

6.3.9 Metabolomics data processing

Metabolites were identified using metabolite retention times and fragmentation patterns in TraceFinder (v3.3, Thermo Fisher Scientific, Waltham, MA). Identified metabolites were quantified using the selected ion count peak area for specific mass ions, and standard curves generated from reference standards run in parallel. The mean, standard deviation, and 95.0 % confidence interval for each quantified metabolite was calculated for each cell line and treatment condition. A two-sample homoscedastic students t-test was used to compare treatment conditions of each metabolite and each cell line

6.3.10 ^{13}C stable isotope tracing and metabolic flux quantification

To quantify metabolic fluxes from substrates into metabolites, the mass isotope distribution vector (MDV) for known fragments of carbon backbone labeled amino acids and carboxylic acids was retrieved and ^{13}C tracer-to-tracee ratios were calculated [35-37]. GCMS MDV data from fractionally labeled [U- ^{13}C] D-glucose or L-glutamine samples was quantified to determine pool and isotopomer distribution of intracellular metabolites. Identified fragments contained either the whole carbon skeleton of the metabolite or resulted from a loss of the carboxyl carbon, or for some amino acids contained only the backbone minus the side-chain. For each fragment, mass ion counts were retrieved for the lightest isotopomer (M+0, without any heavy isotopes), and cumulative isotopomers for heavier mass counts with increasing mass units (M+1 up to M+6) relative to M0. Mass ion counts were normalized by dividing by the sum of M0 to M6, and corrected for the natural abundance of heavy isotopes of the elements H, N, O, Si, and C. By using probabilistic matrix-based multiplication one arrives at normalized MDVs corrected for naturally occurring isotopes in atoms of fragments of the metabolite backbone. ^{13}C -labeling data is expressed as fraction of the MDV and corresponds to stable isotope enrichment per carbon in a measured metabolite for a set of biological replicates with number of experiments N=6 for each condition. ^{13}C -

labeling data is converted into metabolic flux from carbon source by dividing by percent labeling of respective carbon source, 50 % [U-¹³C₆] of total 2.0 g/L D-glucose or 100 % [U-¹³C₅] of total 2.0 mM L-glutamine. A two-sample students t-test with a minimum significance level $\alpha=5.00E-02$ was used to compare average stable isotope enrichment per carbon of each metabolite between conditions.

6.3.11 L-glutamine deprivation and glutaminase inhibition

Cells were plated in white 96-well assay plates at a density of 10,000 cells/well in 100 μ L of media containing either no L-glutamine, 2.0 mM L-glutamine, or 2.0 mM L-glutamine with 1.0 mM selective glutaminase inhibitor bis-2-(5-phenylacetamido-1,3,4-thiadiazol-2-yl)ethyl sulfide (BPTES, SML0601, Sigma Merck, Darmstadt, Germany). After 24 h, cells were equilibrated at room temperature before being treated with 100 μ L/well of CellTiter-Glo luminescent cell viability assay (CTG, G7571, Promega, Madison, WI). Cells were then shaken for 2.0 min and incubated for 8 min protected from light before being analyzed in a multi-mode microplate reader (Synergy HT, BioTek, Winooski, VT)

6.4 Results

6.4.1 Somatic activation of BCL2 in lymphoma

In lymphoma, one of the most frequent somatic copy number alteration (SCNA) events is arm-level amplification of chromosome 18 with a recurrence frequency of 30 % in The Cancer Genome Atlas (TCGA) dataset (Figure 1A). In DLBC, significant arm-level SCNAs include: chr18pq, 30 %, 7.66E-04; chr7pq, 26 %, 4.57E-04; chr3pq, 23 %, 1.43E-02; chr11pq, 19 %, 1.43E-01; chr21q, 21 %, 1.08E-01; chr12q, 19 %, 2.83E-02; chr8q, 18 %, 1.75E-01; and chr1q, 13 %, 2.48E-01. These SCNA events enhance function of oncogenes and tumor suppressors in lymphoma (Figure 1A-B). Specifically, a sharply-defined focal region around chromosome band 18q21

(genome coordinates chr18:48582939-78077248) is significantly amplified with a q-value of 0.065049. Further, multi-omics integration reveals that BCL2 activation is often observed at multiple different levels including copy number, gene expression, and/or protein expression (Figure 1C). Elevated BCL2 activity has a negative effect on overall decreased patient survival (Figure 1C-D) [38-42].

Somatic BCL2 amplification shows significant co-occurrence with other oncogenic drivers observed in DLBC and highlights synergistic effects of structural somatic events in disease initiation and progression. Together with somatic amplification of BCL2 the following SCNA events are observed and constitute some of the most frequent and significant focal SCNA events in DLBC: deletion of cyclin dependent kinase inhibitor 2A and 2B (CDKN2A, Gene ID: 1029, CDKN2B, Gene ID: 1030, chr9p21); amplification of proto-oncogene and NF- κ B interaction partner REL (REL, REL proto-oncogene, NF- κ B subunit, Gene ID: 5966, chr2p16), B-cell CLL/lymphoma 11A (BCL11A, Gene ID: 53335, chr2p16), B-cell CLL/lymphoma 6 (BCL6, Gene ID: 604, chr3q27), non-receptor tyrosine kinase ABL proto-oncogene 2 (ABL2, Gene ID: 27, chr1q25) (Figure 1, Table 1). Taken together, genomic concertation and correlation of focal chromosome aberrations at the copy number level with focal BCL2 amplification emphasizes tissue-specific oncogenic driver pathways in lymphoma.

B-cell activation, selection, and maturation rely on apoptotic and pro-survival pathways mediated by BH domain proteins. BCL2 holds a tissue-specific gene expression program in the B-cell lineage and in lymphatic cancers. We therefore, sought to compare incidence of BCL2 activation in lymphomas with all other cancer tissues. Somatic activation of BCL2 is observed in less than 0.1 % of 10944 specimens across 37 pan-cancer tissues. There are two cases of gene fusions of BCL2 with a chromatin remodeler and a neural regulator: ATRX-BCL2 in lower grade glioma and NEDD4L-BCL2 fusion pair in breast cancer in combination with SCNAs activate the gene product. Therefore, across all cancers, DLBC stands out as cancer tissue with frequent arm-level amplification of chromosome 18 and distinct transcriptional activation of BCL2. In comparison to all other cancers, DLBC with a cohort size of 48 specimens is highly enriched for somatic amplification of chromosome 18. The detected DLBC cases represent about half

of all highly amplified focal amplification cases observed across more than 10,000 cancer specimens.

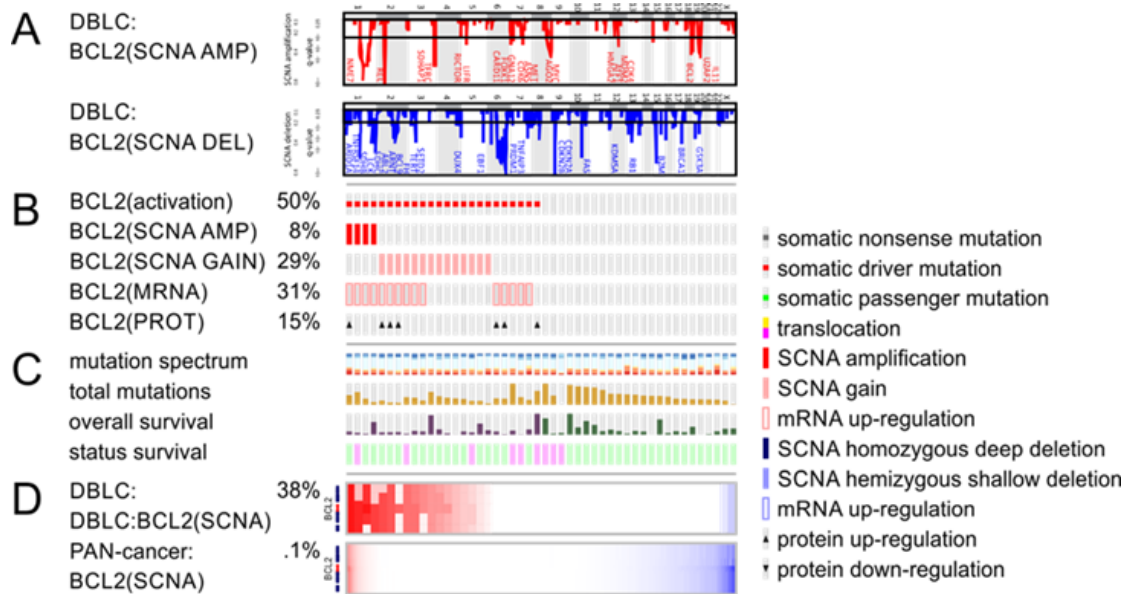


FIGURE 6.1: Frequent somatic copy number aberration of chromosome 18 in B-cell lymphoma results in amplification and somatic activation of BCL2. A) Landscape of somatic copy number aberrations (SCNAs) of diffuse large B-cell lymphoma (DLBC) with significant amplifications (red) and deletions (blue). B) Frequency and mechanism of somatic activation of B-cell lymphoma 2 (BCL2, Gene ID: 596) in DLBC. C) Mutation spectrum and impact of BCL2 activation on overall survival. D) Comparison of somatic aberrations of BCL2 in DLBC vs all cancer tissues (PAN-cancer) cohort in The Cancer Genome Atlas (TCGA)

6.4.2 Enrichment of inflammatory and metabolic pathways in specimens with BCL2 activation

In order to prioritize pathways affected by BCL2 activation, the DLBC patients were divided into two sub-cohorts: on the one hand, specimens were assigned to an unaltered sub-cohort with normal BCL2 status. On the other hand, a sub-cohort was defined with BCL2 activation based on somatic copy number amplification and differential expression of RNA-Seq V2 RSEM data. Using these two sub-cohorts, we queried whether activation of BCL2 resulted in enrichment of significantly deregulated transcripts and proteins. In protein arrays, BCL2

TABLE 6.1: Gene ontology and pathways enriched with BCL2 activation

NAME	FRAMEWORK	SIZE	NES	p-value	q-value
Regulation of amino acid process	GO	56	2.41	0.00E+00	1.20E-03
TCA cycle and respiratory chain	GO	114	2.12	0.00E+00	3.10E-03
Amine metabolic process	GO	85	1.82	0.00E+00	5.60E-02
Metabolism of amino acids	GO	136	1.69	0.00E+00	7.00E-02
Precursor metabolites and energy	GO	238	1.71	0.00E+00	8.80E-02
Cellular amide metabolic process	GO	594	1.46	1.20E-03	2.00E-01
Oxidative phosphorylation	KEGG	196	2.72	0.00E+00	0.00E+00
Epithelial mesenchymal transition	KEGG	173	2.69	0.00E+00	0.00E+00
Coagulation	KEGG	92	2.64	0.00E+00	0.00E+00
Interferon gamma response	KEGG	189	2.57	0.00E+00	0.00E+00
Interferon alpha response	KEGG	94	2.57	0.00E+00	0.00E+00
Complement	KEGG	163	2.52	0.00E+00	0.00E+00
Inflammatory response	KEGG	160	2.47	0.00E+00	0.00E+00
TNF γ signaling via NF κ B	KEGG	181	2.28	0.00E+00	0.00E+00
Allograft rejection	KEGG	175	2.15	0.00E+00	0.00E+00
IL2 STAT5 signaling	KEGG	183	2.02	0.00E+00	3.40E-04
Hypoxia	KEGG	166	1.9	0.00E+00	7.70E-04
Glycolysis	KEGG	170	1.91	0.00E+00	8.30E-04
Apoptosis	KEGG	148	1.86	0.00E+00	9.60E-04
TP53 pathway	KEGG	180	1.67	1.30E-03	5.90E-03
IL6 JAK STAT3 signaling	KEGG	73	1.63	4.60E-03	9.20E-03
Fatty acid metabolism	KEGG	132	1.55	7.20E-03	1.80E-02
Angiogenesis	KEGG	29	1.58	1.80E-02	1.40E-02
\$STAT5A	TF	174	1.73	0.00E+00	1.30E-02
\$NFKB1	TF	195	1.7	0.00E+00	1.40E-02
\$STAT5B	TF	148	1.67	0.00E+00	1.50E-02
\$E2F	TF	200	1.66	0.00E+00	1.60E-02
\$AP1	TF	170	1.64	1.40E-03	1.60E-02
\$HIF1A	TF	225	1.63	1.60E-03	6.60E-03
\$ARNT	TF	257	1.62	5.00E-03	1.50E-02
\$YY1	TF	206	1.61	2.70E-02	1.90E-02

overexpression was maintained at the protein level with a p-value of 3.77E-07 (Figure 2A). This is an important data point to validate, since the query cohort was selected exclusively based on genomic and transcriptional activation. One of the strongest activated proteins was the L-glutamine-hydrolyzing metabolic enzyme asparagine synthetase (ASNS, Gene ID: 440) (Figure 2B). Remarkably, focal SCNA amplification on chr7q21 of ASNS (Figure 1A) occurs in 29.2% of patients and coincides with SCNA of BCL2 with a p-value of 1.70E-02. In addition, a set of cycle genes was enriched including cyclin dependent kinase inhibitor 1B (CDKN1B, Gene ID: 1027), proliferating cell nuclear antigen (PCNA, Gene ID:

5111), cyclin B1 (CCNB1, Gene ID: 891), and cyclin E1 (CCNE1, Gene ID: 898) with a p-values below 1.00E-02 (Figure 2C-D). Cyclin dependent kinase inhibitor protein CDKN1B binds to and prevents the activation of cyclin E-CDK2 or cyclin D-CDK4 complexes. In the altered, BCL2-activated gene set, there was significant enrichment of metabolic pathways including amino acid processing, oxidative phosphorylation, hypoxic and glycolytic metabolism with p-values below 1.0E-10 (Table 1). Significantly enriched transcriptional networks included complexes of signal transducer and activator of transcription (STATs, specifically 3/5A/5B), nuclear factor kappa B (NF- κ B), NF- κ B subunit REL proto-oncogene (REL), JUN proto-oncogene/FOS proto-oncogene complex (AP1), yin yang (YY) transcription factor, hypoxia inducible factor (HIF), and aryl hydrocarbon receptor nuclear translocator (ARNT) transcription factor families with p-values below 2.0E-02. In addition, pathways in cancer, interferon response, inflammatory response, janus kinase (JAK)-STAT signaling, and the tumor protein p53 pathway (TP53, Gene ID: 7157) were enriched with p-values below 1.4E-03. The analysis indicates that BCL2 has the ability to activate a specific effector network impacting cell cycle, inflammation, and metabolism.

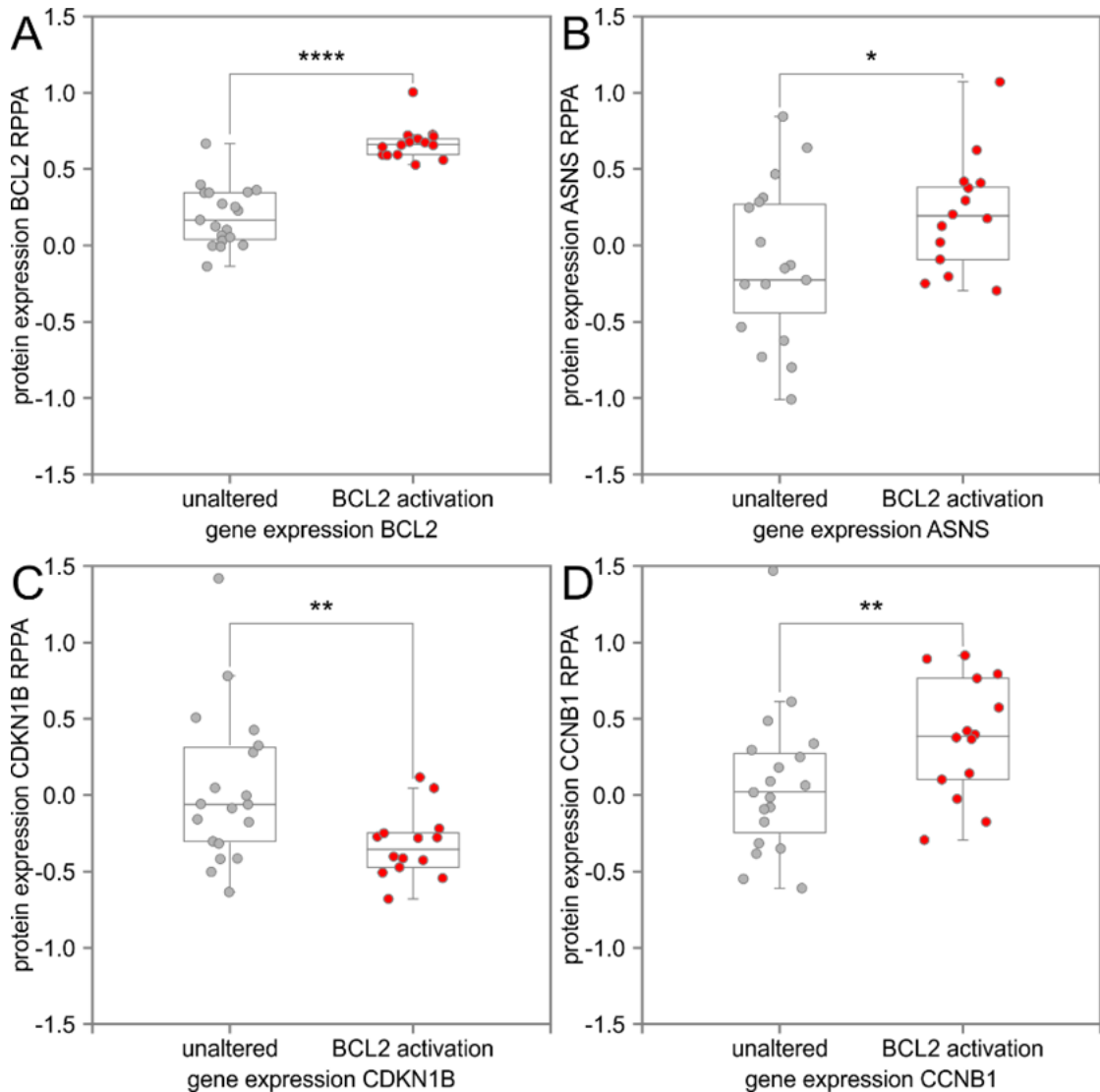


FIGURE 6.2: BCL2 activation significantly modulates metabolic and cell cycle regulators at the protein level. Protein expression level of lymphoma patients with unaltered BCL2 status was compared to patients with BCL2 activation. A) Specimens with BCL2 activation were selected based on altered somatic copy number or differential expression and had significantly higher BCL2 protein levels. B) asparagine synthetase (ASNS, Gene ID: 440) protein levels were elevated in lymphoma patients with genomic or transcriptomic BCL2 activation. C) The cyclin dependent kinase inhibitor 1B (CDKN1B, Gene ID: 1027) controls cell cycle progression and had lower median levels in patients with BCL2 activation. Degradation or loss of this protein is required for transition to a highly proliferative state. D) Cell cycle regulator cyclin B1 (CCNB1, Gene ID: 891) showed higher median protein levels with BCL2 activation. Analysis of protein expression levels was performed on reverse phase protein arrays (RPPA) of The Cancer Proteome Atlas (TCPA). Quartile box plots illustrate distribution following data normalization. Significance level of differential expression is indicated by asterisks according to p-value thresholds (* p-value $\leq 5.00E-02$, ** p-value $\leq 1.00E-02$, **** p-value $\leq 1.00E-04$)

6.4.3 Validation of dysregulated metabolic and transcriptional networks by transcriptomic profiling arrays

We utilized custom-designed gene expression profiling arrays based on identified genomic and transcriptomic alterations with BCL2-activation in DLBC. Differential gene expression analysis of the in vitro lymphoma progression model of BCL2 activation validated important regulatory molecules and control points of the metabolic and transcriptional machinery related to the oncogenic effector network of BCL2. We identified 28 transcripts of 75 tested target genes to be significant differentially expressed in response to BCL2 overexpression with p-values below 1.0E-05 (Figure 3). The differential gene expression analysis took into consideration: basal expression level and directionality of regulation highlighting transcription factors (Figure 4A) and functionally redundant metabolic isoenzymes (Figure 4B). For enhanced clarity, two-dimensional plotting of gene expression values of multiple conditions facilitates visual inspection of differential regulation (Figure 3), while bar graphs in direct comparison of conditions emphasize basal expression level and trends in directionality (staggered presentation of gene expression of pro-B-cell line overexpressing BCL2, pro-B control cell line, and BCL2(G145E) mutant) (Figure 4). For instance, the target gene ASNS has higher gene expression in the pro-B-cell line overexpressing BCL2 but lower expression in the BCL2(G145E) mutant. Its gene expression values are therefore plotted above and below the diagonal, respectively, against the pro-B control cell line (Figure 3A). The data indicates that ASNS expression is favored upon BCL2 overexpression but decreased if BH domain interactions are lost in the mutant. Many metabolic enzymes showed opposite directionality of regulation following BCL2 or BCL2(E145G) mutant overexpression including asparagine synthetase glutamine-hydrolyzing (ASNS, Gene ID: 440), hexokinase 2 (HK2, Gene ID: 3099), glucose-6-phosphate dehydrogenase (G6PD, Gene ID: 2539), transketolase (TKT, Gene ID: 7086), glyceraldehyde-3-phosphate dehydrogenase (GAPDH, Gene ID: 2597), glyceraldehyde-3-phosphate dehydrogenase, spermatogenic (GAPDHS, Gene ID: 26330), lactate dehydrogenase A (LDHA, Gene ID: 3939), and pyruvate dehydrogenase kinase 3 (PDK3, Gene ID: 5165) (Figure 3A, Figure 4B). HIF/ARNT and STAT transcription factor

recognition sites are common to this set of metabolic target genes. Regulators of the L-glutamine metabolite pool, ASNS, and pyruvate flux, PDK3, take pivotal roles standing out as strongest, most significantly regulated target genes (Figure 3A). In contrast, GCK, HK3, PFKM, PFKP, PDHA1, PDHB, and PDK1 were down-regulated following BCL2 overexpression (Figure 3B). Further, prominent transcription factors, RELA proto-oncogene (RELA, NF- κ B subunit, NFKB3, p65, Gene ID: 5970), nuclear factor kappa B subunit 1 (NFKB1, p105, p50, Gene ID: 4790), hypoxia inducible factor 1 alpha subunit (HIF1A, BHLHE78, Gene ID: 3091), aryl hydrocarbon receptor nuclear translocator (ARNT, Gene ID: 405), signal transducer and activator of transcription 5A (STAT5A, Gene ID: 6776), signal transducer and activator of transcription 5B (STAT5B, Gene ID: 6777), signal transducer and activator of transcription 6 (STAT6, Gene ID: 6778), and Jun proto-oncogene, AP1 transcription factor subunit (JUN, AP1, Gene ID: 3725), showed significant regulation in both test conditions (Figure 3A-C, Figure 4A). The *in vitro* analysis validated activation of heterodimeric transcription factor complex components NFKB1/REL, HIF1A/ARNT, AP1, E2F, and STAT5A/5B/6 with BCL2 activation in agreement with the genomic data (Table 1, Figure 4A). Gene ontology and pathway analysis pointed toward activation of amino acid metabolism, enhanced glycolysis, and TCA cycle with BCL2 activity. The profiling of metabolic enzymes validated this finding at the transcriptional level and showed up-regulation of key metabolic mediators of glycolysis, TCA cycle, and anaplerosis (Table 1, Figure 2B, Figure 4B).

6.4.4 BCL2 overexpression increases cellular proliferation and mitochondrial mass

To characterize the effect of BCL2 overexpression on the proliferation of lymphocytic and lymphoma cell lines automated, serial cell counts were obtained. BCL2 overexpression resulted in significantly higher growth rates ρ with p-values below 1.00E-04 compared to the parental and mutant BCL2-G145E cell lines (Figure 5A). Despite an initial plateau of the overexpressing cell line, it was possible to obtain fitted exponential maximum growth rates ρ^{\max} for all cell lines with an

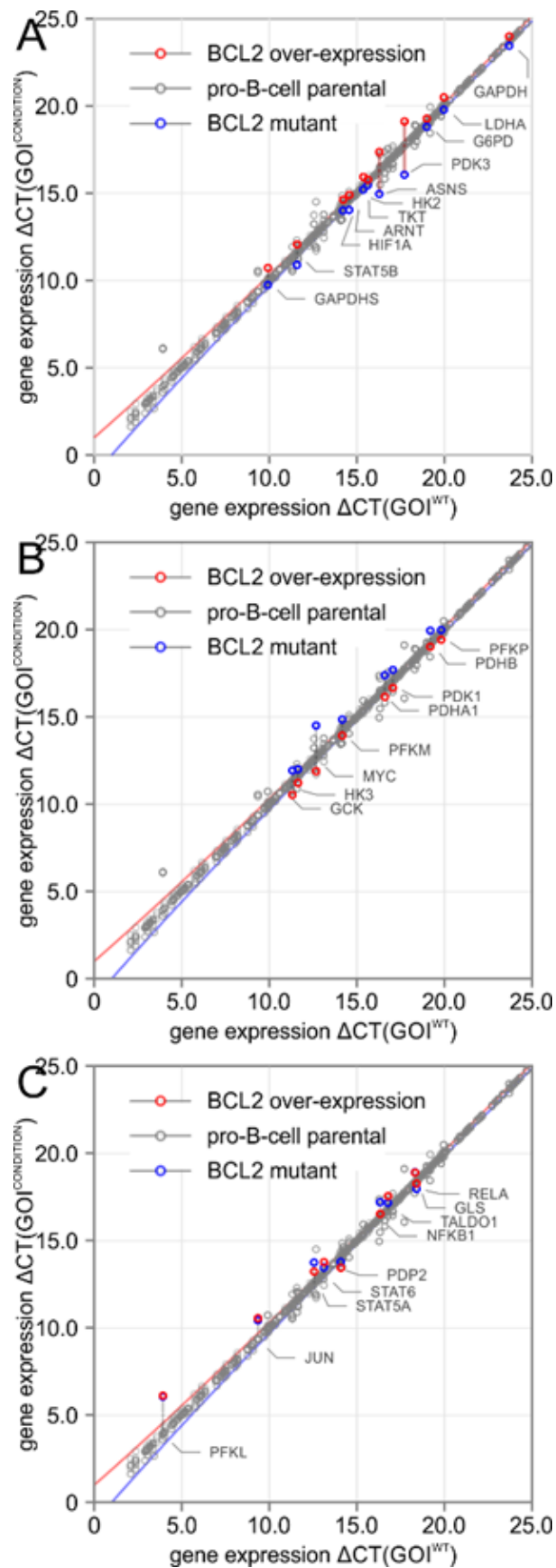


FIGURE 6.3: Real-time quantitative polymerase chain reaction (RT-QPCR) profiling arrays of central carbon metabolic enzymes and their regulators validate significant deregulation of mitochondrial metabolism at the gene expression level. Gene expression level of the gene of interest (GOI) is shown as negative threshold cycle (-CT) relative to the house keeping gene for the parental control (WT) in grey on x-axis, and cell lines overexpressing BCL2 in red, or BCL2(G145E) in blue on y-axis. In case, there is no change of expression level, the data point for the GOI will reside on the diagonal within 95.0 % confidence interval shown as solid lines. A) Differential expression of transcripts with significantly increased levels of GOI upon BCL2 overexpression but opposite directionality of levels of GOI in the BCL2 mutant. pyruvate dehydrogenase kinase 3 (PDK3, Gene ID: 5165) and asparagine synthetase (ASNS, Gene ID: 440) are two highly expressed and significantly dysregulated genes identified by the screen. PDK3 is a protein kinase that regulates and deactivates the pyruvate dehydrogenase complex by phosphorylation thereby shutting off flux from lower glycolysis into the TCA cycle. ASNS supports biosynthetic and anaplerotic flux in a L-glutamine-coupled reaction, which transfers an amide from L-glutamine to aspartate to generate asparagine. B) Differential expression of transcripts with decreased levels upon BCL2 overexpression and up-regulation in the BCL2 mutant. C) Differential expression upon BCL2 overexpression but no change of directionality in the BCL2 mutant.

explained variation R_2 above 0.970 of the regression model (Figure 5B). Notably, ρ can undergo dramatic changes up to 50% decrease depending on nutrient supply, cell density, and growth phase [43]. Maximum proliferation rates at exponential growth were $\rho^{\max}=9.59\text{E-}02 \pm 2.20\text{E-}03$, $R^2=9.73\text{E-}01$, $t_2^{\max}=10.4$ h for parental pro-B cell line, $\rho^{\max}=1.08\text{E-}01 \pm 3.24\text{E-}03$, $R^2=9.83\text{E-}01$, $t_2^{\max}=9.29$ h, 112.2% increase, p-value= $6.70\text{E-}03$ for BCL2 overexpression, and $\rho^{\max}=8.75\text{E-}02 \pm 4.93\text{E-}04$, $R^2=9.78\text{E-}01$, $t_2^{\max}=1.14\text{E+}01$, 10.7% decrease, p-value= $5.42\text{E-}03$ for the BCL2 mutant.

Additionally, cell diameter measurements indicate that BCL2 overexpressing cells were significantly smaller on average than were parental or mutant cells. Automated cell gating with thresholds between 8-10 μm and 12-14 μm showed smaller BCL2 overexpressing cells and larger BCL2 mutant cells than the parental cell lines with p-values below $1.00\text{E-}04$ (Figure 5C). Given the increased flux of D-glucose and L-glutamine into the TCA cycle, we next asked whether BCL2 overexpression affected mitochondrial dynamics more generally. Mitochondrial staining with MitoTracker green fluorescent mitochondrial stain (MTG) followed by flow cytometry

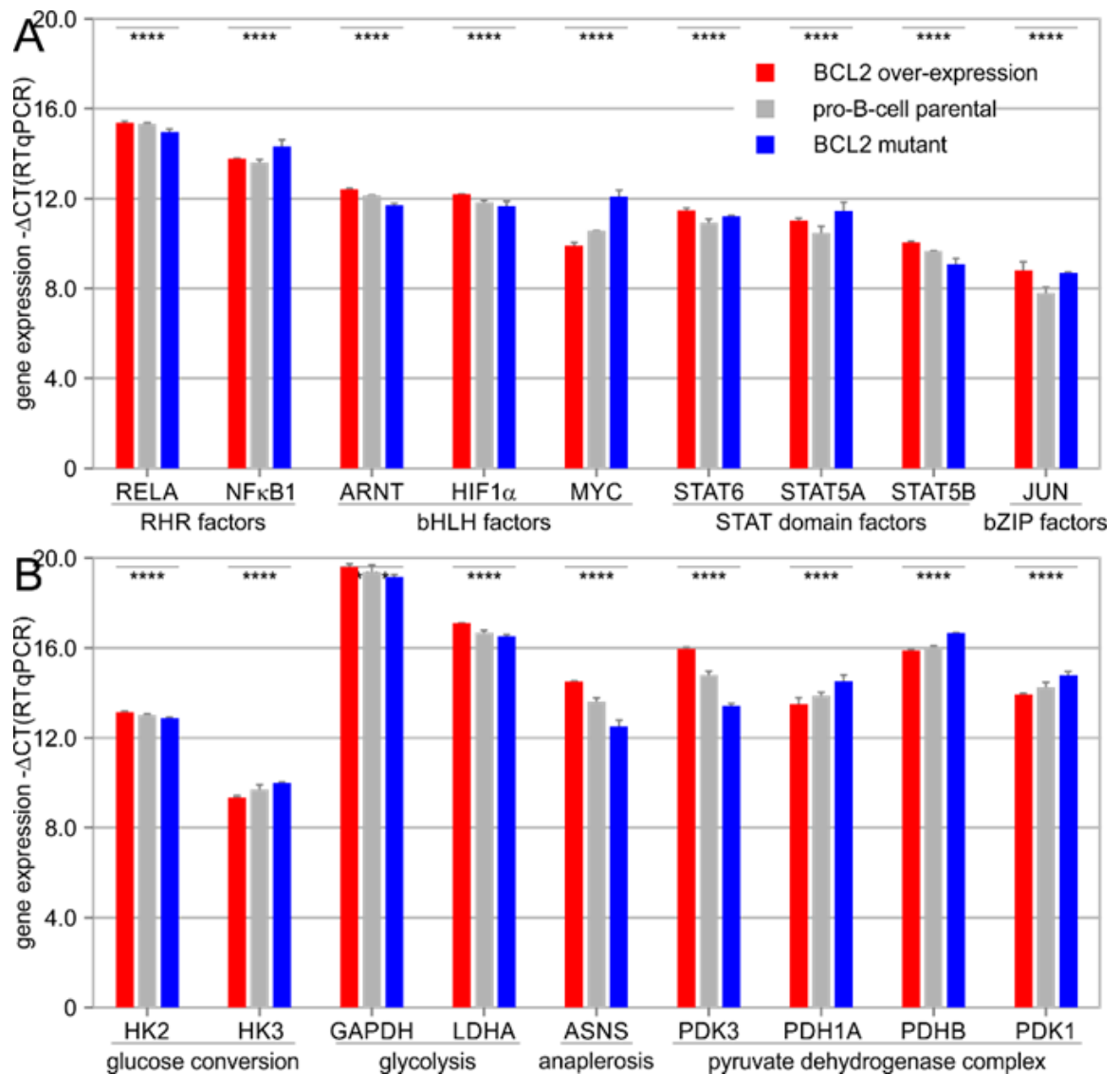


FIGURE 6.4: Elevated BCL2 expression causes differential expression of transcription factors and metabolic enzymes. Real-time quantitative polymerase chain reaction (RT-QPCR) validates significant deregulation of A) transcription factors and B) central carbon metabolic enzymes and their regulators. Gene expression level is shown as negative threshold cycle ($-\Delta CT$) quantified relative to the house keeping gene with significant differential expression marked by **** and p-values below $1.0E-05$.

revealed an increase in mitochondrial staining (Figure 6A). This is indicative of increased mitochondrial mass within BCL2 overexpressing cells, despite these cells being smaller (Figure 5C). Staining for mitochondrial membrane potential and superoxide generation by the mitochondrial superoxide indicator, MITOSOX fluorescein isothiocyanate, did not reveal any difference between BCL2-overexpressing lymphoma and the parental lymphocytic cell line (Figure 6B-C).

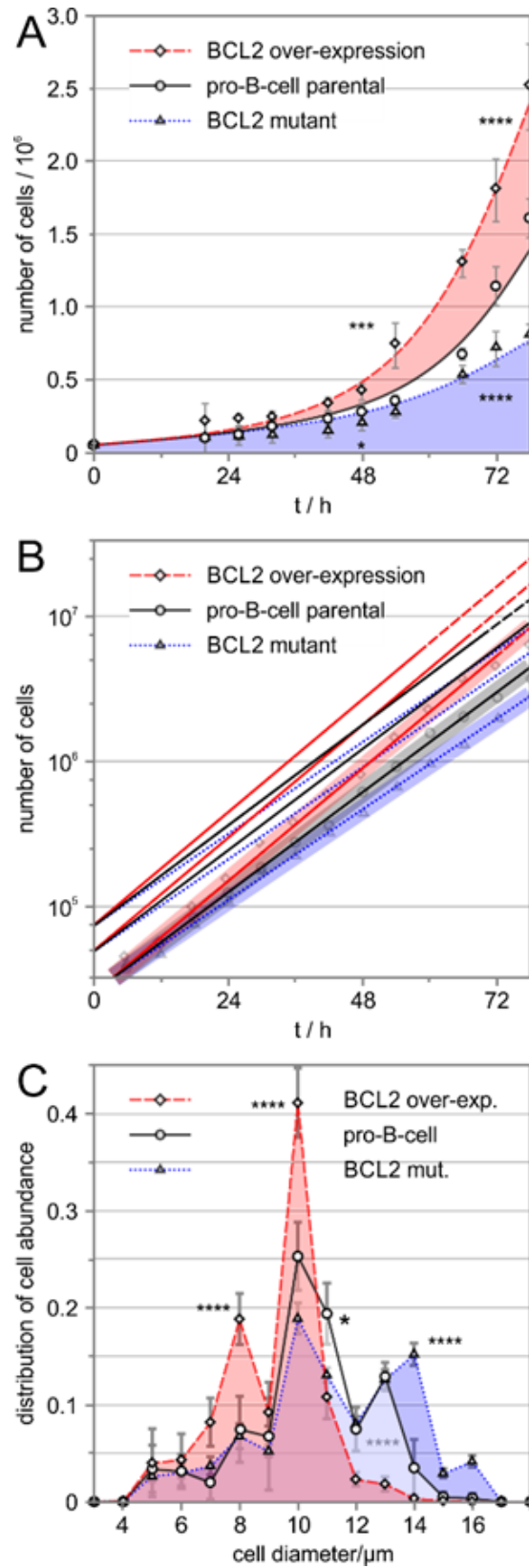


FIGURE 6.5: Elevated BCL2 expression significantly increases proliferation rate and decreases cell size. A) Proliferation rates of parental lymphocytic pro-B-cell lines and BCL2 overexpressing lymphoma cell lines were quantified using automated cell counting. BCL2 overexpression resulted in 12.2 % increased cellular proliferation, while expression of BCL2(G145E) mutant reduced cellular proliferation by 10.7 %. Significance levels are indicated with asterisks according to p-value thresholds (* p-value $\leq 5.00E-02$, ** p-value $\leq 1.00E-02$, *** p-value $\leq 1.00E-03$: **** p-value $\leq 1.00E-04$). B) BCL2 overexpressing lymphoma cell lines have a significantly higher fraction of cells with smaller cell diameters (8-10 μm) than parental lymphocytic pro-B-cell lines, while BCL2 mutant cells have a higher fraction of cells with larger cell diameters (14-16 μm). Distribution of cell size is shown as fraction of observed cell counts for each measured cell diameter.

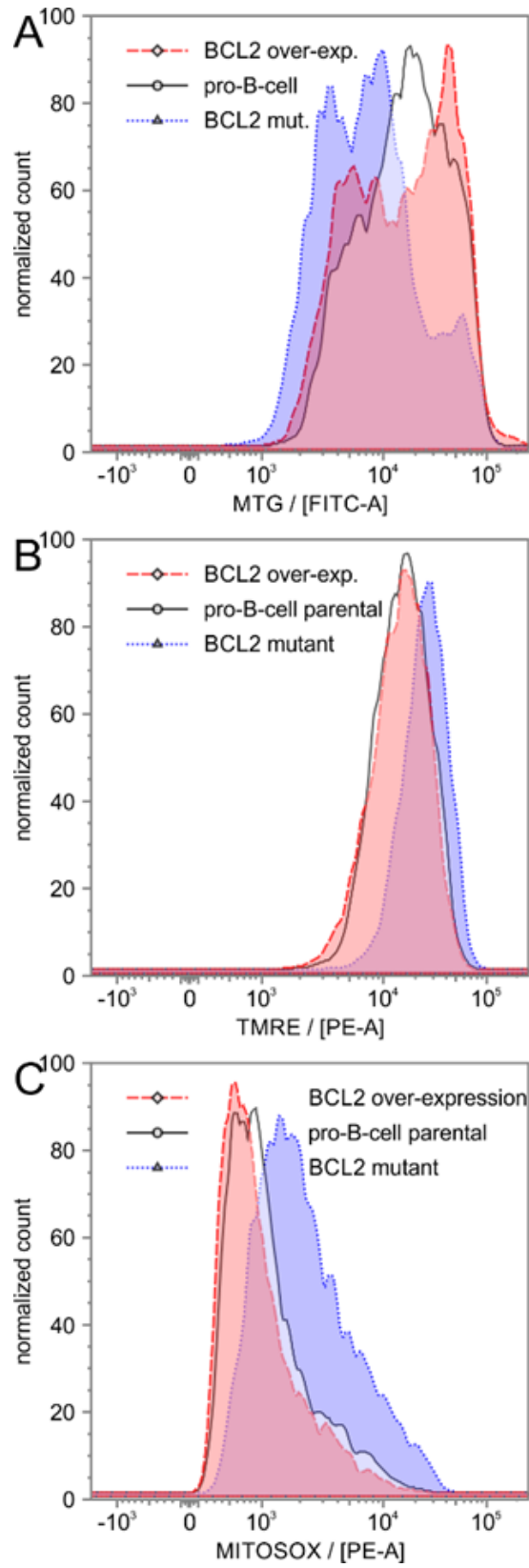


FIGURE 6.6: BCL2 overexpression increases mitochondrial mass Lymphoma and parental pro-B-cell lines were treated with fluorescent mitochondrial dyes to quantify mitochondrial size, mitochondrial membrane potential, and intracellular superoxide levels by flow cytometric cell scanning. Flow cytometric cell scanning plots show normalized cell counts of 100,000 events of lymphatic and lymphoma cell lines. Markers quantified: A) fluorescence of mitochondrial tracker green (MTG, correlates with mitochondrial size, green fluorescence), B) tetramethylrhodamine ethyl ester (TMRE, determines mitochondrial membrane potential, red fluorescence), and C) mitochondrial superoxide indicator (MITOSOX, fluorescein isothiocyanate (FITC) conjugate).

6.4.5 BCL2 overexpression increases glycolytic flux

Increased glycolysis is a hallmark of cancer cells and an important feature of physiological and pathologic lymphoid cell proliferation. To assess glycolytic flux in response to BCL overexpression we used GCMS-based stable isotope tracing. Following incubation with [U- $^{13}\text{C}_6$] D-glucose, the lymphoma cell line overexpressing BCL2 exhibited increased incorporation of labeled carbon in pyruvate and lactate compared to parental and mutant cell lines, indicating increased glycolytic and fermentative flux from D-glucose (Figures 7-8). Moreover, BCL2 overexpression displayed increased flux of glycolytic carbon into the TCA cycle. In accordance, analysis of conditioned media samples using GCMS revealed increased D-glucose uptake and lactate secretion by the BCL2 overexpressing cell 1

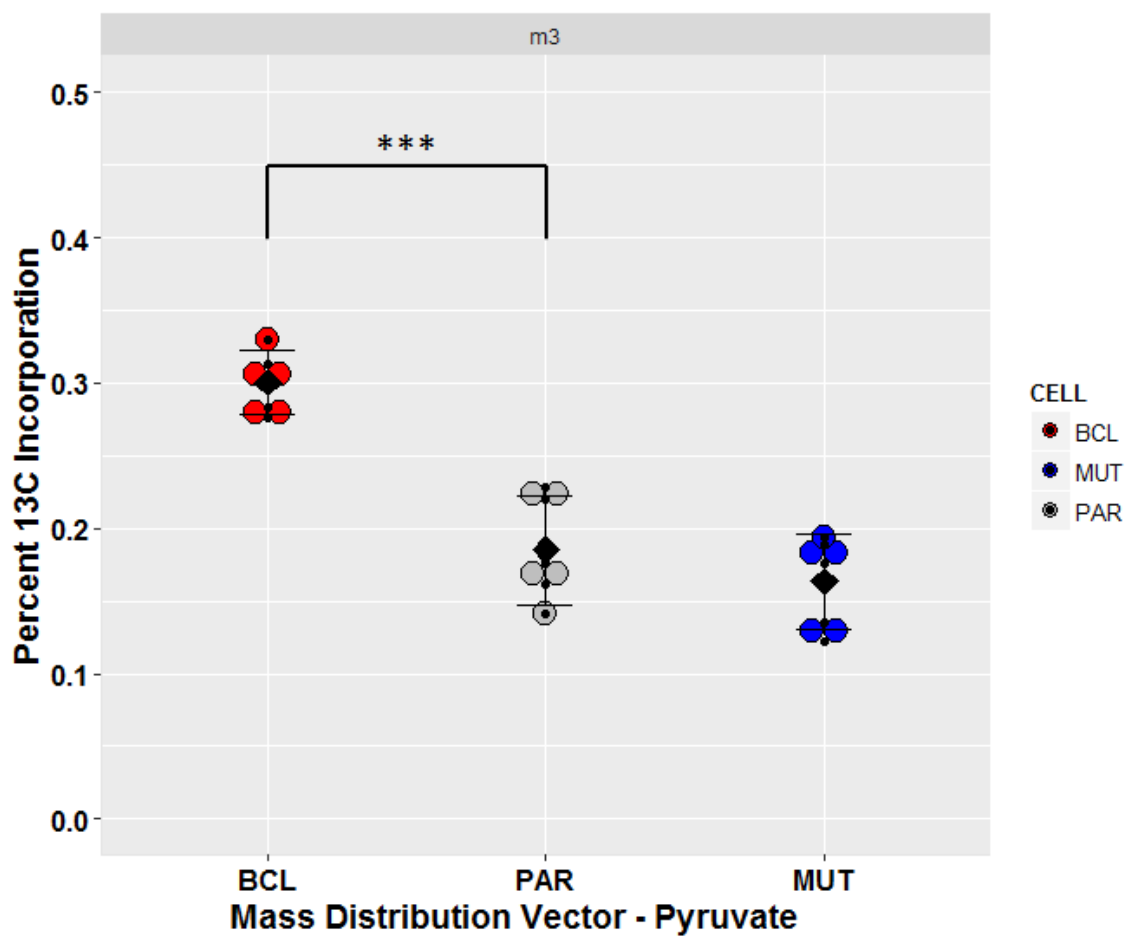


FIGURE 6.7: Stable isotope labeling shows an increased percentage of pyruvate containing Carbon-13 from labeled glucose. Significance level of differential incorporation is indicated by asterisks based on a p-value threshold of 1.00E-03

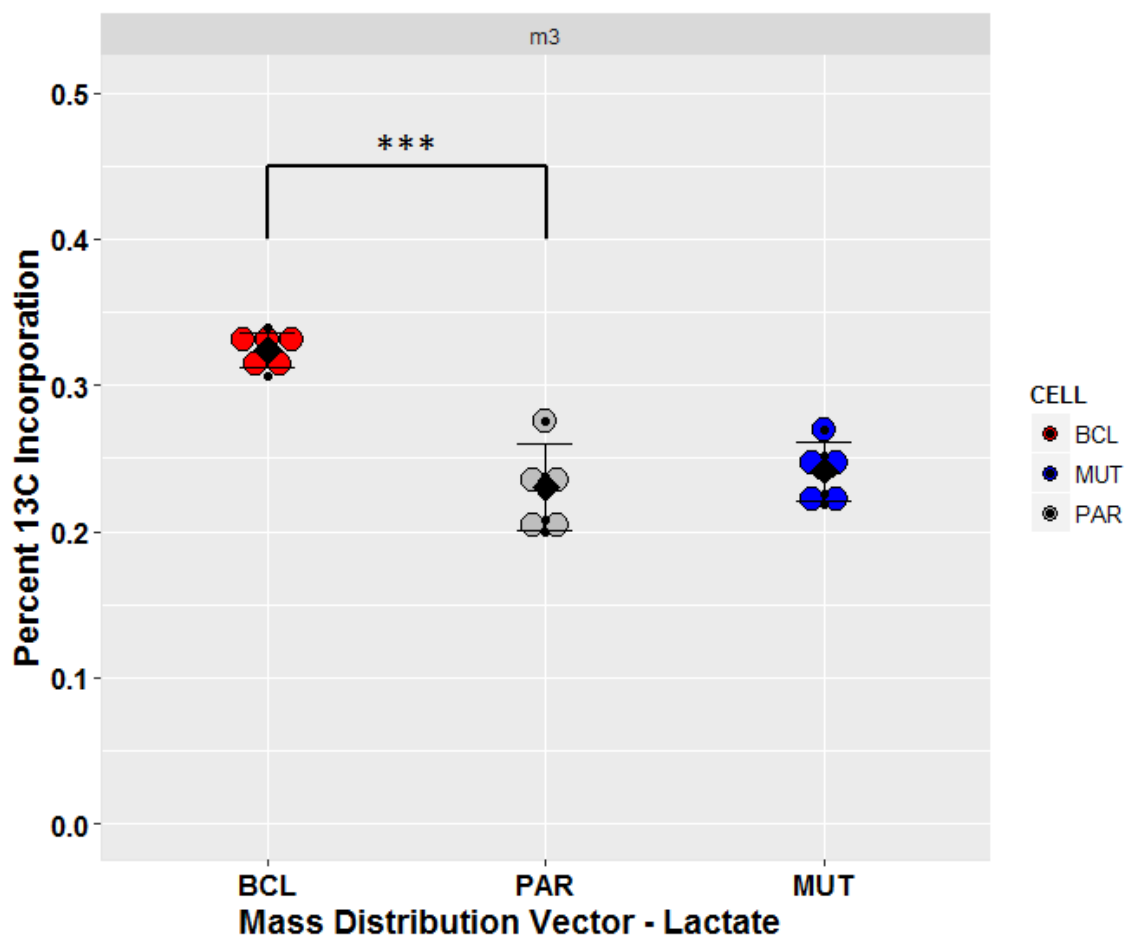


FIGURE 6.8: Stable isotope labeling shows an increased percentage of lactate containing Carbon-13 from labeled glucose. Significance level of differential incorporation is indicated by asterisks based on a p-value threshold of 1.00E-03

6.4.6 BCL2 increases glutaminolysis and anaplerotic flux into TCA cycle

A prominent feature of several malignancies is a dependency on anaplerotic flux to fuel TCA and reverse TCA fluxes [35, 44]. We therefore examined whether BCL2 overexpression increased glutaminolysis and L-glutamine influx into the TCA cycle. Following incubation with [U- $^{13}\text{C}_5$] L-glutamine, BCL2 overexpression had increased incorporation of ^{13}C stable isotopes into citrate, succinate, fumarate,

L-aspartate, L-asparagine, L-glutamate and other TCA cycle intermediates compared with parental and mutant cells. In detail, the isotope composition of citrate, succinate, fumarate, aspartate, and L-asparagine showed significant increase in the M+4 feature with a p-value below 5.00E-02 in the BCL2 overexpressing cell line indicating predominantly oxidative, forward flux of the TCA cycle (Figure 9). Other TCA cycle intermediates and TCA cycle associated amino acids including L-aspartate and L-asparagine track with four-carbon TCA cycle precursor organic acids characterized by reduced pool size and increased stable isotope incorporation from L-glutamine upon BCL2 overexpression. Cellular uptake of L-glutamine and glucose from extracellular media was also significantly greater in the BCL2 overexpressing cell line with p-values below 5.00E-02 (Figure 10-11). Given such increased utilization of extracellular L-glutamine, we next tested whether L-glutamine deprivation preferentially affected the BCL2 overexpressing cell line. Removing L-glutamine completely from extracellular media for a period of 24 hours abolished cellular growth of pro-B-cell and BCL2 overexpressing cell lines (Figure 12). In contrast, pro-B-cells with BCL2 mutant protein showed increased survival in the absence of L-glutamine with a p-value below 5.00E-02 (Figure 7F). Furthermore, treatment with the selective glutaminase (GLS, Gene ID: 2744) inhibitor BPTES over a period of 24 hours more adversely affected the BCL2 overexpressing lymphoma cell line in comparison to the non-tumorigenic lymphocytic cell lines with p-values below 5.00E-02 (Figure 13). Taken together, BCL2 activation in the overexpressing cell line showed increased glycolytic and TCA cycle capacity, while creating a strong dependency on TCA cycle support via glutaminolytic anaplerosis.

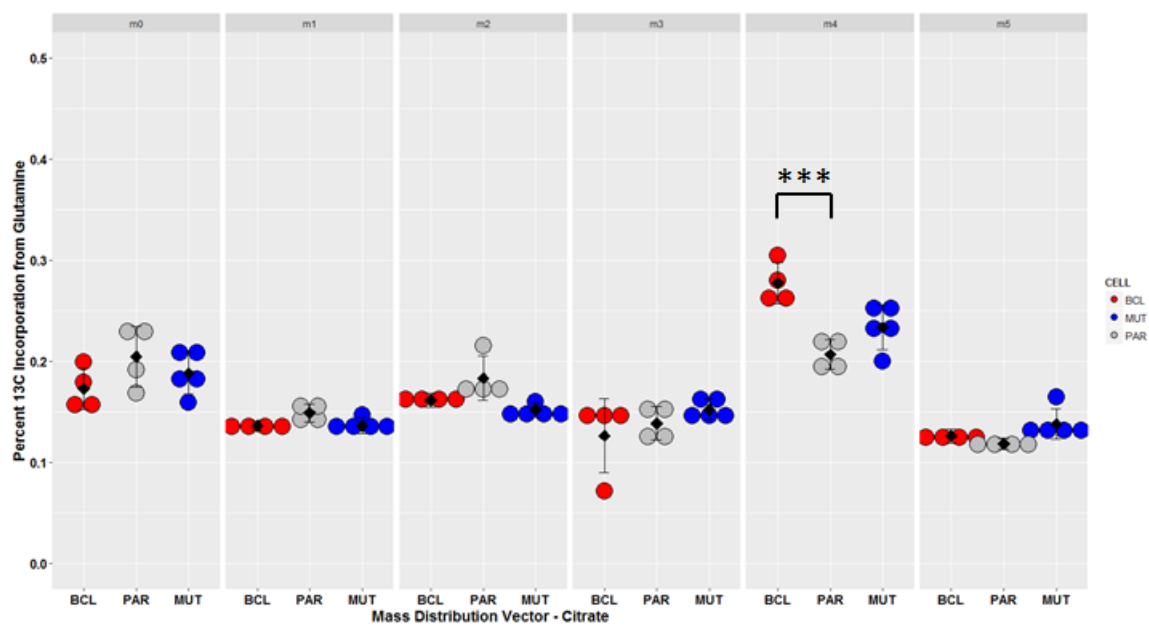


FIGURE 6.9: Stable isotope labeling shows an increased percentage of citrate containing Carbon-13 from labeled glutamine. Significance level of differential incorporation is indicated by asterisks based on a p-value threshold of 1.00E-03

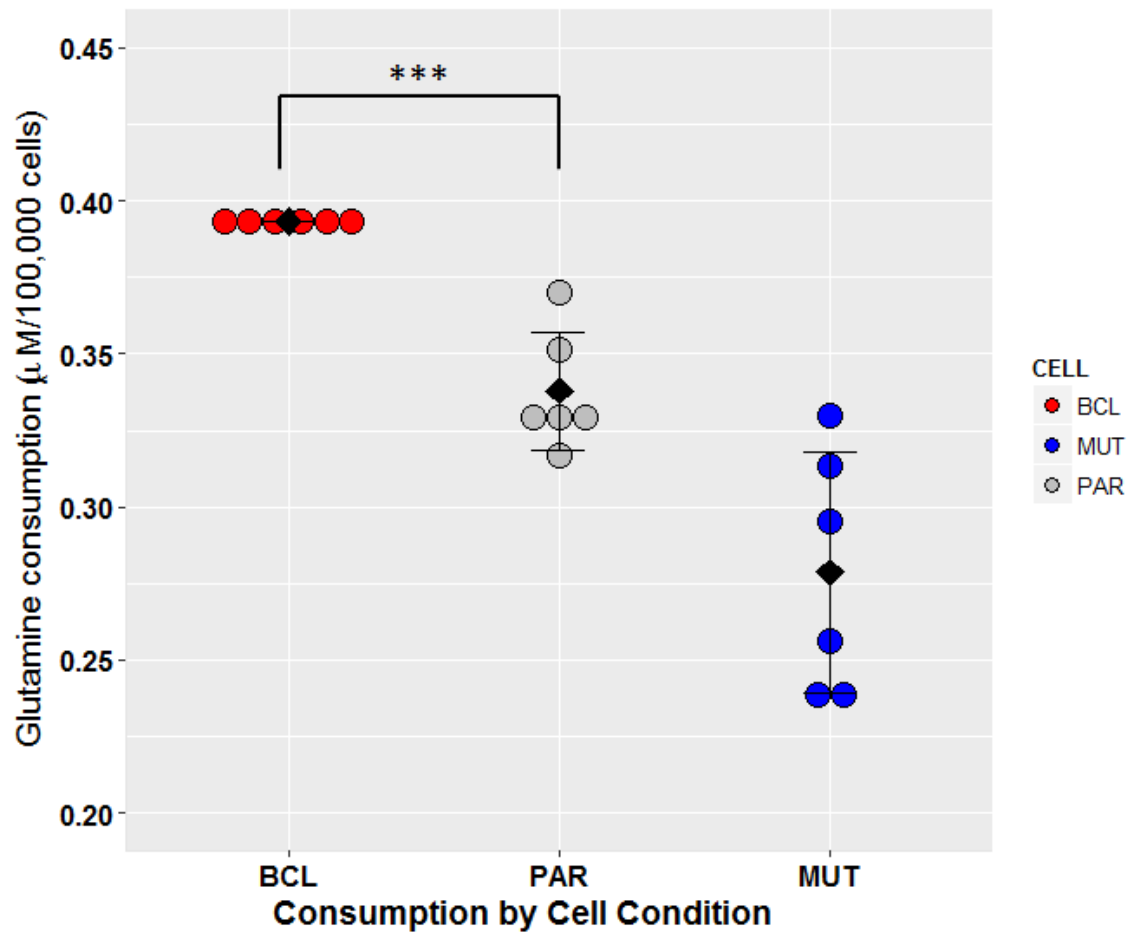


FIGURE 6.10: BCL mutant cells exhibit increased consumption of glutamine from extracellular media. Significance level of differential incorporation is indicated by asterisks based on a p-value threshold of 1.00E-03.

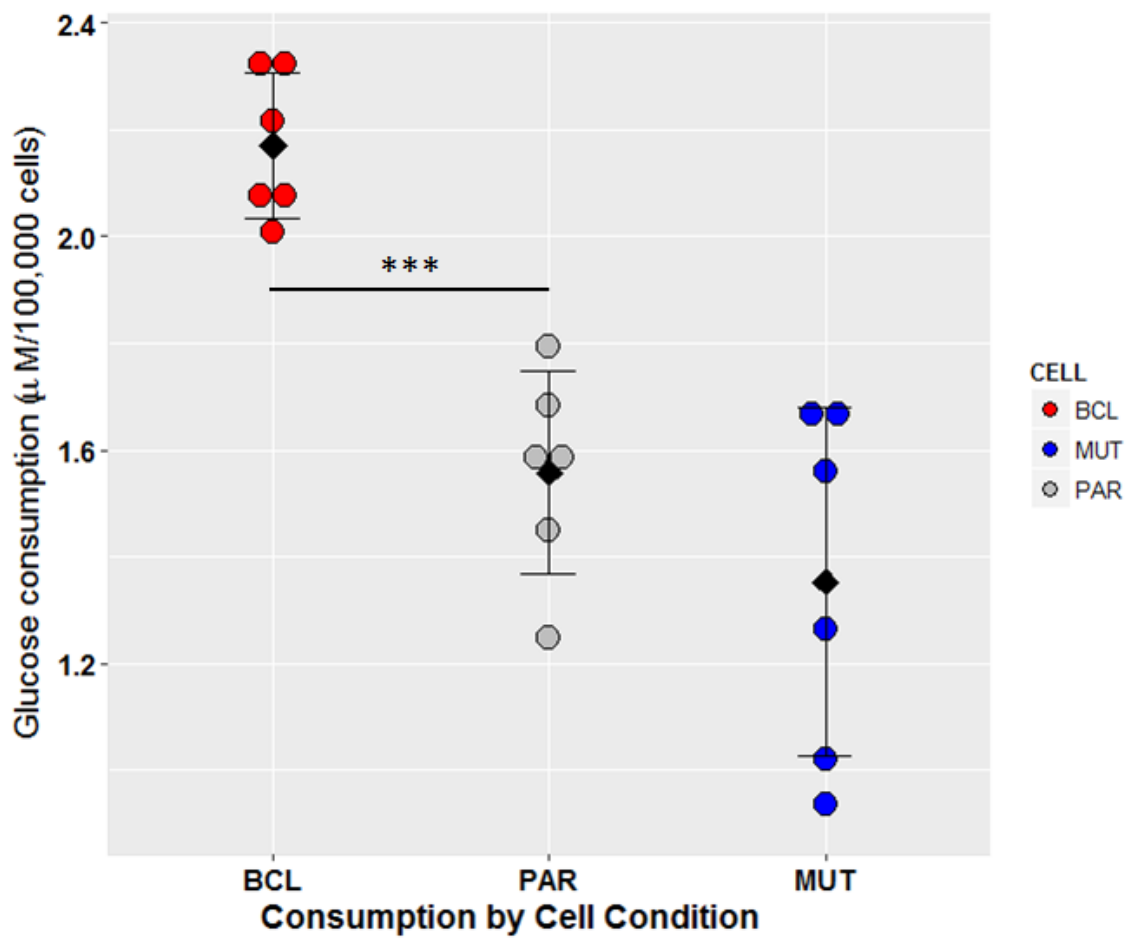


FIGURE 6.11: BCL mutant cells exhibit increased consumption of glucose from extracellular media. Significance level of differential incorporation is indicated by asterisks based on a p-value threshold of $1.00\text{E-}03$.

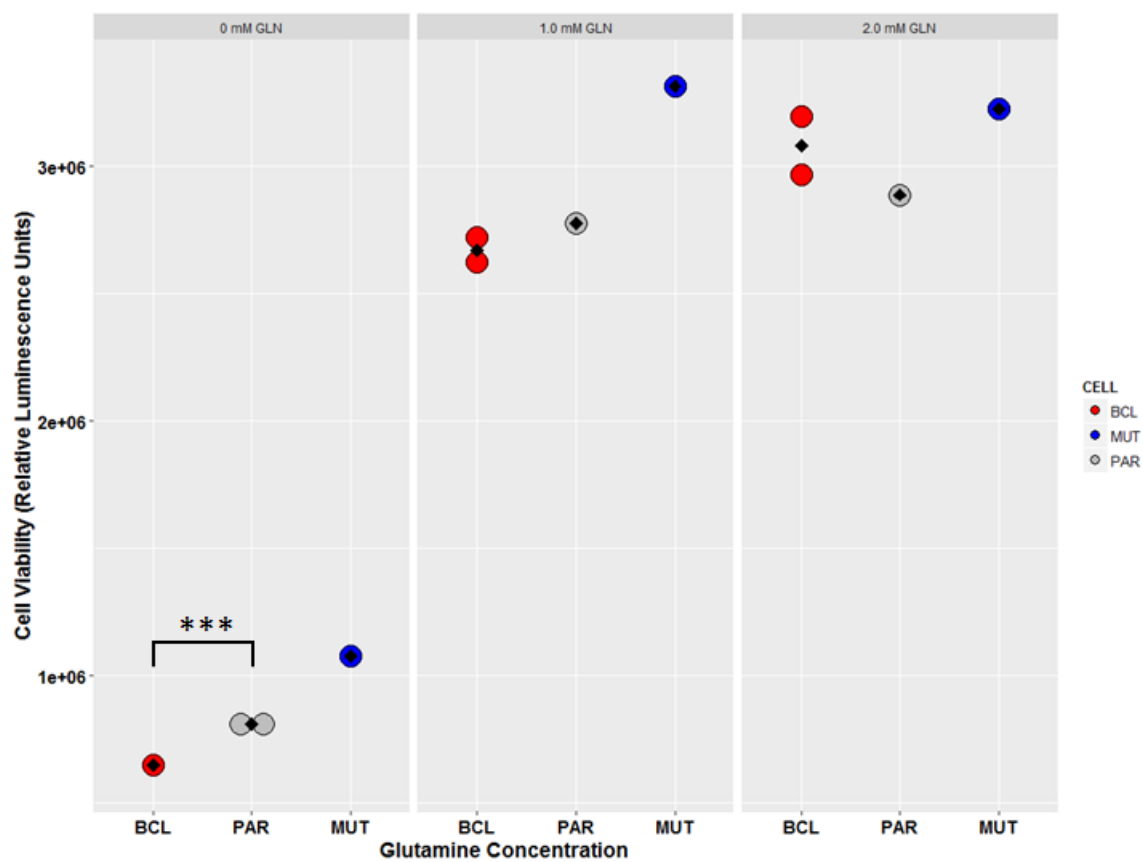


FIGURE 6.12: Relative cell viability measured in response to depleted glutamine levels. Significance level of differential viability is indicated by asterisks based on a p-value threshold of 1.00E-03.

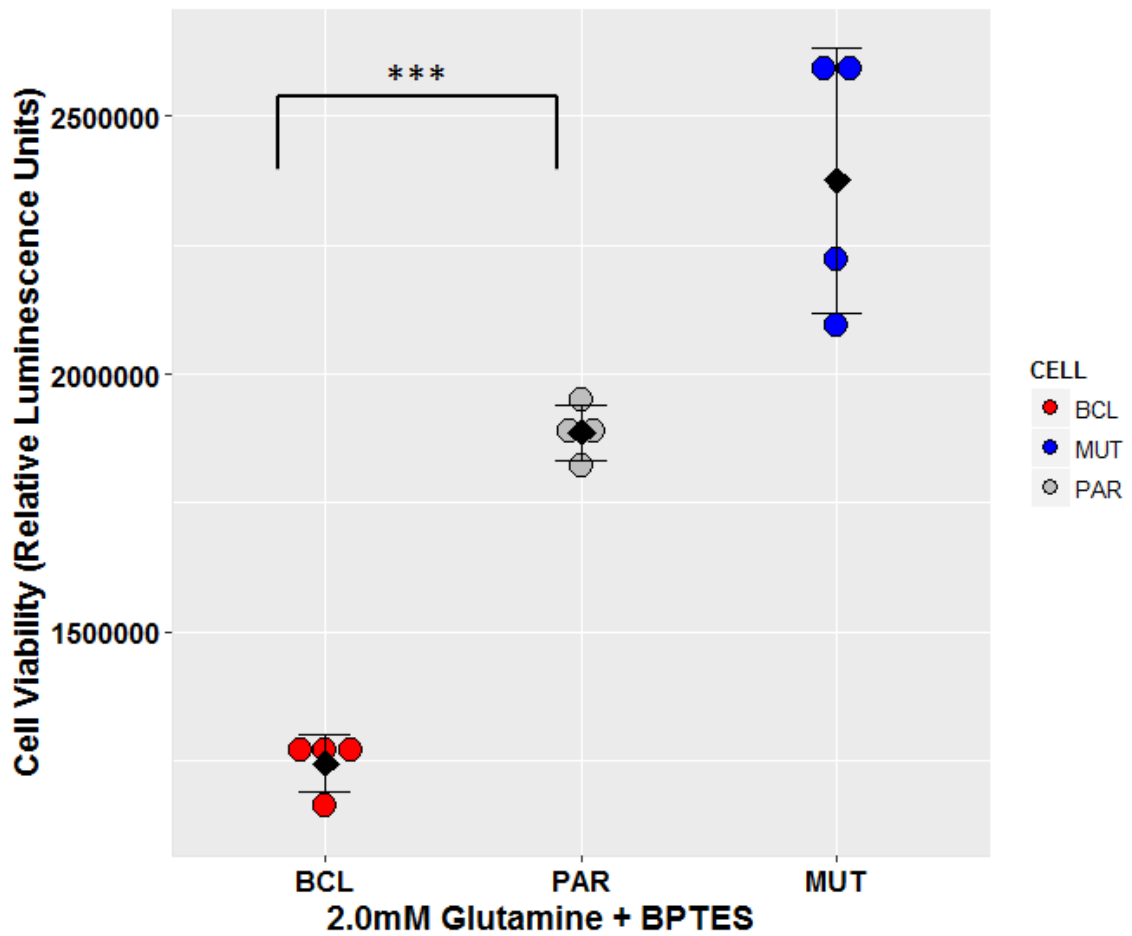


FIGURE 6.13: Relative cell viability measured in response to incubation with the glutaminase inhibitor BPTES. Significance level of differential viability is indicated by asterisks based on a p-value threshold of 1.00E-03.

6.5 Discussion

6.5.1 Pro-survival function of BCL2 beyond its anti-apoptotic role

Elevated expression of the proto-oncogene BCL2 is a key element discovered in hematological malignancies [9, 45, 46]. The B-cell lymphocytic lineage utilizes

programmed cell death as selection mechanism relying on BCL2 as deciding factor for survival or in its absence apoptosis. In response to BCL2 overexpression, pro-apoptotic BH members are bound by BCL2 preventing initiation of outer membrane permeabilization in the process of apoptotic cell death [47]. While this observation accounts for the protective, anti-apoptotic effect of BCL2, it does not explain other aspects of BCL2 activity particularly in cancer. In malignant melanoma, myeloma, lung adenocarcinoma and stomach adenocarcinoma, overexpression of BCL2 is associated with oncogenesis and poor outcome [49-52]. Overexpression of BCL2 in pro-B lymphocytic cell lines exhibits resistance to mitochondrial apoptosis and induces lymphoma upon injection in mice [20, 25, 48]. Correspondingly, loss of the BCL2 gene in murine models leads to widespread apoptosis, hypopigmentation, and polycystic kidney disease pointing to an important homeostatic role [53]. Surprisingly, despite its fundamental role in apoptosis and cancer, there is little molecular or mechanistic data on the effects of BCL2 expression levels on transcriptional and metabolic networks.

6.5.2 Somatic activation of BCL2 by somatic copy number amplification

In cancer, increased levels of BCL2 have been observed at the transcriptional, epigenetic, or copy number level [45, 54-56]. Congruently, the t(14:18) chromosomal translocation causes constitutive overexpression of BCL2 by juxtaposing it to immunoglobulin heavy chain gene enhancer elements. Our somatic copy number analysis identified locus chr18q21 as a frequently amplified hotspot in both, focal and arm level, genomic alterations (Figure 1, Supplementary table 1). The analysis confirmed prior described correlations between BCL2 amplification and MYC amplification, which are associated with poor prognostic outcome [43, 57, 58]. Further, we detected co-occurrence between BCL2 and NF- κ B/REL signaling [57, 59]. Curiously, frequent, focal SCNA amplification of the metabolic enzyme ASNS on chr7q21 of DLBC patients coincides with amplification of BCL2 (Figure 1A). Together, these observations raise questions for functional implications of BCL2 amplification for transcriptional and metabolic regulatory networks.

6.5.3 BCL2 serves a pro-survival role by modulating and controlling genes required for apoptotic cell death

Most oncogenes, like BCL2, if they are not transcription factors themselves, are activators of transcriptional programs. Our analyses identified BCL2 overexpression as an activator of several highly regulated and inducible transcription factors, including NF- κ B subunits NFKB1/2 and REL/A/B, basic helix-loop-helix (BHLH) family members, HIF1A or MYC, AP1 factors, JUN and FOS, and STAT family members. Stimulation of these pathways, in turn, increases expression of target genes that are necessary for growth and protection from apoptosis. The anti-apoptotic potential of BCL2 has been demonstrated to be partially attributed to its complexing with various components of the NF- κ B complex in the nucleus, thereby modulating nuclear gene expression with a strong pro-inflammatory and oncogenic outcome [60, 61]. Since inducible transcription factors are activated by specific regulators, detection of unusually active transcription factors also points to upstream signal transduction pathways, potentially identifying therapeutic options for inhibition in BCL2-driven cancers. Our dataset contains three pieces of independent evidence at the genomic, transcriptomic and effector target gene level that NF- κ B/REL signaling is closely connected to the oncogenic, pro-survival function of BCL2.

6.5.4 The cellular model of BCL2 activation supports NFKB-positive subtypes of DLBC

In B-cell neoplasias, DLBCs represent a group of different subtypes including activated B cell-like (ABC), primary mediastinal center B cell-lymphoma (PMBL), and germinal center B cell-like (GCB) DLBC. BCL2 amplification and transcriptional activity were found in chr18q21 in ABC and PMBL [62]. One of the most important differences among the DLBC subgroups is the constitutive activity of the NF- κ B pathway in ABC and PMBL but not GCB DLBC. Significantly, of the three DLBC subtypes, only ABC and PMBL responded to inhibitors of the NF- κ B pathway, whereas GCB was impervious to these agents [62, 63]. In DLBC,

JAK-STAT signaling is a feature of the ABC DLBC subtype and triggered by autocrine production of interleukins under the control of NF- κ B/REL. STATs also stimulate NF- κ B target genes, which could be due to the ability of STATs to form a complex with the NF- κ B transcription factor complex [64]. This emerging evidence suggests that BCL2 and NF- κ B/REL positive DLBCs critically depend on sustained activity of the NF- κ B pathway, which, among others, is achieved through numerous distinct genomic and transcriptomic aberrations [60, 61]. In the BCL2 overexpression model, the BCL2-NF- κ B-STAT axis stood out as consistently altered at the genomic and transcriptional level emphasizing its role as important oncogenic driver pathway in lymphoma. Systems-level connections of transcriptional networks now enable us to propose target therapeutic intervention strategies that target oncogenic BCL2 signaling and dysregulated NF- κ B activity

6.5.5 Pleiotropic effects of BCL2 on transcription factors

RNA-Seq enrichment and RT-QPCR validation show activation of transcription factor programs of NF- κ B/REL, HIF1A/ARNT, AP1, and STAT complexes in the presence of elevated BCL2. In concordance, transcriptional profiling of cellular DLBC models, members of NF- κ B, HIF, CREB and other transcription factor families were found overexpressed or inappropriately activated [65]. The pro-B-cell lymphocytic lineage provides a useful model system independent of MYC activation. Overexpression of BCL2 in these cells was shown to suppress MYC, a target gene of NF κ B1, by influencing the DNA-binding activity of NF κ B1, thereby negatively affecting MYC transcription [60]. In this case, similar to our presented model system, NF κ B1 serves as upstream regulator of MYC and other transcription factors [59] and up-regulates MYC transcript levels in the absence of wildtype BCL2 expression (Figure 4A). Conversely, overabundance of BCL2 suppresses MYC. Independent of transcriptional regulation, there is genomic synergy between BCL2 and MYC at the copy number level (Supplementary table 1). Therefore, transcriptional control of MYC expression by BCL2 via NF κ B1 can be overridden by genomic alterations of MYC, which negatively impacts patient survival. An additive adverse patient survival effect of BCL2 activation

in combination with MYC or NFKB1 overexpression has been reported [66, 67] correlating with experiments on transgenic BCL2 and MYC animal models in lymphomagenesis [68, 69]. Despite poor prognosis, MYC rearrangements are rare in BCL2-enforced lymphomagenesis in humans. Importantly, BCL2 and NFKB1 correlate at genomic, transcriptional, and network levels in DLBC patients strengthening and supporting the in vitro data.

6.5.6 Reversal of the phenotype by BH interaction mutant of BCL2

Interactions of BCL2 with BH members regulate mitochondrial outer membrane permeabilization in the process of apoptotic cell death. In addition to canonical BH domains, structurally similar non-canonical BH domains can be found in numerous proteins, potentially making them responsive to overabundant BCL2. It is important to mention that the chosen approach of profiling in combination with enrichment analysis is not able to resolve protein-protein interactions. However, the approach prioritizes cellular networks in an unbiased way and identifies NF- κ B signaling, amino acid metabolism, and inflammation as important signatures of BCL2 associated dysregulation. Further, the BCL2(G145E) mutant, which is unable to bind BH3 domains, provides a useful control, since phenotypic differences between cell lines overexpressing BCL2 wildtype vs mutant, can be attributed to an inability to bind or interact with the BH3 domain of BCL2 [23]. Indeed, overexpression of mutant BCL2 reversed the cellular phenotype observed with wildtype BCL2 overexpression. This indicates that lack of BH domain interaction in the mutant reduces proliferation rate, increases cell size, and results in smaller mitochondria compared with wildtype BCL2 or control pro-B cell lines (Figure 5-6). Similarly, transcriptomic and metabolic assays point to phenotypic nodes, which are responsive to BCL2 overexpression and which can be reversed by the interaction mutant. Specifically, transcription factors RELA, ARNT, HIF1A, and STAT5B correlate positively with an increase in BCL2 expression and BH interactions (Figure 3A and 4A). Similarly, transcriptional levels of metabolic

effector enzymes HK2, GAPDH, LDHA, ASNS, and PDK3 follow BCL2 activity (Figure 3A and Figure 4B).

6.5.7 Dysregulated amino acid and TCA cycle metabolism as part of the BCL2 effector network in cancer

The integral relationship between BCL2 and mitochondria suggests that it may function in regulating cellular metabolism independent of its role in apoptosis. Stable isotope-assisted metabolic flux measurements showed that elevated BCL2 expression increases carbon utilization necessary to support cell cycle progression and cellular proliferation. Tumorigenic overexpression of BCL2 significantly increased flux from D-glucose into pyruvate and lactate, which is indicative of oxidative fermentation and the Warburg effect in cancer cells. Transcriptional networks responding to BCL2 overexpression include activation of NF- κ B, HIF1A, STAT5A and AP1 target genes ensuring activation of fermentative glycolysis and oxidative glutaminolysis (Table 1). The glycolytic phenotype is carried out by transcriptional up-regulation of rate-limiting enzymes HK2, GAPDH, and LDHA. The pentose phosphate pathway is increased, judged by up-regulation of gatekeeper enzymes G6PD, TKT, and TALDO1. The transcription factor complex HIF1A/ARNT controls glycolytic enzyme levels and supports rapid growth. However, by deregulating PDK3, which is another HIF1A target gene, the mitochondrial acetyl-CoA pool is separated from the glycolytic one. The TCA gatekeeping pyruvate dehydrogenase (PDH) complex is switched off by elevated activity of PDK3, which causes inhibition of the PDH complex. The activator of PDHs, PDP2, as well as enzymatic subunits of PDH, PDHA1, and PDHB, are down-regulated to prevent the irreversible conversion from pyruvate into acetyl CoA. At the same time, any other PDK isoforms, PDK1, PDK2, and PDK4, are down-regulated emphasizing PDK3 as sole regulatory step for switching off PDHs. Decoupling of glycolysis depletes TCA cycle metabolite pool sizes and increases dependence on anaplerosis to replenish TCA cycle intermediates [44]. Anaplerotic L-glutamine metabolism is engaged via up-regulation of GLS and ASNS to com-

pensate and support mitochondrial TCA cycle metabolism. The tight connection between BCL2 and ASNS is illustrated by co-occurring SCNAs, synergistic transcriptional regulation, joint strong up-regulation at the protein level, and increased metabolic flux (Figure 1A, 2B, 3A, 4B, 7D). ASNS supports biosynthetic and anaplerotic flux in an L-glutamine-coupled reaction by transferring an amide group from L-glutamine to aspartate thereby generating L-asparagine. L-glutamine, -ketoglutarate, and L-asparagine metabolism is not only important for cancer cell survival but also in oxidative stress and tumor vascularization to offset nutrient and oxygen limitations.

subsection Metabolic bottlenecks upon BCL2 overexpression and dependency on anaplerotic support

Combined metabolic and transcriptional analyses highlight distinct switches attributed to overexpression of BCL2. Enhanced BCL2 expression and BH binding scaffolds stimulate pro-survival interactions and promote mitochondrial stability. In addition, BCL2 overabundance stimulates non-canonical nuclear interactions leading to activation of transcriptional networks facilitating onco-metabolism. Of the tested transcription factors, transcriptional complexes of NFkB1, RELA, HIF1A, ARNT, and STATs are prominently expressed and able to modulate expression of metabolic target genes. Beyond the traditional Warburg effect, which is focused on cytosolic fermentation, the TCA cycle-gatekeeper, PDK3, separates glycolysis and mitochondrial TCA cycle. Congruently, anaplerotic L-glutamine and L-asparagine conversion supports oxidative TCA cycle metabolism and fuels elevated bioenergetics demands of rapidly growing BCL2-positive cells. Since the discovery of L-asparagine-sensitive lymphomas [70], a great deal of research has probed the nature of L-asparagine turnover in cancer and its value as a therapeutic target [71]. In BCL2 overexpressing cell lines, targeting of L-glutamine turnover was immediately responsive, likely due to a metabolic bottleneck created by increased dependency on anaplerotic support. Moreover, ¹³C-assisted stable isotope tracing showed how BCL2-driven lymphoma cell lines are able to reroute TCA cycle related amino acid metabolism and sustain L-glutamine and L-asparagine pathways. Details of how anti-apoptotic regulation generates specific conditions

under which non-essential amino acids becomes indispensable for cancer cells deserve future attention.

6.6 Conclusion

The field of BH domain interactions is at an exciting point. Extensive knowledge and datasets including high-resolution structural and systems biology allow to build on decades of research on pro- and anti-apoptotic mediators providing useful insights into transcriptome, proteome, and interactome of the BH family. Importantly, the therapeutic potential of BCL2 activation by somatic amplification or transcriptional up-regulation has been recognized and offers a genotype-match approach for precision targeting of cancers affected by dysregulation in the pro-survival BH family of onco-proteins. These results suggest DLBC subtype-specific biomarkers based on genomic and transcriptomic alterations of BCL2 and encourage stratification of DLBC patients for targeted therapy with BCL2 inhibitors. Based on genomic, transcriptional, and metabolic readouts of BCL2-activated lymphoma, BCL2 has a pronounced oncogenic phenotype. By triggering a non-canonical network of transcription factors it promotes a metabolic and mitogenic program. Anaplerotic L-glutamine metabolism is engaged via up-regulation of GLS and ASNS creating metabolic vulnerability. Significantly, there is an increased sensitivity to glutaminase inhibition and glutamine deprivation in BCL2-driven lymphoma cells. This is supported by ^{13}C -assisted metabolomics data indicating increased anaplerotic glutamine and asparagine flux. The NF- $\kappa\beta$ /REL complex stands out as master regulator of pro-inflammatory and mitogenic target networks. In addition, it is controlling and impacting downstream transcriptional networks of stimulated STAT and repressed MYC transcription factor networks. The BCL2-NF- $\kappa\beta$ -STAT axis recommends itself as biomarker and anti-cancer target to address an unmet clinical need for the precision management of lymphoma. Dual, BCL2- and NF- $\kappa\beta$ -expressing lymphomas identify a distinct molecular subset of DLBC. In the treatment of such dual BCL2- and NF- $\kappa\beta$ -expressing lymphomas, agents targeting BH domain interactions, immunotherapy,

and chemotherapy focused on metabolic vulnerability should offer significant therapeutic benefit.

6.7 References

- 1 Green DR, Reed JC. Mitochondria and apoptosis. *Science* 1998; 281: 1309-1312.
- 2 Gross A, Katz SG. Non-apoptotic functions of BCL-2 family proteins. *Cell Death Differ* 2017; 24: 1348-1358.
- 3 Yunis JJ, Oken MM, Kaplan ME, Ensrud KM, Howe RR, Theologides A. Distinctive chromosomal abnormalities in histologic subtypes of non-Hodgkin's lymphoma. *N Engl J Med* 1982; 307: 1231-1236.
- 4 Crescenzi M, Seto M, Herzig GP, Weiss PD, Griffith RC, Korsmeyer SJ. Thermostable DNA polymerase chain amplification of t(14;18) chromosome breakpoints and detection of minimal residual disease. *Proc Natl Acad Sci U S A* 1988; 85: 4869-4873.
- 5 Gauwerky CE, Haluska FG, Tsujimoto Y, Nowell PC, Croce CM. Evolution of B-cell malignancy: pre-B-cell leukemia resulting from MYC activation in a B-cell neoplasm with a rearranged BCL2 gene. *Proc Natl Acad Sci U S A* 1988; 85: 8548-8552.
- 6 Tsujimoto Y, Finger LR, Yunis J, Nowell PC, Croce CM. Cloning of the chromosome breakpoint of neoplastic B cells with the t(14;18) chromosome translocation. *Science* 1984; 226: 1097-1099.
- 7 Reed JC, Tsujimoto Y, Alpers JD, Croce CM, Nowell PC. Regulation of bcl-2 proto-oncogene expression during normal human lymphocyte proliferation. *Science* 1987; 236: 1295-1299.
- 8 Nunez G, Seto M, Seremetis S, Ferrero D, Grignani F, Korsmeyer SJ et al. Growth- and tumor-promoting effects of deregulated BCL2 in human B-lymphoblastoid cells. *Proc Natl Acad Sci U S A* 1989; 86: 4589-4593.

- 9 Reed JC, Meister L, Tanaka S, Cuddy M, Yum S, Geyer C et al. Differential expression of *bcl2* protooncogene in neuroblastoma and other human tumor cell lines of neural origin. *Cancer Res* 1991; 51: 6529-6538.
- 10 Miyashita T, Reed JC. *bcl-2* gene transfer increases relative resistance of S49.1 and WEHI7.2 lymphoid cells to cell death and DNA fragmentation induced by glucocorticoids and multiple chemotherapeutic drugs. *Cancer Res* 1992; 52: 5407-5411.
- 11 Chiou SK, Rao L, White E. Bcl-2 blocks p53-dependent apoptosis. *Mol Cell Biol* 1994; 14: 2556-2563.
- 12 Pattingre S, Tassa A, Qu X, Garuti R, Liang XH, Mizushima N et al. Bcl-2 antiapoptotic proteins inhibit Beclin 1-dependent autophagy. *Cell* 2005; 122: 927-939.
- 13 Oltsersdorf T, Elmore SW, Shoemaker AR, Armstrong RC, Augeri DJ, Belli BA et al. An inhibitor of Bcl-2 family proteins induces regression of solid tumours. *Nature* 2005; 435: 677-681.
- 14 Tse C, Shoemaker AR, Adickes J, Anderson MG, Chen J, Jin S et al. ABT-263: a potent and orally bioavailable Bcl-2 family inhibitor. *Cancer Res* 2008; 68: 3421-3428.
- 15 Souers AJ, Levenson JD, Boghaert ER, Ackler SL, Catron ND, Chen J et al. ABT-199, a potent and selective BCL-2 inhibitor, achieves antitumor activity while sparing platelets. *Nat Med* 2013; 19: 202-208.
- 16 Roberts AW, Davids MS, Pagel JM, Kahl BS, Puvvada SD, Gerecitano JF et al. Targeting BCL2 with Venetoclax in Relapsed Chronic Lymphocytic Leukemia. *N Engl J Med* 2016; 374: 311-322.
- 17 London L, McKearn JP. Activation and growth of colony-stimulating factor-dependent cell lines is cell cycle stage dependent. *J Exp Med* 1987; 166: 1419-1435.
- 18 McKearn JP, McCubrey J, Fagg B. Enrichment of hematopoietic precursor cells and cloning of multipotential B-lymphocyte precursors. *Proc Natl Acad Sci U S A* 1985; 82: 7414-7418.

- 19 Mayo MW, Wang XY, Algate PA, Arana GF, Hoyle PE, Steelman LS et al. Synergy between AUUUA motif disruption and enhancer insertion results in autocrine transformation of interleukin-3-dependent hematopoietic cells. *Blood* 1995; 86: 3139-3150.
- 20 Meijerink JP, Van Lieshout EM, Beverloo HB, Van Drunen E, Mensink EJ, Macville M et al. Novel murine B-cell lymphoma/leukemia model to study BCL2-driven oncogenesis. *Int J Cancer* 2005; 114: 917-925.
- 21 Ikushima S, Inukai T, Inaba T, Nimer SD, Cleveland JL, Look AT. Pivotal role for the NFIL3/E4BP4 transcription factor in interleukin 3-mediated survival of pro-B lymphocytes. *Proc Natl Acad Sci U S A* 1997; 94: 2609-2614.
- 22 Bojes HK, Feng X, Kehrer JP, Cohen GM. Apoptosis in hematopoietic cells (FL5.12) caused by interleukin-3 withdrawal: relationship to caspase activity and the loss of glutathione. *Cell Death Differ* 1999; 6: 61-70.
- 23 Yin XM, Oltvai ZN, Korsmeyer SJ. BH1 and BH2 domains of Bcl-2 are required for inhibition of apoptosis and heterodimerization with Bax. *Nature* 1994; 369: 321-323.
- 24 Oltvai ZN, Milliman CL, Korsmeyer SJ. Bcl-2 heterodimerizes in vivo with a conserved homolog, Bax, that accelerates programmed cell death. *Cell* 1993; 74: 609-619.
- 25 Hockenbery D, Nunez G, Milliman C, Schreiber RD, Korsmeyer SJ. Bcl-2 is an inner mitochondrial membrane protein that blocks programmed cell death. *Nature* 1990; 348: 334-336.
- 26 Simonian PL, Grillot DA, Nunez G. Bcl-2 and Bcl-XL can differentially block chemotherapy-induced cell death. *Blood* 1997; 90: 1208-1216.
- 27 Cheng EH, Wei MC, Weiler S, Flavell RA, Mak TW, Lindsten T et al. BCL-2, BCL-X(L) sequester BH3 domain-only molecules preventing BAX- and BAK-mediated mitochondrial apoptosis. *Mol Cell* 2001; 8: 705-711.

- 28 Thomenius MJ, Wang NS, Reineks EZ, Wang Z, Distelhorst CW. Bcl-2 on the endoplasmic reticulum regulates Bax activity by binding to BH3-only proteins. *J Biol Chem* 2003; 278: 6243-6250.
- 29 Bassik MC, Scorrano L, Oakes SA, Pozzan T, Korsmeyer SJ. Phosphorylation of BCL-2 regulates ER Ca²⁺ homeostasis and apoptosis. *EMBO J* 2004; 23: 1207-1216.
- 30 Enis DR, Dunmore B, Johnson N, Pober JS, Print CG. Antiapoptotic activities of bcl-2 correlate with vascular maturation and transcriptional modulation of human endothelial cells. *Endothelium* 2008; 15: 59-71.
- 31 Dingley S, Chapman KA, Falk MJ. Fluorescence-activated cell sorting analysis of mitochondrial content, membrane potential, and matrix oxidant burden in human lymphoblastoid cell lines. *Methods Mol Biol* 2012; 837: 231-239.
- 32 Mermel CH, Schumacher SE, Hill B, Meyerson ML, Beroukhi R, Getz G. GISTIC2.0 facilitates sensitive and confident localization of the targets of focal somatic copy-number alteration in human cancers. *Genome Biol* 2011; 12: R41.
- 33 Tiffen J, Wilson S, Gallagher SJ, Hersey P, Filipp FV. Somatic Copy Number Amplification and Hyperactivating Somatic Mutations of EZH2 Correlate With DNA Methylation and Drive Epigenetic Silencing of Genes Involved in Tumor Suppression and Immune Responses in Melanoma. *Neoplasia* 2016; 18: 121-132.
- 34 Guan J, Gupta R, Filipp FV. Cancer systems biology of TCGA SKCM: efficient detection of genomic drivers in melanoma. *Sci Rep* 2015; 5: 7857.
- 35 Filipp FV, Scott DA, Ronai ZA, Osterman AL, Smith JW. Reverse TCA cycle flux through isocitrate dehydrogenases 1 and 2 is required for lipogenesis in hypoxic melanoma cells. *Pigment Cell Melanoma Res* 2012; 25: 375-383.
- 36 Lanning NJ, Castle JP, Singh SJ, Leon AN, Tovar EA, Sanghera A et al. Metabolic profiling of triple-negative breast cancer cells reveals metabolic vulnerabilities. *Cancer Metab* 2017; 5: 6.
- 37 Singh SJ, Turner W, Glaser DE, McCloskey KE, Filipp FV. Metabolic shift in density-dependent stem cell differentiation. *Cell Commun Signal* 2017; 15: 44.

- 38 Shivakumar L, Armitage JO. Bcl-2 gene expression as a predictor of outcome in diffuse large B-cell lymphoma. *Clin Lymphoma Myeloma* 2006; 6: 455-457.
- 39 Markovic O, Marisavljevic D, Cemerikic V, Perunicic M, Savic S, Filipovic B et al. Clinical and prognostic significance of apoptotic profile in patients with newly diagnosed nodal diffuse large B-cell lymphoma (DLBCL). *Eur J Haematol* 2011; 86: 246-255.
- 40 Akyurek N, Uner A, Benekli M, Barista I. Prognostic significance of MYC, BCL2, and BCL6 rearrangements in patients with diffuse large B-cell lymphoma treated with cyclophosphamide, doxorubicin, vincristine, and prednisone plus rituximab. *Cancer* 2012; 118: 4173-4183.
- 41 Miura K, Takahashi H, Nakagawa M, Izu A, Sugitani M, Kurita D et al. Clinical significance of co-expression of MYC and BCL2 protein in aggressive B-cell lymphomas treated with a second line immunochemotherapy. *Leuk Lymphoma* 2016; 57: 1335-1341.
- 42 Wang JH, Bi XW, Li PF, Xia ZJ, Huang HQ, Jiang WQ et al. Overexpression of MYC and BCL2 Predicts Poor Prognosis in Patients with Extranodal NK/T-cell Lymphoma, Nasal Type. *J Cancer* 2017; 8: 793-800.
- 43 Iqbal J, Neppalli VT, Wright G, Dave BJ, Horsman DE, Rosenwald A et al. BCL2 expression is a prognostic marker for the activated B-cell-like type of diffuse large B-cell lymphoma. *J Clin Oncol* 2006; 24: 961-968.
- 44 Filipp FV, Ratnikov B, De Ingeniis J, Smith JW, Osterman AL, Scott DA. Glutamine-fueled mitochondrial metabolism is decoupled from glycolysis in melanoma. *Pigment Cell Melanoma Res* 2012; 25: 732-739.
- 45 Monni O, Joensuu H, Franssila K, Klefstrom J, Alitalo K, Knuutila S. BCL2 overexpression associated with chromosomal amplification in diffuse large B-cell lymphoma. *Blood* 1997; 90: 1168-1174.
- 46 Ikegaki N, Katsumata M, Minna J, Tsujimoto Y. Expression of bcl-2 in small cell lung carcinoma cells. *Cancer Res* 1994; 54: 6-8.

- 47 Teijido O, Dejean L. Upregulation of Bcl2 inhibits apoptosis-driven BAX insertion but favors BAX relocalization in mitochondria. *FEBS Lett* 2010; 584: 3305-3310.
- 48 Nichele I, Zamo A, Bertolaso A, Bifari F, Tinelli M, Franchini M et al. VR09 cell line: an EBV-positive lymphoblastoid cell line with in vivo characteristics of diffuse large B cell lymphoma of activated B-cell type. *PLoS One* 2012; 7: e52811.
- 49 Sale MJ, Cook SJ. The BH3 mimetic ABT-263 synergizes with the MEK1/2 inhibitor selumetinib/AZD6244 to promote BIM-dependent tumour cell death and inhibit acquired resistance. *Biochem J* 2013; 450: 285-294.
- 50 Han B, Park D, Li R, Xie M, Owonikoko TK, Zhang G et al. Small-Molecule Bcl2 BH4 Antagonist for Lung Cancer Therapy. *Cancer Cell* 2015; 27: 852-863.
- 51 Min KW, Kim DH, Son BK, Kim EK, Seo J, Ahn SB et al. A High Ki67/BCL2 Index Could Predict Lower Disease-Free and Overall Survival in Intestinal-Type Gastric Cancer. *Eur Surg Res* 2017; 58: 158-168.
- 52 Deng J, Park D, Wang M, Nooka A, Deng Q, Matulis S et al. BCL2-BH4 antagonist BDA-366 suppresses human myeloma growth. *Oncotarget* 2016; 7: 27753-27763.
- 53 Veis DJ, Sorenson CM, Shutter JR, Korsmeyer SJ. Bcl-2-deficient mice demonstrate fulminant lymphoid apoptosis, polycystic kidneys, and hypopigmented hair. *Cell* 1993; 75: 229-240.
- 54 Zhao K, Zhang Y, Kang L, Song Y, Wang K, Li S et al. Epigenetic silencing of miRNA-143 regulates apoptosis by targeting BCL2 in human intervertebral disc degeneration. *Gene* 2017; 628: 259-266.
- 55 Rui L, Drennan AC, Ceribelli M, Zhu F, Wright GW, Huang DW et al. Epigenetic gene regulation by Janus kinase 1 in diffuse large B-cell lymphoma. *Proc Natl Acad Sci U S A* 2016; 113: E7260-E7267.
- 56 Garcia-Ramirez I, Tadros S, Gonzalez-Herrero I, Martin-Lorenzo A, Rodriguez-Hernandez G, Moore D et al. Crebbp loss cooperates with Bcl2 overexpression to promote lymphoma in mice. *Blood* 2017; 129: 2645-2656.

57 Davis RE, Brown KD, Siebenlist U, Staudt LM. Constitutive nuclear factor kappaB activity is required for survival of activated B cell-like diffuse large B cell lymphoma cells. *J Exp Med* 2001; 194: 1861-1874.

58 Schuetz JM, Johnson NA, Morin RD, Scott DW, Tan K, Ben-Nierah S et al. BCL2 mutations in diffuse large B-cell lymphoma. *Leukemia* 2012; 26: 1383-1390.

59 Cai Q, Tu M, Xu-Monette ZY, Sun R, Manyam GC, Xu X et al. NF-kappaB p50 activation associated with immune dysregulation confers poorer survival for diffuse large B-cell lymphoma patients with wild-type p53. *Mod Pathol* 2017; 30: 854-876.

60 Hour TC, Chen L, Lin JK. Suppression of transcription factor NF-kappaB activity by Bcl-2 protein in NIH3T3 cells: implication of a novel NF-kappaB p50-Bcl-2 complex for the anti-apoptotic function of Bcl-2. *Eur J Cell Biol* 2000; 79: 121-129.

61 Ivanov VN, Deng G, Podack ER, Malek TR. Pleiotropic effects of Bcl-2 on transcription factors in T cells: potential role of NF-kappa B p50-p50 for the anti-apoptotic function of Bcl-2. *Int Immunol* 1995; 7: 1709-1720.

62 Staudt LM, Dave S. The biology of human lymphoid malignancies revealed by gene expression profiling. *Adv Immunol* 2005; 87: 163-208.

63 Ok CY, Xu-Monette ZY, Li L, Manyam GC, Montes-Moreno S, Tzankov A et al. Evaluation of NF-kappaB subunit expression and signaling pathway activation demonstrates that p52 expression confers better outcome in germinal center B-cell-like diffuse large B-cell lymphoma in association with CD30 and BCL2 functions. *Mod Pathol* 2015; 28: 1202-1213.

64 Yang J, Liao X, Agarwal MK, Barnes L, Auron PE, Stark GR. Unphosphorylated STAT3 accumulates in response to IL-6 and activates transcription by binding to NFkappaB. *Genes Dev* 2007; 21: 1396-1408.

65 Fan J, Zeller K, Chen YC, Watkins T, Barnes KC, Becker KG et al. Time-dependent c-Myc transactomes mapped by Array-based nuclear run-on reveal transcriptional modules in human B cells. *PLoS One* 2010; 5: e9691.

66 Hu S, Xu-Monette ZY, Tzankov A, Green T, Wu L, Balasubramanyam A et al. MYC/BCL2 protein coexpression contributes to the inferior survival of activated B-cell subtype of diffuse large B-cell lymphoma and demonstrates high-risk gene expression signatures: a report from The International DLBCL Rituximab-CHOP Consortium Program. *Blood* 2013; 121: 4021-4031; quiz 4250.

67 Ennishi D, Mottok A, Ben-Neriah S, Shulha HP, Farinha P, Chan FC et al. Genetic profiling of MYC and BCL2 in diffuse large B-cell lymphoma determines cell-of-origin-specific clinical impact. *Blood* 2017; 129: 2760-2770.

68 McDonnell TJ, Korsmeyer SJ. Progression from lymphoid hyperplasia to high-grade malignant lymphoma in mice transgenic for the t(14; 18). *Nature* 1991; 349: 254-256.

69 Strasser A, Harris AW, Bath ML, Cory S. Novel primitive lymphoid tumours induced in transgenic mice by cooperation between myc and bcl-2. *Nature* 1990; 348: 331-333.

70 Broome JD. Evidence that the L-asparaginase of guinea pig serum is responsible for its antilymphoma effects. I. Properties of the L-asparaginase of guinea pig serum in relation to those of the antilymphoma substance. *J Exp Med* 1963; 118: 99-120.

71 Xu Y, Lv F, Zhu X, Wu Y, Shen X. Loss of asparagine synthetase suppresses the growth of human lung cancer cells by arresting cell cycle at G0/G1 phase. *Cancer Gene Ther* 2016; 23: 287-294.

Chapter 7

Inhibition of metabotropic
glutamate receptor 1 and
glutaminase in GRM1-expressing
melanoma restricts glutamate
bioavailability

Inhibition of metabotropic glutamate receptor 1 (GRM1) and glutaminase (GLS) in GRM1-expressing melanoma restricts glutamate bioavailability

Raj Shah ^{1*}, Simar J. Singh ^{3*}, Fabian V. Filipp ^{3#}, Suzie Chen ^{1,2#}

¹ Susan Lehman Cullman Laboratory for Cancer Research, Ernest Mario School of Pharmacy, Department of Chemical Biology, Rutgers University, Piscataway, NJ, USA

² Rutgers Cancer Institute of New Jersey, New Brunswick, NJ, USA

³ Systems Biology and Cancer Metabolism, Program for Quantitative Systems Biology, University of California Merced, Merced, CA, USA

* These authors contributed equally to this work.

Abstract

Aberrant glutamatergic signaling has been implicated in altered metabolic activity in many cancer types including malignant melanoma. Previously, we have illustrated the role of metabotropic glutamate receptor 1 (GRM1) in neoplastic transformation of melanocytes in vitro and spontaneous metastatic melanoma in vivo. Glutamate is the natural ligand of GRM1. It is one of the most abundant amino acids in the human body and the predominant excitatory neurotransmitter in the vertebrate central nervous system.

GRM1-expressing tumor cells including melanoma exhibit elevated extracellular glutamate levels. Autocrine stimulation constitutively activates the glutamate receptor and downstream mitogenic signaling. In addition, significant upregulation of glutaminase (GLS) expression was detected in these GRM1+ cells. GLS catalyzes the first step in the conversion of glutamine to glutamate. In cultured GRM1+ melanoma cells, inclusion of CB-839, a potent, selective, and orally bioavailable inhibitor of GLS, resulted in a profound suppression of cell proliferation. Exposing GRM1+ tumor cells to an inhibitor of glutamate release, riluzole promoted apoptotic cell death in vitro and in vivo. Riluzole is an FDA approved drug for the treatment of amyotrophic lateral sclerosis (ALS) that is mediated by the pathological accumulation of glutamate. In melanoma, combined CB-839 and riluzole treatment proofed to be superior to single agent treatments. Targeting both, metabolic conversion and release, via combined CB-839 and riluzole treatment restricted glutamate bioavailability and led to effective suppression of tumor cell proliferation.

Hyper-activation of GRM1 in malignant melanoma is an oncogenic driver of malignant melanoma, which acts in a BRAF/NRAS independent fashion. Ectopic GRM1 expression promotes a metabolic phenotype that supports increased glutamate production and autocrine glutamatergic signaling, which can be pharmacologically targeted by decreasing the glutaminase-dependent glutamine to glutamate conversion and bioavailability.

Introduction

Melanoma is the most aggressive type of skin cancer and its incidence is on the rise worldwide, accounting for almost 10,000 deaths every year [1, 2]. Although surgically curable at early stages, late stage melanoma is difficult to treat due to genomic tumor variability and therapy resistance [3]. The constitutive activation of the mitogen activated protein kinase pathway is frequently altered in melanoma and initially responsive to targeted treatment [4]. However, disease relapse and tumor progression impedes long-term survival [5]. Newer immunotherapies including CTLA-4 or PD-1 blockade initially display great therapeutic efficacies in patients with advanced melanoma [6, 7]. However, almost all patients acquire resistance to these therapies after varying periods of time [8, 9]. Therefore, there is a clear need for improved combinatorial treatments to combat melanoma.

Utilizing a transgenic mouse model [10], we have established the genotype and tumorigenicity of aberrant expression of metabotropic glutamate receptor 1 (GRM1) in melanoma [11]. In addition to glutamate being the natural ligand of GRM1, our interest in exploring the consequences of altered glutaminolytic glutamate

production is based on previous studies demonstrating that increased resistance to targeted therapy is a result of augmented glutamine dependency in melanoma cells [12, 13]. Consistent with this, we have demonstrated that a reduction in expression or function of GRM1 resulted in a decrease in melanoma cell proliferation in vitro and tumor burden in vivo [14].

GRM1-expressing melanoma cells release excess glutamate into the extracellular environment to warrant constitutive activation of the receptor [15]. Glioma cells use glutamate as an autocrine or paracrine signal to promote cellular migration and invasion [16]. Glioma cells release excess glutamate through a cystine-glutamate antiporter system (xCT), which causes the excitotoxic death of neurons and permits tumor cell expansion [17, 18]. The brain is a common metastatic site for secondary tumors to arise in metastatic melanoma [19]. In addition, enhanced glutamate release has been observed in both breast cancer and prostate cancer cells [20, 21].

Glutamine is the most abundant and multifaceted biomolecule that plays a fundamental role in multiple metabolic processes and signaling in human cells. The vital role of glutamine metabolism in cancer cell proliferation suggests that glutaminolytic enzymes feeding into the tricarboxylic acid (TCA) cycle could be appealing targets for therapy. It has been shown that GLS (glutaminase), an important glutaminolytic enzyme involved in the conversion of glutamine to glutamate, has elevated activity in tumors and is positively correlated with transformation and oncogenesis [22-25]. These findings brought about the design and development of CB-839, a potent, selective, and orally bioavailable GLS inhibitor. Recent studies have shown that CB-839 exhibits anti-proliferative activity in vitro against a panel of triple-negative breast cancer (TNBC) cell lines, as well as in vivo breast cancer models, suggesting that GLS inhibition could lead to therapeutic benefit in patients with TNBC and other glutamine-dependent tumors [26]. In addition, CB-839 is well tolerated in preclinical studies in mice, with no weight loss or toxicity observed [26]. Recent reports also suggest that combining potent GLS inhibitors with other targeted therapies increases the durability of therapeutic responses in a variety of cancers [27, 28]. These results prompted us to investigate a novel therapeutic approach to inhibit glutaminolytic glutamate production and utilization in GRM1+ melanoma through combined actions of CB-839 and riluzole.

Methods

Reagents and antibodies

CB-839 (PubChem CID: 71577426) and riluzole (PubChem CID: 5070) were purchased from Selleckchem, Houston, TX). CB-839 and riluzole were dissolved in dimethyl sulfoxide (DMSO, Fisher Scientific) as 50 mM and 100 mM stock solutions, respectively, and used in treatments at the indicated concentrations. Anti-GLS antibody was purchased from Novus Biologicals (NBP158044, Littelton, CO). Monoclonal α -tubulin antibody was purchased from Sigma Aldrich (T6074, St. Louis, MO). Anti-GRM1 antibody was purchased from Lifespan BioSciences (LSC354444, Seattle, WA).

Cell lines, cell culture reagents and conditions

C8161/C81-61 human melanoma cells were provided by Dr. Mary J.C. Hendrix (Children's Memorial Research Center, Chicago, IL). These cell lines were cultured in RPMI-1640 medium supplemented with 10% fetal bovine serum (FBS). hTERT/CDKR24C/p53DD (AR7119; immortalized normal human melanocytes) cells was provided by Dr. David Fisher (Harvard Medical School, Boston, MA) and maintained in Medium 254 with human melanocyte growth supplements (M-254, Invitrogen, Carlsbad, CA) [29]. All cell lines were maintained at 37 °C in a humidified 5% CO₂ incubator.

For metabolite quantification experiments, 100,000 cells per well were seeded in replicate (n=6) in 6-well plates (657160, Greiner Bio-One, Kremmünster, Germany) in DMEM (10-017, Corning Cell-Gro, Manassas, VA) supplemented with 10% FBS, 1% Penicillin-Streptomycin (30-002-CI, Corning Cell-Gro, Manassas, VA), and 1% MEM Non-Essential Amino Acids (25025-C, Corning Cell-Gro, Manassas, VA). 24 hours following seeding, media was aspirated and replaced with MEM (Corning Cell-Gro, Manassas, VA) supplemented with 1 g/L D-Glucose (0188, Amresco, Solon, OH), 2 mM L-Glutamine (G3126, Sigma Merck, Darmstadt, Germany), 10% FBS, and 1% MEM Vitamins (25-020-CI, Corning Cell-Gro, Manassas, VA).

TGS melanoma model

TGS mice were derived from crosses between TG-3 and SKH-1 for 17 years. TG-3 mice were established as a result of a classic case of insertional mutagenesis that led to the ectopic expression of GRM1 in melanocytes. TG-3 mice spontaneously develop metastatic melanoma with 100% penetrance. Genotypes of TGS mice were performed as described for TG-3 [11].

MTT cell proliferation/viability assays

Cell proliferation was ascertained using MTT reagent as previously described [15]. Briefly, each cell line was cultured in 96-well culture plates (~2500 cells per well) followed by treatment with vehicle (DMSO), CB-839 or/and riluzole at varying concentrations. At indicated time points, the number of viable cells was determined by measuring absorbance (at 560 nm with a reference wavelength of 750 nm) using a 96-well plate reader (Infinite M200 Tecan USA, Durham, NC).

Constructing melanoma cell lines with altered GRM1 expression

Stable C8161 TetR siGRM1 B22-20 clone (C8161si) was generated and maintained in 1 µg/ml blasticidin and 10 µg/ml hygromycin as described [30]. Induction of siGRM1 was carried out by incubating the cells with 10 ng/ml of doxycycline for 4 days. Stable C81-61 GRM1-6 (C8161OE) clone that expresses elevated GRM1 levels compared to parental cell lines was selected with 10 µg/ml blasticidin as illustrated [31].

Glutamate quantification

Glutamate concentration in the conditioned media was measured after 0, 2 or 4 days in culture with glutamate-free MEM using the Glutamine/Glutamate Determination Kit (GLN1, SigmaAldrich) according to the manufacturer's instructions. The determination of L-glutamate was done by measuring the dehydrogenation of L-glutamate to α-ketoglutarate accompanied by reduction of NAD⁺ to NADH. The conversion of NAD⁺ to NADH was determined by measuring absorbance at 340 nm using a 96-well plate reader (Infinite M200 Tecan USA, Durham, NC). The amount of NADH is proportional to the amount of glutamate in each sample.

Metabolite extraction

Following 24 hours incubation in supplemented MEM, 5 µL of supernatant containing conditioned media was transferred to micro centrifuge tubes (MT-0200-BC, Biotix, San Diego, CA) with 1 mL of cold [-20 °C (253 K)] extraction buffer consisting of 50% methanol (A452, Fisher Scientific, Fair Lawn, NJ) in ultrapure (18.2 MΩ x cm) water with 20 µM L-Norvaline (N7627 Sigma Merck, Darmstadt, Germany) and 20 µM DL-Norleucine (N1398, Sigma Merck, Darmstadt, Germany) and dried by vacuum centrifugation in a speedvac concentrator (DNA1200P115, Savant, Thermo Fisher Scientific, Waltham, MA) overnight. The remaining media was aspirated and the cells washed quickly with cold 0.9% sodium chloride in ultrapure water

(Amresco) and placed on ice. To each well, 1 mL of cold extraction buffer was added, the cells scraped on ice and the entire solution was then transferred to a pre-chilled micro centrifuge tube. Tubes were then frozen in liquid nitrogen, thawed, and placed in a digital shaking dry bath (8888-0027, Thermo Fisher Scientific, Waltham, MA) set to 1100 rpm for 15 min at 4 °C (277K). Samples were then centrifuged for 15 min at 4 °C (277 K) and 12500 g in a refrigerated centrifuge (X1R Legend, Sorvall, Thermo Fisher Scientific, Waltham, MA) using a fixed-angle rotor (F21-48x1.5, Sorvall, Thermo Fisher Scientific, Waltham, MA). Supernatants were transferred to new micro centrifuge tubes and dried by vacuum centrifugation overnight.

Metabolite derivatization

Dried, extracted cell samples or media supernatants were derivatized by addition of 20 µL of 2.0% methoxyamine-hydrochloride in pyridine (MOX, TS-45950, Thermo Fisher Scientific, Waltham, MA) followed by 90 min incubation in a digital shaking dry bath at 30 °C (303 K) and 1100 rpm. Then 90 µL of N-methyl-N-trimethylsilyltrifluoroacetamide (MSTFA, 39486610X1ML, Sigma Merck, Darmstadt, Germany) was added and samples incubated at 37 °C (310 K) and 1100 rpm for 30 min before centrifugation for 5 min at 14,000 rpm and 4 °C. The supernatant was transferred to an auto sampler vial (C4000LV3W, Thermo Fisher Scientific, Waltham, MA) with screw cap (C5000-53B, Thermo Fisher Scientific, Waltham, MA) for analysis by gas chromatography (GC, TRACE 1310, Thermo Fisher Scientific, San Jose, CA) coupled to a triple-quadrupole GC mass spectrometry system (QQQ GCMS, TSQ8000EI, TSQ8140403, Thermo Fisher Scientific, San Jose, CA).

GCMS

Samples were analyzed on a QQQ GCMS system equipped with a 0.25 mm inner diameter, 0.25 µm film thickness, 30 m length 5% diphenyl/95% dimethyl polysiloxane capillary column (Trace GOLD TG-5MS, 26098-1420, Thermo Fisher Scientific, Waltham, MA) and run under electron ionization at 70 eV. The GC was programmed with an injection temperature of 250 °C (523 K) and split less injection volume of 1.0 µL. For media samples, a 1:20 split injection was used. The GC oven temperature program started at 50 °C (323 K) for 1 min, rising to 300 °C (573 K) at 10 K/min with a final hold at this temperature for 6 min. The GC flow rate with helium carrier gas (HE, HE 5.0UHP, Praxair, Danbury, CT) was 1.2 mL/min. The transfer line temperature was set at 290 °C (563 K) and ion source

temperature at 295 °C (568 K). A range of 50-600 m/z was scanned with a scan time of 0.25 s.

Metabolomics data processing

Metabolites were identified using Trace Finder (Version 3.3, Thermo Fisher Scientific, Waltham, MA) based on in-house libraries of metabolite retention times and fragmentation patterns. Identified metabolites were quantified using the selected ion count peak area for specific mass ions, and standard curves generated from reference standards run in parallel. Peak intensities were normalized for extraction efficiency using L-norvaline as an internal standard. The mean and standard deviation for each quantified metabolite was calculated for each cell line and treatment condition. A univariate t-test was used to compare means for each metabolite and cell line.

Statistical analysis

Statistical significance of experimental data was calculated using the Stat Plus software (Version 6.2.30) on Microsoft Excel® evaluated by the t-test or ANOVA depending on variables. The statistical significance was set at a p value of *p<0.05, **p<0.01 or ***p<0.001.

Results

Elevated circulating plasma glutamate levels

We derived TGS mice from crosses between melanoma-prone TG-3 [9, 31-33] with hairless SKH-1. Onset and progression of pigmented lesions are very similar in TG-3 and TGS mice; in the absence of hair the pigmented lesions are readily visible in TGS mice. Homozygous TGS mice that harbor two copies of the disrupted endogenous GRM1 gene succumb to large tumor burden by 4-5 months old; thus, frequently are not included in our studies. Heterozygous GRM1+/- TGS mice are viable and show highly pigmented tumors indicating that GRM1 signaling stimulates melanogenesis (Figure 1A). Comparison of glutamate levels in circulating blood plasma between 6-month old heterozygous TGS (harbor only one copy of the disrupted GRM1) and wild type (no disrupted GRM1) TGS mice showed elevated glutamate levels in heterozygous TGS mice (Figure 1B), suggesting aberrant GRM1 expression may promote an increase in ligand, glutamate, to ensure constitutive activation of GRM1 receptor; similar observation was made in in vitro culture cells [15].

Elevated GLS detected in GRM1+ human melanoma cells

Elevated GLS detected in GRM1+ human melanoma cells

Ectopic expression of GRM1 is sufficient to induce cellular transformation in vitro and spontaneous melanoma development in vivo [9]. To investigate a possible relationship between GRM1 expression, glutamine metabolism, and glutaminase (GLS), we first confirmed GRM1 expression in C8161 and UACC903 human melanoma cells, plus immortalized normal human melanocytes, hTERT/CDKR24C/p53DD (AR7119). C8161 is a malignant human melanoma cell line that expresses wild type BRAF. UACC903 is another malignant melanoma cell line that harbors a BRAF (V600E) mutation. Both C8161 and UACC903 demonstrated significantly elevated levels of GRM1 and GLS compared to hTERT/CDKR24C/p53DD cells with almost undetectable GRM1 and much lower GLS expression (Figure 2).

GLS inhibition reduces proliferation/viability of GRM1+ human melanoma cells

In in vitro MTT assays both GRM1-expressing human melanoma cells, C8161 (with 0.5µM CB-839) and UACC903 (with 50µM CB-839) displayed modest efficacy in suppressing cell growth in the presence of CB-839 as compared with the control vehicle (DMSO) group regardless of their BRAF genotypes (Figure 3). To determine if GRM1 modulates the responsiveness to GLS inhibition, exogenous human GRM1 cDNA was introduced into an early stage melanoma cell line, C81-61, which does not express endogenous GRM1 (Figure 6E). Characterization of several GRM1-expressing C81-61 clones confirmed that these clones were transformed and tumorigenic [30]. Here we chose to compare the growth rate of the parental C81-61 cells to the C81-61 GRM1-6 clone in the presence of CB-839. A marked reduction in the cell proliferation of C81-61 GRM1-6 was seen with 0.5µM CB-839 as compared to the vehicle (DMSO) control (Figure 3). Strikingly, very little if any changes was detected in growth of the parental C81-61 cells with analogous treatment conditions (Figure 3). These results suggest that GRM1 expression may influence the responsiveness of melanoma cells to GLS inhibition.

Combinatorial treatment with CB-839 and riluzole leads to enhanced inhibition of GRM1+ melanoma cell proliferation

Suppressive effects of riluzole on GRM1+ melanoma cell proliferation [15, 34, 35]. Here, the consequences of including both CB-839 and riluzole on the cell proliferation of two GRM1-expressing human

melanoma cell lines were investigated. As shown in Figure 4, C8161 cells were treated for 7 days with 0.5 μ M CB-839, 10 μ M riluzole or 0.5 μ M CB-839 + 10 μ M riluzole. Treatment with either CB-839 or riluzole reduced C8161 cell proliferation by ~40%, while combining both CB-839 and riluzole led to a decrease of ~85% when compared to vehicle treated control cells. However, a higher concentration of CB839 and riluzole was needed to reduce cell growth with another GRM1-expressing melanoma cell line (UACC903) that harbor mutated BRAF (Figure 4), similar to our earlier observations [14]. Furthermore, increasing evidence illustrate that the presence of a mutation in BRAF frequently makes cancer cells less responsive to various targeted treatments. UACC903 cells harbor a BRAF (V600E) mutation where as C8161 cells do not. Taken together, our results suggest that CB-839 combined with riluzole can enhance the anti-proliferative properties of CB-839, and that higher doses may be needed to administered in BRAF-mutant cells.

CB-839 treatment leads to inhibition of glutamate release from GRM1+ human melanoma cells

Inclusion of riluzole in cultured media modulated the amount of glutamate released by melanoma cells [15]. To determine the consequences on the amount of glutamate released by GRM1+ melanoma cells upon treatment with CB-839 only or riluzole + CB-839 (treatment concentrations were determined by MTT results shown in Figure 4). C8161 cells were plated in glutamate-free MEM media followed by collection of conditioned media at days 0, 2 and 4. We plated different number of C8161 cells so at time of collecting the conditioned-media samples, the cell numbers were very similar among the different days (Figure 5A). In parallel we also performed cell viability/cell proliferation MTT assays to ensure that the treated cells were viable, as the levels of glutamate release were determined. Results from the Glutamine/Glutamate Determination Kit showed that extracellular glutamate levels were significantly reduced in the conditioned culture media isolated from CB-839, riluzole or CB-839+riluzole treated C8161 cells compared to the untreated cells (Figure 5B).

Modulation of GRM1 alters the intracellular production of glutaminolytic and glycolysis metabolites in human melanoma cells

We next asked whether modulation of GRM1 expression affects the intracellular levels of key glutaminolytic and glycolytic metabolites. To investigate the effect of modulating GRM1 expression, we analyzed

both overexpression of GRM1 in a GRM1 low background (parental C81-61 and C81-61OE) and suppression of GRM1 in a GRM1 high background (parental C8161 and C8161si). While suppression or overexpression of GRM1 failed to alter intracellular lactate concentration (Figure 6A), higher levels of GRM1 were accompanied by significantly increased levels of intracellular citrate, alpha-ketoglutarate, and glutamate ($p < 0.01$) (Figures 6B-D). This indicates that GRM1 expression does not increase lactate fermentation but does increase levels of TCA cycle intermediates. The increased intracellular pool size of glutamate could be a direct result of increased conversion of glutamine into glutamate via the activity of GLS. To determine whether modulating GRM1 expression affects the level of GLS, we assayed GLS protein levels by western blot. Consistent with our observed glutamate concentrations, cells with higher levels of GRM1 also had higher levels of GLS protein (Figure 6E). These results suggest that GRM1 expression increases glutamate production by increasing GLS expression.

Discussion

The high frequency of ectopic GRM1 expression in melanoma, and its signaling cascades implicated in cellular transformation, has made it a principal research interest among many groups seeking better therapeutic strategies for the treatment of melanoma. In this study, the role of metabotropic glutamate receptor 1 (GRM1) in modulating glutamate bioavailability in melanoma cells was explored. Our results suggest that GRM1 expression promotes a metabolic phenotype that supports increased glutamate production and autocrine glutamatergic signaling. Glutamatergic signaling through GRM1 leads to increased expression of GLS, potentially increasing the conversion of glutamine into glutamate. However, the exact mechanism by which GRM1 regulates GLS remains under investigation. Melanoma cells heavily depend on anaplerosis via glutamine [36, 37]. GRM1-positive melanoma cells upregulate GLS to support increased levels of glutamate. Excess amounts of intracellular glutamate get excreted, where it serves as trigger for the GRM1 receptor. In neuronal cell lineages, cytoplasmic glutamate is exported via vesicular glutamate transporters or cystine-glutamate exchangers [40].

We demonstrate elevated glutamate in systemic circulation of heterozygous TGS mice (harbor only one copy of the disrupted GRM1) compared to that of wild type TGS mice (no disrupted GRM1). This may lead to the constitutively activated GRM1 receptor, further promoting cell proliferation and metabolism pathways. To break such positive feedback signals, we tested different

pharmacological vulnerabilities of glutamate signaling and metabolism. While inhibition of glutamatergic signaling by decreasing glutamate release via riluzole or inhibition of GLS activity via CB-839 resulted in a proliferative relieve, the combination of both approaches was most effective. We also expected to see enhanced reduction of glutamate in the conditioned media after co-treatment with riluzole and CB-839 but this was not the case. Tumor cells have the ability to compensate for GLS inhibition and can overcome glutamate deprivation [39].

While the role of glutamine metabolism in cancer cells is well established, less clear is how this role is influenced by the tumor microenvironment, which can face shortages of oxygen and various nutrients [40]. Recently, we discovered that one of the consequences of aberrant GRM1 signal transduction is the downstream activation of hypoxia-induced transcription factor 1, HIF-1 α , which promotes angiogenesis even in normoxic conditions [30]. Further, the molecular basis for alterations in glutamine metabolism of mammalian cells is linked to HIF-1 α activity [41]. Whether HIF-1 α is the link between GRM1 and GLS is being investigated. Lastly, we observe robust changes in TCA cycle intermediates but no changes in intracellular lactate levels upon GRM1 modulation likely suggesting that GRM1 preferentially manipulates glutamine metabolism over glucose metabolism. Furthermore, recent reports demonstrate that GLS inhibition enhances the effectiveness of chemotherapy in ovarian cancer cells [42] and also improves the efficacy of other targeted therapies [26, 27], suggesting the critical role of targeting GLS in an attempt to improve overall patient response. These insights, combined with our data, support the rationale to combine riluzole with CB-839 to combat GRM1-positive human neoplasia including melanoma.

Acknowledgements

This research has been funded in part by a grant from New Jersey Health Foundation and Veterans Administration Research award 101BX003742 to S.C.. F.V.F. is grateful for the support of grant CA154887 from the National Institutes of Health, National Cancer Institute and grant CRN-17-427258 by the University of California, Office of the President, Cancer Research Coordinating Committee, the Goethe Institute, Washington, DC, USA, and the Federal Foreign Office, Berlin, Germany.

Figures

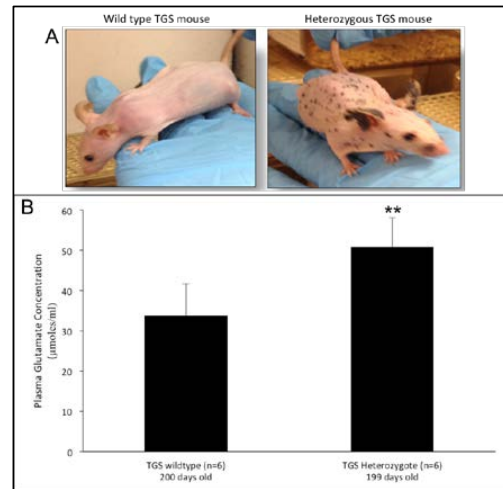


Figure 1: Phenotypes of wild type and heterozygous TGS genotypes

A) Pigmented lesions on the skin of heterozygous TGS mice are easily visualized compared to the WT with no copies of the disrupted endogenous GRM1 gene. Homozygous (not shown) and heterozygous TGS mice are indistinguishable; the major difference is the onset of the disease, 6-8 weeks for homozygous TGS, and 7-8 months for heterozygous TGS.

B) Elevated circulating glutamate levels in plasma isolated from heterozygous TGS mice: Glutamate concentration in plasma isolated from wild type (200 days old) or heterozygous TGS mice (199 days old) was measured using the Glutamate Determination Kit (GLN1, Sigma-Aldrich) according to the manufacturer's instructions. Data are given as μ moles of glutamate per mL of plasma and represented as mean \pm STDEV (n=6). Student's t-test was used to calculate statistical significance. **p<0.01

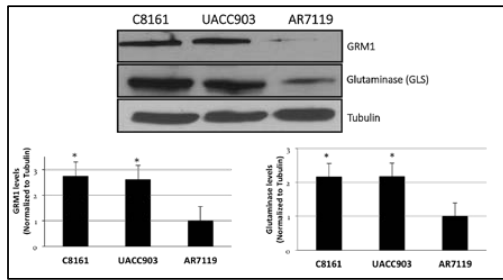


Figure 2: Visualization of epigenomic and transcriptional cooperation illustrates redundancy and complexity of a target network.

Hierarchical trees of human transcription factors correspond to transcription factor superclass, class, and family from inward out. Transcription factor motifs often get recognized by multiple members of the same transcription factor family due to structural homology of DNA binding domains. The transcription factor target analysis (TFT) is carried out on sequence-specific epigenomics data.

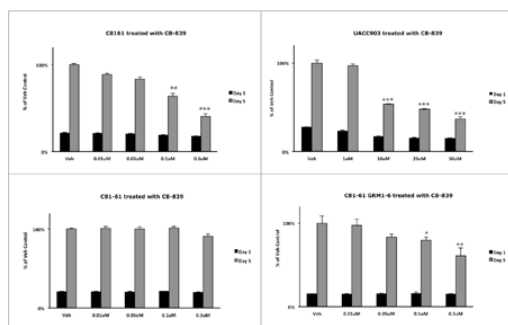


Figure 3: Inhibition of GLS reduces proliferation of GRM1-expressing melanoma cells.

MTT cell viability/proliferation assays were performed on GRM1-positive C8161, UACC903 and C81-61 GRM1-6 cells, and GRM1-negative C81-61 cells. The conditions for all cells except UACC903 were vehicle (DMSO) or CB-839 at 0.01, 0.05, 0.1 and 0.5 μ M. For UACC903, higher concentrations (1, 10, 25 and 50 μ M) of CB-839 were used. Each time point and concentration shown represents a mean \pm STDEV of four independent reads. A one-way ANOVA test with Bonferroni's post-hoc analysis was used to calculate statistical significance between experimental and control groups. * p <0.05; ** p <0.01, *** p <0.001.

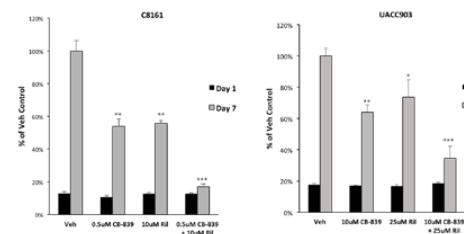


Figure 4: Enhanced suppression of proliferation of GRM1-expressing human melanoma cells with CB-839 and Riluzole.

MTT cell viability/proliferation assays were performed on GRM1-expressing C8161 and UACC903 cells. For C8161 cells, the treatment conditions were vehicle (DMSO), CB-839 or/and riluzole at 0.5 μ M and 10 μ M respectively. For UACC903 cells, CB-839 or/and riluzole were used at 10 μ M and 25 μ M respectively. Each time point and concentration shown represents a mean \pm STDEV of four independent reads. A two-way ANOVA test with Bonferroni's post-hoc analysis was used to calculate statistical significance between experimental and control groups. * p <0.05; ** p <0.01; *** p <0.001.

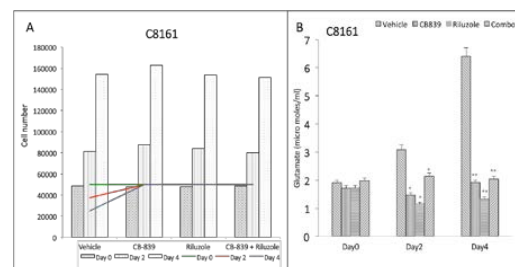


Figure 5: CB-839 treatment leads to inhibition of glutamate release in GRM1+ human melanoma cells.

Human melanoma C8161 cells were assessed for the amount of glutamate they release into the extracellular medium after treatment with CB-839, riluzole or CB-839 + riluzole. (A) Different number of cells was plated such that comparable numbers of cells were present at time of sample (conditioned medium) collection. The line chart refers to the number of total cells that were plated at day 0 and the bar graph represents the number of viable cells during sample collection at day 0, day 2 or day 4. (B) Concentrations of extracellular glutamate within each treatment group are shown. Statistical analysis was performed between control (vehicle) and treated pairs to

show significance. Each bar represents mean \pm STDEV, n=3. *p<0.05; **p<0.01.

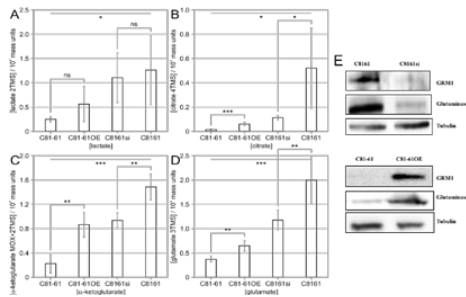


Figure 6: Modulation of GRM1 alters the intracellular production of glutaminolytic and glycolytic metabolites in human melanoma cells.

The intracellular concentrations of lactate (A), citrate (B), α -ketoglutarate (C), and glutamate (D) were detected in C81-61, C81-61OE, C8161 and C8161si cells by GCMS analysis. Data represent the average of six independent reads (mean \pm STDEV). *p<0.05; **p<0.01; ***p<0.001; ns=no significance. (E) Modulations in GRM1 and subsequent changes in glutaminase protein levels in C81-61, C81-61OE, C8161 and C8161si cells were determined by Western blot. Tubulin was used as the loading control.

References

1. Siegel, V., Adding patient education of skin cancer and sun-protective behaviors to the skin assessment screening on admission to hospitals. *Medsurg Nurs*, 2012. 21(3): p. 1834.
2. Siegel, R.L., K.D. Miller, and A. Jemal, Cancer statistics, 2016. *CA: A Cancer Journal for Clinicians*, 2016. 66(1): p. 7-30.
3. Sabel, M.S., Y. Liu, and D.M. Lubman, Proteomics in Melanoma Biomarker Discovery: Great Potential, Many Obstacles. *International Journal of Proteomics*, 2011. 2011: p. 181890.
4. Filipp, F.V., Precision medicine driven by cancer systems biology. *Cancer Metastasis Reviews*, 2017. 36(1): p. 91-108.
5. Zecena, H., et al., Systems biology analysis of mitogen activated protein kinase inhibitor resistance in malignant melanoma. *BMC Systems Biology*, 2018. 12: p. 33.

6. Bucheit, A.D. and M.A. Davies, Emerging insights into resistance to BRAF inhibitors in melanoma. *Biochem Pharmacol*, 2014. 87.

7. Johnson, D.B. and J.A. Sosman, Therapeutic Advances and Treatment Options in Metastatic Melanoma. *JAMA Oncol*, 2015. 1(3): p. 380-6.

8. Poulidakos, P.I., et al., RAF inhibitor resistance is mediated by dimerization of aberrantly spliced BRAF(V600E). *Nature*, 2011. 480(7377): p. 387-90.

9. Poulidakos, P.I. and N. Rosen, Mutant BRAF melanomas--dependence and resistance. *Cancer Cell*, 2011. 19(1): p. 11-5.

10. Zhu, H., et al., Development of early melanocytic lesions in transgenic mice predisposed to melanoma. *Pigm. Cell Res.*, 2000. 13: p. 158-164.

11. Pollock, P.M., et al., Melanoma mouse model implicates metabotropic glutamate signaling in melanocytic neoplasia. *Nat Genet*, 2003. 34(1): p. 108-12.

12. Baenke, F., et al., Resistance to BRAF inhibitors induces glutamine dependency in melanoma cells. *Molecular Oncology*, 2016. 10(1): p. 73-84.

13. Hernandez-Davies, J.E., et al., Vemurafenib resistance reprograms melanoma cells towards glutamine dependence. *Journal of Translational Medicine*, 2015. 13(1): p. 210.

14. Shin, S.S., et al., Oncogenic activities of metabotropic glutamate receptor 1 (Grm1) in melanocyte transformation. *Pigment Cell Melanoma Res*, 2008a. 21(3): p. 368-78.

15. Namkoong, J., et al., Metabotropic glutamate receptor 1 and glutamate signaling in human melanoma. *Cancer Research*, 2007. 67(5): p. 2298-305.

16. Lyons, S.A., et al., Autocrine glutamate signaling promotes glioma cell invasion. *Cancer Res*, 2007. 67(19): p. 9463-71.

17. Sontheimer, H., A role for glutamate in growth and invasion of primary brain tumors. *J Neurochem*, 2008. 105(2): p. 287-95.

18. Ye, Z.C., J.D. Rothstein, and H. Sontheimer, Compromised glutamate transport in human glioma cells: reduction-mislocalization of sodium-dependent glutamate transporters and enhanced activity of cystine-glutamate exchange. *J Neurosci*, 1999. 19(24): p. 10767-77.

19. Xie, T.X., et al., Activation of stat3 in human melanoma promotes brain metastasis. *Cancer Res*, 2006. 66(6): p. 3188-96.

20. Seidltz, E.P., et al., Cancer cell lines release glutamate into the extracellular environment. *Clin Exp Metastasis*, 2009. 26(7): p. 781-7.
21. Koochekpour, S., et al., Serum glutamate levels correlate with Gleason score and glutamate blockade decreases proliferation, migration, and invasion and induces apoptosis in prostate cancer cells. *Clin Cancer Res*, 2012. 18(21): p. 5888-901.
22. Lora, J., et al., Antisense glutaminase inhibition decreases glutathione antioxidant capacity and increases apoptosis in Ehrlich ascitic tumour cells. *European Journal of Biochemistry*, 2004. 271(21): p. 4298-4306.
23. Cairns, R.A., I.S. Harris, and T.W. Mak, Regulation of cancer cell metabolism. *Nat Rev Cancer*, 2011. 11(2): p. 85-95.
24. Wang, J.B., et al., Targeting mitochondrial glutaminase activity inhibits oncogenic transformation. *Cancer Cell*, 2010. 18(3): p. 207-19.
25. Filipp, F.V., et al., Glutamine-fueled mitochondrial metabolism is decoupled from glycolysis in melanoma. *Pigment Cell Melanoma Res*, 2012. 25(6): p. 732-9.
26. Gross, M.I., et al., Antitumor activity of the glutaminase inhibitor CB-839 in triplenegative breast cancer. *Mol Cancer Ther*, 2014. 13(4): p. 890-901.
27. Momcilovic, M., et al., Targeted inhibition of EGFR and glutaminase induces metabolic crisis in EGFR mutant lung cancer. *Cell reports*, 2017. 18(3): p. 601-610.
28. Xie, C., et al., Inhibition of mitochondrial glutaminase activity reverses acquired erlotinib resistance in non-small cell lung cancer. *Oncotarget*, 2016. 7(1): p. 610-621.
29. Garraway, L.A., et al., Integrative genomic analyses identify MITF as a lineage survival oncogene amplified in malignant melanoma. *Nature*, 2005a. 436(7047): p. 117-22.
30. Wangari-Talbot, J., et al., Functional Effects of GRM1 Suppression in Human Melanoma Cells. *Mol Cancer Res*, 2012.
31. Wen, Y., Li, J., Koo, j., Shin, S., Lin, Y., Jeong, B., Chen, S., Mehnert, J., Cohen-Solal, K. and Goydos, J., Activation of the glutamate receptor GRM1 enhances angiogenic signaling to drive melanoma progression. *Cancer Research*, 2014.
32. Ohtani, Y., et al., Metabotropic glutamate receptor subtype-1 is essential for in vivo growth of melanoma. *Oncogene*, 2008. 27: p. 7162-7170.
33. Chen, S., et al., Spontaneous melanocytosis in transgenic mice. *J. Invest. Dermatol.*, 1996. 106: p. 1145-1150.
34. Zhu, H., et al., Development of heritable melanoma in transgenic mice. *J. Invest. Dermatol.*, 1998. 110: p. 247-252.
35. Le, M.N., et al., The Glutamate Release Inhibitor Riluzole Decreases Migration, Invasion and Proliferation of Melanoma Cells. *The Journal of investigative dermatology*, 2010. 130(9): p. 2240-2249.
36. Isola, A.L., et al., Exosomes released by metabotropic glutamate receptor 1 (GRM1) expressing melanoma cells increase cell migration and invasiveness. *Oncotarget*, 2018. 9(1): p. 1187-1199.
37. Lee, H.J., et al., Glutamatergic pathway targeting in melanoma; single agent and combinatorial therapies. *Clin Cancer Res*, 2011. 17: p. 7080-7092.
38. Scott, D.A., et al., Comparative Metabolic Flux Profiling of Melanoma Cell Lines: BEYOND THE WARBURG EFFECT. *The Journal of Biological Chemistry*, 2011. 286(49): p. 42626-42634.
39. Filipp, F.V., et al., Reverse TCA cycle flux through isocitrate dehydrogenases 1 and 2 is required for lipogenesis in hypoxic melanoma cells. *Pigment cell & melanoma research*, 2012. 25(3): p. 375-383.
40. Schallier, A., et al., Region- and age-specific changes in glutamate transport in the AbetaPP23 mouse model for Alzheimer's disease. *J Alzheimers Dis*, 2011. 24(2): p. 287300.
41. Mayers, J.R. and M.G. Vander Heiden, Famine versus feast: understanding the metabolism of tumors in vivo. *Trends in biochemical sciences*, 2015. 40(3): p. 130-140.
42. Metallo, C.M., et al., Reductive glutamine metabolism by IDH1 mediates lipogenesis under hypoxia. *Nature*, 2012. 481(7381): p. 380-4.
43. Masamha, C.P. and P. LaFontaine, Molecular targeting of glutaminase sensitizes ovarian cancer cells to chemotherapy. *Journal of Cellular Biochemistry*. 0(0).

Chapter 8

Future Studies

Metabolic rewiring, including increased glucose and glutamine consumption, is a prominent feature of malignant melanoma[14]. GRM1 expressing cells increase their production and release of glutamate, thereby engaging in an autocrine loop involving leading to increased GRM1 mediated oncogenic signaling[59]. Treatment with riluzole, which blocks glutamate release, disrupts GRM1 mediated signaling and exhibits anti-tumor properties[913].

The source of increased glutamate production in GRM1+ melanoma cells remains unclear. Glutamate can be generated by the deamination of imported glutamine by glutaminases[9] (glutaminase, GLS, Gene ID: 2744 and glutaminase 2, GLS2, Gene ID: 27165) with subsequent oxidation in a process termed glutaminolysis. Given the relatively direct metabolic path from glutamine to glutamate, and the increased dependence upon glutamine metabolism in melanoma, it has been speculated that this is the preferred route of glutamate production in cancer. Alternatively, glycolytic pyruvate can enter the TCA cycle via either decarboxylation into acetyl-CoA or carboxylation into oxaloacetic acid, eventually generating oxoglutarate (alpha-ketoglutarate) [AKG]. AKG can then undergo transamination forming glutamate, a reaction catalyzed by several aminotransferases including AST, ALT. In addition, amination of AKG with ammonium may be reversibly catalyzed by glutamate dehydrogenase (GLUD1, Gene ID: 2746).

Understanding the metabolic pathways enlisted by GRM1+ melanoma to increase glutamate production may lead to the development of rational drug combinations targeting aberrant GRM1 signaling and accompanying metabolic rewiring. To determine the relative and absolute contributions of glucose and glutamine towards glutamate production, ^{13}C based tracer studies and GCMS could be used to measure isotopic enrichment in glutamate following labeling with ^{13}C glucose or ^{13}C glutamine (Figure 8.1). This would identify the major source of glutamate, and how metabolic flux into glutamate is affected by drug treatments, such as with riluzole or GLS inhibition.

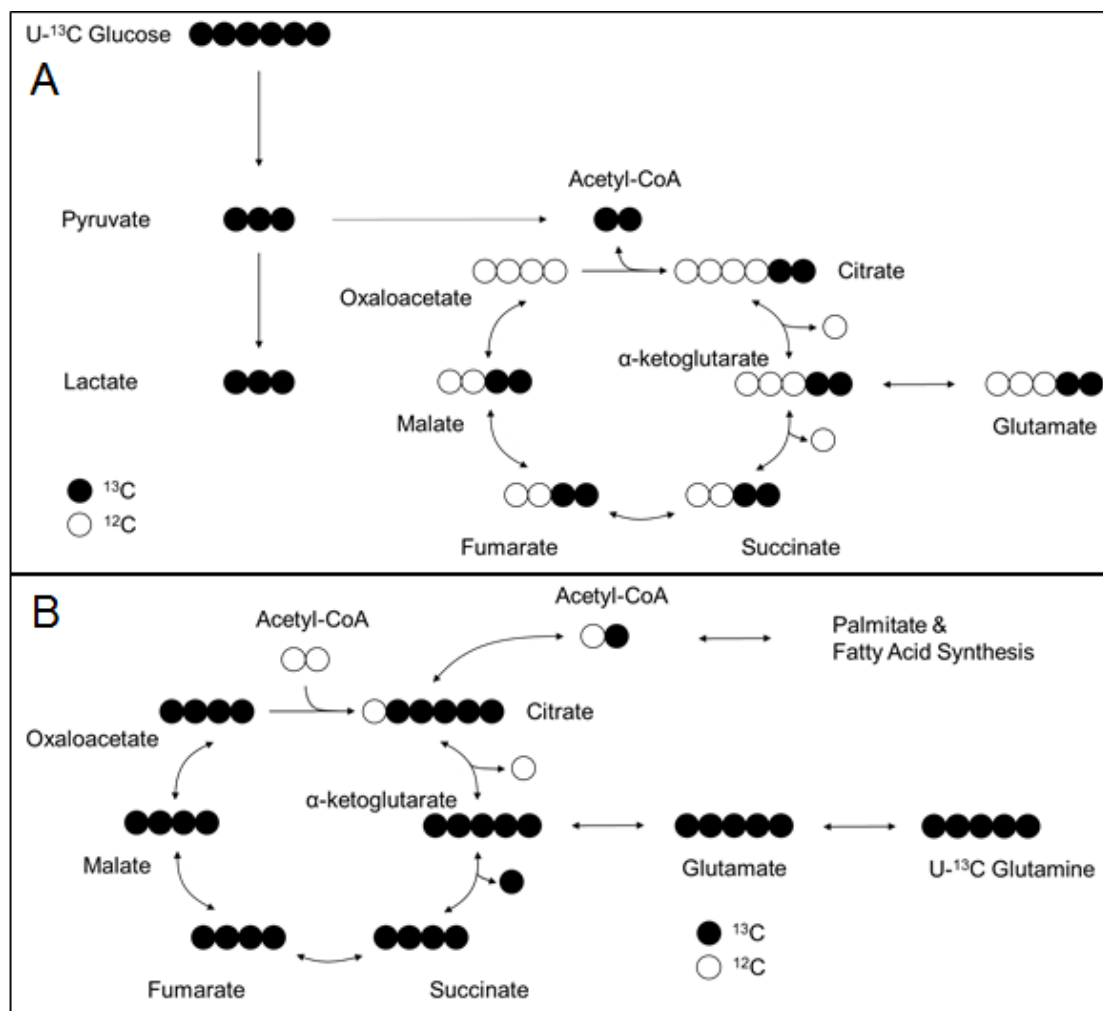


FIGURE 8.1: Atom transition map for ^{13}C labeling with A) U- ^{13}C Glucose and B) U- ^{13}C Glutamine

To validate this approach, combination therapies targeting glutamate production via pathways identified by stable isotope tracing should be utilized in additional pre-clinical studies, including murine xenograft models. Another area for future study is the contribution of the tumor micro-environment to glutamate secretion. It is possible that tumor stromal cells and other infiltrating cells support melanoma cell survival by increasing the supply of extracellular glutamate available for GRM1 activation on tumor cells. Single-cell RNA-seq analysis of tumor tissue would help identify the expression level of metabolic enzymes implicated in glutamate production in these adjoining cell populations, potentially identifying a new mechanistic link between metabolism, signaling, and the tumor microenvironment. Confirming and then inhibiting the metabolism of glutamate production in other tumor-associated cell types could help limit tumor growth.

Reference

1. Scott DA, Richardson AD, Filipp F V, et al. Comparative metabolic flux profiling of melanoma cell lines: beyond the Warburg effect. *J Biol Chem.* 2011;286(49):42626-42634. doi:10.1074/jbc.M111.282046.
2. Filipp FV, Ratnikov B, De Ingeniis J, Smith JW, Osterman AL, Scott DA. Glutamine-fueled mitochondrial metabolism is decoupled from glycolysis in melanoma. *Pigment Cell Melanoma Res.* 2012;25(6):732-739. doi:10.1111/pcmr.12000.
3. Filipp FV, Scott DA, Ronai ZA, Osterman AL, Smith JW. Reverse TCA cycle flux through isocitrate dehydrogenases 1 and 2 is required for lipogenesis in hypoxic melanoma cells. *Pigment Cell Melanoma Res.* 2012;25(3):375-383. doi:10.1111/j.1755-148X.2012.00989.x.
4. Fischer GM, Vashisht Gopal YN, McQuade JL, Peng W, DeBerardinis RJ, Davies MA. Metabolic strategies of melanoma cells: Mechanisms, interactions with the tumor microenvironment, and therapeutic implications. *Pigment Cell Melanoma Res.* 2018;31(1):11-30. doi:10.1111/pcmr.12661.
5. Shin S-S, Namkoong J, Wall BA, Gleason R, Lee HJ, Chen S. Oncogenic activities of metabotropic glutamate receptor 1 (Grm1) in melanocyte transfor-

- mation. *Pigment Cell Melanoma Res.* 2008;21(3):368-378. doi:10.1111/j.1755-148X.2008.00452.x.
6. Namkoong J, Shin S-S, Lee HJ, et al. Metabotropic glutamate receptor 1 and glutamate signaling in human melanoma. *Cancer Res.* 2007;67(5):2298-2305. doi:10.1158/0008-5472.CAN-06-3665.
 7. Seidlitz EP, Sharma MK, Saikali Z, Ghert M, Singh G. Cancer cell lines release glutamate into the extracellular environment. *Clin Exp Metastasis.* 2009;26(7):781-787. doi:10.1007/s10585-009-9277-4.
 8. Koochekpour S, Majumdar S, Azabdaftari G, et al. Serum glutamate levels correlate with Gleason score and glutamate blockade decreases proliferation, migration, and invasion and induces apoptosis in prostate cancer cells. *Clin Cancer Res.* 2012;18(21):5888-5901. doi:10.1158/1078-0432.CCR-12-1308.
 9. Shah R, Singh SJ, Filipp F V., Chen S. Inhibition of GRM1 and GLS in metabotropic glutamate receptor 1-expressing melanoma restricts glutamate bioavailability. *Cancer Res.* 2018. - *Submitted*
 10. Wall BA, Wangari-Talbot J, Shin SS, et al. Disruption of GRM1-mediated signalling using riluzole results in DNA damage in melanoma cells. *Pigment Cell Melanoma Res.* 2014;27(2):263-274. doi:10.1111/pcmr.12207.
 11. Wall BA, Yu LJ, Khan A, Haffty B, Goydos JS, Chen S. Riluzole is a radiosensitizing agent in an in vivo model of brain metastasis derived from GRM1 expressing human melanoma cells. *Pigment Cell Melanoma Res.* 2015;28(1):105-109. doi:10.1111/pcmr.12327.
 12. Rosenberg SA, Niglio SA, Salehomoum N, et al. Targeting Glutamatergic Signaling and the PI3 Kinase Pathway to Halt Melanoma Progression. *Transl Oncol.* 2015;8(1):1-9. doi:10.1016/j.tranon.2014.11.001.
 13. Mehnert JM, Silk AW, Lee JH, et al. A phase II trial of riluzole, an antagonist of metabotropic glutamate receptor 1 (GRM1) signaling, in patients with advanced melanoma. *Pigment Cell Melanoma Res.* 2018. doi:10.1111/pcmr.12694.

Chapter 9

Conclusion

Understanding how metabolism supports cell fate decisions is an important question in development biology, tissue engineering, and oncology. In the first project, density-dependent VPC differentiation was found to be a process in which cell-cell contacts reinforce a metabolic shift away from glycolysis, lactate fermentation and proliferation towards oxidative metabolism and cell growth. ESCs cultured at high density were more efficiently differentiated into VPCs, a phenomenon that coincided with an increase in the expression of cell adhesion molecules and a decrease in lactate production and glucose utilization. This metabolic shift supported increased differentiation and growth of VPC while also helping reduce cell proliferation. Future studies could expand on this work by quantitatively determining nutrient conditions that promote or inhibit VPC differentiation. Additionally, stable isotope labeling and metabolic flux analysis could help identify other metabolic pathways utilized during the differentiation process. This would allow precise engineering of metabolic pathways to promote target cell differentiation via genetic and chemical means.

The metabolism of cancer cells is known to support continued growth under a diverse set of nutrient conditions. However, being able to effectively translate this knowledge of cancer cell metabolism into rationally designed therapeutic regimens is not yet widespread. In the second project described in this work, mass spectrometry based metabolic profiling of TNBC cells identified the metabolic heterogeneity

among TNBC subtypes, and in the process revealed metabolic vulnerabilities that sensitize these cells to targeted tyrosine kinase therapy. Hierarchical clustering of intracellular metabolite levels showed that molecular subtypes of TNBC display different metabolic responses to drug inhibition, suggesting significant metabolic heterogeneity amongst subtypes. Chief amongst these differential responses was a reduction in TCA cycle intermediates, which are vital not only for oxidative metabolism, but also for the generation of fatty acids via reductive carboxylation. When an siRNA screen against metabolic pathways was applied to TNBC cells following RTK inhibition, it was found that knockdown of pathways dependent upon TCA anaplerosis, such as fatty acid and nucleotide synthesis, were highly lethal to subtypes of TNBC with reduced TCA metabolite concentrations. This suggests that by metabolically characterizing the intracellular levels of metabolites in cancer cells, one could systematically identify synthetically lethal combinations of molecular therapies. Future studies should expand on this hypothesis by creating predictive models of synthetic lethality based on intracellular metabolite concentrations. One could then test these predictions by modulating the level of intracellular metabolites and targeting biochemical pathways reliant upon those metabolite pools.

Mitochondria play an integral role in both metabolism and the control of cell death. While it is well established that the BCL2 family of proteins regulate apoptosis, it is less clear what if any role the anti-apoptotic mitochondrial BCL2 protein plays in regulating metabolism. Moreover, though BCL2 is amplified in many cancers which exhibit an altered metabolic phenotype, it is unknown if BCL2 amplification affects metabolism. In the third project detailed in this work, an examination of non-canonical BCL2 mediated effects were elucidated using genomic, transcriptomic and metabolomics approaches. Tumorigenic amplification of BCL2 was detected to co-occur with amplification of the metabolic enzyme ASNS and several metabolism regulating transcription factors, including HIF, MYC, NF-KB and STAT family members. Furthermore, overexpression of BCL2 in a pro-B cell line increased the expression of these transcription factors. On a metabolic level, stable isotope tracing indicated that BCL2 overexpression increased glycolytic flux into lactate and glutaminolytic flux into the TCA cycle and asparagine. This

decoupling of glycolytic and mitochondrial metabolism increased the dependence of BCL2 overexpressing cells to glutamine deprivation and glutaminases inhibition. These effects were reversed by the use of a BCL2 mutant incapable of binding to BAX. Together these results indicate that BCL2 expression produces a profound oncogenic phenotype consisting of significant transcriptional and metabolic regulation. This combined analysis of transcriptional and metabolic networks identified a metabolic dependency on glutamine and asparagine metabolism that should offer significant therapeutic benefit.

Melanoma cells employ diverse metabolic strategies to adapt and survive under varied micro-environmental conditions. Two such strategies include the rewiring of metabolism to support growth in the presence of MAPK inhibition and to promote autocrine signaling through the metabotropic glutamate receptor GRM1, detailed in the fifth and sixth chapters of this work respectively. Transcriptional analysis of BRAF inhibitor resistant melanoma revealed a significant non-genomic rewiring of mitogenic signaling and metabolic pathways. This approach identified several transcription factor families whose activity may play a role in the development of BRAF inhibitor resultant melanoma. It will be useful to combine this transcriptomic data with data from metabolomics experiments to better understand how transcriptional changes are related to metabolic adaptations in the generation of resistance. Genome scale models using transcriptomic profiling could be created and then validated with experimental determination of metabolite pool sizes, pathway fluxes, and uptake rates for formal metabolic flux analysis. This would be the first such examination of kinase inhibitor resistance in cancer.

Melanoma and several other cancers rely upon mitogenic autocrine signaling through the GRM1 receptor. The results presented in this work indicate that signaling through GRM1 is responsible for increased expression of the glutamate producing enzyme GLS and increased glutamate production by melanoma cells in-vivo. Inhibition of GLS and glutamate release lowers cell viability and proliferation in melanoma cells. This suggests that reducing the bioavailability of glutamate could serve as an effective treatment for GRM1 expressing melanoma cells. Important questions regarding the biochemical pathways that support increased glutamate production remain. For instance, are there routes other than glutaminolysis

which help GRM1 expressing cells produce glutamate? Stable isotope tracing studies should resolve the relative contribution of glutamine and glucose towards glutamate production, thereby identifying additional enzyme targets for inhibition alongside GLS.

Together these results highlight the important role metabolism plays in supporting cellular function. Further development of metabolomics based analytical techniques in conjunction with other omics strategies will permit systems biologists to better characterize key cellular states and processes. The application of systems biology principles to clinical problems will continue to usher in an era of precision guided, personalized medicine.